

Physics and Chemistry of Interstellar Ice

Physics and Chemistry of Interstellar Ice

PROEFSCHRIFT

ter verkrijging van
de graad van Doctor aan de Universiteit Leiden,
op gezag van de Rector Magnificus prof. mr. dr. C. J. J. M. Stolker,
volgens besluit van het College voor Promoties
te verdedigen op dinsdag 26 mars 2013
klokke 15.00 uur

door

Karoliina Marja-Riitta Guss (née Isokoski)
geboren te Nivala, Finland
in 1982

Promotiecommissie

Promotores: Prof. dr. H. V. J. Linnartz
Prof. dr. E. F. van Dishoeck

Overige leden: Prof. dr. A. G. G. M. Tielens
Prof. dr. H. J. A. Rottgering
Dr. M. R. Hogerheijde
Dr. G. M. Muñoz Caro
Dr. M. E. Palumbo
Dr. S. Cazaux

Centro de Astrobiología
Osservatorio Astrofisico di Catania
Kapteyn Astronomical Institute

Table of Contents

1	Introduction	1
1.1	Formation and evolution of interstellar ice	2
1.2	Complex molecules in the laboratory	5
1.3	Morphology of interstellar ice	7
1.4	Composition of interstellar ice	9
1.5	Complex organic molecules	10
1.6	This thesis	11
1.7	Main conclusions	13
2	Thermal collapse of porous amorphous solid water	15
2.1	Introduction	16
2.2	Experimental methods	17
2.3	Results	20
2.3.1	Interference data and infrared spectra during deposition	20
2.3.2	Thermal processing of different ice morphologies	21
2.4	Discussion	24
2.5	Conclusions	27
3	Morphology of porous ASW and CO₂ containing ices	29
3.1	Introduction	30
3.2	Experimental methods	32
3.2.1	Experimental setup	32
3.2.2	Optical interference	32
3.2.3	IR spectroscopy	35
3.3	Results	36
3.3.1	Deposition	36
3.3.2	Thermal annealing	41
3.3.3	Thickness	42
3.3.4	IR spectroscopy	44
3.4	Discussion	45
3.4.1	Refractive index of pure H ₂ O	45
3.4.2	Thermal annealing of pure H ₂ O	46
3.4.3	Density of pure H ₂ O	48
3.4.4	Residual porosity in annealed H ₂ O	48
3.4.5	Pure CO ₂ ice	49
3.4.6	H ₂ O-CO ₂ binary ice	50
3.4.7	CO ₂ segregation	51
3.5	Summary and conclusions	53

4	CO mixed in CH₃OH ice: answer to the missing 2152 cm⁻¹ band?	55
4.1	Introduction	56
4.2	Experimental methods	58
4.3	Observations of the red component	59
4.4	Dangling-OH blocking by CO ₂	62
4.5	CO mixed with CH ₃ OH	65
4.6	Conclusions and astrophysical implications	67
5	Highly resolved infrared spectra of pure CO₂ ice	69
5.1	Introduction	70
5.2	Experimental procedure	72
5.3	Results	73
5.3.1	Corrections	75
5.4	Discussion	76
5.5	Optical Constants and Grain Shape-Corrections	80
5.6	Summary	83
6	Laser-desorption TOF mass spectrometry of cryogenic ices	85
6.1	Introduction	86
6.2	Instrumentation	87
6.2.1	Substrate	89
6.2.2	Sample deposition	89
6.2.3	Processing	89
6.2.4	Laser desorption	89
6.2.5	Entrainment	90
6.2.6	Time-of-flight mass analysis	91
6.2.7	EI Ionization	91
6.3	Results	92
6.3.1	Calibration	92
6.3.2	Carrier gas profile	92
6.3.3	Laser desorption of pure ices	93
6.3.4	Sensitivity	96
6.3.5	VUV photoprocessed C ₂ H ₆	96
7	Chemistry of massive young stellar objects with a disk-like structure	99
7.1	Introduction	100
7.2	Observations	102
7.2.1	Observed sources	102
7.2.2	Observational details	105
7.3	Data analysis	106
7.3.1	Rotation diagrams	106
7.3.2	Spectral modeling	107
7.4	Results	109
7.4.1	General results and comparison between sources	109

7.4.2	Optical depth determinations	110
7.4.3	Temperatures	110
7.4.4	Column densities	112
7.5	Discussion	116
7.5.1	Comparison to massive YSOs without a disk structure	116
7.5.2	Chemical and physical implications	122
7.6	Summary and conclusions	124
7.7	Appendix	125
7.7.1	Detected lines per species for all sources	125
7.7.2	Rotation diagrams	144
7.7.3	Weeds and CASSIS model parameters	150
7.7.4	Additional detections	153
	Literature	156
	Nederlandse samenvatting	167
	Publications	173
	Curriculum vitae	175
	Acknowledgements	177

Chapter I

INTRODUCTION

The importance of ice in the interstellar medium (ISM) is indisputable. Gas phase reactions relying on three-body collisions are exceedingly rare in the sparse medium between the stars. On solid surfaces, atoms and molecules can reside and rove the surface until a reaction takes place. Upon reaction, the released energy is dissipated into the grain, allowing the new species to form. Solid surfaces thus act as sites for chemical processes, that would otherwise be very slow, or not take place at all.

Interstellar processes influence the structure, composition and evaporation of ices. Astronomical observations of ices and gas evaporated from them, are direct probes of the physical conditions in the interstellar medium. Ices can therefore trace the evolution of material and shed light on essential processes, such as the formation of solar systems like our own.

Owing to the strong hydrogen bonding in interstellar ices, sticking of small icy dust grains may be enhanced. Porous ice structures dissipate collision energy and hence facilitate the aggregation at high velocities. This can promote coagulation and the formation of larger solar system bodies and planetesimals.

Interstellar ices are important repositories of complex organic molecules and have a potential prebiotic bearing on the origin of life. Icy comets may have delivered volatiles and organic material relevant for the origin of life on the early Earth. Also water in our oceans may derive from this reservoir. With the growing number of detected exoplanets, this may be universally important.

Hence, the composition and physical structure of interstellar ice are of fundamental importance to our understanding of the formation of stars, planets and the origin of life. This thesis is devoted to the understanding of the physical and chemical properties of interstellar ice using a range of observational and experimental techniques.

1.1 Formation and evolution of interstellar ice

No discussion of interstellar ices would be meaningful without an understanding of the environment in which they are formed: dense molecular clouds. The interstellar medium – material between stars in the galaxy – is an inhomogenous distribution of gas (99 mass %) and dust (1 mass %). The most dense regions of the ISM are the protostellar cores, where the density is high enough to lead to a gravitational collapse resulting in the birth of new stars and planets (Shu et al. 1987, McKee & Ostriker 2007). The collapsing regions are fed from a larger molecular cloud, the density of which is high enough (10^3 – 10^5 cm⁻³) to provide shielding from the harsh external UV field. It is under these conditions that interstellar ices form on cold dust grains. At average molecular cloud densities of 10^4 cm⁻³ atoms and molecules land on the surface of a sub-micron sized dust grain in average once per day (e.g., Tielens & Allamandola 1987). The low temperatures allow particles to accrete, rove the surface and form new molecules. Sheltered from the strong UV field, molecules are able to accumulate on the grain to form a mantle of interstellar ice (Fig. 1.1).

The composition of interstellar ice is determined by the physical conditions in the ambient gas. Most carbon arrives on the dust grain in the form of carbon monoxide (CO). Hydrogen (H), nitrogen (N) and oxygen (O) may be in atomic or molecular form. Even at

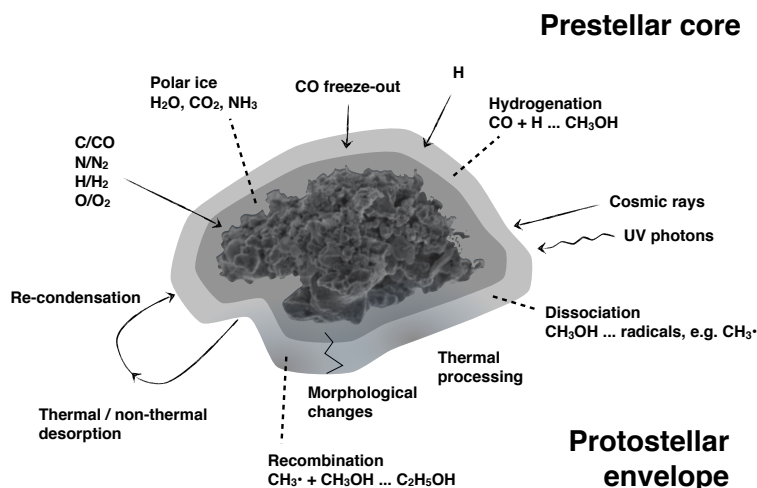


Figure 1.1 – Processes in interstellar ices.

the low temperatures of the cloud ~ 10 K, atoms are able to scan the grain surface and find other atoms and molecules to react with. Hydrogen atoms do so by quantum tunneling (Manicò et al. 2001), while heavier atoms such as C and O through thermal hopping (Tielens & Allamandola 1987). The resulting ice layer is a result of simple atom addition reactions. The molecular composition of these pristine interstellar ices is expected to be dominated by water (H_2O), with significant amounts of H_2CO , N_2 , CO_2 , H_2O_2 , NH_3 , and CO (Tielens & Hagen 1982).

A number of interstellar ice surveys have been carried out (Gibb et al. 2000, 2004, Knez et al. 2005, Boogert et al. 2008, Pontoppidan et al. 2008, Öberg et al. 2011a, Bottinelli et al. 2010). Fig. 1.2 shows the ice composition towards a dust-embedded high mass young stellar object (YSO) W33A obtained with *Infrared Space Observatory* (ISO) (Gibb et al. 2000). This typical spectrum of interstellar ice shows silicate features from the dust as well as small molecules frozen as interstellar ice. Ices are dominated by water (H_2O), with significant amounts of CO, CO_2 and CH_3OH , as well as smaller abundances of NH_3 , CH_4 , H_2CO , HCOOH , OCS and several ionic species (van Dishoeck 2004). Methanol (CH_3OH) is one of the more common ice components with abundances varying from 2 to 15 % relative to H_2O (Bottinelli et al. 2010, Boogert et al. 2008). CH_3OH forms on the cold dust grains through successive hydrogenation of CO (Tielens & Hagen 1982, Tielens & Allamandola 1987, Hiraoka et al. 2002, Watanabe & Kouchi 2002, Fuchs et al. 2009) and is considered an important intermediate in the production of complex organic molecules in the star-forming regions (Charnley 1997, Garrod & Herbst 2006, Garrod et al. 2008, Öberg et al. 2009b).

Ice mantles covering the interstellar dust are inhomogeneous in their composition. Species with relatively low volatility accumulate more readily on the grain surface than

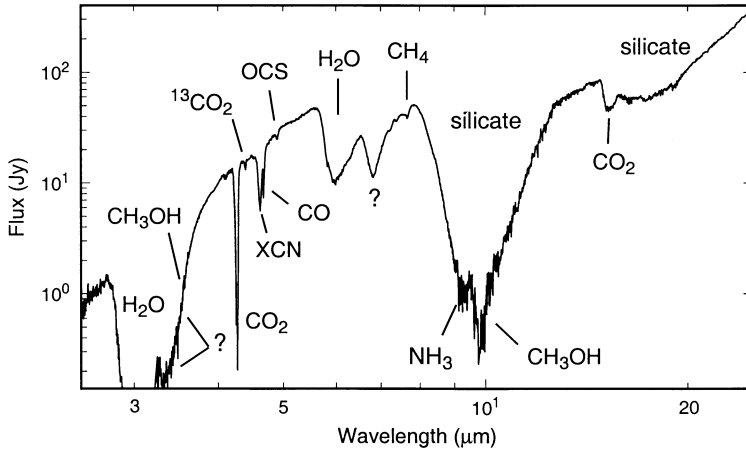


Figure 1.2 – 2.4–25 μm SWS flux spectrum of W33A from [Gibb et al. \(2000\)](#).

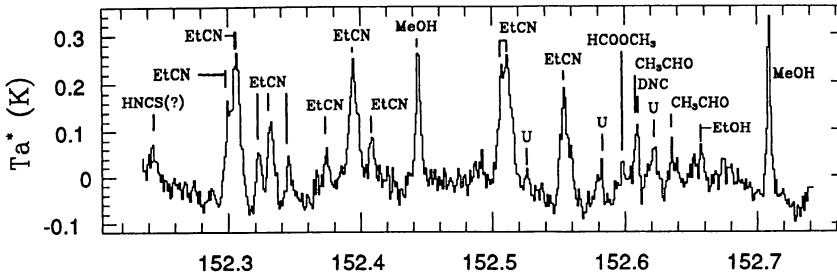


Figure 1.3 – Spectrum of Orion-KL from [Ziurys & McGonagle \(1993\)](#).

those with high volatility. As the cloud collapses and the density and shielding gradually increase, the dust will first acquire a polar layer dominated by H_2O , followed by CO freeze-out into a separate apolar layer ([Bergin et al. 2005](#), [Knez et al. 2005](#), [Pontoppidan 2006](#)). Furthermore, temperature changes in the cloud can cause distillation and segregation of mixed ice components ([Öberg et al. 2009a](#), [Fayolle et al. 2011](#)). As the majority of the CO_2 forms simultaneously with H_2O on the grain ([Bergin et al. 2005](#)), this process is considered responsible for the presence of pure CO_2 in interstellar ices ([Gerakines et al. 1999](#), [Pontoppidan et al. 2008](#), [Kim et al. 2012](#)). Various mechanisms are suggested to return ice molecules into the gas phase, including grain heating by cosmic rays, mantle explosions, ejection upon chemical reaction, sputtering through low-velocity shock waves and grain-grain collisions ([Willacy et al. 1998](#), [Bergin et al. 1998](#), [Charnley et al. 2001](#), [Markwick et al. 2000](#), [Dickens et al. 2001](#)).

While the majority of the features observed in ices (Fig. 1.2) can be explained by non-

energetic surface reactions, there is evidence that interstellar ices are subject to energetic processing. One of such is the XCN feature around $4.62\ \mu\text{m}$ (Gibb et al. 2000), which is attributed to OCN^- formed by UV photolysis, ion bombardment and/or thermal reactions (e.g., Grim & Greenberg 1987, Bernstein et al. 1995, Schutte & Greenberg 1997, Demyk et al. 1998, Bernstein et al. 2000, Palumbo et al. 2000). Indeed, interstellar ices are not shielded from cosmic rays which can penetrate deep into the cloud. In addition to direct interaction with the ice, cosmic rays generate an internal UV field in the cloud through secondary electron excitation of H_2 (Prasad & Tarafdar 1983, Gredel et al. 1989). The resulting flux of $10^3\ \text{photons cm}^{-2}\ \text{s}^{-1}$, while much smaller than in the unshielded regions outside of the cloud, is strong enough to drive photochemistry in the ice. Both UV photons and cosmic rays break bonds in ice molecules producing highly reactive radicals. The radicals may directly recombine to reform the parent species or be left with enough energy to relocate and react with another molecule. Radicals can also become trapped in the ice, immobilized until further changes in the ice conditions.

In the early phase of cloud collapse, atoms and molecules radiatively cool the cloud (Bergin & Tafalla 2007). As the cloud opacity increases with density, energy can no longer escape, which inevitably leads to heating of the ices in the surrounding envelope. One of the consequences of increasing temperature for ices is the mobilization of larger species in the ice, and consequent recombination of radicals into larger, complex organic molecules (Garrod et al. 2008). It is difficult to find observational evidence for molecular complexation in interstellar ices (Schutte et al. 1999, Gibb et al. 2004). Fundamental vibrational transitions of ice species are located in a relatively narrow spectral window. Line broadening caused by the solid environment leads to overlapping features, that are dominated by the most abundant ice components. The abundance of species decreases with complexity, making IR spectroscopy of ices a futile method to study complex molecules in the interstellar medium.

Large number of complex molecules are observed in the gas phase around high- and low-mass protostars (Herbst & van Dishoeck 2009) (Fig. 1.3). The temperature in these regions has increased beyond 100 K, leading to the evaporation of ices. The origin of these complex molecules was initially thought to be the rich gas phase chemistry of evaporated species (e.g., Herbst et al. 1977, Millar et al. 1991, Charnley et al. 1992, 1995). However, recent experimental work shows the inefficiency of gas phase reactions (Horn et al. 2004, Geppert et al. 2006) and that according to models many of the observed molecules must be primarily produced in ices prior to evaporation (Garrod & Herbst 2006, Garrod et al. 2008, Wakelam et al. 2010).

1.2 Complex molecules in the laboratory

A large portion of experimental astrochemistry is dedicated to the simulation of interstellar ices in the laboratory. These interstellar ice analogs are grown and processed under space-like conditions; high- or ultra-high vacuum (10^8 – $10^5\ \text{particles cm}^{-3}$) and low temperatures (10–300 K). Under controlled laboratory settings, astronomical processes can be isolated and characterized, and their astronomical relevance assessed, e.g., though as-

trochemical models.

Energetic processing of simple interstellar ice analogs drives the formation of complex molecules in the ice (*e.g.*, [Hagen et al. 1979](#), [Allamandola et al. 1988](#), [Schutte et al. 1993b](#), [Bernstein et al. 1995](#), 2002, [Muñoz Caro et al. 2002](#), [Muñoz Caro & Schutte 2003](#), [Bennett & Kaiser 2007](#), [Elsila et al. 2007](#)). The products depend primarily on the available reactants and the ice temperature. In UV irradiated pure CH₃OH ice, the photo-fragments: CH₃, CH₂OH, HCO and CH₃O, recombine to produce complex organic species such as C₂H₅OH, HCOOCH₃ and CH₃OCH₃ ([Gerakines et al. 1996](#), [Öberg et al. 2009b](#)), all of which have been observed in the ISM. In general the production of complex molecules sets off at elevated temperatures (≥ 50 K) as the radical fragments become mobile. While CH₃OH is able to provide the fragments for many of the observed gas phase molecules, the presence of NH₃ opens new reaction pathways to nitrogen containing, biologically interesting molecules. NH₃ catalyzes the thermal polymerization of H₂CO to polyoxymethylene (POM) $-(CH_2-O)_n-$ ([Schutte et al. 1993b,a](#), [Bernstein et al. 1995](#)). In mixed ices, the hydrogen atoms tend to be replaced by active functional groups $-OH$ and $-NH_2$. In UV photoprocessed interstellar ice analogs, a large portion of NH₃ is converted into a cyclic hexamethylenetetramine (HMT) – a precursor of amino acids ([Bernstein et al. 1995](#)).

Correlation of results obtained from interstellar ice analogs with ices in the interstellar medium requires critical evaluation of the applicability of those results. One of the main concerns for the solid state production of complex molecules is the reliability of the analysis techniques; are the produced molecules formed under interstellar conditions or during the sample analysis? In order to avoid the latter, non-intrusiveness of the analysis methods is important. IR spectroscopy reveals the composition of ice remotely through excitation of vibrational modes of the molecules. As is the case for astronomical ice observations, the main problem for H₂O dominated interstellar ices is the large width of the solid state absorption features, caused by the broad energy range of the trapping sites. Line widths of trapped species that do not participate in the hydrogen bonding network, such as CO (ν_3) stretch ($4.6\ \mu m$), are around $10\ cm^{-1}$ compared to the $2.2\ cm^{-1}$ in pure form ([Bouwman et al. 2007](#)). IR spectra of complex organic species are characterized by their functional groups (*e.g.*, ketones C=O) which coincide for different molecules belonging to the same group. Due to these factors, the applicability of IR spectroscopy is limited to relatively simple ices.

Mass spectrometry is a sensitive technique in which molecules are transported from the ice to the sensor where the identification is based on their mass. Mass spectrometry requires relocation of the sample, which poses a challenge to maintain the chemical composition during sample analysis. Relocation of volatile ice components is currently done by slowly warming the ice until species evaporate. This temperature-programmed desorption (TPD) provides an inventory of molecules produced in the ice, but is blind to the low temperature chemistry and the transient species in the ice. For the understanding of complex ice chemistry, the large involatile species are of particular interest. UV photoprocessed interstellar ice analogs leave behind a significant residue at room temperature. The chromatographic analysis of the material reveals the presence of a number of complex species including amino-acids (Fig. 1.4). Again, only a final inventory can be obtained.

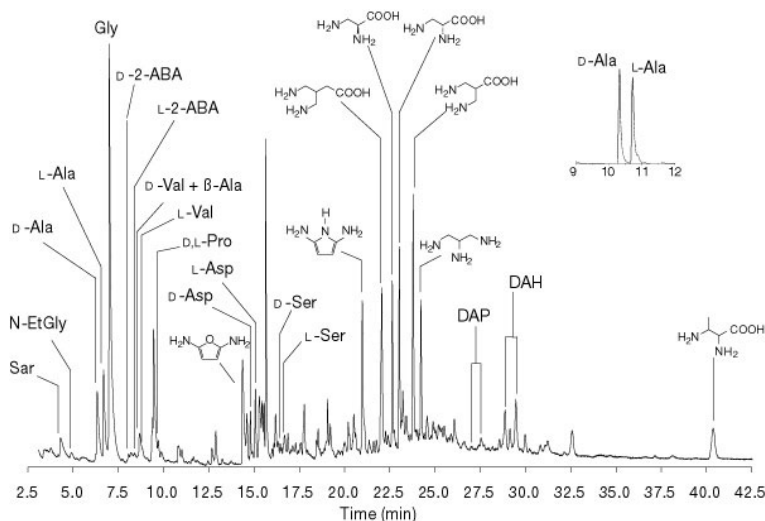


Figure 1.4 – Gas chromatography mass spectrum (GC-MS) of a room-temperature residue of UV photoprocessed interstellar ice analogue from [Muñoz Caro et al. \(2002\)](#).

Moreover, the analysis requires chemical alteration which may generate molecules, that are not present in the ices prior to analysis. For the characterization of the processes and evaluation of their importance in an astronomical environment, the experimental challenges described above remain to be dealt with.

1.3 Morphology of interstellar ice

H₂O dominates the composition of interstellar ice (*e.g.*, [Whittet et al. 1998](#), [Gibb et al. 2004](#), [Pontoppidan et al. 2004](#), [Boogert et al. 2008](#)). In the gas phase H₂O has abundances varying from 10⁻⁸ (with respect to H₂) in cold dense regions where most of it resides in ices on interstellar dust grains, to 10⁻⁴ in warm gas and shocked regions where it evaporates or is sputtered from the ice ([van Dishoeck & Helmich 1996](#), [Melnick & Bergin 2005](#), [Bjerkeli et al. 2009](#)). Gas-phase chemistry cannot reproduce the H₂O abundances observed in the interstellar medium ([d'Hendecourt et al. 1985](#), [Hasegawa et al. 1992](#)). Formation of H₂O through several different grain-surface routes was suggested by [Tielens & Hagen \(1982\)](#), and in recent years has been subject to a number of studies, both theoretical ([Cuppen & Herbst 2007](#), [Goumans et al. 2009](#), [Cazaux et al. 2010](#)) and experimental ([Miyachi et al. 2008](#), [Ioppolo et al. 2008](#), [Matar et al. 2008](#), [Oba et al. 2009](#), [Mokrane et al. 2009](#), [Ioppolo et al. 2010](#), [Cuppen et al. 2010](#), [Dulieu et al. 2010](#), [Ennis et al. 2011](#), [Romanzin et al. 2011](#), [Jing et al. 2011](#)). While the importance of different routes remains to be confirmed, the origin of H₂O in surface-catalyzed reactions is now recognized.

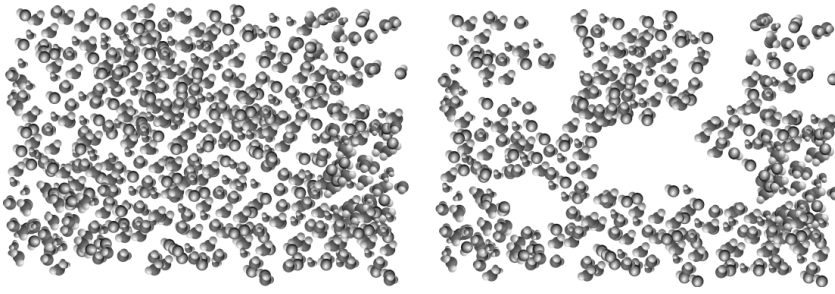


Figure 1.5 – Illustration of compact (left) and porous (right) amorphous solid water.

The morphology of H_2O is dominated by its hydrogen-bonding character. Depending on the pressure and temperature, H_2O can exist in 15 different forms, differentiated by the degree of crystalline structure, ordering and density. In the biosphere, practically all water is in crystalline I_h form, with hexagonal symmetry and near tetrahedral bonding angles. In astronomical environments, most observed H_2O is in amorphous form, deduced from the broad absorption feature around $3.07 \mu\text{m}$, corresponding to the bulk asymmetric OH stretching (ν_3) mode. Amorphous solid water (ASW) exhibits tetrahedral H-bonding network, but lacks long range crystalline order. The unordered structure provides a broad range of trapping sites, making the absorption features broad (Hagen 1981). ASW can be subdivided into three distinct structures, defined by the distance between adjacent O atoms: low-density ASW (I_{lda}) with a density of 0.94 g cm^{-3} (Narten et al. 1976), high-density ASW (I_{hda}) with a density of 1.17 g cm^{-3} (Mishima et al. 1984), and very high-density ASW (I_{vhda}) with a density of 1.26 g cm^{-3} (Mishima 1996, Loerting et al. 2001). The structure of vapor deposited H_2O , relevant for some interstellar ices, depends on the temperature. In the laboratory, deposition onto a surface below 30 K results in I_{hda} , while $\geq 30 \text{ K}$ I_{lda} is produced (Jenniskens et al. 1995). I_{vhda} has not been shown to form through vapor deposition. Upon increase in temperature, I_{hda} restructures to I_{lda} at 38–68 K (Jenniskens & Blake 1994) owing to defects in the ice structure. At 148 K, the ice structure changes into cubic crystalline I_c until its evaporation between 180 and 188 K.

In the interstellar medium, particles land on the dust grain in random trajectories. On the cold $< 130 \text{ K}$ surfaces, where diffusion is limited, larger particles become incorporated in the ice near their landing site. For H_2O , this "hit and stick" film growth results in porous ice structure (Buch 1992, Barabási & Stanley 1995, Cuppen & Herbst 2007). Porous ASW, as opposed to compact ASW (Fig. 1.5) has mm-sized cavities with internal surface area from hundreds to thousands of m^2/g (Mayer & Pletzer 1986, Bar-Nun et al. 1987, Manca 2000, Martin 2002, Ayotte et al. 2001). The porosity of ASW depends on the ice growth conditions such as temperature, growth rate and directionality of H_2O molecules landing on the ice surface (Berland et al. 1995, Westley et al. 1998, Stevenson et al. 1999, Kimmel et al. 2001b,a, Dohnálek et al. 2003). Energetic processing in the ISM is expected to reduce the porosity of ASW. The compaction of porous ASW has been experimentally

demonstrated to be driven by cosmic rays and UV photons (Palumbo 2006, Palumbo et al. 2010, Raut et al. 2008), as well as by thermal processing (Bar-Nun & Owen 1998, Bossa et al. 2012).

In the interstellar medium, porosity can have an important impact on chemical processes relying on surface accessibility. Porous ice provides large effective surface areas for adsorption of atoms and molecules, catalysis of chemical reactions, and further retention of these species. Large quantities of molecules are stored inside pores and later thermally released (Collings et al. 2003, Raut et al. 2007a). Structural changes in interstellar ices (intrinsic phase transitions and reduction of porosity) can have interesting consequences for the chemistry. Pore collapse at low temperatures may drive diffusion limited recombination of radicals trapped in interstellar ices (Schutte 1988, Jenniskens & Blake 1994).

1.4 Composition of interstellar ice

The band profiles of molecules trapped in interstellar ices provide a wealth of information about the ice composition. The lattice environment influences the strength of molecular bonds, and the vibrational frequencies become shifted from the corresponding gas-phase values. The presence of multiple trapping sites manifests itself as an overall broadening of absorption features. The lattice environment is primarily determined by the molecular composition of the ice. The composition of interstellar ice can therefore be inferred from the shape of the observed absorption features. Moreover, certain ice features may be influenced by the shape of the grain. While this complicates the interpretation of the ice composition, it can also be used as an indication of how the ice layer has been formed.

A number of laboratory studies have focussed on the characterization of the band profiles of abundant ice species, particularly that of CO₂ and CO (Sandford et al. 1988, Sandford & Allamandola 1990, Tielens et al. 1991, Palumbo & Strazzulla 1993, Ehrenfreund et al. 1996, 1997, 1998, 1999, van Broekhuizen et al. 2006, Bouwman et al. 2007, White et al. 2009). Observations of these features towards icy sources, and comparison to laboratory spectra, has revealed the presence of CO in multiple solid environments, namely pure CO, CO₂-containing or crystalline CO and CO in polar, possibly H₂O-rich environment (Pontoppidan et al. 2003b). For CO₂, comparison of laboratory spectra with observations imply co-existence with both H₂O-rich and H₂O-poor, as well as in pure form (*e.g.*, Gerakines et al. 1999, Keane et al. 2001, Pontoppidan et al. 2008).

The molecular environment can constrain the chemical correlations between different molecules, as well as the formation processes of the ices. The presence of abundant pure CO component, supports its freeze-out separate from other components, while intimate mixing with CO₂ supports the chemical correlation between the two. For CO₂, the presence of pure component is taken as an evidence for thermal processing, which segregates it from its native H₂O-rich environment (Ehrenfreund et al. 1998, Öberg et al. 2009a, Fayolle et al. 2011). The lattice structure of a particular ice composition changes with ice morphology, and can give further insight into the thermal history of the ice. The absorption features in crystalline (ordered) structure are typically more narrow than those

in amorphous (unordered) structure (*e.g.*, [Hagen 1981](#)).

Porosity of H₂O-dominated ice influences the absorption spectra by *e.g.*, an emergence of an additional features corresponding to interaction with a dangling OH bond of H₂O in the surfaces of the pores ([Tielens et al. 1991](#), [Al-Halabi et al. 2004](#)). The H₂O-rich CO component has not been able to reproduce in the laboratory, and it has been suggested that the discrepancy results from different ice morphologies ([Palumbo 2005](#)).

Interpretation of the astronomical ice features is complicated by not only the simultaneous influence of all above, but also the fact that an observational spectrum along a given line of sight typically contains several ice compositions at different evolutionary stages. Not all band profiles have been assigned to a specific molecule in a specific molecular and morphological environment. Therefore the interpretation of the observed features varying in ice composition and morphology presents a great challenge to experimentalists aiming to reproduce interstellar ices in the laboratory.

1.5 Complex organic molecules

More than 150 different gas phase molecules have been observed in the interstellar medium, mainly through rotational emission spectra ([Woon 2008](#)). Many of them are considered complex molecules having more than 6 carbon atoms and are found in circumstellar envelopes around evolved stars, cold interstellar cores, hot cores and corinos, lukewarm corinos and outflows ([Herbst & van Dishoeck 2009](#)). Millimeter lines from complex organic molecules are widely associated with high-mass star forming regions and indeed form one of the signposts of the deeply embedded phase of star formation (*e.g.*, [Blake et al. 1987](#), [Hatchell et al. 1998](#), [Gibb et al. 2000](#), [Fontani et al. 2007](#), [Requena-Torres et al. 2008](#), [Belloche et al. 2009](#), [Zernickel et al. 2012](#)). The richest molecular source in the galaxy is the hot core Sgr B2 (N), located in the Galactic Center giant cloud Sgr B2 ([Snyder 2006](#)). Among the observed species are acetone (CH₃COCH₃), ethylene glycol [(CH₂OH)₂], glycolaldehyde (HOCH₂CHO).

Most chemical models invoke grain surface chemistry to create different generations of complex organic molecules ([Tielens & Charnley 1997](#)). Hydrogenation of solid O, C, N and CO during the cold (< 20 K) pre-stellar phase leads to ample production of CH₃OH and other hydrogenated species ([Tielens & Hagen 1982](#)). Exposure to UV radiation results in photodissociation of these simple ices, with the fragments becoming mobile as the cloud core heats up during the protostellar phase. First generation complex molecules result from the subsequent recombination of the photofragments, and will eventually evaporate once the grain temperature rises above the ice sublimation temperature of ~100 K ([Garrod & Herbst 2006](#), [Garrod et al. 2008](#)). Recent studies suggest that the production of molecules, such as C₂H₅OH, HCOOCH₃ and CH₃OCH₃, relies on UV irradiation of interstellar ices ([Öberg et al. 2009b](#)). Subsequent to ice evaporation, hot core gas phase chemistry between evaporated molecules can drive further complexity in second generation species (*e.g.*, [Millar et al. 1991](#), [Charnley et al. 1992](#), 1995).

Observation of complex molecules evaporated from interstellar ices can be used to constrain the ice processes prior to evaporation. One of the most widely used method of

analyzing spectra of complex organic molecules is the rotation diagram method (Goldsmith & Langer 1999). The observed intensities from rotational emission lines may be translated to physical parameters, such as temperature and column density. Under local thermodynamic equilibrium (LTE) the rotational states are populated by excitation through molecular collisions, producing a Boltzmann distribution. The temperature of the gas can be derived from the relative intensity of the emission lines from the states with different energy. The column density of the gas is determined from the overall intensity of the emission lines.

1.6 This thesis

This thesis is dedicated to the study of the composition and physical characteristics of ices using a variety of experimental techniques and combined this with the analysis and interpretation of astronomical observations. The overall goal is to shed light on the processes that chemically enrich planet-forming regions. The specific objectives are to characterize morphological changes (Chapters 2 and 3) and molecular composition (Chapters 4 and 5) in interstellar ices, to explore new experimental techniques to study solid state reactions (Chapter 6), and to use complex molecules to probe large scale astronomical phenomena (Chapter 7).

Ice morphology

Chapter 2 and 3 focus on the morphology of interstellar ice. In the interstellar medium ice is expected to form with different morphologies. These chapters deal with thermally induced changes in porous, vapor deposited ice.

In Chapter 2, the thermally induced collapse of porous H₂O ice is studied using thin-film interference – a method conventionally used to monitor ice growth. This chapter shows that the decrease in internal surface area is accompanied by a 12 % decrease in ice thickness. Ice collapses gradually over the entire temperature range between 20 and 120 K.

Chapter 3 extends the work in chapter 2. The accuracy of the thickness measurement is increased by using sample specific optical properties and through instrumental improvements. The intrinsic phase transition from high-density to low-density amorphous H₂O triggers enhanced collapse of the porous structure. The structural collapse is found to be incomplete. The initial ice morphology influences the behavior of the ice until evaporation of the ice. The persistence of cavities may influence the surface chemistry and trapping of species at elevated temperatures. The study is extended to include CO₂, the dominant impurity of interstellar H₂O ice. CO₂ is found to have a profound impact on the H₂O morphology, particularly grown at low temperatures where porosity of the ice dominates the morphology.

Ice spectroscopy

Chapters 4 and 5 deal with the interpretation of astronomical ice observations using laboratory spectra of known composition and temperature.

Chapter 4 focuses on the observed CO ice feature at $4.65\ \mu\text{m}$, and in particular on the red component which is characterized as CO in a polar ice environment. As laboratory mixtures of CO and H₂O have not been able to reproduce the observed feature, the possibility of a three-component polar mixture is examined, in which CO₂ blocks the dangling OH bond, responsible for the discrepancy between the observed and laboratory spectrum. It is shown that this scenario is not feasible, and that the observed feature can be solely explained by CO mixed with CH₃OH. The resulting CO line profile is consistent with a wide range of observations. The presented results are consistent with the chemical correlation between CO and CH₃OH (through hydrogenation). It also constrains the formation mechanism of CO₂, which according to this result has no parent in the H₂O matrix.

Chapter 5 focuses on the spectral properties of pure CO₂ ice. The interpretation of the CO₂ (ν_2) bending mode at $15.2\ \mu\text{m}$ towards an exceptional young stellar object HOPS-68 requires high-resolution spectra, which are here made available. This CO₂ feature exhibits a particularly prominent fine structure, and cannot be reproduced in the same way as in most other sources. It is shown that the reason for the difference is an high thermal processing of the ices. The heating is manifested as a large amount of pure CO₂, as well as spherical shape of the grains, which results from fast re-condensation of the icy mantle.

Complex organic molecules

Chapter 6 introduces a new experimental technique to study the formation of complex organic molecules in interstellar ices. The experiment employs laser desorption time-of-flight mass spectrometry to increase the sampling sensitivity of interstellar ices while maintaining the conditions relevant to interstellar ices. This chapter demonstrates that laser desorption is a promising technique for vaporization of interstellar ices prior to mass spectroscopic analysis, and shows preliminary results on vacuum UV photo-processed interstellar ices.

Chapter 7 employs complex molecules as probes of massive star formation process, which to date remains poorly understood (Zinnecker & Yorke 2007). Formation similar to low-mass stars leads to a flattening of the accretion disk and opening of an outflow cavity. These structures have been observed for only few massive YSOs. The presence of an outflow cavity allows more UV light to escape from the central object, and to illuminate the walls of the outflow cavity where ices reside. The goal of this chapter is to compare the relative abundances of complex organic molecules in sources where disks have been observed and with those where this is not the case. It is found that there is no substantial difference in the abundance of complex molecules between the two source types. It is argued that this may be either because all massive stars form in similar geometry. An alternative possibility for the lack of difference is that the additional UV light from the central object is insignificant in the production of complex molecules, and that

their formation is dominated in the quiescent cold phase of the molecular cloud.

1.7 Main conclusions

- Thermal collapse of vapor deposited ice is a significant process which influences the solid-state chemistry in interstellar ices. The large ice surface area provided by porous ice at low temperatures decreases at elevated temperatures. While the mobility of ice components increases at higher temperatures, the available catalytic surface area decreases. Thermal collapse of the solid ice structure at low temperature can trigger chemistry before the mobilization of fragments.
- The initial morphology of the ice determines the ice structure until crystallization and beyond. Cavities remain in the ice throughout the solid phase. This enables trapping of other species until H₂O evaporation.
- IR spectroscopy of the dangling OH bond is not an adequate measure of ice morphology for thermally processed ices. Large cavities remain in the ice when dangling OH bonds have disappeared. The non-detection of the dangling OH bond is therefore not a valid argument for compactness of interstellar H₂O ice.
- The observed CO ice feature can be explained by a combination of three ice compositions: pure CO, CO in CO₂ or crystalline CO and CO in CH₃OH ice. CO:CH₃OH ice solves the mystery of the astronomically missing 2152 cm⁻¹ feature present in the laboratory spectra of CO:H₂O ice. The polar CO component is therefore due to CH₃OH, which supports the chemical link between CO and CH₃OH. The lack of a CO:H₂O component constrains the formation mechanism of CO₂, which has been suggested to form by UV irradiation of CO:H₂O ice.
- The abundance of complex organic molecules in hot cores of massive YSOs does not correlate with the detection of a disk geometry. Either the chemical complexity is already fully established in the ices in the cold pre-stellar phase or the material experiences similar physical conditions and UV exposure through outflow cavities during the short embedded lifetime.

Chapter II

THERMAL COLLAPSE OF POROUS AMORPHOUS SOLID WATER

Thermal collapse of porous interstellar ice

J.-B. Bossa, K. Isokoski, M. S. de Valois, and H. Linnartz

Astronomy & Astrophysics, 545, A82 (2012)

Abstract

Amorphous solid water (ASW) is the major constituent of interstellar ice. Freeze-out of water onto cold grain surfaces in the interstellar medium is expected to result in porous ASW with large internal surface area. Energetic processing has been shown to decrease the porosity in laboratory ices and may explain why observations towards icy sources do not show dangling OH groups that are taken as a signature of porosity. A decrease in porosity may affect the chemical activity of the ice: collapse of porous interstellar ASW can accelerate diffusion-limited surface-reactions at low temperatures, while at elevated temperatures the surface area available for catalysis will dramatically decrease. The collapse of porous ASW therefore likely will influence the overall efficiency of solid-state processes taking place in interstellar ices. In this work we study the thermal collapse of porous ASW by direct monitoring of the ice film thickness using laser optical interference. The ASW film thickness is measured continuously during ice growth and subsequent thermal processing from 15 to 190 K. The changes in ice morphology during thermal collapse are confirmed by comparison with different ice morphologies and by FTIR spectroscopy of dangling OH groups. Thermal annealing of vapor deposited porous ASW results in a gradual and irreversible thinning of the ice layer. We derive a thinning of 12 % between 15 and 120 K, which we interpret as a collapse of the porous structure, as the thinning is accompanied by a decrease in the dangling OH groups. We demonstrate that laser optical interference, commonly used to monitor the growth of laboratory ices, is a simple and powerful tool to monitor the change in morphology of porous structures. Our experiments show that thermal collapse of porous ASW is a gradual and irreversible process which may influence the interstellar grain-surface chemistry already at very low temperatures.

2.1 Introduction

Amorphous solid water (ASW) is the main component of interstellar and cometary ices (Hagen 1981, Tielens & Allamandola 1987). It provides an environment for other species, sequentially accreted or formed via solid state astrochemical processes (Öberg et al. 2011b). Water has been experimentally shown to form from atomic hydrogen and oxygen via low-temperature grain-surface reactions (Ioppolo et al. 2008, Dulieu et al. 2010, Ioppolo et al. 2010, Cuppen et al. 2010, Romanzin et al. 2011) with a compact (non-porous) structure (Oba et al. 2009). Remote identification of morphology and, more precisely the porosity relies on relatively weak absorption features around 2.7 μm due to the dangling OH bonds of water on the surface of pores. Up to date, there is no observational evidence for the existence of dangling OH bonds in interstellar ices (Keane et al. 2001, Gibb et al. 2004) leading to a conclusion that porous ASW is rare in space. Given the diversity of the environments of interstellar ices (Kouchi & Yamamoto 1995, Gálvez et al. 2010), and the limited sample of available ice observations, the absence porosity is however not conclusive. In shock regions and outflows, the sputtering of frozen water molecules from grain mantles redistributes ice on the remaining cold surfaces that may lead to the formation

of a vapor-deposited ASW coating on grains. The main characteristic of vapor-deposited water ice is its porosity (Baragiola 2003). Porous ice is expected to be chemically more reactive as it provides large effective surface areas for catalysis, for further freeze-out of atoms and molecules, and for gas retention. Adsorption areas can be hundreds of m^2/g . As a consequence, a large amount of molecules can be stored inside pores at low temperatures influencing the efficiency of solid state astrochemical processes. In a later stage these species and eventual reaction products are thermally released (Collings et al. 2003).

In the laboratory, the morphology of ASW depends on the experimental conditions such as temperature, deposition rate and deposition direction of water molecules onto the substrate (Stevenson et al. 1999, Kimmel et al. 2001b, Dohnálek et al. 2003). Background deposition of water vapor onto a cold surface results in highly porous ASW (Stevenson et al. 1999, Kimmel et al. 2001b). After deposition, the ice morphology may change depending on external influences. A disappearance of pores has been observed in ion and UV photon irradiation experiments (Palumbo 2006, Palumbo et al. 2010, Raut et al. 2008). Furthermore, thermal annealing triggers a phase transition between 38 to 68 K (Jenniskens & Blake 1994), and makes ASW more compact by closing pores thereby trapping other co-deposited gases (Mayer & Pletzer 1986, Bar-Nun & Owen 1998, Collings et al. 2003). The mechanisms responsible for these morphological changes are not fully understood, particularly at low temperature, where diffusion of molecules is limited (Garrod et al. 2008). In previous studies a collapse of pores has also been concluded following X-ray and electron diffraction studies (Hallbrucker et al. 1989, Jenniskens et al. 1995), temperature programmed desorption (Collings et al. 2003), infrared spectroscopy (Hagen et al. 1983, Rowland & Devlin 1991, Rowland et al. 1991), internal friction (Hessinger et al. 1996) and gas adsorption experiments (Bar-Nun & Owen 1998, Kimmel et al. 2001b, Horimoto et al. 2002).

This chapter presents a new and generally applicable method yielding experimental results that directly demonstrate the thickness decrease of porous ASW upon thermal annealing. Sect. 2.2 describes details on experiment and data analysis. Sect. 2.3 presents the results obtained during deposition and thermal processing of different water ice morphologies. The discussion is given in Sect. 2.4, and includes a quantitative analysis of the experimental results followed by astrophysical implications. A summary and concluding remarks are given in the final section.

2.2 Experimental methods

Experiments are performed in a high-vacuum chamber with a base pressure of 2×10^{-7} Torr at room temperature. The experimental set-up (Fig. 2.1) has been described in detail by Gerakines et al. (1995) and has been further adapted to the configuration described here. Different water ices are grown either on a CsI window or on a silicon (Si) substrate at 15 and 140 K. The substrate is mounted on a closed-cycle helium cryostat that, in conjunction with resistive heating, allows an accurate temperature control from 15 to 300 K

with a precision of 0.1 K. We use milli-Q grade water that is further purified by three freeze-pump-thaw cycles prior to deposition. Depending on the experimental conditions, water ices with different morphology is produced: (i) porous amorphous, (ii) semi-porous amorphous, and (iii) crystalline solid water. Semi-porous ASW is obtained by deposition at 15 K by using a gas inlet (2 mm diameter) directed toward the substrate at normal angle of incidence (Kimmel et al. 2001b). Porous ASW and crystalline solid water are grown by background deposition at 15 and 140 K, respectively. In background deposition the gas inlet is directed away from the substrate, which allows the water molecules to impinge the surface with random trajectories (Stevenson et al. 1999, Dohnálek et al. 2003).

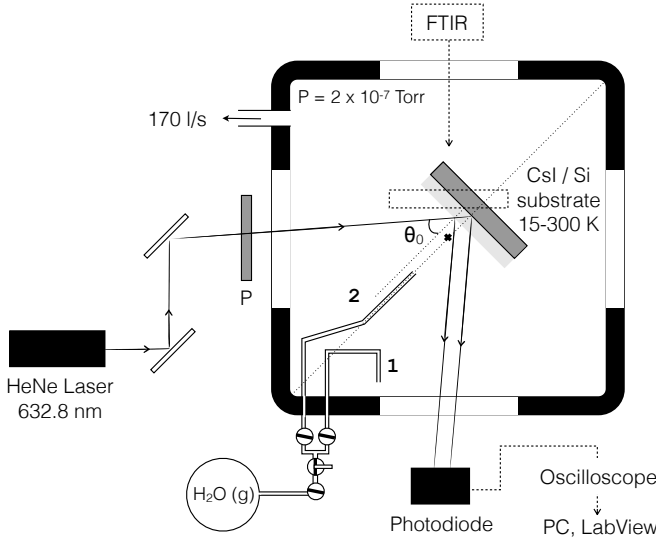


Figure 2.1 – Experimental setup used to measure thin-film interference in interstellar ice analogs. P = linear polarizer.

The ice thickness is monitored during both deposition and thermal annealing by optical interference using a linearly polarized helium-neon (He-Ne) laser. The laser beam is s-polarized (perpendicular to the plane of incidence), and strikes the substrate at an incident angle $\theta_0 = 35 \pm 5^\circ$. The reflected light is collected at a photodiode and digitized by an oscilloscope. A second photodiode is used prior to the vacuum chamber to monitor the laser fluctuations from scattered light. The signal is recorded as a function of time using LabVIEW 8.6 (National Instruments) software package. The ice thickness d can be expressed as a function of interference fringes (m):

$$d = \frac{m \lambda}{2 n_1 / n_0 \cos \theta_1}, \quad (2.1)$$

where λ corresponds to the wavelength of the laser (632.8 nm), n_0 and n_1 are the refractive indices of vacuum and ice, respectively. θ_1 is the angle of refraction related to the

angle of incidence through the Snell's law ($\sin \theta_0 n_0 = \sin \theta_1 n_1$). To exclude the influence of the gas deposited on the backside of the substrate, we use the Si substrate that is opaque to the laser wavelength. We use $n_0 = 1$ for vacuum, $n_1 = 1.19$ for porous ASW at 15 K (extrapolated from the data reported in [Dohnálek et al. \(2003\)](#)), and $n_1 = 1.29$ for semi-porous ASW ([Westley et al. 1998](#)). The ice thickness during deposition is obtained by correlating the interference fringe pattern of subsequent minima and maxima (m) and the corresponding deposition time. An exponential fit to this data provides the best representation of the deposition rate as depicted in Fig. 2.2. This exponential behavior is expected as the pressure in the gas reservoir decreases with deposition time. The system is cycled through up to about 2.75 interference fringes, corresponding to an ice thickness of 837^{+34}_{-29} nm. The accuracy of the thickness determination is limited by the uncertainty in the literature values of the optical constants, and the incident angle of the laser beam ([Baratta & Palumbo 1998](#)). After deposition, the ice thickness is monitored as a function of temperature between 15 to 120 K using different heating rates from 1 to 4 K min⁻¹.

Infrared spectra are obtained with a Fourier Transform Infrared spectrometer (Varian 670-IR FTIR) and recorded in transmission mode between 4000 and 400 cm⁻¹ at a resolution of 1 cm⁻¹, co-averaging 256 scans. The samples used for the IR measurements, are grown on the CsI window. The spectrometer is flushed with dry air to minimize background fluctuations due to atmospheric absorptions. Background spectra are acquired at 15 K prior to deposition for each experiment.

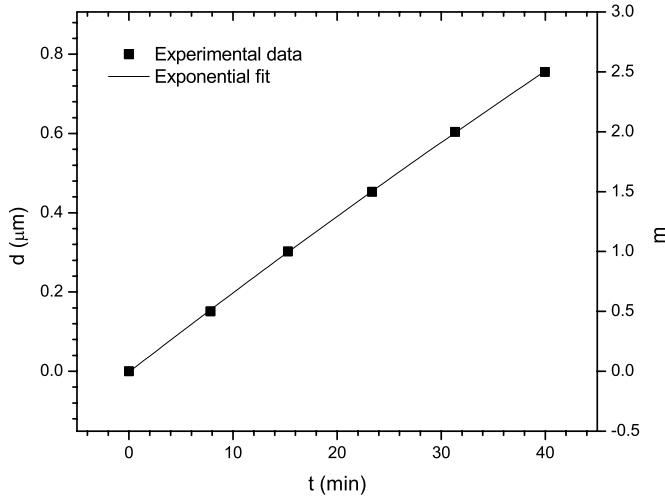


Figure 2.2 – Exponential fit to subsequent interference fringes minima and maxima (m) and the corresponding thicknesses vs. deposition time.

2.3 Results

2.3.1 Interference data and infrared spectra during deposition

Fig. 2.3 shows experimental interference data corresponding to the intensity of the reflected laser beam as a function of ice thickness, collected during a porous ASW growth on the Si substrate. The interference pattern exhibits a small decrease in amplitude with ongoing deposition. This amplitude change can have different reasons; a loss of coherence of the reflected light because of surface roughness, cracks, and/or wide boundaries (Baragiola 2003, Howett et al. 2007, Romanescu et al. 2010). The distance between subsequent minima and maxima is constant within 1% indicating that the density of the porous ASW does not change significantly during deposition (Westley et al. 1998).

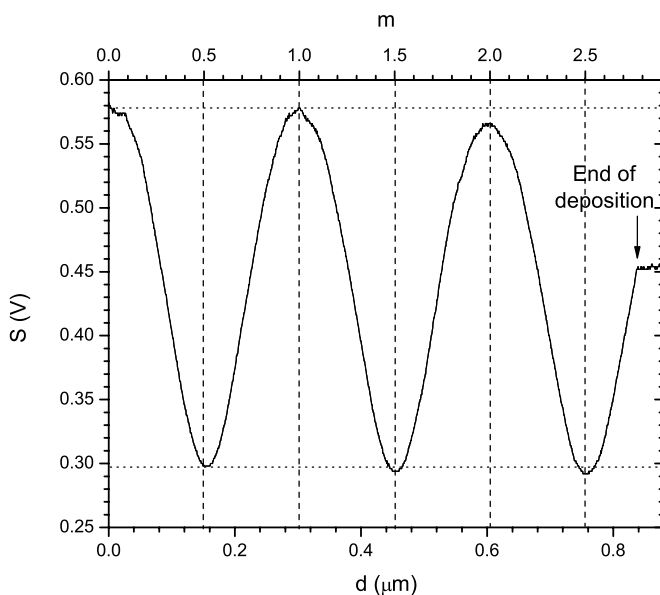


Figure 2.3 – Interference data for porous ASW grown on a Si substrate at 15 K following background deposition. The reflected intensity oscillates between constructive and destructive interference as the ice grows. The deposition is stopped at a point with maximum sensitivity to changes in ice thickness. The error in the thickness measured is about 4%.

The deposition is stopped at the rising slope of the interference pattern ($m = 2.75$). Change in He-Ne signal can thus be interpreted as change in ice thickness, such that an increasing photodiode signal corresponds to thickening of the ice whereas a decreasing signal corresponds to thinning of the ice.

The FTIR transmission spectra of porous ASW, semi-porous ASW, and crystalline solid water grown on the CsI window are depicted in Fig. 2.4 in the $3760 - 3660 \text{ cm}^{-1}$ range that covers the O-H dangling mode of water ice. This mode is used to visualize the

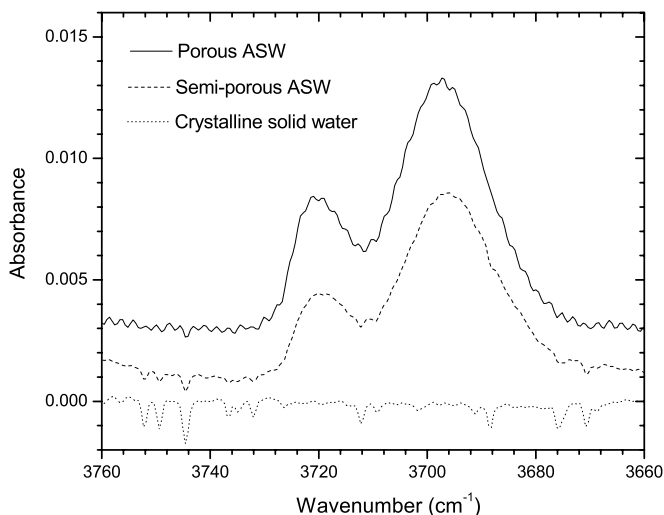


Figure 2.4 – Infrared transmission spectra of the O-H dangling mode of porous ASW, less-porous ASW, and crystalline solid water at 15 K. The absorption band related to the bulk O-H stretching modes has been subtracted and the resulting spectra have been offset for clarity.

level of porosity. To characterize the porosity of each water ice sample, all spectra are corrected with a baseline, and normalized to the bulk O-H stretching modes, located at lower wavenumbers (not shown here). For porous and semi-porous ASW, two absorption bands are found at 3720 and 3696 cm^{-1} that correspond to the O-H dangling mode of the two- and three-coordinate surface-water molecule, respectively. These two bands have been taken as a typical porosity signature (Rowland & Devlin 1991, Rowland et al. 1991), and their intensities reflect the abundance of pores. For crystalline solid water, there is no O-H dangling mode. Therefore, we conclude that at fixed temperature (15 K), the porosity decreases from porous ASW to semi-porous ASW, and from semi-porous ASW to crystalline solid water. These results are in good agreement with earlier reports (Stevenson et al. 1999, Kimmel et al. 2001b, Dohnálek et al. 2003, Palumbo 2006), and depict the different morphologies of the deposited samples.

2.3.2 Thermal processing of different ice morphologies

Using optical interference, we can now monitor the thermal evolution of porous ASW, semi-porous ASW, and non-porous crystalline solid water. The results are shown in Fig. 2.5. The corresponding interference data are scaled in order to get the same amplitude between the second constructive interference ($m = 2.0$) and the third destructive interference ($m = 2.5$) in the fringe patterns. The small offset is introduced for better visibility. At temperatures above 120 K, diffusion of water molecules becomes significant, and molecules rearrange to a thermodynamically favored crystalline structure (Raut et al. 2008). Hence,

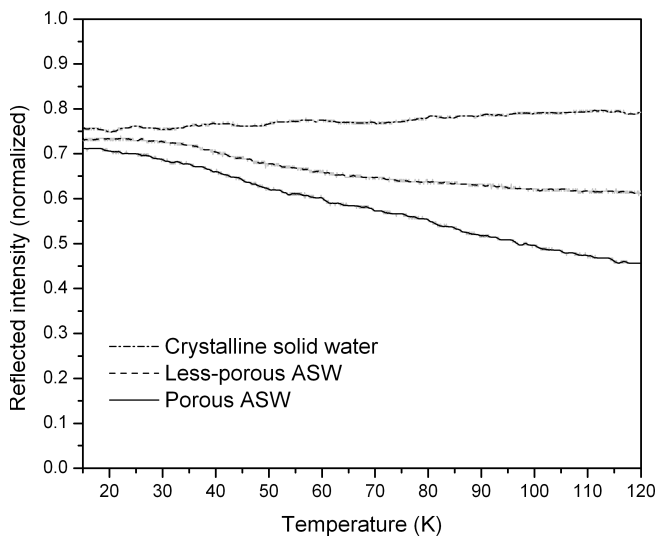


Figure 2.5 – Interference data from the *end of deposition* point onwards (Fig. 2.3), during the thermal annealing experiment on porous ASW, less-porous ASW, and crystalline solid water grown on a Si substrate, with an heating rate set to 2 K min^{-1} . The gray lines represent the raw experimental data, and the black lines are the smoothed data.

we exclude all data at temperatures higher than this threshold.

For crystalline solid water, the He-Ne signal is stable between 15 and 120 K, indicating that the ice thickness remains constant in this temperature range. The result is consistent with the lack of porosity of the sample deposited at 140 K, and then cooled down to 15 K, as confirmed by infrared spectroscopy in Fig. 2.4. For porous ASW, and semi-porous ASW the He-Ne signal does not change between 15 and 20 K. Above 20 K, we observe a gradual drop in the interference signal, which reflects a structural change of the ices; the ices get thinner. Fig. 2.5 shows that the decrease in the signal is stronger for the porous ASW, indicating that the magnitude of the thickness decrease is related to the initial porosity of the sample.

In order to check the temperature dependence of the observed thickness decrease, we monitor the He-Ne beam reflected from porous ASW samples that are warmed up with different heating rates ($1, 2, \text{ and } 4 \text{ K min}^{-1}$). Before each measurement, we use the same background deposition protocol in order to allow accurate comparisons. Fig. 2.6 shows the interference signal for different heating rates. The signal decay as function of temperature is comparable for the different thermal annealing experiments, indicating that the thickness decrease of porous ASW is a fully thermally determined process. Fig. 2.7 shows that the intensity of the O-H dangling feature decreases during the warm-up. This is consistent with the expected porosity loss as discussed in the literature (Baragiola 2003) and references therein; this porosity loss takes place together with the observed thickness decrease.

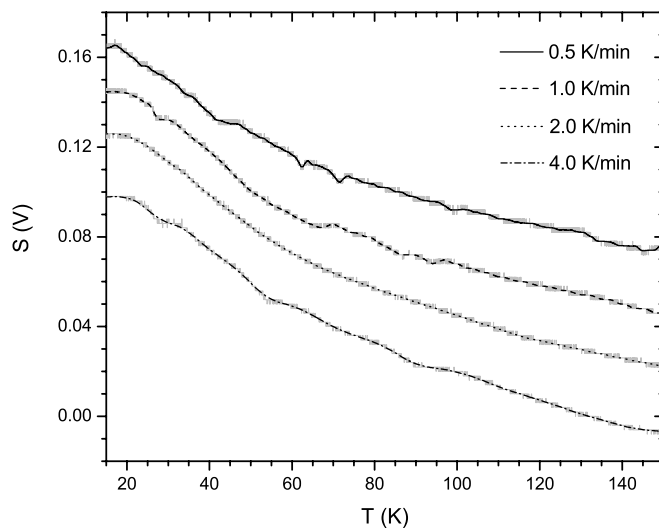


Figure 2.6 – Interference data during the thermal annealing experiment on porous ASW grown on a Si substrate, with different heating rates (1, 2, and 4 K min⁻¹). The gray lines represent the raw experimental data, and the black lines are the smoothed data. The data are offset for clarity. The artifacts in particularly the 0.5 K/min trace are due to laser intensity fluctuations.

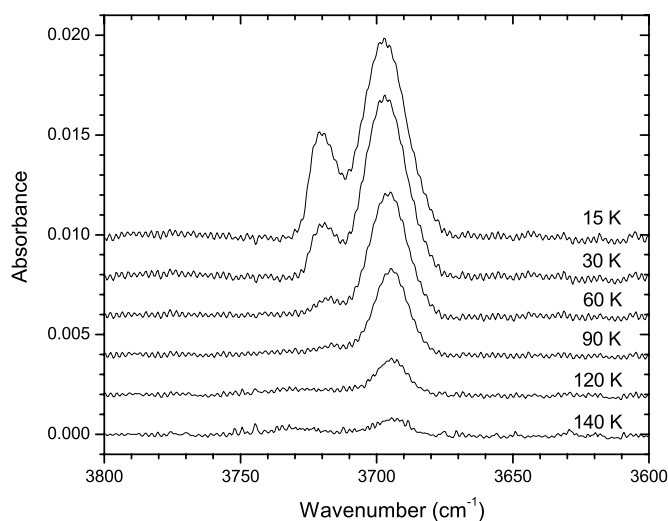


Figure 2.7 – Evolution of the OH dangling modes during annealing of porous ASW from 15 to 120 K. Bulk OH stretching mode has been subtracted and the resulting spectra have been offset for clarity.

2.4 Discussion

Previous work has shown a decrease in both porosity and gas-adsorption capacity of ASW with increasing temperature. We have directly demonstrated here that vapor deposited ASW undergoes a temperature-induced structural change upon heating. A quantitative analysis of the observed thickness decrease in porous ASW is possible by determining the ice thickness at different temperatures. This can be achieved by relating the reflected He-Ne laser intensity $|R|^2$ to the ice thickness during thermal annealing. For layered structures, the reflection coefficient R can be written as a function of the Fresnel reflection coefficients according to the relation (Westley et al. 1998, Dohnálek et al. 2003):

$$R = \frac{r_{01} + r_{12} e^{-i2\beta}}{1 + r_{01} r_{12} e^{-i2\beta}}. \quad (2.2)$$

The Fresnel reflection coefficients r_{01} and r_{12} are associated to the vacuum/ice and ice/substrate interfaces, respectively, and are functions of the refractive indices of vacuum (n_0), ice (n_1), and substrate (n_2). The values of the Fresnel reflection coefficients are given by the following equations and depend on the light polarization. For s-polarized light:

$$r_{01s} = \frac{n_0 \cos \theta_0 - n_1 \cos \theta_1}{n_0 \cos \theta_0 + n_1 \cos \theta_1}. \quad (2.3)$$

$$r_{12s} = \frac{n_1 \cos \theta_1 - n_2 \cos \theta_2}{n_1 \cos \theta_1 + n_2 \cos \theta_2}. \quad (2.4)$$

Snell's law relates the angles of incidence (θ_0 , θ_1 , and θ_2) with the complex indices of refraction (n_0 , n_1 , and n_2). We use constant refractive indices $n_0 = 1$ for vacuum, and $n_2 = 3.85 - 0.07i$ for the Si substrate (Mottier & Valette 1981). The refractive index of porous ASW, however, is temperature dependent, and increases linearly from 22 to 120 K; $n_1(T)$ values are available from Dohnálek et al. (2003). We assume that the $n_1(T)$ values obtained depositing the sample at a given temperature are the same as those of the sample warmed up from 15 K to that temperature. The imaginary component, k , is very close to zero (light is not absorbed in the ice film), and can be neglected (Warren 1984, Dohnálek et al. 2003). The exponential term β in Eq. 2.2 describes the phase change of the light as it passes through the ice with:

$$\beta = \frac{2\pi d}{\lambda} n_1(T) \cos \theta_1. \quad (2.5)$$

We assume that the amplitude of the reflected light at a given thickness and temperature is proportional to the photodiode signal (S), with a proportionality constant (A), calculated at 15 K with the initial ice thickness d_0 (here $d_0 = 837$ nm):

$$|R(d_0, T)|^2 = A_{15\text{K}}^{d_0} \times S. \quad (2.6)$$

In order to measure the thickness of the ice for other temperatures, we need to take into account the variation of $n_1(T)$ with temperature, and to find the closest root (d) to the

initial ice thickness that satisfies the following equation:

$$|R(d,T)|^2 - \left(A_{15\text{K}}^{d_0} \times S\right) = 0. \quad (2.7)$$

Fig. 2.8 shows the calculated ice thickness versus temperature. We find a thickness change for porous ASW from ~ 833 nm at 20 K to ~ 733 nm at 120 K, which corresponds to a decrease of 12 ± 1 %. The top and bottom edges of the gray shaded area delimit the error in the initial ice thickness measurement. We observe the same thickness decrease value of about 12% for both upper and lower d_0 values, indicating that the accuracy of the derived thickness change is not strongly affected by the uncertainty of the initial thickness. This derived thickness change is a lower limit since the background accretion of the residual components remaining in the chamber is not explicitly taken into account. The results presented here are confirmed by recent theoretical work; molecular dynamics simulations performed on porous ASW show a thickness decrease of $\sim 10\%$ from 0 to 150 K (Elkind & Fraser 2012). For semi-porous ASW the exact thickness decrease cannot be determined as the $n_1(T)$ values are unknown. Fig. 2.5 indicates that the thickness change is less than for porous ASW, but definitely not zero as for crystalline solid water. The structural collapse of porous ASW is not large in terms of thickness but a decrease of the order of 12% may correspond to a substantial loss in terms of surface area; Bar-Nun & Owen (1998) report an effective surface area loss as large as 90%. The physical mechanism involved during the collapse is poorly understood. It has been proposed that at 38 K, on average, the breaking of one hydrogen bond per molecule becomes possible, restructuring the ice (Jenniskens & Blake 1994, Jenniskens et al. 1995). This is in line with the results found here, with the exception that an onset of a structural change is already observed at 20 K. Our results agree with those of Hagen (1981), who observed irreversible spectral changes in the bulk OH stretching band immediately upon annealing from the 10 K deposition temperature.

The O-H dangling mode characteristic for porous ASW has not been observed in the infrared spectra of interstellar ices, reason why ASW in space is considered to be compact. Previous laboratory experiments are in line with this conclusion, and suggest that over the lifetime of a molecular cloud, pores in interstellar ices are lost upon cosmic ray bombardments (Palumbo 2006, Raut et al. 2008). The present study indicates that a structural change is also realized through heating, i.e., in a protoplanetary disk through radiation from the protostar. This also applies to less-porous ASW.

Upon heating the number of reaction sites becomes scarce, and a chemistry dominated by bulk processes may shift to a chemistry governed by surface processes. A decrease of reaction sites will naturally reduce the reaction efficiency. On the other hand, a low temperature structural collapse may facilitate reactions between adsorbates, and reaction efficiencies will increase with increasing temperature, as the mobility of reacting species gets larger. Gálvez et al. (2010) demonstrated that the thermal processing of porous ASW leads to a marked enhancement of low temperature acid-base reaction yields, in contrast to compact ASW. So far, a thermally induced ice collapse has not been taken explicitly into account in astrochemical models. The situation for mixed ices is likely even more complicated. How do CO or CO₂ affect the water ice structure, morphology, and porosity

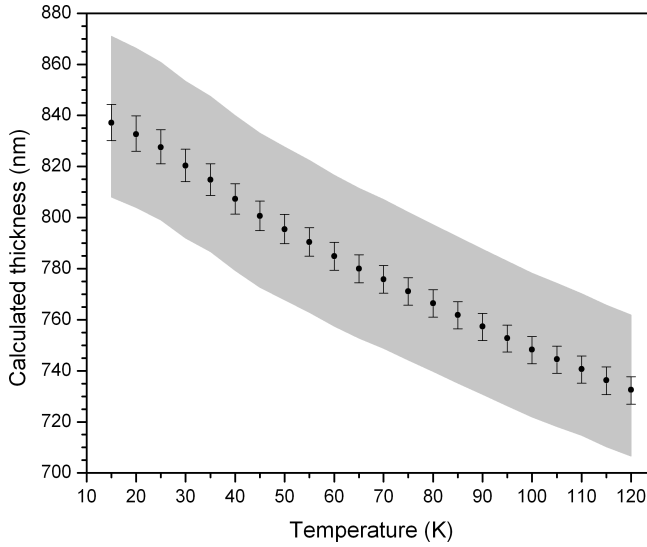


Figure 2.8 – Calculated thicknesses versus temperature during the thermal annealing experiment (2 K min^{-1}) of porous ASW grown on a Si substrate. The vertical bars give the dispersion due to the resolution of the optical interference technique. The gray shaded area takes into account the dispersion due to the error in the initial thickness measured at 15 K.

loss upon heating? With the new technique discussed here, this question can be addressed, as soon as temperature dependent refraction indices have become available.

2.5 Conclusions

We have measured the thickness decrease of porous ASW upon heating for astronomically relevant temperatures, using a new experimental technique, based on optical interference and FTIR transmission spectroscopy.

1. We find for porous ASW a thickness decrease of 12 ± 1 % upon heating from 20 to 120 K. For less-porous ASW this value is lower, and negligible for crystalline solid water.
2. The thickness decrease observed by optical interference is accompanied by the compaction (porosity loss) observed by FTIR.
3. Thermal compaction provides an additional explanation why porous ASW has not been observed in space so far.
4. The observed structural collapse likely will influence the efficiency of the overall chemical solid state network in inter- and circumstellar ices.

Chapter III

MORPHOLOGY OF POROUS AMORPHOUS SOLID WATER AND CO₂ CONTAINING ICES

Morphology of porous amorphous solid water and CO₂ containing ices

K. Isokoski, J.-B. Bossa, K. and H. Linnartz

Astronomy & Astrophysics, 2013, to be submitted

Abstract

This article aims to characterize the morphological changes in porous amorphous solid water (ASW) upon thermal annealing in pure form and mixed with CO₂. We use laser optical interference to derive refractive indices for H₂O, CO₂, and binary H₂O-CO₂ ice at different temperatures. The morphological changes during thermal annealing are inferred by a combination of optical interference and FTIR spectroscopy. Optical interference is used to monitor the ice thickness in real time, while FTIR spectroscopy gives information about the changes in molecular environment. The refractive index and thermal collapse of pure ASW show a non-linear temperature dependence. The intrinsic I_{hda} → I_{lda} phase transition in ASW is visible as discontinuity in thermal collapse at 38–70 K. The structure of porous ASW is not fully compacted by thermal annealing. Depending on the growth temperature, the residual porosity after annealing to 120 K is around 20 %. Large cavities remain in the ice throughout the solid phase, not observable through infrared spectroscopy.

The presence of CO₂ in porous ASW influences the ice morphology throughout the solid phase. Significant morphological changes occur around the I_{hda} → I_{lda} phase transition. CO₂ segregation is observed at 70-80 K, and its efficiency depends on the ice morphology. A high initial porosity leads to a higher extent of CO₂ segregation. The morphology of H₂O containing ices is dominated by both intrinsic structure of ASW as well as porosity. Both influence the dynamics in low-temperature ices, and may have significant consequences on the solid state chemistry in interstellar ices. The initial porosity of the ice determines its structural evolution throughout the solid phase until ice evaporation. H₂O rich ices formed by vapor deposition on cold interstellar dust grains may contain large cavities that persist over a large temperature range, and affect the catalytic potential of the ice as well as the trapping of gases. The presence of CO₂ rich porous ASW in the ISM may have interesting consequences for ice dynamics. The growth conditions influence the morphology of mixed ices, which is retained at higher temperatures affecting astronomically relevant processes such as ice segregation.

3.1 Introduction

Amorphous solid water (ASW) is the main component of interstellar and cometary ices (Whittet et al. 1998, Boogert et al. 2008). It provides a matrix environment for other species, such as carbon dioxide CO₂, adsorbed or formed on the ice surface. ASW is able to support a highly porous structure containing large scale internal cavities. The internal surface area of porous ASW ice can be hundreds of m²/g (Mayer & Pletzer 1986, Bar-Nun et al. 1987), making ice morphology an important factor for interstellar chemical processes relying on surface accessibility. Porous ice provides large effective surface areas for adsorption of atoms and molecules, catalysis of chemical reactions, and further retention of the involved species. Large quantities of molecules can be stored inside pores and later thermally released (Collings et al. 2003, Raut et al. 2007b).

The exact morphology of ice in the interstellar medium (ISM) is still under debate.

The available remote observations of H₂O rich ices (Keane et al. 2001, Gibb et al. 2004) indicate a compact (non-porous) structure inferred from the absence of the dangling OH feature around 2.7 μm (Rowland & Devlin 1991, Rowland et al. 1991, Buch & Devlin 1991). In the laboratory, H₂O formation through surface reactions indeed seems to produce compact ASW (Oba et al. 2009). However, H₂O condensation from the gas phase onto cold surfaces has been shown to lead to porous ASW (Dohnálek et al. 2003). Formation of porous grain mantles in the ISM through vapor deposition of H₂O is expected to occur in dark clouds (Williams et al. 1992, Papoular 2005), but may also be relevant in shock regions and protostellar outflows, where the sputtering of frozen water molecules from grain mantles redistributes ice on the remaining cold surfaces. Vapor deposition from the gas phase may be also relevant in protoplanetary disks where material is transported back and forth across the snow line (*e.g.*, Wooden et al. 2005).

Energetic processing in the ISM is expected to reduce the porosity of ASW. The compaction of porous ASW has been experimentally demonstrated to be driven by cosmic rays and UV photons (Palumbo 2006, Palumbo et al. 2010, Raut et al. 2008), as well as by thermal processing (Bar-Nun & Owen 1998, Bossa et al. 2012). Many of the observations covering the 2.7 μm region are targeting embedded sources with processed ices, where porosity may have decreased (Whittet et al. 1998, Boogert et al. 2008). Given the diversity of astronomical ice environments, the absence of porous ASW is therefore not conclusive (Kouchi & Yamamoto 1995, Gálvez et al. 2010).

The transformation from porous to compact ice may have interesting consequences for the chemistry in interstellar ice. Pore collapse at low temperatures drive diffusion limited recombination of radicals trapped in interstellar ices. In UV irradiated interstellar ice analogs (Schutte 1988), the observed low-temperature chemical evolution has been attributed to a structural phase transition in the ice between 38 and 68 K (Jenniskens & Blake 1994). Spectral changes, however, are observed prior to this and therefore cannot be directly due to the phase transition only. In our previous work, we showed that the thermally induced collapse of porous ASW begins at temperatures as low as 20 K and continues gradually throughout the amorphous phase (Bossa et al. 2012). Low-temperature pore collapse may thus be responsible for chemical evolution at low temperatures. Porosity of interstellar ice may be also relevant in planet formation. It has been suggested that porous ice mantles facilitate the coagulation of dust grains in the process of forming larger solar system bodies (Krijt private communication).

The morphology of ASW grown in the laboratory depends on experimental conditions such as temperature, growth rate and directionality of H₂O molecules landing on the ice surface (Berland et al. 1995, Westley et al. 1998, Stevenson et al. 1999, Kimmel et al. 2001b, Dohnálek et al. 2003). Omnidirectional background deposition onto a cold surface leads to highly porous ASW. Monitoring the decrease in porosity during energetic processing is typically done through IR spectroscopy, where compaction is derived from the decrease in intensity of the dangling OH bonds (*e.g.*, Palumbo 2006), or by gas absorption probing the available pore volume (*e.g.*, Raut et al. 2007b). In Bossa et al. (2012), we employed optical interference to monitor the porous ASW thickness during thermal annealing. This technique is commonly used to monitor ice growth during the preparation of interstellar ice analogs.

In this paper, we extend the work in [Bossa et al. \(2012\)](#) and study in more detail the thermally induced changes in the morphology of astronomically relevant ices. We focus on porous ASW, pure CO₂ ice and the H₂O-CO₂ (4:1) binary ice mixture. CO₂ is the most common impurity in interstellar H₂O ice with ratios as high as ~30 % and is therefore important for its morphology. We use optical interference to derive the specific refractive indices of different ice samples. Following instrumental improvements we are now more sensitive to changes in ice thickness, in particular during thermal annealing.

3.2 Experimental methods

3.2.1 Experimental setup

The experimental setup was originally described by [Gerakines et al. \(1995\)](#) and has been adapted to the configuration described here (Fig. 3.1). A stainless steel chamber is evacuated by a turbomolecular pump (Pfeiffer TPH 170) and a mechanical pump (Edwards E2M8) equipped with an oil mist filter to a base pressure of 2×10^{-7} Torr at room temperature. Ice samples are grown on a silicon substrate located in the center of the chamber. The substrate is mounted on a closed-cycle helium cryostat that, in conjunction with resistive heating, allows for temperature control from 17 to 300 K with a precision of 0.1 K.

Samples are prepared in a glass bulb by standard manometric techniques using an external gas mixing line with a base pressure of 1×10^{-5} mbar. We use milli-Q grade H₂O that is further purified by three freeze-pump-thaw cycles. CO₂ (Praxair, 99.998 % purity) is used without further purification. Each sample is prepared at a total pressure of 20 mbar. The H₂O-CO₂ (4:1) gas sample is prepared by placing H₂O vapor (16 mbar) into a pre-evacuated bulb. CO₂ is subsequently introduced into the bulb by a rapid gas expansion from an external volume, pre-filled to give the desired CO₂ partial pressure (4 mbar). The bulb valve is closed immediately after expansion to prevent diffusion of H₂O into the external volume. Gas samples with two components are prepared ~20 h prior to deposition. This allows the gas mixture to equilibrate with the bulb walls, ensuring a reproducible ice composition.

Samples are admitted into the vacuum chamber through a needle valve. The ices are grown by *background deposition* where the gas inlet is directed away from the substrate. This method allows the molecules to impinge on the surface with random trajectories, producing a porous ice structure ([Stevenson et al. 1999](#), [Dohnálek et al. 2003](#)). The pressure in the chamber during deposition is set to $1.0 \pm 0.1 \times 10^{-5}$ Torr. We use a gas reservoir with a large volume (2 L) to ensure a constant deposition rate. The deposited ice samples are thermally annealed at a constant rate of 2.0 K min⁻¹ until desorption.

3.2.2 Optical interference

The refractive indices of the ice samples as well as their thickness throughout the experiment (deposition and thermal annealing) are derived using optical interference. The interference of coherent light reflecting off the two interfaces of a thin film depends on the

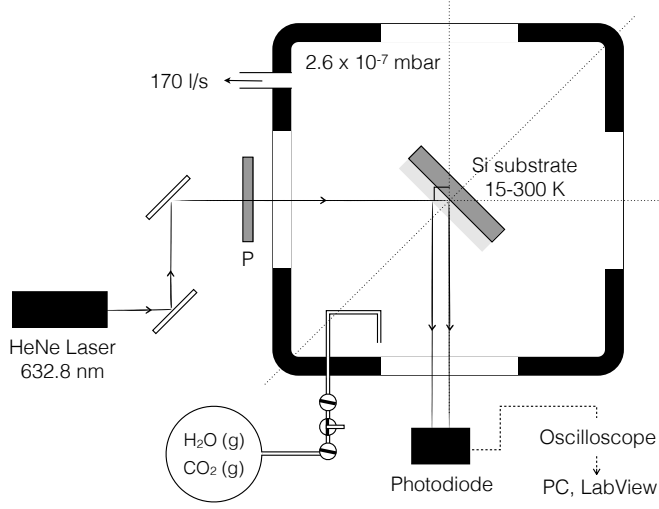


Figure 3.1 – Schematic drawing of the experimental setup used to measure thin-film interference in interstellar ice analogs. P = linear polarizer.

optical properties of the media involved, as well as the thickness of the film. We employ a linearly polarized, intensity stabilized HeNe laser (Thorlabs HRS015). An additional polarizer is placed in the beam path admitting only s-polarized light, perpendicular with respect to the plane of incidence. The laser beam strikes the substrate surface at an incident angle of 45°. For the purpose of the interference experiment a porous ice film with nm-scale surface features presents an effectively flat surface to the laser beam (spot size 2 mm). The reflected light is collected at a photodiode (Thorlabs PDA36A) and digitized by an oscilloscope (Textronix TDS 2022B). The photodiode signal together with time and substrate temperature from the (Lakeshore 330) temperature controller is recorded using the LabVIEW 8.6 software package (National Instruments).

For a surface with a three-phase structure, as depicted in Fig. 3.2, the total reflection coefficient R can be described by Eq. 3.1 (Westley et al. 1998, Dohnálek et al. 2003):

$$R = \frac{r_{01} + r_{12}e^{-i2\beta}}{1 + r_{01}r_{12}e^{-i2\beta}}; \text{ with} \quad (3.1)$$

$$\beta = \frac{2\pi d}{\lambda} \times n_1 \cos \theta_1$$

where r_{01} and r_{12} are the Fresnel reflection coefficients for the vacuum/ice and ice/substrate surface interfaces, d is the thickness of the ice, λ is the wavelength of the laser (632.991 nm) and n_1 is the refractive index of the ice. θ_1 is the angle of refraction, derived from the angle of incidence θ_0 through $n_0 \sin \theta_0 = n_1 \sin \theta_1$ (Snell's law). For s-polarized light the

Fresnel reflection coefficients can be written as:

$$r_{01s} = \frac{n_0 \cos \theta_0 - n_1 \cos \theta_1}{n_0 \cos \theta_0 + n_1 \cos \theta_1} \quad (3.2)$$

and

$$r_{12s} = \frac{n_1 \cos \theta_1 - n_2 \cos \theta_2}{n_1 \cos \theta_1 + n_2 \cos \theta_2} \quad (3.3)$$

where n_0 and n_2 are the refractive indices of vacuum and substrate. We use constant refractive indices $n_0 = 1$ for vacuum and $n_2 = 3.85 - 0.07i$ for the Si substrate (Mottier & Valette 1981).

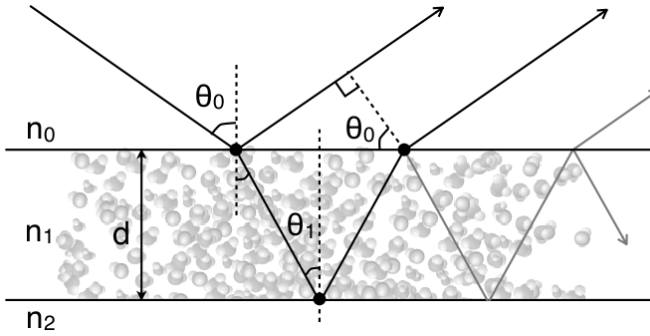


Figure 3.2 – Optical interference in a three-phase (vacuum/ice/substrate) structure. Light incident on the surface interface between two media partially reflects from and partially refracts into the layer, depending on the Fresnel reflection coefficients (r_{01} and r_{12}). The difference in optical path length leads to a phase shift and an alternating constructive and destructive interference during layer growth. The intensity of the sum reflection depends on the refractive indices (n_0 , n_1 and n_2) and film thickness (d).

We relate the experimentally measurable photodiode signal (S) to the reflected intensity $|R|^2$ through an empirical scaling factor α , which allows us to correlate S with n_1 and d (Eq. 3.4).

$$S = \alpha \times \left| \frac{r_{01} + r_{12}e^{-i2\beta}}{1 + r_{01}r_{12}e^{-i2\beta}} \right|^2 \quad (3.4)$$

The refractive indices of ice samples for different temperatures are determined by fitting Eq. 3.4 to the photodiode signal during ice growth (Eq. 3.5).

$$S(t) = \alpha \times \left| \frac{r_{01}(n_1) + r_{12}(n_1)e^{-i2\beta(t)}}{1 + r_{01}(n_1)r_{12}(n_1)e^{-i2\beta(t)}} \right|^2 \quad (3.5)$$

The thickness d , contained in the β term, is constrained by a linear equation corresponding to a constant growth rate (Eq. 3.6):

Table 3.1 – IR band strengths (A_i) of H₂O and CO₂ stretching modes in pure ices at 14 K.

Mode	Band position [cm ⁻¹]	A_i (14 K) [cm molecules ⁻¹]	Ref.
H ₂ O, O–H stretch	3280	2.0E-16	(1)
CO ₂ , ¹³ C=O (ν_3) stretch	2283	7.8E-17	(2)

References: (1) [Hagen \(1981\)](#); (2) [Gerakines et al. \(1995\)](#)

$$d(t) = \gamma t \quad (3.6)$$

where γ is a constant corresponding to the deposition rate in nm s⁻¹. The decrease of the deposition rate in [\(Bossa et al. 2012\)](#) is here avoided by doubling the volume of the sample reservoir. In the fitting procedure α , γ and n_1 are allowed to vary freely.

We assume that the refractive indices obtained for ices deposited at a particular temperature, are applicable to ice which has been thermally annealed to that temperature. The ice thickness during thermal annealing $d(T)$ can then be derived by finding the closest root (d) to the initial ice thickness that satisfies Eq. 3.7:

$$|R(d, T)|^2 - |R(d_0, T_0)|^2 = 0 \quad (3.7)$$

where $|R(d, T)|^2$ is the reflected intensity at temperature T and $|R(d_0, T_0)|^2$ is the reflected intensity in the beginning of the thermal annealing.

3.2.3 IR spectroscopy

Infrared (IR) spectra are recorded with a Fourier transform infrared spectrometer (Varian 670-IR FTIR) in transmission between 4000 and 400 cm⁻¹ with a resolution of 1 cm⁻¹. A total of 256 interferograms are averaged to improve the S/N ratio. Background spectra are acquired at 17 K prior to sample deposition. At annealed temperatures, the ice samples are allowed to relax for 5 min before recording the spectrum.

The column density of molecules in the ice, N (in molecules cm⁻²), is derived from IR spectra by Eq. 3.8 ([Gerakines et al. 1995](#)):

$$N = \frac{\ln 10 \times \int A d\bar{\nu}}{A_i} \times \cos \theta \quad (3.8)$$

where $\int A d\bar{\nu}$ is the integrated intensity of a particular absorption band and A_i is the band strength in cm molecules⁻¹. The last term in Eq. 3.8 corrects the overestimation of N resulting from the non-orthogonal orientation of the IR beam and the ice sample ([Bennett et al. 2004](#)). Table 3.1 lists the band strengths for the fundamental vibrational modes in pure H₂O and CO₂ ices used here.

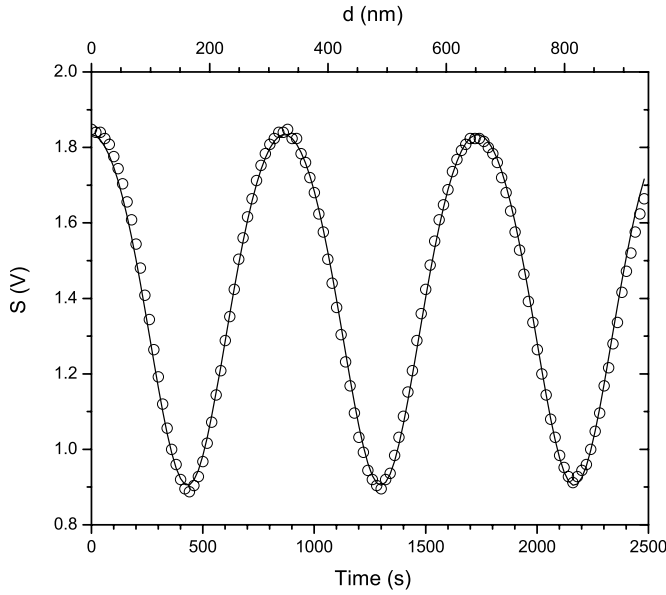


Figure 3.3 – Optical interference signal (S) during deposition of H₂O ice at 17 K (open circles) and fit using Eq. 3.5 (black trace) for the deposition fringe pattern.

3.3 Results

3.3.1 Deposition

Fig. 3.3 shows the interference signal (S) during the deposition of pure H₂O ice at 17 K. All samples are grown at a similar rate, and cycled through ~ 3 fringes, resulting in a thickness ranging between 0.9 and 1.0 μm . The deposition is stopped towards the top of the rising slope of one of the interference fringes. Changes in the interference signal thus correspond directly to changes in ice thickness, simplifying real-time interpretation of the results. Moreover, as the ice thickness, d , generally decreases during further processing, the dynamic range of the signal is maximized in this setting. The growth rate for H₂O at 17 K is fairly constant throughout the deposition with $<5\%$ variation in the half-period. For all samples, the observed amplitude of the deposition fringes decreases somewhat during the deposition, likely due to an increasing loss of photons through scattering. For H₂O ice deposited at 17 K the decrease in amplitude is 2 % per period. The black trace in Fig. 3.3 shows the fit of Eq. 3.5 to the fringe pattern. The fitted region is determined by the experimentally noted start and end of deposition. The best fit parameters for all studied samples are given in Table 3.2. Fig. 3.4 shows the R^2 (coefficient of determination) plot describing the goodness of the fit for H₂O deposition at 22 K. A single R^2 maximum demonstrates that the fit has a unique solution.

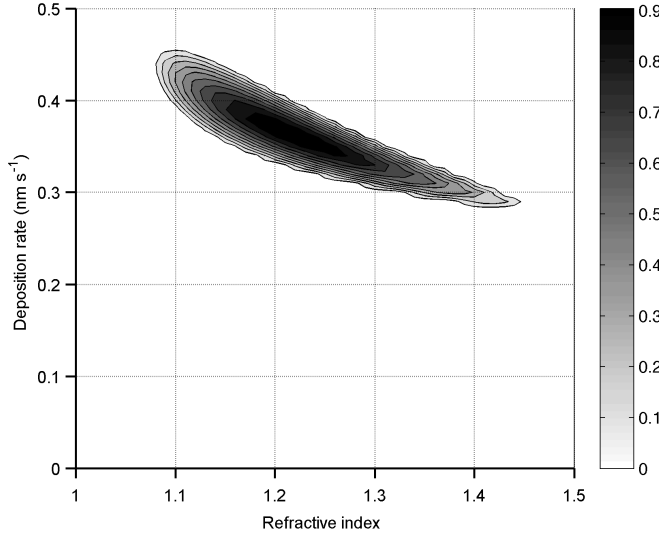


Figure 3.4 – R^2 (coefficient of determination) from the fit using Eq. 3.5 for H_2O deposition fringe pattern at 22 K as a function of refractive index (n_1) and deposition rate (γ), with the scaling factor (α) fixed to an optimized value.

3.3.1.1 Refractive indices

Fig. 3.5 (left panel) shows the refractive indices (n_1) for H_2O , CO_2 and $\text{H}_2\text{O}-\text{CO}_2$ ices as a function of deposition temperature. For pure H_2O ice, we consider temperatures between 17 and 120 K, where H_2O exists in amorphous form. Under our experimental conditions pure CO_2 ice evaporates between 80 and 90 K, limiting the presented data to 80 K. Mixed $\text{H}_2\text{O}-\text{CO}_2$ (4:1) ice is also studied at 90 K, where the co-deposited CO_2 does not stick onto the substrate but may influence the morphology of the condensing H_2O ice.

For pure H_2O , n_1 increases from 17 to around 40 K, followed by a decrease towards 60 K. Above 60 K n_1 increases linearly with temperature towards 120 K. For pure CO_2 , n_1 increases with temperature from 17 K, reaching a maximum at around 60 K. After 60 K, n_1 decreases towards 80 K. The n_1 obtained for $\text{H}_2\text{O}-\text{CO}_2$ (4:1) ice resembles that of pure CO_2 ice. Below 40 K, however, n_1 remains higher than for pure CO_2 or H_2O ice. For $\text{H}_2\text{O}-\text{CO}_2$ ice deposited at 90 K, n_1 remains above the value interpolated for pure H_2O ice, suggesting that the co-deposited CO_2 does indeed influence the morphology of the condensing H_2O ice.

Table 3.2 – Best deposition fringe fit parameters for H₂O, CO₂ and H₂O-CO₂ (4:1) ices. n_1 = refractive index, $1/\alpha$ = inverse scaling factor, γ = deposition rate and R^2 = coefficient of determination.

H ₂ O												
T_d [K]	17	22	30	40	45	50	60	70	80	100	120	
n_1	1.199	1.212	1.216	1.22	1.213	1.212	1.209	1.217	1.221	1.239	1.26	
$1/\alpha$ [V ⁻¹]	3.906	3.959	3.966	3.949	3.88	3.911	3.844	3.864	3.851	3.967	3.809	
γ [nm s ⁻¹]	0.377	0.365	0.345	0.355	0.37	0.322	0.318	0.291	0.304	0.276	0.247	
R^2	0.99606	–	0.99576	0.99626	0.98889	0.99039	0.98829	0.98907	0.97713	0.99216	0.98999	

CO ₂									
T_d [K]	20	30	40	45	50	60	70	80	
n_1	1.221	1.257	1.278	1.293	1.315	1.313	1.309	1.272	
$1/\alpha$ [V ⁻¹]	3.854	3.864	3.809	3.833	3.842	3.79	3.78	3.45	
γ [nm s ⁻¹]	0.298	0.271	0.213	0.208	0.213	0.191	0.192	0.207	
R^2	0.99118	0.98113	0.9861	0.98644	0.98431	0.9392	0.9593	0.93363	

H ₂ O-CO ₂ (4:1)									
T_d [K]	20	30	40	45	50	60	70	80	90
n_1	1.261	1.271	1.274	1.286	1.295	1.295	1.285	1.269	1.251
$1/\alpha$ [V ⁻¹]	3.951	4.009	3.935	3.831	3.856	3.918	3.841	3.736	3.989
γ [nm s ⁻¹]	0.352	0.31	0.179	0.197	0.151	0.172	0.199	0.185	0.158
R^2	0.99779	0.99823	0.99416	0.99382	0.98955	0.98553	0.99121	0.98312	0.98364

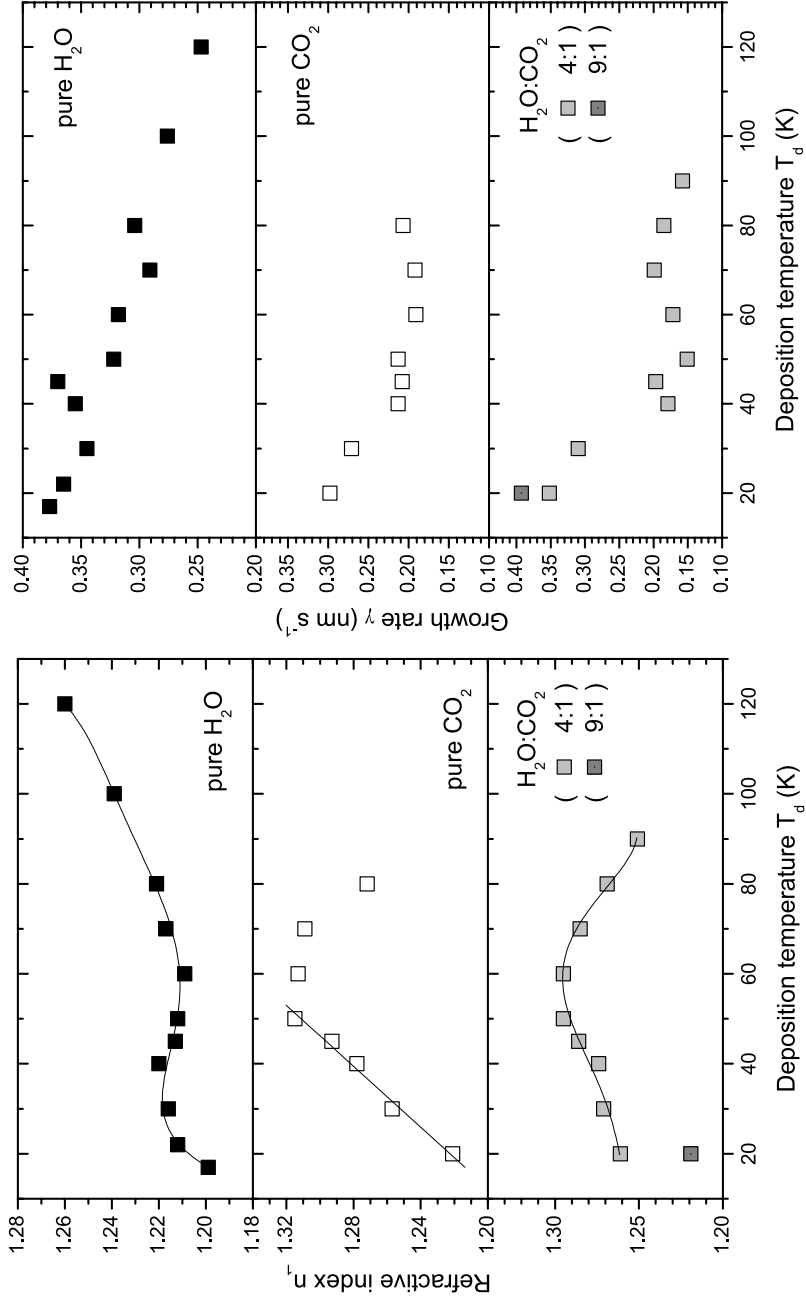


Figure 3.5 – Refractive indices (n_1) (left panel) and growth rates (γ) (right panel) for H₂O, CO₂, and H₂O-CO₂ ices as a function of deposition temperatures. The 5th order polynomial and linear fits of $n(T)$ are shown as black traces in the left panel (see Sect. 3.3.3).

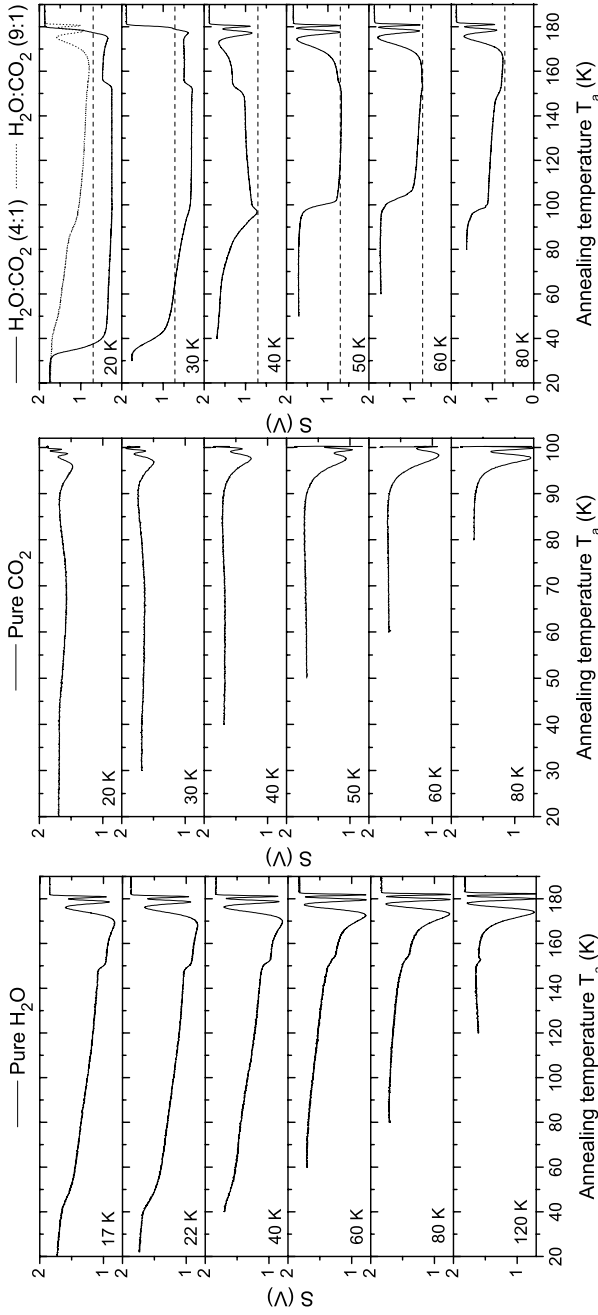


Figure 3.6 – Interference signal (S) during thermal annealing of pure H₂O ice (left panel), pure CO₂ ice (middle panel) and H₂O-CO₂ binary ice mixture (right panel). The different traces correspond to samples deposited at different temperatures as indicated in each panel. A dashed line is drawn in the right panel at $S \approx 0.7$ V corresponding to the approximate level of full destructive interference during the deposition of H₂O-CO₂ (4:1) ices.

3.3.1.2 Growth rates

Fig. 3.5 (right panel) shows the growth rates (γ) for H₂O, CO₂ and H₂O-CO₂ ices as a function of deposition temperature. Assuming that the sticking coefficient does not significantly change with temperature, γ can be inversely correlated with the density of the growing ice: higher density requires more molecules per unit volume, which for a constant molecular deposition rate manifests itself as a slower ice growth rate. However, variations in the growth rate smaller than 10 % cannot be assigned to density effects because of the uncertainty in the experimentally set deposition pressure. The growth rate of pure H₂O ice generally decreases with temperature, suggesting an increasing density. At around 40 K, however, the density is lower than for adjacent points. For pure CO₂ ice, γ decreases with temperature reaching a minimum around 60 K, before increasing towards 80 K. The density of CO₂ ice is thus highest for ice at ~60 K. This is consistent with the found n_1 , which reaches a maximum at about 60 K. For H₂O-CO₂ (4:1) ice the decrease in γ and increase in density is dramatic between 30 and 40 K. Indeed, as will be shown in Sect. 3.3.2, ices grown at 20 and 30 K exhibit qualitatively different behavior upon thermal annealing when compared to ice grown at 40 K.

3.3.2 Thermal annealing

Fig. 3.6 shows the interference signal (S) during thermal annealing of H₂O, CO₂ and H₂O-CO₂ ices deposited at different temperatures. The starting point here coincides with the end of deposition in Fig. 3.3. For the H₂O sample deposited at 17 K (top panel), the signal decreases gradually as the temperature increases. A phase of faster decrease is observed between 40 and 50 K, after which the slow gradual decrease continues. The signal drops quickly at around 150 K corresponding to the temperature region where H₂O crystallization takes place. Above 160 K H₂O starts to thermally desorb. During desorption, the signal cycles back through the interference fringes as the ice becomes thinner. Qualitatively similar behavior is seen for ices grown at higher temperatures (20-120 K). However, the amplitude of the desorption fringe pattern is visibly smaller for ices grown at a lower temperature.

For pure CO₂ ice, which crystallizes between 35 and 50 K (Falk 1987), the interference signal remains relatively constant until 90 K. For CO₂ grown below 50 K, a slight decrease in signal is observed above 45 K. As is the case for H₂O, the amplitude of the desorption fringe pattern for pure CO₂ ice appears smaller for ices grown at low temperature. For CO₂, however, the fringes resulting from thermal annealing cannot be fully resolved due to fast desorption.

For H₂O-CO₂ (4:1) ice, there are clear qualitative differences between ices deposited at different temperatures. For ices deposited at 50, 60 and 80 K (bottom three panels of Fig. 3.6), the signal is stable until 90-95 K after which it drops and reaches a phase of slow decrease around 110 K. As the ice temperature is further increased, the signal gradually approaches the desorption fringe pattern. For ices deposited at 20 and 30 K (top two panels of Fig. 3.6), the signal decreases abruptly after 30 K and continues to dive below the level of complete destructive interference (marked with a dashed horizontal rule). A

value of S smaller than that for complete destructive interference can only be due to loss of photons – likely due to a significant change in the optical quality of the sample. For H₂O-CO₂ (4:1) ice deposited at 40 K, the above is not observed; the signal decreases exponentially towards 100 K until it reaches the fringe turning point and continues to increase again. A sudden change in S around 150 K, similar to pure H₂O samples, is visible for mixed ices, although at somewhat varying temperatures. Thermal annealing of H₂O-CO₂ ice with a higher mixing ratio (9:1) deposited at 17 K, does not exhibit this anomalous behavior (Fig. 3.6). The signal decrease follows that of pure H₂O, with a drop between 40 and 50 K. Another drop in signal is observed around 80–90 K, similar to the H₂O-CO₂ (4:1) samples deposited at higher temperatures, and coincident with the desorption temperature of pure CO₂.

3.3.3 Thickness

In order to derive the degree of thermal collapse of ices, we use Eq. 3.7 to calculate the thickness (d) of the ice at a particular temperature. $n_1(T)$ is obtained by fitting 5th order polynomial (H₂O and H₂O-CO₂) or linear (CO₂) equations to the datasets in Fig. 3.5. For pure CO₂ ice, the thickness is derived between 20 and 50 K only, as possible changes in the surface reflectance after crystallization prohibit interpretation above 50 K. The same reasoning limits the analysis of the H₂O ice data to 120 K.

Fig. 3.7 shows the thermal evolution of the thickness in H₂O, CO₂, and H₂O-CO₂ (4:1) ices deposited at 22, 20 and 40 K, respectively. Pure H₂O ice shows periods of rapid and slow collapse. Rapid collapse occurs around 22–30 K and 38–49 K. The collapse continues after these two stages but significantly slower. Above about 70 K, the decrease is linear with increasing temperature. The total thinning for pure H₂O between 22 and 120 K is 12 %. The CO₂ ice thickness decreases linearly with temperature over the studied temperature range. The thermal collapse for pure CO₂ ice between 20 and 50 K is 11 %. For H₂O-CO₂ (4:1), the thermal collapse can only be derived for ice grown at 40 K. The thickness decreases linearly between 40 and 50 K. After this, the thickness reaches a plateau and at 80 K, the total thermal collapse from 40 K is 4 %. At around 83 K, the thickness drops rapidly, likely due to loss of the CO₂.

Fig. 3.8 shows the total thermal collapse (in %) for pure H₂O and CO₂ ice deposited at different temperatures. For CO₂ ice, the collapse is linearly smaller for samples grown at higher temperatures, consistent with the thermal collapse in Fig. 3.7. For H₂O samples grown at 17, 22 and 30 K, the total collapse decreases linearly with growth temperature. For H₂O ice grown at 40 K, the thermal collapse is larger than for the adjacent points. From 40 K onwards, the magnitude of the collapse exhibits a near linear decrease with temperature. The larger total thermal collapse for H₂O ice grown at 40 K is consistent with the low initial density deduced from the sample growth rates in Fig. 3.5.

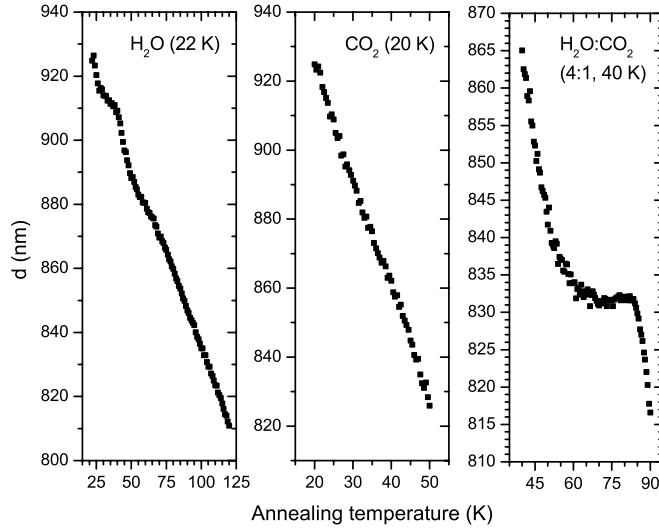


Figure 3.7 – Decrease of thickness upon thermal annealing of H_2O , CO_2 , and $\text{H}_2\text{O}-\text{CO}_2$ (4:1) ices deposited at 22, 20 and 40 K. Note that the thickness and temperature ranges are not the equal.

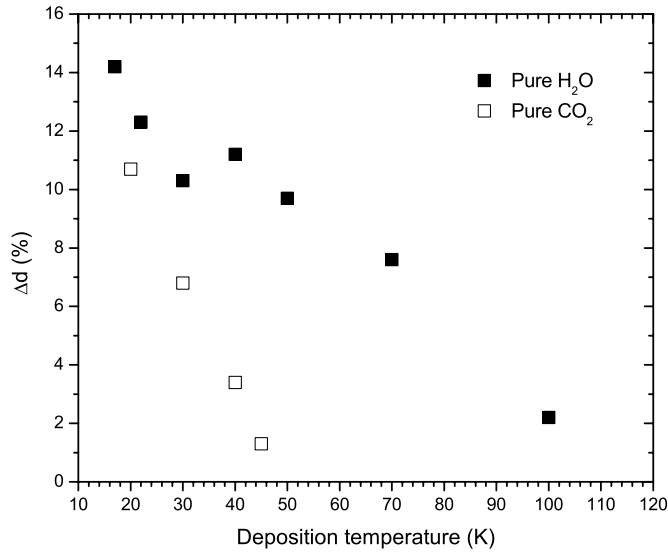


Figure 3.8 – Total decrease of thickness (in %) of H_2O and CO_2 ices grown at different temperatures. The collapse for H_2O and CO_2 is calculated until 120 and 50 K, respectively.

Table 3.3 – Density and surface coverage for background deposited pure H₂O and CO₂ ices, as well as the H₂O-CO₂ (4:1) binary mixture.

Sample	ρ_n [molecules cm ⁻³]	ρ g cm ⁻³	$\rho_{n,xy}$ molec cm ⁻²
H ₂ O (17 K)	2.5×10^{22}	0.73	0.84×10^{15}
CO ₂ (20 K)	1.5×10^{22}	1.09	0.61×10^{15}
H ₂ O-CO ₂ (40 K)	2.1×10^{22}	–	0.75×10^{15}

3.3.4 IR spectroscopy

3.3.4.1 Density

We derive the number density (ρ_n , in molecules cm⁻³) of pure H₂O and CO₂ using Eq. 3.9:

$$\rho_n = \rho_{n,z}^3 = \left(\frac{N}{d \times \rho_{n,xy}} \right)^3 \quad (3.9)$$

where N is the column density (in molecules cm⁻²) obtained using Eq. 3.8 from the integrated intensity of an IR absorption feature, $\rho_{n,xy}$ is the monolayer coverage (in molecules cm⁻²), d is the ice thickness (in cm) obtained from the optical interference measurement and $\rho_{n,z}$ is the vertical number density (along the surface normal, in molecules cm⁻¹). While a surface coverage of 1×10^{15} molecules cm⁻² is typically used for interstellar ice analogs, we assume isotropic density $\rho_{n,z}^2 = \rho_{n,xy}$, *i.e.*, such that the ice density does not depend on the direction.

Table 3.3 gives the densities and adapted surface coverage values for pure H₂O and CO₂ ice, as well as H₂O-CO₂ (4:1) binary ice. For H₂O, we used $\int A d\tilde{\nu}$ from the bulk OH stretching band (around 3300 cm⁻¹). For CO₂, $\int A d\tilde{\nu}$ was derived from the ¹³C=O stretching band (at 2283 cm⁻¹) using a relative ¹³C (¹³CO/¹²CO) abundance of 1.1 %. In the H₂O-CO₂ ice, the molecular environment changes the intrinsic band strengths of the IR features, and those derived for pure ices cannot be used for mixed ice. The density of H₂O-CO₂ (4:1) ice can be derived indirectly using the molecular deposition rate of pure ices (in molecules cm⁻² s⁻¹), which, assuming a similar sticking coefficient, does not depend on the ice composition. The molecular deposition rates derived for pure H₂O and CO₂ are 9.2 and 4.4×10^{14} molecules cm⁻² s⁻¹, respectively. The density given for H₂O-CO₂ ice in Table 3.3 is calculated using a deposition rate average of the pure ices (6.8×10^{14} molecules cm⁻² s⁻¹) and a thickness derived from the interference data.

3.3.4.2 IR spectra of H₂O-CO₂ (4:1) ice

Fig. 3.9 shows the selected IR features in H₂O-CO₂ (4:1) binary ice grown at 16 K and annealed to 140 K. The left panel shows the region covering the CO₂ ($\nu_1 + \nu_3$) combination and ($2\nu_2 + \nu_3$) combination/overtone bands as well as the H₂O (ν_3) dangling OH band. The

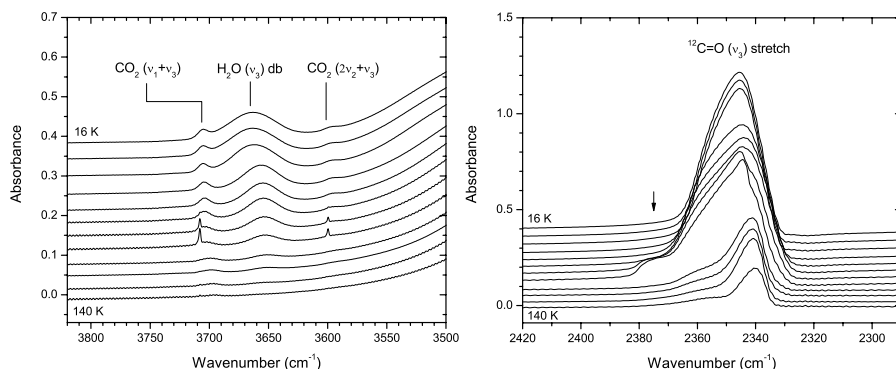


Figure 3.9 – IR spectra of H₂O-CO₂ (4:1) ice around the H₂O (ν_3) dangling OH bond and CO₂ ($\nu_1+\nu_3$) combination and ($2\nu_2+\nu_3$) combination/overtone bands (left panel), and ¹²C=O (ν_3) anti-symmetric stretching band (right panel). The spectra are recorded at 16, 20, 30, 40, 50, 60, 70, 80, 90, 100, 120 and 140 K. The spectra are offset for clarity.

right panel shows the ¹²C=O (ν_3) antisymmetric stretching band. Thermal evolution of the ¹²C=O (ν_3) band shows a clear change in the band profile between 30 and 40 K, as well as between 60 and 90 K. The former is seen as a flattening of the band profile. At 70 and 80 K, the ¹²C=O (ν_3) feature shows significant substructure, not visible in the low-temperature spectra. In particular, a shoulder appears at around 2375 cm⁻¹ indicated by an arrow and the main feature shows a superposed peak around 2345 cm⁻¹. A significant amount of CO₂ remains frozen after the thermal desorption temperature of pure CO₂ ice between 80 and 90 K.

The CO₂ ($\nu_1+\nu_3$) combination and ($2\nu_2+\nu_3$) combination/overtone modes are visible in the low temperature spectra as broad absorption profiles. At 70 and 80 K, these bands show sharp and narrow profiles, which disappear before 90 K. Particularly the stronger CO₂ ($\nu_1+\nu_3$) band remains visible as a broad profile under the sharp feature and persists upon further annealing. The dangling OH band gradually decreases with temperature and is barely visible in the 100 K spectrum.

3.4 Discussion

3.4.1 Refractive index of pure H₂O

The refractive index (n_1) derived for pure H₂O (Fig. 3.5) grows linearly with temperature between 60 and 120 K. Between 17 and 60 K, n_1 first increases with temperature reaching a maximum at 40 K and subsequently decreases towards 60 K. By using the same method (optical interference), Dohnálek et al. (2003) derived n_1 with an overall linear temperature dependence between 22 and 140 K. Because of the small number of data points the non linearity of their data between 22 and 40 K may have been missed. Berland et al. (1995)

report a near linear temperature dependence at deposition temperatures above 35 K. Excluding the non linearity at lower temperatures, our values are in general agreement with those available from the literature. Some variation in the obtained n_1 values is expected due to different experimental conditions, such as deposition pressure (Berland et al. 1995) and the incident angle of the laser beam (Baratta & Palumbo 1998). To our knowledge, this is the first time the refractive index of porous ASW has been studied for such low temperatures, and with a temperature resolution enough to distinguish the non-linearity.

3.4.2 Thermal annealing of pure H₂O

3.4.2.1 Thermal collapse

As we already showed in Bossa et al. (2012), thermal annealing of porous ASW between 20 and 120 K results in a pore collapse accompanied by 12 % thinning of the ice. There the collapse was derived using the linear $n_1(T)$ from (Dohnálek et al. 2003). Ices studied here are grown under identical experimental conditions as those in Bossa et al. (2012). In the present work a number of improvements are implemented. The optical interference is induced by an intensity stabilized laser. Furthermore, the larger angle of incidence of the laser allows for greater sensitivity to changes in the ice thickness. The $n_1(T)$ values used are sample specific at a particular growth temperature. The thermal collapse derived in this work, 12 % for the sample grown at 22 K and annealed to 120 K, is in excellent agreement with the value obtained in Bossa et al. (2012).

3.4.2.2 $I_{\text{hda}} \rightarrow I_{\text{lda}}$ phase transition at 38-68 K

In our experiments, the interference signal during thermal annealing of pure H₂O shows a consistent discontinuity around 40–50 K, where the signal decreases faster than for adjacent regions. The ice thickness derived from the interference signal and $n_1(T)$ indeed shows a faster thinning between 38 and 49 K, followed by a slow thinning between 49 and 70 K. This temperature region coincides with the phase transition in ASW from high-density form (I_{hda}) to low-density form (I_{lda}), which takes place at 38–68 K (Jenniskens & Blake 1994). The transition allows H₂O molecules to reposition themselves into a more energetically favorable configuration, which intrinsically leads to a less compact lattice structure. This phase transition, expected to occur around 72-78 K based on the hydrogen bond enthalpy, occurs at lowered temperature due to defects in lattice structure (Sciortino et al. 1992, Jenniskens et al. 1995).

The $I_{\text{hda}} \rightarrow I_{\text{lda}}$ phase transition, however, only describes the change in the intrinsic structure of ASW, disregarding the pores in the ice structure. While the intrinsic density of ASW decreases as a result of the phase transition, the global density may not. In fact, our results suggest that the onset of the phase transition at 38 K triggers enhanced pore collapse manifesting itself as a faster decrease in thickness. Enhanced formation of complex organics demonstrated in vapor deposited ices around the ASW phase transition (Jenniskens & Blake 1994, Schutte 1988), may therefore not be directly due to an intrinsic phase change, but due to a rapid pore collapse triggering premature recombination of

radicals. Indeed, slow changes in the chemical composition of these samples is already observed below 38 K and the onset of the phase transition.

Jenniskens et al. (1995) showed that vapor deposition of H_2O below 30 K results in I_{hda} . The total thermal collapse of pure H_2O samples grown at different temperatures shows a distinct behavior for samples deposited at ≤ 30 K and ≥ 40 K, respectively (Fig. 3.10). The total thermal collapse (in % of thickness) for both regimes decreases linearly with increasing deposition temperature. However, the values ≥ 40 K are offset and in general higher than those ≤ 30 K. Assuming that porosity in the ice decreases gradually with increasing deposition temperature, the discontinuity between the values derived for ≤ 30 K and ≥ 40 K is implied to be due to different intrinsic structure of the ice. Extrapolation of the values ≥ 40 K (I_{lda}) by a linear fit to 30 K gives a total thermal collapse of 12.8 % for a hypothetical case of the I_{lda} with porosity corresponding to ice deposited at 30 K. The total thermal collapse of I_{hda} grown at this temperature is 10.3 %. The difference in the thermal collapse of I_{hda} and I_{lda} normalized for porosity is 19.5 %. The difference in the density of I_{hda} and I_{lda} (1.17 g cm^{-3} , Mishima et al. (1984), and 0.94 g cm^{-3} , Narten et al. (1976), respectively) is strikingly similar, 19.7 %. We conclude that the offset in

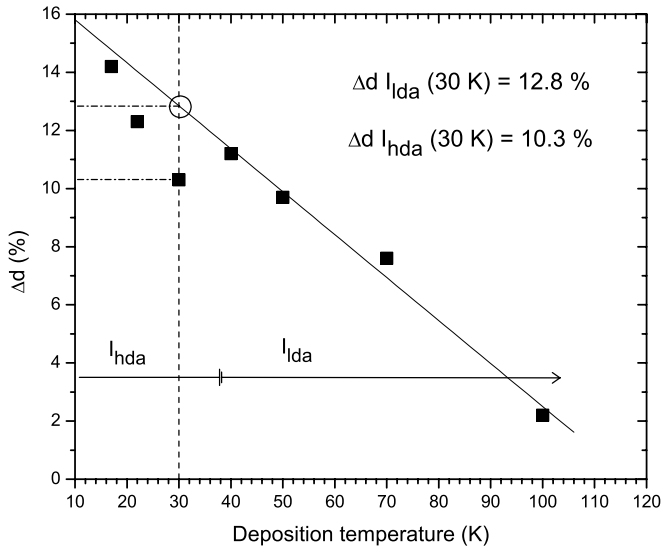


Figure 3.10 – Total thermal collapse of pure H_2O ices grown at different temperatures and annealed to 120 K. The data points at $T \geq 40$ K are linearly extrapolated to obtain a hypothetical data point corresponding to I_{lda} ice with porosity consistent with 30 K. The temperature regions dominated by I_{hda} and I_{lda} from annealing experiment (Jenniskens & Blake 1994) are indicated in the figure.

the total thermal collapse for porous ASW grown ≤ 30 K and ≥ 40 K is purely due to the different intrinsic density of the morphologies formed in the two regimes. This is also in agreement with the discontinuity observed at 38–49 K upon thermal annealing being

related to the $I_{\text{hda}} \rightarrow I_{\text{lda}}$ phase change.

Through X-ray diffraction, [Jenniskens & Blake \(1994\)](#) observed the intrinsic phase change to occur gradually between 38 and 68 K. In our samples, the fast thickness decrease observed at 38–49 K is followed by a phase of slow thinning until ~70 K. This is consistent with continuing $I_{\text{hda}} \rightarrow I_{\text{lda}}$ phase change beyond 49 K, where the gradual thinning due to the decrease in porosity is compensated by expanding intrinsic structure. After the phase transition is complete around 70 K, the thickness decrease continues at a slightly faster phase. The enhanced thinning around 38–49 K was not observed in our previous study ([Bossa et al. 2012](#)) despite identical ice growth conditions. We presume that the improved conditions in the present work allow to visualize this effect, that must have been just below the detection sensitivity in [Bossa et al. \(2012\)](#).

It is interesting to note that a phase of rapid thinning is also observed at 22–30 K followed by a slower collapse until 38 K (Fig. 3.7). The interpretation of this region, however, is difficult due to experimental constraints. In particular, $n_1(T=17\text{ K})$ is obtained at the base temperature of the cryostat without temperature adjusting and may influence the thickness derived at low temperatures. Experiments at lower temperatures are needed to properly characterize n_1 below 22 K. In the current setting this is not possible. Nevertheless, it is clear that at least some thermal collapse already occurs at these low temperatures.

3.4.3 Density of pure H₂O

The density derived spectroscopically for H₂O ice at 17 K is 0.73 g cm⁻³, markedly higher than that from the Lorentz-Lorenz relation in the form used in [Dohnálek et al. \(2003\)](#), which gives 0.63 g cm⁻³. The value derived using the intrinsic band strength of the H₂O (ν_3) stretching mode from [Hagen \(1981\)](#), may be influenced by the spectral differences between ice grown with different morphology. The ices studied in [Hagen \(1981\)](#) are likely to have had lower porosity than the ices studied here, due to a different deposition method; a 5 % error in the intrinsic band strength is enough to explain the difference. [Berland et al. \(1995\)](#) derived a density of 0.68 g cm⁻³ for ice deposited at 35 K and [Dohnálek et al. \(2003\)](#) ~0.62 g cm⁻³ for ice at 22 K. [Raut et al. \(2007b\)](#) derived a density of 0.69 g cm⁻³ for H₂O ice grown through directed deposition (45°) at 30 K.

3.4.4 Residual porosity in annealed H₂O

For porous H₂O ice grown at 17 K the total thermal collapse upon annealing to 120 K is 14 %. Due to the direct inverse correlation between thickness and density¹ the increase in density should be 14 %. Adopting an initial density from the Lorentz-Lorenz relation (0.63 g cm⁻³) gives a density of 0.72 g cm⁻³ after annealing. This is below the density of ice deposited at 120 K (0.83 g cm⁻³), implying that initial porosity in the ice is fully destroyed in the annealing process. Fig. 3.11 shows the porosity $1 - \rho/\rho_c$ before and after annealing to 120 K for pure H₂O ices deposited at different temperatures. The density

¹ $\rho = n/(A \times d)$; assuming negligible desorption ($n = \text{constant}$) and one dimensional collapse ($A \gg d$)

of fully compact ASW (ρ_c) is approximated to be equal to the intrinsic density of I_{lda} (0.94 g cm^{-3}) (Raut et al. 2007a, Westley et al. 1998). It is evident that ice deposited at 120 K has a significant degree of porosity. The residual porosity in samples grown <120 K and annealed to 120 K is about double of that in H_2O deposited at 120 K. It is clear that porous ASW has a "memory" of its original morphology at least throughout the amorphous phase. The ice is still likely to have a significant number of cavities, which makes the global ice density low.

The persistence of porosity upon thermal annealing poses a contradiction to the original approximation, that $n_1(T)$ is the same for both ice deposited at temperature T , and ice annealed to temperature T . Underestimation of porosity for annealed samples results in overestimation of n_1 . This translates to underestimation of ice thickness after annealing and thus overestimation of thermal collapse. Therefore, the values of thermal collapse given in Fig. 3.8 are upper limits. Since porosity in general depends on deposition temperature, the overestimation is likely to be highest for ices deposited at the lowest temperatures.

The presence of cavities throughout the solid phase, beyond crystallization, is consistent with the observation that the amplitude of the fringe pattern during ice desorption, is smaller for ices grown at lower temperature (Fig. 3.6). While the decrease in amplitude may also be due to a change in refractive index, the signal intensity at the constructive interference is a direct indication of loss of photons due to scattering in the ice. Scattering may be more prominent for initially more porous ice if thermal collapse is not able to fully close the pores. Cavities may then remain in the ice throughout the crystalline phase. It has been suggested that scattering may also be due to cracking of the ice (Bargiola 2003) although such effects are more likely for ices that are significantly thicker than studied here (Westley et al. 1998). H_2O ice containing large pores (2-50 nm, *mesoporous* ASW) has been shown to retain a third of the original porosity beyond crystallization (Raut et al. 2007a). Mesoporous ices were obtained through collimated deposition with a large incident angle (77°), known to produce exceptionally porous structures (Stevenson et al. 1999, Kimmel et al. 2001b,a, Dohnálek et al. 2003). These cavities remaining at high temperatures are not visible through IR spectroscopy of the dangling OH bonds, which disappear before crystallization. This has been interpreted as either coalescence of smaller pores into larger pores, preferential destruction of small pores or decrease of surface roughness of the pores (Raut et al. 2007b). Our results support this picture and suggest that omnidirectional background deposition of H_2O – applicable to the vapor deposition in the ISM – possibly results in large pores sustained in the ice upon thermal annealing.

3.4.5 Pure CO_2 ice

The refractive index (n_1) of pure CO_2 ice (Fig. 3.5) grows linearly with temperature until the completion of crystallization at 50 K, after which it decreases. Our results generally agree with those in Satorre et al. (2008), within 2 %. The thermal collapse of CO_2 (Fig. 3.7) proceeds linearly with temperature, with a total collapse of 11 % in thickness for ice deposited at 20 K. Satorre et al. (2008) report a linear density correlation with

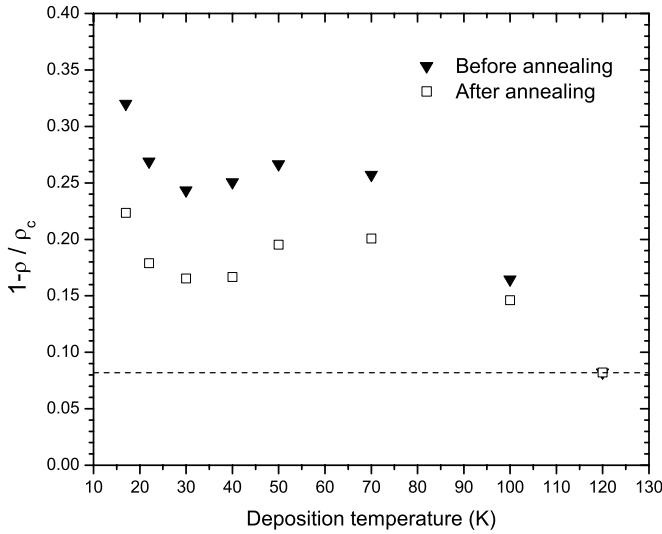


Figure 3.11 – Porosity $1-\rho/\rho_c$ derived for the porous ASW ices annealed to 120 K. ρ values are derived from the Lorentz-Lorenz equation taking into account the thermal collapse. For $\rho_c=0.94 \text{ g cm}^{-3}$ (Narten et al. 1976) is used.

temperature, consistent with our thermal collapse. We derive a density of 1.09 g cm^{-3} for CO₂ ice grown at 20 K, in excellent agreement with Satorre et al. (2008) (1.06 g cm^{-3}).

3.4.6 H₂O-CO₂ binary ice

The refractive indices measured for H₂O-CO₂ ice (Fig. 3.5) resemble those of pure CO₂ ice. The values at 20 and 30 K, however, differ from the trend observed for pure CO₂ ice. The same is true for the density inferred from the deposition rate, which is much lower for 20 and 30 K compared to 40 K and above. A qualitative difference is also observed in the interference signal during annealing of H₂O-CO₂ ices deposited at different temperatures (Fig. 3.6). For H₂O-CO₂ binary ice grown at 20 and 30 K, the interference signal decreases beyond the theoretical minimum set by total destructive interference, and returns only upon ice evaporation. The total loss of photons can only result from severe scattering in the ice and suggests that a H₂O-CO₂ binary ice deposited at temperatures at $\leq 30 \text{ K}$ is qualitatively different to that deposited at higher temperatures. The transition temperature coincides with that of the onset of the $I_{\text{hda}} \rightarrow I_{\text{lda}}$ phase transition in amorphous ASW. A similar loss of signal is not observed for H₂O-CO₂ binary ice with a larger mixing ratio (9:1), which indicates that the effect is determined by the relative amount of CO₂ in the binary ice. It has been shown that co-deposition of compact (non-porous) Ar:H₂O ice at 5 K, followed by thermal cycling results in porous ice (Givan et al. 1996). Possible migration/compaction of the CO₂ component in the H₂O-CO₂ ice may leave the ice surface

rough and causing optical scattering. At lower mixing ratio, this effect may be less effective or result in finer roughness, not probed by the laser. It is interesting to note that the difference in density between 30 and 40 K is much more dramatic for H₂O-CO₂ binary ice than for either of the pure ices, emphasizing the structural difference in also the mixed ice between the temperature regimes ≤ 30 K and ≥ 40 K. The thermal evolution of the $^{12}\text{C}=\text{O}$ (ν_3) IR feature in H₂O-CO₂ ice deposited at 16 K (Fig. 3.9), indeed shows a change in band profile between 30 and 40 K, although the spectral interpretation of this change is difficult. For pure CO₂, the change in the $^{12}\text{CO}_2$ feature upon thermal annealing is seen as narrowing and increasing of the peak intensity (Isokoski et al. in prep.).

For H₂O-CO₂ ice deposited at 40 K, we are able to derive a thermal collapse of 3.9 % (40–80 K), slightly lower than for pure H₂O ice within the same temperature range (5.1 %). However, the optical analysis of two-component ices may be problematic for components with very different refractive indices (Raut et al. 2007b). For H₂O and CO₂ the difference in n_1 is 0.7–8 % depending on the temperature, and more elaborate optical analysis is necessary to reliably quantify the thermal collapse. We are currently conducting a more detailed analysis of mixed ices by employing Bruggemans and Maxwell-Garnett rules (Born & Wolf 1975) in the interference, which may account for the presence of CO₂ and vacuum enclosures in the H₂O ice in a more precise way (Bossa et al. in prep.).

3.4.7 CO₂ segregation

Segregation of ice components is typical for thermally annealed ices containing H₂O and CO₂. Segregation of CO₂ occurs around 60–90 K before its bulk desorption and is evidenced by the appearance of IR features characteristic of pure CO₂ ice (Hodyss et al. 2008, Öberg et al. 2009a). The emergence of several spectral features attributed to pure CO₂ is found at temperatures of 70 and 80 K. In particular, the $^{12}\text{C}=\text{O}$ (ν_3) feature shows significant substructure, and a prominent shoulder at 2375 cm⁻¹ is only visible in the 70 and 80 K spectra. This shoulder has been shown to appear in IR spectra of pure CO₂ ice, recorded at an angle that is not normal to the ice surface (Baratta et al. 2000). The CO₂ ($\nu_1+\nu_3$) combination and ($2\nu_2+\nu_3$) combination/overtone bands are sensitive to the matrix environment (Keane et al. 2001). While these bands are visible for the H₂O-CO₂ ice at all temperatures, at 70 and 80 K sharp peaks appear at 3708 and 3600 cm⁻¹, characteristic for pure CO₂ ice (Sandford & Allamandola 1990), and consistent with a segregation process in which H₂O and CO₂ separate.

Hodyss et al. (2008) studied segregation in compact H₂O-CO₂ binary ices (4:1 and 9:1) through IR spectroscopy. Their samples were grown through directed deposition and therefore have a more compact structure than our samples. The extent of segregation was determined through quantification of the pure (crystalline) CO₂ fraction by fitting the $^{13}\text{CO}_2$ (ν_3) band as a sum of two line profiles centered at 2282 and 2277 cm⁻¹, corresponding to a pure CO₂ component and a component where CO₂ is isolated in the H₂O matrix,

respectively:

$$\text{Pure CO}_2 \text{ fraction} = \frac{\int A(2282 \text{ cm}^{-1}) d\bar{\nu}}{\int A(2277 \text{ cm}^{-1}) d\bar{\nu} + \int A(2282 \text{ cm}^{-1}) d\bar{\nu}}$$

They found that the amount of pure CO₂ depends strongly on the temperature at which the ice has been grown. While for ice grown at 70 K the crystalline fraction can be as high as 90 %, for ices grown below 60 K, and subsequently annealed to 70 K, the crystalline fraction remains below 40 %. Particularly interesting is, that for ices grown between 15 and 50 K, the resulting crystalline fraction is larger for lower growth temperatures. This result may imply a link between initial morphology (porosity) and the extent of segregation. As our ices are inherently more porous than those studied by [Hodyss et al. \(2008\)](#), we attempt to confirm this link.

The ¹³CO₂ (ν_3) feature does not depend on the angle of the IR beam ([Baratta et al. 2000](#)) and can therefore be compared with the results of [Hodyss et al. \(2008\)](#). Fig. 3.12 shows the pure CO₂ fraction in H₂O-CO₂ (4:1) ice deposited at <20 K upon annealing to 120 K for porous ice studied here and compact ice from [Hodyss et al. \(2008\)](#). For the spectra ≥ 70 K, the positions of Gaussians were fixed to those used in [Hodyss et al. \(2008\)](#) while the other parameters were allowed to vary freely. For the spectra ≤ 60 K, the use of only two fixed-position Gaussians does not result in a good fit, and we add an additional feature around 2279 cm⁻¹. The position of the two Gaussians remains fixed during the fitting. The width of these features is fixed to those found at 70 K while all the parameters of the 2279 cm⁻¹ feature are allowed to vary freely. For porous H₂O, we derive a maximum pure CO₂ fraction of 70 %, occurring at 80 K. This is significantly higher than found by [Hodyss et al. \(2008\)](#) (40 %). [Fayolle et al. \(2011\)](#) showed that segregation in H₂O-CO₂ is influenced by the mixing ratio as well as the ice thickness. We conclude therefore that porosity also influences the segregation process: In ice grown at temperatures below the onset of CO₂ segregation, greater porosity results in more effective segregation upon annealing.

Fig. 3.12 shows a considerable amount of pure CO₂ ice even at low temperature, before the onset of segregation. This was not reported by [Hodyss et al. \(2008\)](#). Below 60 K the ¹³CO₂ (ν_3) feature is not adequately fitted with two Gaussians, and the additional feature required at 2279 cm⁻¹ may contribute to the intensity of the 2282 cm⁻¹ feature and consequently to the pure CO₂ fraction. While the interpretation of the low-temperature feature is beyond the scope of this work, the comparison of spectral differences between compact and porous ices may be beneficial for understanding the morphology in mixed ices.

[Hodyss et al. \(2008\)](#) found that for binary ice deposited at the temperatures of CO₂ segregation, a much larger pure fraction results. This result is consistent with our interpretation of the desorption fringe pattern. For H₂O-CO₂ ice deposited at 60 K, before onset of the segregation, the amplitude of the desorption fringe pattern is large compared to that for 80 K (Fig. 3.6). At 80 K, segregation occurs during deposition allowing large pockets of pure CO₂ to form ([Öberg et al. 2009a](#)). These pockets may be large enough to cause optical inhomogeneities and scattering of our interference laser.

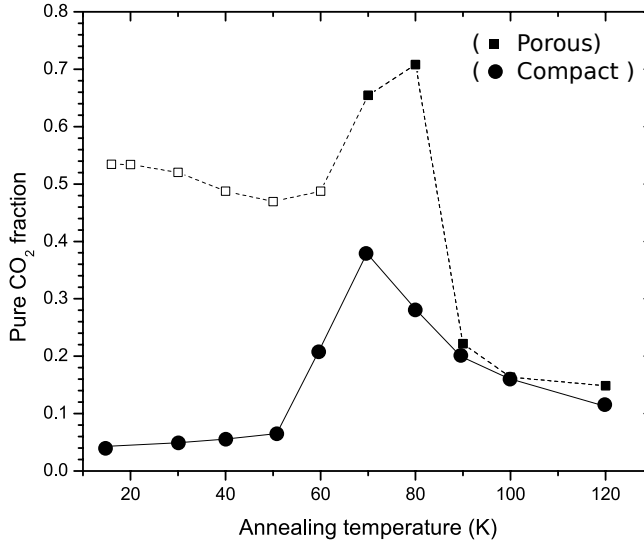


Figure 3.12 – Pure CO₂ ice fraction in H₂O-CO₂ ice upon thermal annealing for porous ice (squares) and compact ice (circles, from (Hodyss et al. 2008)). The data points for porous ice are derived by fitting the ¹³CO₂ (ν_3) feature with two-component Gaussian fit (filled squares) and with three-component Gaussian fit (open squares).

3.5 Summary and conclusions

We have studied the morphology of porous amorphous H₂O, CO₂, and H₂O-CO₂ ices in the astronomically relevant temperature range 17-200 K. Using laser optical interference together with FTIR spectroscopy, we have found the following:

1. Porous ASW (H₂O) undergoes a gradual thermal collapse throughout the amorphous regime. A total thinning of 12 % is derived between 22 and 120 K. This value is an upper limit.
2. The intrinsic $I_{\text{hda}} \rightarrow I_{\text{lda}}$ phase transition in ASW is seen as an enhanced decrease in thickness at 38–49 K and appears to accelerate the pore collapse. The thinning of porous H₂O between 38 and 70 K appears as a combined effect of pore collapse and lattice expansion due to this phase transition.
3. H₂O grown in a porous way is not fully compacted by thermal annealing. Depending on the growth temperature, the residual porosity after annealing to 120 K is around 20 %. Large cavities remain in the ice throughout the solid phase, not observable though infrared spectroscopy.
4. The porous structure of H₂O is retained in the presence of CO₂ at ≤ 30 K. The morphology and changes upon thermal annealing are highly dependent on the initial

ice porosity and mixing ratio. Significant morphological changes occur around the $I_{\text{hda}} \rightarrow I_{\text{lda}}$ phase transition, which are not related to CO₂ segregation occurring at higher temperatures.

5. A high initial porosity leads to a higher extent of CO₂ segregation at 70–80 K.

The morphology of the H₂O containing ices is dominated by both the intrinsic structure of ASW as well as porosity. Both influence the dynamics in low-temperature ices, and may have significant consequences for the solid state chemistry in interstellar ices loaded with reactive intermediates.

The initial porosity of the ice determines its structure throughout the solid phase until ice evaporation. H₂O rich ices formed by vapor deposition on cold interstellar dust grains may contain large cavities that persist over a large temperature range, and affect the catalytic potential of the ice as well as the trapping of gases.

The assumption that ASW in space is compact is likely not fully correct. Energetic processing and thermal annealing decrease the porosity, but the non-detection of the dangling OH bond cannot be taken as a proof that interstellar ice is poreless.

CO₂ is the most common impurity in astronomical H₂O ice, with relative abundances varying from 15 to 40 %. For mixed ices, growth conditions influence the morphology, which at higher temperatures affects astronomically relevant processes such as segregation.

Chapter IV

CO MIXED IN CH₃OH ICE: ANSWER TO THE MISSING 2152 cm⁻¹ BAND?

IV

CO ice mixed with CH₃OH: the answer to the non-detection of the 2152 cm⁻¹ band?

H. M. Cuppen, E. M. Penteado, K. Isokoski, N. van der Marel and H. Linnartz
Monthly Notices of the Royal Astronomical Society 417, 2809 (2011)

Abstract

With this paper we provide a solution to a disagreement between astronomical and laboratory based CO-ice spectroscopic data. In observations towards icy sources, the CO-ice stretching band comprises a prominent and broad ‘red component’ around 2136.5 cm⁻¹. This feature is generally attributed to solid CO mixed in a hydrogen-bonded environment like H₂O, but, as far as we are aware, laboratory spectra have not been able to fully reproduce this feature. Water-containing CO ice cannot reproduce the observed band position and bandwidth without simultaneously producing a shoulder at 2152 cm⁻¹ (4.647 μm). This band, believed to originate from the interaction of dangling-OH bonds with CO, is not observed in astronomical spectra. [Fraser et al. \(2004\)](#) suggested that the 2152 cm⁻¹ feature is suppressed in astronomical ices by blocking of dangling-OH bonds by other species such as CO₂ and CH₃OH. In the present paper, we test this hypothesis by a systematic spectroscopic study of different H₂O:CO:CO₂ mixtures. It is shown that even though the 2152 cm⁻¹ band is suppressed in low temperature spectra, the width and peak position of the red component cannot be reproduced at the same time. An ice mixture containing only CO and CH₃OH, however, does reproduce the spectra at low temperatures, both in terms of peak position and width of the red component and the 2152 cm⁻¹ band does not appear. This indicates that CO may reside in water poor (rather than water-rich) ice in space. The astrophysical implications are discussed.

4.1 Introduction

The comparison of observational and laboratory infrared spectra of interstellar ices is a powerful tool to study their composition and structure. Since the shape, width and position of the absorption bands are sensitive to the molecular environment, temperature and level of energetic or chemical processing, infrared spectroscopy cannot only be used to obtain the overall composition of interstellar ices, but also tells us whether the ice components are mixed or layered, which separate fractions exist, and under which temperature and radiation conditions the ice was formed.

The astronomically observed CO-ice absorption feature consists of multiple components: two relatively narrow features around 2139.7 and 2143.7 cm⁻¹ and a broader component around 2136.5 cm⁻¹. These components are usually referred to as the middle, blue and red component, respectively. The middle component is usually attributed to CO in an ‘apolar’ environment, *i.e.*, an environment where weak van der Waals interactions dominate, like in a pure CO ice. The small blue component at 2143.7 cm⁻¹ is either ascribed to mixtures of solid CO and CO₂ ([Boogert et al. 2002](#), [van Broekhuizen et al. 2006](#)) or to crystalline CO ice ([Pontoppidan et al. 2003b](#)). The so-called broad ([Tielens et al. 1991](#)) or red ([Pontoppidan et al. 2003b](#)) component of the CO absorption band occurs around 2136.5 cm⁻¹ and is the focus of the present work. This feature has been observed along many lines of sight (*e.g.*, [Tielens et al. 1991](#), [Ehrenfreund et al. 1997](#), [Teixeira et al. 1998](#), [Boogert et al. 2002](#), [Pontoppidan et al. 2003b](#), and references therein) and CO in a hydrogen bonding environment, like H₂O and CH₃OH containing ices, is generally considered to be responsible for the observed component ([Sandford et al. 1988](#), [Tielens et al. 1991](#)). Since H₂O is the most abundant interstellar ice species, a CO:H₂O mixed ice is

usually considered to be the carrier of the red component. A CH_3OH mixture with CO has previously been suggested as another possible carrier (Sandford et al. 1988, Tielens et al. 1991), but this concept has been largely ignored and has so far not been verified experimentally.

Most interstellar ice spectra are consistent with low-temperature and non-processed hydrogenated ices. The red component of the CO absorption band forms an exception to this. As mentioned earlier, this feature is generally attributed to solid CO mixed in water, but, as far as we are aware, laboratory spectra have not been able to fully reproduce this feature. The large width and red-shifted position of the CO band are only reproduced by spectra of mixed $\text{H}_2\text{O}:\text{CO}$ ices with large concentrations of water (*e.g.*, Kerr et al. 1993, Chiar et al. 1994, Boogert et al. 2002). Under these circumstances the laboratory spectra show a shoulder at 2152 cm^{-1} ($4.647\text{ }\mu\text{m}$) which is not present in the observed astronomical spectra (*e.g.*, Sandford et al. 1988, Palumbo 2006).

The 2152 cm^{-1} feature is associated with CO adsorbed on ‘dangling-OH’ bonds at the H_2O -ice-vacuum interface (Al-Halabi et al. 2004). ‘Dangling-OH’ features have been experimentally shown to disappear upon energetic processing by for instance heating (Mennella et al. 2004) or ion bombardment (Palumbo 2005). Processed ices have therefore been suggested to be responsible for the red component (Mennella et al. 2004, Palumbo 2005, 2006). However, the profiles for ice mixtures at higher temperature have a full width half maximum (FWHM) that is too small to reproduce the observational feature. Moreover, no other signatures of irradiation like the presence of OCN^- or aliphatics have been seen along many of the lines of sight where the red component is detected (Pontoppidan et al. 2003b).

In the past the astronomical non-detection of the 2152 cm^{-1} feature was explained by the low spectral resolution or low signal-to-noise ratio in the observations (Ehrenfreund et al. 1997, Sandford et al. 1988) or by other overlapping features at this wavelength (Schmitt et al. 1989). However, observations by Pontoppidan et al. (2003b) showed indisputably that the 2152 cm^{-1} feature is not present in the observational spectra and stringent upper limits could be derived.

Fraser et al. (2004) have therefore tested whether a layered ice of CO and H_2O could explain the discrepancy between astronomical and laboratory spectra. They found that $\text{CO-H}_2\text{O}$ containing interstellar ices are better represented by the evolution of a layered ice model than by a mixed ice, since a strong 2152 cm^{-1} feature would appear in the case that H_2O and CO are intimately mixed. When CO and H_2O are layered, CO only interacts with dangling-OH at the interface which suppresses the 2152 cm^{-1} feature below the detection limit. Moreover, gas-phase CO only depletes in the densest parts of interstellar clouds and solid H_2O has been observed in regions where CO was still in the gas phase. However, a purely layered model cannot explain the presence of the red component and Fraser et al. (2004) suggested that a small fraction of CO diffuses into the H_2O component, which would in turn lead to a shoulder at 2152 cm^{-1} . They further proposed that this feature is suppressed in astronomical spectra by blocking of the dangling-OH by other species such as CO_2 and CH_3OH . In the present paper, we test this hypothesis by a systematic spectroscopic study of different $\text{H}_2\text{O}:\text{CO}:\text{CO}_2$ mixtures and we show that although the 2152 cm^{-1} band can be suppressed in low temperature spectra, the width and

peak position of the red component cannot be reproduced at the same time.

A mixture of CO and CH₃OH, however, reproduces the astronomical spectra, *i.e.*, the laboratory features match the astronomically observed red component data and the 2152 cm⁻¹ feature does not show up. This is consistent with a number of recent findings. Laboratory experiments show that CH₃OH can be formed on icy grains from CO (Watanabe et al. 2004, Fuchs et al. 2009) and model simulations of CH₃OH formation in dense cores indeed result in grain mantles with CO and CH₃OH intimately mixed (Cuppen et al. 2009). Bottinelli et al. (2010) recently showed for *Spitzer* observations of solid methanol lines that the methanol profiles are consistent with CH₃OH:CO = 1:1 mixtures. Although, a separate CH₃OH-rich and H₂O-poor component fit the observations as well.

The present paper is structured as follows. Section 4.2 presents the experimental procedure for obtaining the laboratory spectra. Section 4.3 gives the fitting procedure used to extract the spectral characteristics from observed CO ice absorption bands. Section 4.4 tests the hypothesis of the suppression of the 2152 cm⁻¹ band by CO₂ and Section 4.5 extends this to the case of methanol and discusses CO:CH₃OH mixtures as carriers for the red component at 2136.5 cm⁻¹. Section 4.6 concludes and gives the astrophysical implications of this work.

4.2 Experimental methods

All experiments are performed in a high vacuum (HV) setup, which has a base pressure of 5×10^{-7} mbar at room temperature and is described in detail by Gerakines et al. (1995) and Bouwman et al. (2007). In short, the CsI sample window is cooled to 15 K by a closed-cycle helium cryostat and the samples are then deposited from the gas phase on the window with the direction along the surface normal. To enable a direct comparison of the spectra obtained for the different ice mixtures, the amount of deposited H₂O and CH₃OH is kept constant at 3000 ML for H₂O:CO:CO₂ and CH₃OH:CO mixtures, respectively.

Transmission Fourier transform infrared spectra of the ice mixtures are recorded in a single pass with a Bio-Rad 40-A spectrometer and a Varian 670-IR FTIR spectrometer for the H₂O:CO:CO₂ and CH₃OH:CO mixtures, respectively. Spectra are taken between 4000-400 cm⁻¹ (2.5-25 μ m) with a resolution of 1 cm⁻¹ using a total of 256 scans per spectrum to increase the SNR. The spectrometer is flushed with dry air to minimize background fluctuations due to atmospheric absorptions. Background spectra are acquired prior to deposition for each experiment. Each sample is measured at fixed temperatures between 15 and 135 K, at 15, 22, 25, 30, 45, 60, 75, 90, 105 and 135 K. The sample is heated with a resistive heater, using a Lakeshore temperature controller unit. The temperature is measured by a silicon diode. After each heating step, the sample is allowed to stabilize for two minutes.

The gas mixtures are prepared separately in a glass vacuum line with a base pressure of 10^{-5} mbar. The gases CO (Praxair, 99.999% purity for H₂O:CO:CO₂ mixtures and Linde, 99.997% for CH₃OH:CO) and CO₂ (Praxair, 99.98% purity) are directly used from the high pressure gas bottle, whereas deionised H₂O and CH₃OH (Sigma-Aldrich, 99.9% purity) are further purified by three freeze-pump-thaw cycles. In the present study,

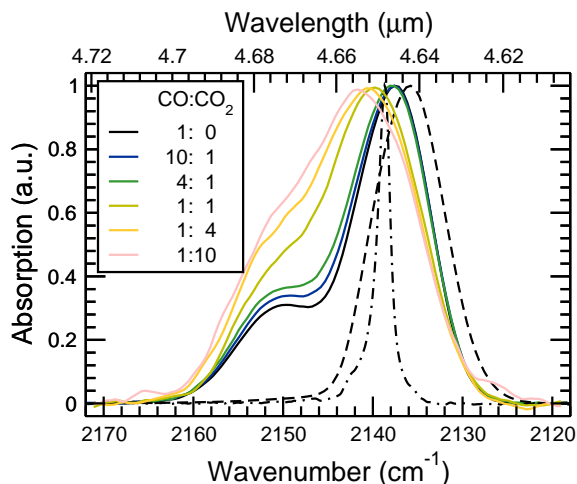


Figure 4.1 – Experimental spectra of CO absorption band in $\text{H}_2\text{O}:\text{CO}:\text{CO}_2$ mixtures (solid curves) and $\text{CH}_3\text{OH}:\text{CO} = 1:1$ mixture (dashed curve) at 15 K. The $\text{H}_2\text{O}:\text{CO}:\text{CO}_2$ mixtures have a ratio of $\text{H}_2\text{O}:(\text{CO}+\text{CO}_2) = 4:1$ and different $\text{CO}:\text{CO}_2$ ratios as indicated in the legend. A pure CO spectrum is shown by the dash-dotted curve.

the following mixtures are used: $\text{CH}_3\text{OH}:\text{CO} = 9:1, 4:1, 2:1, 1:1, 1:2, 1:4$ and $1:9$ and $\text{H}_2\text{O}:(\text{CO}+\text{CO}_2) = 4:1, 2:1, 1:1, 1:2$ and $1:4$ for each $\text{H}_2\text{O}:(\text{CO}+\text{CO}_2)$ ratio five different $\text{CO}:\text{CO}_2$ ratios. Figure 4.1 shows a selection of spectra at 15 K for different mixtures. The $\text{H}_2\text{O}:\text{CO}$ spectrum is taken from [Bouwman et al. \(2007\)](#). A pure CO ice has an absorption band at 2139.7 cm^{-1} ($4.65 \mu\text{m}$) (dash-dotted curve) ([Ehrenfreund et al. 1997](#)). All spectra are normalized to the maximum of this feature. Figure 4.1 clearly shows the broadening of the band by the presence of other constituents in the ice as well as the appearance of the shoulder at 2152 cm^{-1} . All features have a line shape that is close to a Gaussian. The peak position and presence of the shoulder at 2152 cm^{-1} is highly dependent on the exact composition of the ice mixture. In the next paragraphs we will extract characteristics such as width, peak position and presence of the 2152 cm^{-1} shoulder from the experimental spectra and compare these to the characteristics of astronomically observed CO ice spectra.

4.3 Observations of the red component

[Pontoppidan et al. \(2003b\)](#) performed a Very Large Telescope (VLT) spectroscopic survey of 39 Young Stellar Objects (YSOs) with high signal to noise ratio and high spectral resolution. We use this data to extract information about the red component in astronomical observations and compare this to laboratory spectra. For this a phenomenological approach is used that has the advantage that spectral characteristics can be compared to a wide range of different experimental data. Another method that is often adopted is the

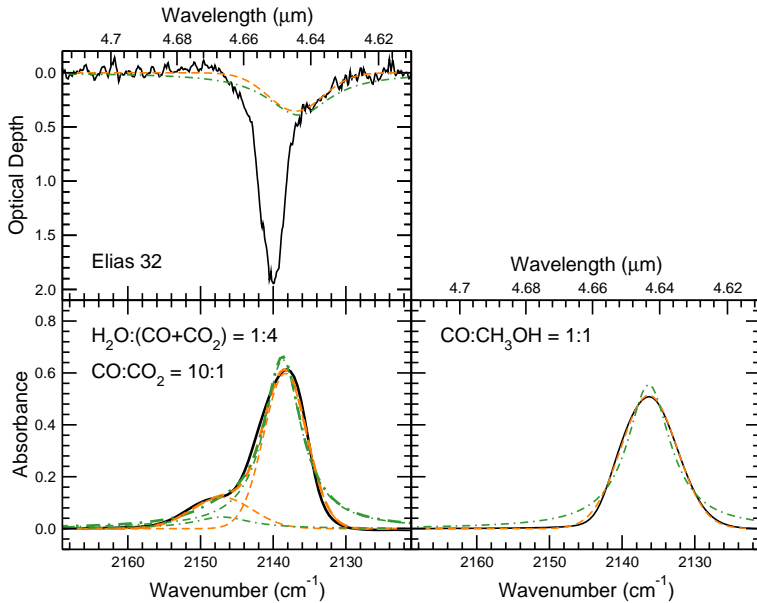


Figure 4.2 – A comparison between fits of the red CO-ice profile by Gaussian line shapes (dashed curves) and by Lorentzian line shapes (dash-dotted). (Top) The Gaussian fit yields the best-fit result for Elias 32 and is used in this study; the Lorentzian result is taken from Pontoppidan et al. (2003b).

so-called mix-and-match approach, in which observational spectra are fitted with a small selection of experimental templates of typical ice mixtures. However, often a degeneracy exists between laboratory spectra recorded under different experimental conditions.

Our phenomenological approach is more geared towards a comparison with the experimental data. For instance, Pontoppidan et al. (2003b) used a Lorentzian line shape to fit the red component and two Gaussians for the blue and middle components, since this would better describe the observational results. They argued that a Lorentzian shape may be a better representation of IR band profiles of CO in an environment which is dominated by weak van der Waals interactions. The blue and middle components have a high CO content, since they are most likely due to a CO:CO₂-ice or crystalline CO ice and a CO-dominated ice, respectively. Because of the high CO content, grain shape effects are important and these could distort the Lorentzian profile to emulate Gaussian line shapes. We however obtain better fits of both the experimental and observational spectra by using Gaussians for all three components as can be seen in Fig. 4.2. Since the red component is most likely caused by CO in a hydrogen bonding environment, we argue that the simple model of Lorentz oscillators breaks down for this component. This is an additional argument to use a Gaussian line shape for our fits.

In addition to the three CO components, some observational spectra show a band around 2175 cm⁻¹, which can be attributed to the stretching mode of CN bonds. The most likely carrier for this bond is OCN⁻ (Schutte & Greenberg 1997, Pendleton et al.

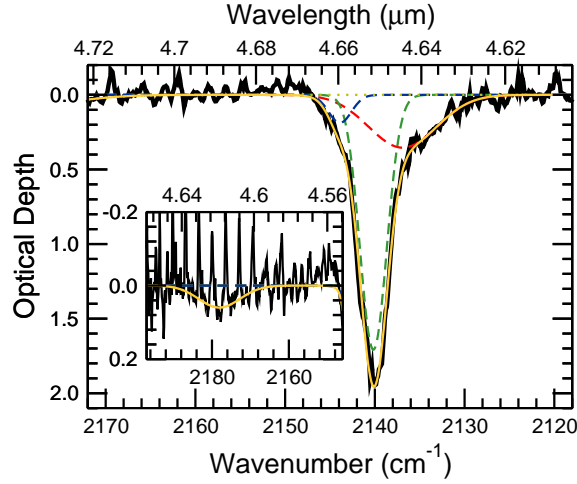


Figure 4.3 – The observational spectra, here Elias 32, are fitted by four Gaussians representing the red (FWHM = 8.9 cm^{-1}), middle, and blue component and the 2175 cm^{-1} band (shown in the inset and likely due to OCN^-).

1999, Novozamsky et al. 2001). This extra component is fitted with a Gaussian as well.

The following fitting procedure has been applied to all spectra. Four Gaussians are fitted to the data in the $2185\text{--}2120 \text{ cm}^{-1}$ range. The peak positions are free for all components. The FWHM is only allowed to vary for the 2175 cm^{-1} feature, similar to the fitting procedure of Pontoppidan et al. (2003b). The FWHM of the blue and middle components are also taken from this work as 3.0 and 3.5 cm^{-1} , respectively. Since the width of the red feature is sensitive to the exact composition of the polar ice, 56 independent fits are performed for each spectrum in which this FWHM is fixed by 56 different values between 3 and 14 cm^{-1} . The final sum-of-squares errors as a function of FWHM determine the best value of the FWHM and its uncertainty (error within 1% of best value). The uncertainty in the peak position is taken from the spread obtained in the fits within the FWHM range. Figure 4.3 shows an example of a fitted observational spectrum. Here the spectrum of Elias 32 is shown which has an average FWHM ($8.9 \pm 0.7 \text{ cm}^{-1}$) and peak position ($2136.7 \pm 2.4 \text{ cm}^{-1}$) for the red component.

Figure 4.4 plots the results for all fits. Outcomes with a small red contribution are excluded from this plot. Most objects lie in the circle $8.5 \pm 3.8 \text{ cm}^{-1}$ and $2136.7 \pm 2.4 \text{ cm}^{-1}$ which serves as a guide to the eye and will later be used to compare to the experimental data. The circle is based on the median value of the position and FWHM and 3 times the median absolute deviation. The median position is in close agreement with Pontoppidan et al. (2003b) who obtained 2136.5 cm^{-1} , whereas the present FWHM value of 8.5 cm^{-1} is smaller than the value of 10.6 cm^{-1} found Pontoppidan et al. (2003b), even though this was for a Lorentzian instead of a Gaussian profile.

As mentioned before, none of the observational spectra shows a 2152 cm^{-1} feature.

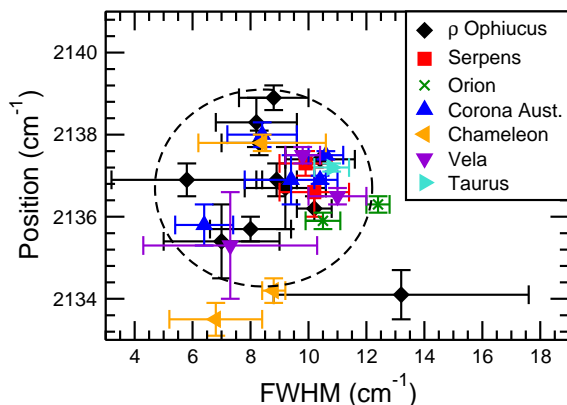


Figure 4.4 – The spread in FWHM and position of the red component in the observational spectra (Pontoppidan et al. 2003b). The circle serves as a guide to the eye.

Pontoppidan et al. (2003b) obtained lower limits on the ratio between the red component at ~ 2136.5 cm⁻¹ and the 2152 cm⁻¹ dangling-OH band for the highest quality interstellar spectra. For most sources these limits fall between 6 and 9 as plotted in their Fig. 21, but several sources have even higher lower limits. In order to explain the observational spectra, laboratory spectra should have a CO-2136/CO-2152 ratio of at least 6 and a FWHM and peak position of the main band that is in agreement with 8.5 ± 3.8 cm⁻¹ and 2136.7 ± 2.4 cm⁻¹. Since CO is probably only a minor species in the ice mixture responsible for the observed 2136.5 cm⁻¹ feature, grain shape effects are assumed to be minimal and the observational data and laboratory data can be directly compared.

4.4 Dangling-OH blocking by CO₂

As mentioned in the introduction, one of the suggestions for the astronomical non-detection of the 2152 cm⁻¹ is blocking of the dangling-OH site of water by other molecules in the interstellar ice. Since one of the other main ice components, besides H₂O and CO, is CO₂, this species was proposed as a potential candidate (Fraser et al. 2004). Since this hypothesis has not been tested by laboratory experiments yet, we performed a systematic spectroscopic study of H₂O:CO:CO₂ mixtures and compared their spectral characteristics to the observed spectra. Spectra of 25 different H₂O:CO:CO₂ mixtures at ten different temperatures between 15 and 135 K were recorded. As explained in Section 4.2, the different mixing ratios are given by H₂O:(CO+CO₂) = 4:1, 2:1, 1:1, 1:2 and 1:4 with CO:CO₂ = 10:1, 4:1, 1:1, 1:4, and 1:10 for each combination. Each of the thus-obtained 250 spectra is fitted by two Gaussians: one representing the 2152 cm⁻¹ feature and one the main feature between 2136.5 and 2139 cm⁻¹.

Figure 4.5 shows a limited set of the spectra (45 out of 250 spectra) to illustrate the effect of ice composition and temperature on the CO absorption feature, together with

the fitted Gaussians. Again all spectra are normalized to maximum of the CO feature. The most differing mixtures are used and the lower temperatures have been selected. At higher temperatures a large fraction of CO has desorbed. The individual panels clearly show that the CO profile is strongly affected by the presence of CO₂ and H₂O. In general, the presence of H₂O and CO₂ appears to have orthogonal effects: more H₂O leads to a red-shift and an increase of the 2152 cm⁻¹ feature, whereas more CO₂ leads to a blue-shift and a suppression of the 2152 cm⁻¹ feature.

The fitted Gaussians are used for the comparison with the observations. The main Gaussian is compared to the red component and the ratio between the optical depths between the CO-main and CO-2152 is compared to the lower limit of the CO-2136/CO-2152 ratio that was observationally determined. Since not all experimental spectra have a feature peaking at 2136.5 cm⁻¹, the main CO feature is used instead. At a later stage we will consider the exact band position of the main feature and the spectra that do not reproduce the astronomically observed position are excluded in that process.

For five mixing ratios a CO-main/CO-2152 larger than 6 was found at low temperatures. Four of these mixing ratios fulfill H₂O:(CO+CO₂) = 1:4 or 1:2 and CO:CO₂ = 1:4 or 1:10 and the fifth mixing ratio is H₂O:CO:CO₂ = 25:90:9 (H₂O:(CO+CO₂) = 1:4 and CO:CO₂ = 10:1). The latter only just fulfills the CO-main/CO-2152 > 6 criterion and only for three low temperatures: 22, 25 and 30 K as can be seen in Fig. 4.5. Other compositions reach CO-main/CO-2152 ratios larger than 6 at elevated ice temperatures ($T > 60$ K) well above the CO desorption temperature (Öberg et al. 2005, $T \sim 28$ K). The top panel of Figure 4.6 plots the position and FWHM of the spectra of the first five mixing ratios at different temperatures. A series of identical symbols reflects the same mixing ratio but for different temperatures, as annotated below each symbol. The circle in this panel is the same circle as plotted in Figure 4.4 and is drawn to simplify the visual comparison between observations and experiments. One can clearly see that the observed combination of position and FWHM is only obtained for a few spectra. These spectra are for H₂O:CO:CO₂ = 25:90:9, which has a CO-main/CO-2152 ratio only just above the threshold value of 6, whereas the astronomical limits are often much higher, and only covers a region at the edge of the circle. This ice combination can therefore not represent the majority of the astronomically observed red CO-ice components.

Summarizing, one can conclude that the addition of CO₂ to a H₂O:CO mixture can indeed reduce the dangling-OH leading to the disappearance of the 2152 cm⁻¹ at low temperatures, but this requires such large quantities of CO₂ that H₂O is no longer the major ice species and the position and width of the main feature no longer agrees with the characteristics of the astronomically observed features. The width and position resemble in this case better a CO:CO₂ ice. Mixtures with smaller fractions of CO₂ reproduce the width and position, but also show substantial shoulders at 2152 cm⁻¹. The addition of CO₂ can therefore not explain the observed spectral features of the red component of the CO absorption band.

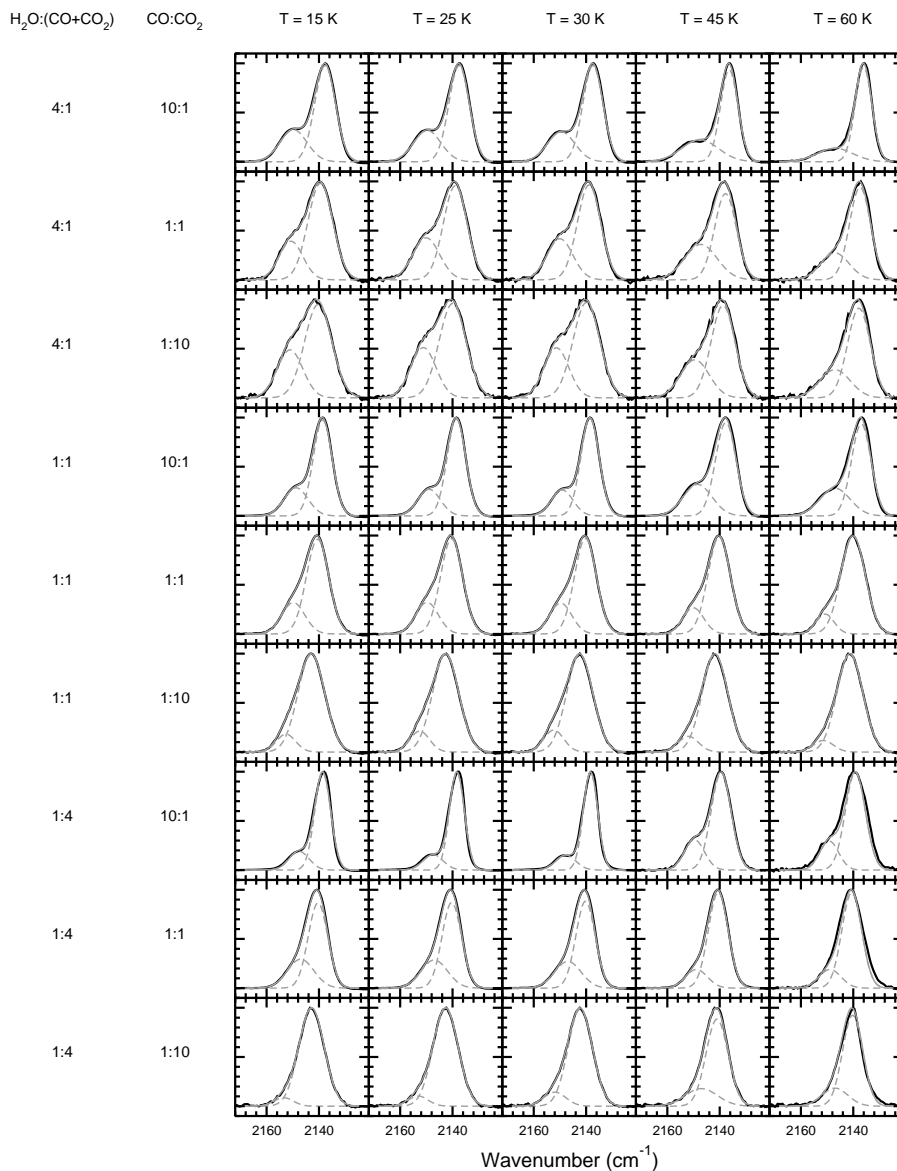


Figure 4.5 – A limited set of CO profiles for different $\text{H}_2\text{O}:\text{CO}:\text{CO}_2$ mixtures at different temperatures, to illustrate how the CO profile — width, position and presence of the 2152 cm⁻¹ feature — changes with composition and temperature. All ices are deposited at 15 K and then subsequently heated to measure the higher temperatures. Spectra are normalized to the maximum of the CO feature.

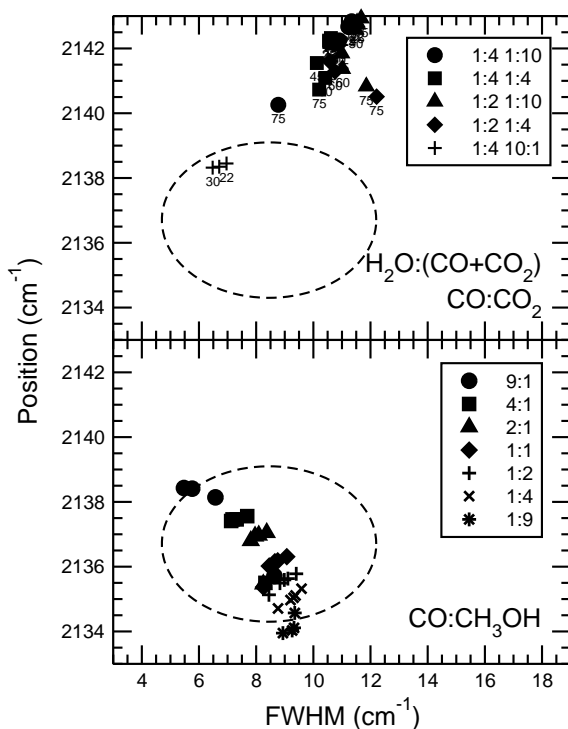


Figure 4.6 – The FWHM and position of the CO absorption band in laboratory spectra of a range of different $\text{H}_2\text{O}:\text{CO}:\text{CO}_2$ (top panel) and $\text{CH}_3\text{OH}:\text{CO}$ (bottom panel) ice mixtures at different temperatures. The circles serve as a guide to the eye to allow easy comparison to the observational data in Figure 4.4.

4.5 CO mixed with CH₃OH

The present section tests whether a mixture of CO with CH₃OH can explain the observed characteristics. As far as we are aware, spectroscopy on unprocessed CO and CH₃OH containing mixtures has not been directly linked to the 2136 cm⁻¹ component (Palumbo & Strazzulla 1993) or has only been performed in the presence of H₂O causing a shoulder at 2152 cm⁻¹ (Sandford et al. 1988, Hudgins et al. 1993), except in Bisschop (2007). Here we investigate CO solely mixed with CH₃OH. Recent observations of solid CH₃OH (Boogert et al. 2008) showed that CH₃OH is most likely present in a water-poor environment and that a mixture of CO:CH₃OH is consistent with the observed width and position of the methanol band (Bottinelli et al. 2010). Furthermore, since CO is a precursor of CH₃OH through H-atom addition reactions (Watanabe et al. 2004, Fuchs et al. 2009), they are likely to be present in the same ice component on the grains.

The dashed curve in Figure 4.1 plots the CO absorption band for CO:CH₃OH = 1:1 mixture at 15 K. It shows that the addition of CH₃OH results in a broad, red-shifted

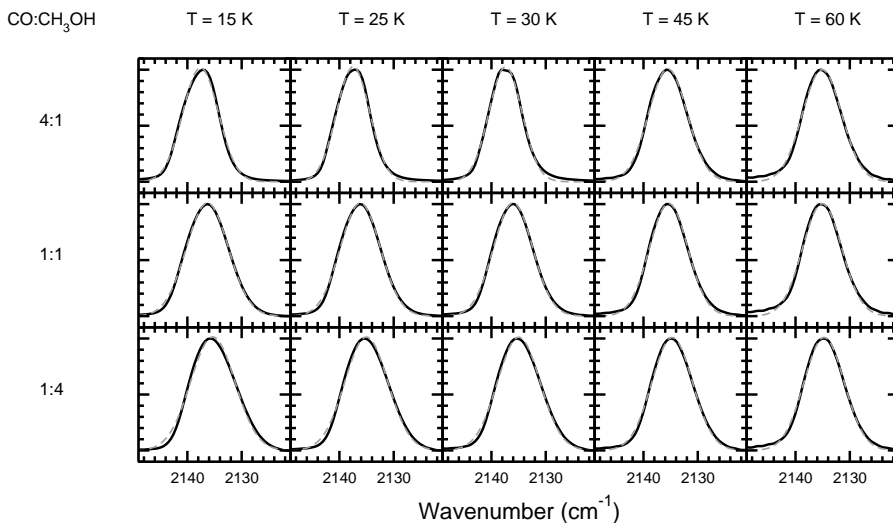


Figure 4.7 – Similar to Fig. 4.5 for CO:CH₃OH ice mixtures.

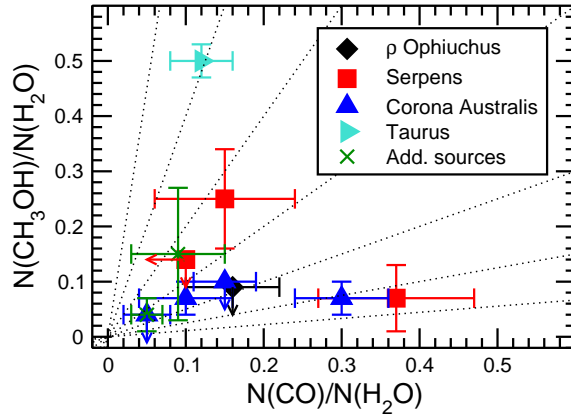
peak without a shoulder at 2152 cm⁻¹. The seven ice compositions used in present work (CO:CH₃OH = 9:1, 4:1, 2:1, 1:1, 1:2, 1:4 and 1:9) cover a large range in mixing ratios and the spectra do not exhibit a shoulder at 2152 cm⁻¹ as can be seen in Fig. 4.7. This figure gives an overview of the CO band profile in a CH₃OH-environment for different mixing ratios and temperatures. The figures shows that the feature become more redshifted and wider with CH₃OH-content. These spectra are again fitted to extract the spectral characteristics. In this case a single Gaussian is used, because of the absence of the shoulder at 2152 cm⁻¹. The resulting fits are plotted in gray with a dashed curve and overlap with the data in most cases. The corresponding positions and FWHMs are given in Table 4.1.

The bottom panel of Figure 4.6 plots the FWHM versus the position of the CO absorption band for different CO:CH₃OH mixing ratios at different temperatures between 15 and 45 K. The circle that marks the observational range is now clearly filled. Moreover, mainly the low temperature spectra fall in the circle. The exact position in the circle depends on the mixing ratio of CO and CH₃OH. Ratios between 1:9 and 9:1 are within the boundaries defined by the circle and reproduce the spectral characteristics of the observations. The majority of the observational spectra are best reproduced by ratios between CO:CH₃OH=1:2 and 4:1.

The ratios based on spectral characteristics are indeed consistent with interstellar CO:CH₃OH ice ratios based on observed ice abundances as can be seen from Figure 4.8. This graph shows the ‘polar’ CO abundance with respect to water ice derived from the red component versus the solid CH₃OH abundance. Column densities for polar CO are taken from Pontoppidan et al. (2003b) and for H₂O and CH₃OH ice from Boogert et al. (2008). The error bars represent 3 σ limits. The dotted lines indicate the different mixing ratios as studied experimentally: from CO:CH₃OH=1:9 (top left) to 9:1 (bottom right). The two

Table 4.1 – The peak position and FWHM for different CO:CH₃OH ice mixtures and temperatures.

CO:CH ₃ OH	position (cm ⁻¹)				FWHM (cm ⁻¹)			
	15 K	25 K	30 K	45 K	15 K	25 K	30 K	45 K
1:9	2134.6	2134.1	2134.0	2133.9	9.35	9.32	9.26	8.94
1:4	2135.3	2135.0	2135.0	2134.7	9.59	9.30	9.20	8.76
1:2	2135.8	2135.6	2135.5	2135.1	9.40	8.98	8.83	8.45
1:1	2136.3	2136.1	2136.0	2135.4	9.07	8.65	8.46	8.26
2:1	2137.0	2136.9	2136.8	2135.5	8.37	7.96	7.81	8.25
4:1	2137.6	2137.5	2137.4	2135.5	7.69	7.17	7.12	8.32
9:1	2138.1	2138.4	2138.4	2135.7	6.57	5.76	5.47	8.64


Figure 4.8 – The observed column densities of polar CO versus CH₃OH w.r.t. H₂O ice. The dotted lines indicate different mixing ratios (9:1, 4:1, 2:1, 1:1, 1:2, 1:4, 1:9).

additional sources are W33A and GL 2136. The figure shows that based on the column densities most observational ratios fall between CO:CH₃OH = 1:2 and 4:1, which is in close agreement with the conclusions based on the spectral characteristics. Note that for large CO:CH₃OH ratios, grain shape effects can have an influence on the observed spectra and the experimental spectra should be adjusted for this. Since the optical constants are not available for the measured spectra, this effect is ignored for the moment in this comparison.

4.6 Conclusions and astrophysical implications

The combined astronomical and laboratory data discussed in the present paper show, that the red component of the CO absorption band can be explained by a mixture of solid CO and CH₃OH without the presence of H₂O. Previously considered water-containing mixtures resulted in the appearance of a shoulder at 2152 cm⁻¹ in laboratory spectra,

which posed a problem, since this feature is not observed astronomically. The discrepancy is solved in the present paper by considering a water-poor mixture. It is credible that other species, chemically related to CH₃OH, are able to reproduce this result as well, but given the direct relation between CO and CH₃OH, methanol is a very likely candidate.

This provides additional proof that CO only freezes out after H₂O has formed on the grain, leading to at least two separate ice components: a H₂O-rich and a CO-rich layer. Observational studies already showed that CO mainly freezes out in the centers of dense cold cloud cores (Pontoppidan 2006, Pontoppidan et al. 2008) where most of the gas is in molecular form and H₂ and CO are the dominant species. In these centers, most of the elemental oxygen is in the form of CO or frozen out onto grains in form of H₂O.

The spectral characteristics of the red component require a high fraction of CH₃OH to be present. This means that almost all CH₃OH is present in the CO:CH₃OH component. This is in general agreement with observations of solid CH₃OH. It is hard to constrain the percentage of CH₃OH mixed with water observationally, since the 9.75 μ m band profile of CH₃OH hardly changes with ice composition, neither in peak shape nor position. The feature only becomes red-shifted when water ice is dominant, *i.e.*, >90% (Bottinelli et al. 2010, Skinner et al. 1992). The 3.54 μ m CH₃OH feature can also be applied to constrain the CH₃OH ice environment (Dartois et al. 1999, Pontoppidan et al. 2003a, Thi et al. 2006). All of these studies generally conclude that at least a fraction of the CH₃OH ice is in a water-poor, CH₃OH-rich environment.

The observation that CH₃OH is predominantly mixed with CO in a H₂O-poor environment leads to the conclusion that CH₃OH is mainly formed through hydrogenation of CO (Watanabe et al. 2004, Fuchs et al. 2009) and not by for instance UV or ion processing of a H₂O containing ice (Hudson & Moore 1999). Grain surface chemistry simulations of CO in a water-poor environment indeed showed that CH₃OH can be formed in this way and that CH₃OH is mainly present on the grain mantles in the pure form or mixed with CO, and that it is not in a water-rich phase (Cuppen et al. 2009).

The presence of separate H₂O-rich and CO/CH₃OH-rich ice fractions has to be taken into account by modelers and experimentalists. In models, often H₂O and CH₃OH are formed simultaneously, since gas phase CO and O are simultaneously deposited. Here we have shown that the subsequent formation of H₂O and CH₃OH is more likely. This should be reflected in the modeled conditions. The same holds for ice experiments, where often CO:H₂O or CH₃OH:H₂O mixtures are used to represent typical interstellar ices. The present study shows again that not all species are intimately mixed in the ice and that the composition of astrophysically relevant ice mixtures should therefore be treated with care.

Chapter V

HIGHLY RESOLVED INFRARED SPECTRA OF PURE CO₂ ICE

Highly resolved infrared spectra of pure CO₂ ice (15-75 K),

K. Isokoski, C. Poteet, and H. Linnartz, *Astronomy & Astrophysics*, 2013, to be submitted.

Part of *Anomalous CO₂ ice towards HOPS-68: a tracer of protostellar feedback*, C. Poteet, K.M. Pontoppidan, S.T. Megeath, D.M. Watson, K.

Isokoski, J.E. Bjorkman, P.D. Sheehan and H. Linnartz, *Astrophysical Journal*, 2013, in press.

Abstract

The ν_2 bending mode of pure CO₂ ice around 15.2 μm exhibits a fine double-peak structure that offers a sensitive probe to study the physical and chemical properties of solid CO₂ in space. Current laboratory spectra do not fully resolve the CO₂ ice features. In order to improve the fitting of the observed CO₂ features, high-resolution solid-state infrared spectra of pure CO₂ ice are recorded in the laboratory for a series of astronomically relevant temperatures and at an unprecedented level of detail. The infrared spectra of pure CO₂ ice are recorded in the 4000 to 400 cm^{-1} (2.5-25 μm) region at a resolution of 0.1 cm^{-1} using Fourier Transform Infrared Spectroscopy. Accurate band positions and band widths (FWHM) of pure CO₂ ice are presented for temperatures of 15, 30, 45, 60 and 75 K. The focus of this spectroscopic work is on the CO₂ (ν_2) bending mode, but more accurate data are also reported for the ¹²CO₂ and ¹³CO₂ (ν_3) stretching mode, and CO₂ ($\nu_1+\nu_3$) and ($2\nu_2+\nu_3$) combination modes.

5.1 Introduction

Solid carbon dioxide, CO₂, is an important tracer of the chemical and physical history of protostars and their surroundings (Whittet et al. 1998, Ehrenfreund et al. 1998, Gerakines et al. 1999, Boogert et al. 2000, Nummelin et al. 2001, Pontoppidan et al. 2008). It constitutes a significant part of interstellar ice with abundances relative to solid H₂O varying from ~15 to 40 % in quiescent dark clouds (d'Hendecourt & Jourdain de Muizon 1989, Whittet et al. 1998, 2007, 2009, Bergin et al. 2005, Knez et al. 2005) and circumstellar envelopes of low- and high-mass protostars (Gerakines et al. 1999, Nummelin et al. 2001, Boogert et al. 2004, Pontoppidan et al. 2008, Zasowski et al. 2009, Cook et al. 2011). The observed abundances of solid CO₂ are a factor of ~100 higher than in the gas phase (van Dishoeck et al. 1996, Boonman et al. 2003) and cannot be reproduced by gas-phase chemical models (Bergin et al. 1995). The formation of CO₂ is therefore assumed to proceed through reactions in ices on interstellar dust grains.

CO₂ is readily produced in UV photoprocessed CO-H₂O laboratory ice, with an efficiency high enough to be driven by cosmic-ray induced UV field in dense interstellar regions (Watanabe & Kouchi 2002). Comparable CO₂ ice abundances are however observed in regions with and without additional UV photons from a nearby protostar, suggesting a formation route which does not depend on the available UV field. Cosmic-ray processing of pure CO laboratory ice has been also shown to be a viable mechanism for CO₂ production in the ISM (Jamieson et al. 2006), and seems plausible given the large abundances of pure CO ice (Pontoppidan et al. 2003b). A number of other reaction schemes have been proposed and/or studied including non-energetic surface-catalyzed CO oxidation (Tielens & Hagen 1982, Roser et al. 2001); hydrogenation of CO-O₂ binary ice, providing a formation route through the CO-OH intermediate (Ioppolo et al. 2011); and energetic processing (low-energy ion irradiation) of ices containing C- and O-bearing molecules as well as carbon grains covered by water ice (Ioppolo et al. 2009). Recent observational and experimental work suggests that interstellar ices are unlikely to contain significant amounts of CO intimately mixed in H₂O (Pontoppidan et al. 2003b, Cuppen et al. 2011). This is inconsistent with the CO₂ formation mechanisms relying on or resulting in CO in H₂O-rich ices. Cuppen et al. (2011) further demonstrate that the observed CO ice feature is better reproduced by CO mixed in CH₃OH ice. Indeed, CH₃OH is readily produced through CO hydrogenation (Watanabe et al. 2004, 2006, Fuchs et al. 2009) and CO₂ produced in water-poor CO ice should therefore be intimately mixed also with CH₃OH.

The molecular environment in which CO₂ is observed provides, therefore, valuable information on its formation mechanism; CO₂ located in ice dominated by H₂O, CO and/or CH₃OH is a direct hint for a possible chemical connection. The CO₂ (ν_2) bending mode at 15.2 μm (660 cm⁻¹) is particularly sensitive to its molecular environment and has been observed towards a number of sources ranging from luminous young stars (Gerakines et al. 1999, Pontoppidan et al. 2008) to cold, quiescent molecular clouds (Knez et al. 2005, Bergin et al. 2005, Whittet et al. 2007). The appearance of absorption features not only depends on ice composition, but also on ice temperature. In order to characterize different ice environments, the observed CO₂ (ν_2) feature can be decomposed phenomenologically into a finite set of known laboratory ice compositions (Pontoppidan et al. 2008) including pure CO₂ ice. While the profile of the CO₂ feature in each component is fixed, the relative contribution varies from source to source, thus characterizing and quantifying the ices along the line of sights.

A large number of laboratory spectra of solid CO₂ in different molecular environments and for different temperatures are available (Sandford & Allamandola 1990, Ehrenfreund et al. 1997, 1999, van Broekhuizen et al. 2006, White et al. 2009). For most sources, the analysis of the CO₂ (ν_2) feature implies the presence of both hydrogen-rich (H₂O:CO₂) and hydrogen-poor (CO:CO₂) CO₂ ice, as well as CH₃OH containing CO₂ ice (Ehrenfreund et al. 1998), consistent with several of the proposed formation schemes. Most sources also exhibit some contribution from pure CO₂ ice. The occurrence of pure CO₂ is considered to be a result of thermal processing, which causes segregation and/or distillation of mixed components with different volatility (Ehrenfreund et al. 1998, Öberg et al. 2009a, Fayolle et al. 2011). Distillation of CO-rich ice happens at 20-30 K (Pontoppidan et al. 2008). In the laboratory, segregation from H₂O-rich ice requires strong (>100 K) heating (Gerakines et al. 1999), but is lowered to 30 K in the ISM due to longer time scales (Öberg et al. 2009a).

Low-temperature (<20 K) H₂O- and CO-rich ices are characterized by a broad single-peaked CO₂ (ν_2) feature, whereas pure CO₂ produces a double-peaked substructure (Ehrenfreund et al. 1997, van Broekhuizen et al. 2006). In a pure CO₂ lattice the axial symmetry of the linear molecule is broken, giving rise to the so-called Davydov splitting (Davydov 1962, Tso & Lee 1985). The splitting makes the CO₂ bending mode a sensitive probe for the changes in its environment. Prior to this work, the available laboratory spectra of pure CO₂ ice (Sandford & Allamandola 1990, Hudgins et al. 1993, Ehrenfreund et al. 1997, Baratta & Palumbo 1998) were recorded at resolutions of 1–2 cm⁻¹, too low to fully resolve the CO₂ (ν_2) bending mode. van Broekhuizen et al. (2006) recorded CO₂ ice spectra at 15-90 K with 0.5 cm⁻¹ resolution but the low S/N ratio prohibit accurate comparison with astronomical data. Particularly for sources with a prominent double-peak structure, such as HOPS-68 (Poteet et al. 2011, Poteet et al. 2013, ApJ, Submitted), the spectral quality of the used pure CO₂ component is important. Using a pure CO₂ component with a properly resolved Davydov splitting can help to avoid overestimation and misinterpretation of the underlying broader features. Ehrenfreund et al. (1997) does not make available the entire temperature series for pure CO₂ ice. Here we have a complete, high-resolution temperature series. In addition to the 15.2 μm bending mode, the resolution of the previous data is not sufficient when studying the narrow ¹³CO₂ ice band or the narrow ($\nu_1 + \nu_3$) combination band. These bands will be assessable with the James Webb Space Telescope. Thus, the high-resolution CO₂ laboratory spectra will be needed here as well.

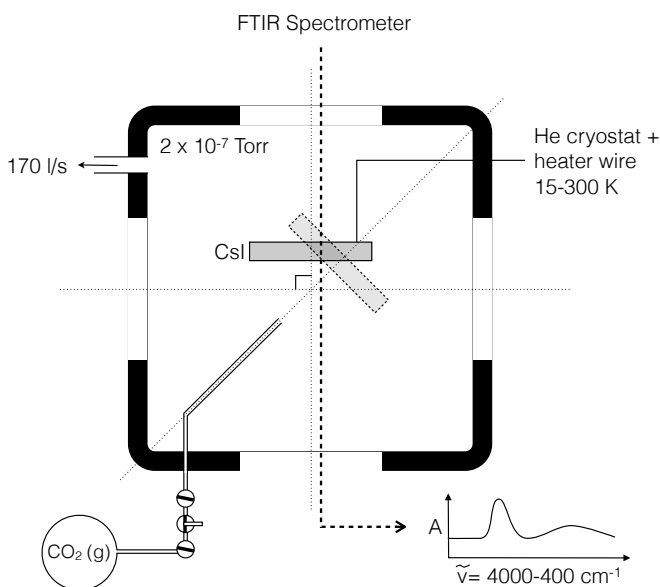


Figure 5.1 – Schematic drawing of the experimental setup for preparation and spectroscopic characterization of the cryogenic CO₂ samples.

5.2 Experimental procedure

The experiments are performed in a high-vacuum (HV) setup first described by Gerakines *et al.* (1995) (Fig. 5.1). A stainless steel chamber is evacuated by a turbomolecular pump (170 l s^{-1} ; Pfeiffer TPH 170) and a rotary vane pump ($6 \text{ m}^3 \text{ hr}^{-1}$; Edwards E2M8) separated by an oil mist filter, allowing a base pressure of 2×10^{-7} Torr at room temperature. The chamber houses a CsI (Caesium Iodide) sample substrate that is cooled down to 15 K by a closed cycle helium cryostat (ADP DE-202). The substrate temperature is controlled between 15 and 300 K, with a precision of 0.1 K, by a resistive heater element and a silicon diode sensor using an external temperature control unit (LakeShore 330). CO₂ (Praxair, 99.998 % purity) is introduced into the system from a gas bulb at 10 mbar filled in a separate vacuum manifold (base pressure $\sim 10^{-5}$ mbar). CO₂ ices are grown onto the substrate at 15 K via effusive dosing of the gaseous sample through a stainless steel capillary along the surface normal. The approximate growth rate is determined by setting the exposure to $\sim 10^{16} \text{ molecules cm}^{-2} \text{ s}^{-1}$. Assuming a monolayer surface coverage of $10^{15} \text{ molecules cm}^{-2}$ and a sticking probability of 1, this results in a growth rate of 10 L s^{-1} ¹. Ices are deposited for 5 min resulting in approximately $\sim 3000 \text{ ML}$. The exact thickness of the samples is derived from the IR band strengths (Sect. 7.5).

The ices are heated from 15 K to 30, 45, 60, 75 and 90 K at a rate of 2 K min^{-1} and allowed to relax for 5 min before recording the absorption spectra. A Fourier Transform InfraRed (FTIR) spectrometer (Varian 670-IR) is used to record the ice spectra in transmission mode from 4000

¹ $1 \text{ L (Langmuir)} = 1 \times 10^{-6} \text{ Torr s} \approx 1 \text{ ML}$

to 400 cm^{-1} ($2.5\text{--}25\text{ }\mu\text{m}$) with a spectral resolution of 0.1 cm^{-1} , averaging a total of 256 scans to increase the S/N ratio. Background spectra are acquired at 15 K prior to deposition and subtracted from the recorded ice spectra. The spectra recorded at different temperatures correspond to different ice samples prepared under identical conditions. This procedure is used to minimize the contamination of samples during the relatively long acquisition time ($\sim 2\text{ h}$).

5.3 Results

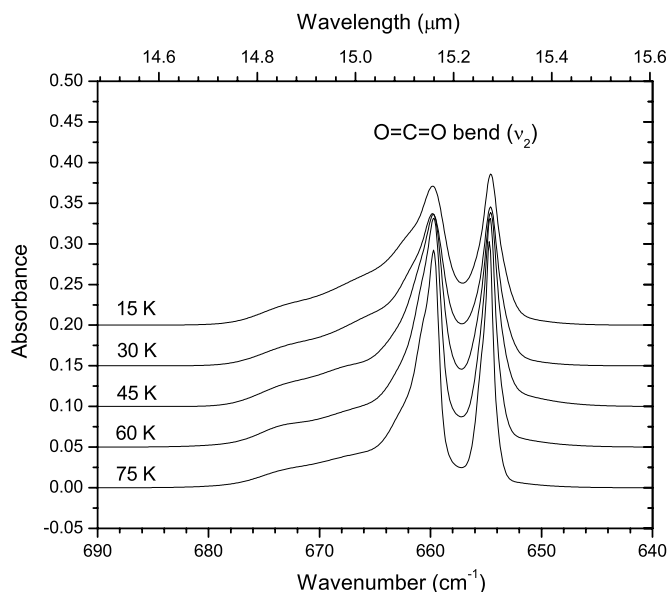


Figure 5.2 – High-resolution (0.1 cm^{-1}) solid-state IR spectra of pure CO_2 ice at 15–75 K showing the $^{12}\text{CO}_2$ (ν_2) bending mode. The displayed spectra are obtained by smoothing through superposition of Gaussians.

Figs. 5.2–5.5 show the high-resolution (0.1 cm^{-1}) FTIR spectra of CO_2 ice at 15, 30, 45, 60 and 75 K. Fig. 5.2 shows the spectral region around the ν_2 bending mode ($680\text{--}645\text{ cm}^{-1}$). Figs. 5.3 and 5.4 show the CO_2 (ν_3) asymmetric stretching fundamental, for ^{12}C and ^{13}C isotopologue (in natural abundance), respectively. Fig. 5.5 shows the two CO_2 combination bands ($\nu_1 + \nu_3$) and ($2\nu_2 + \nu_3$).

The CO_2 bending fundamental (ν_2) has a double-peaked substructure at $\sim 660/655\text{ cm}^{-1}$. The high-frequency component is highly asymmetric with a long blue (high wavenumber) wing, while the low-frequency component is relatively symmetric. The $^{12}\text{CO}_2$ asymmetric stretching fundamental (ν_3) is located at $\sim 2345\text{ cm}^{-1}$ ($4.26\text{ }\mu\text{m}$), and is redshifted from the gas-phase value 2348 cm^{-1} due to interactions with the surrounding matrix environment. The profile is asymmetric with a prominent blue shoulder and a weaker red (low wavenumber) shoulder. The asymmetric stretching fundamental (ν_3) of the $^{13}\text{CO}_2$ isotopologue is found in its natural abundance at $\sim 2283\text{ cm}^{-1}$ ($4.38\text{ }\mu\text{m}$), similarly redshifted from its gas-phase value. $^{13}\text{CO}_2$ (ν_3) also exhibits shoulders on both sides. The

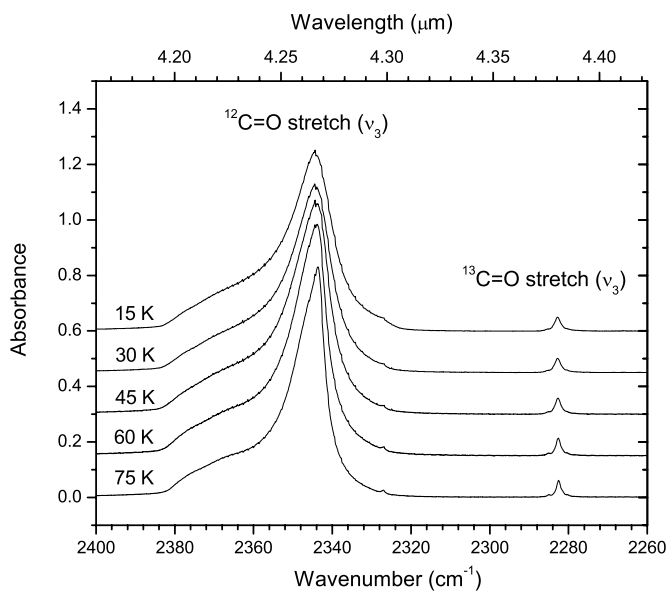


Figure 5.3 – High-resolution (0.1 cm⁻¹) solid-state IR spectra of pure CO₂ ice at 15–75 K showing the ¹²CO₂ and ¹³CO₂ (ν_3) stretching modes. The zoom-in of the latter is shown in Fig. 5.4. The displayed spectra are baseline corrected. Gaseous CO₂ absorption features have been subtracted.

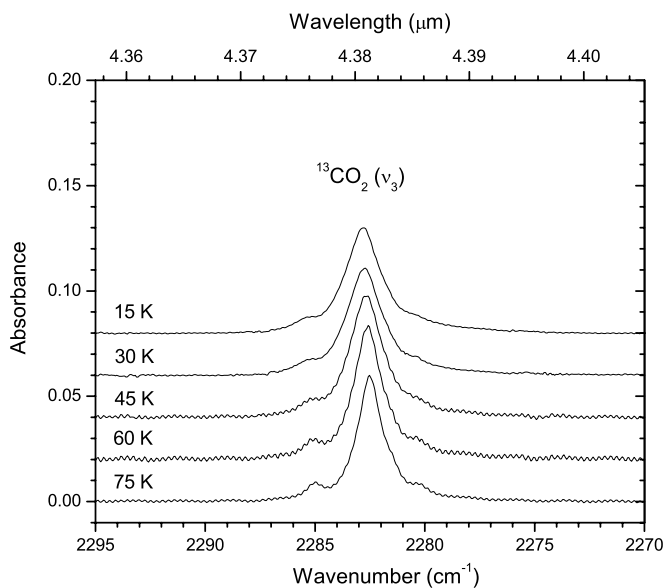


Figure 5.4 – High-resolution (0.1 cm⁻¹) solid-state IR spectra of pure CO₂ ice at 15–75 K showing the ¹³CO₂ (ν_3) stretching mode. The displayed spectra are baseline corrected.

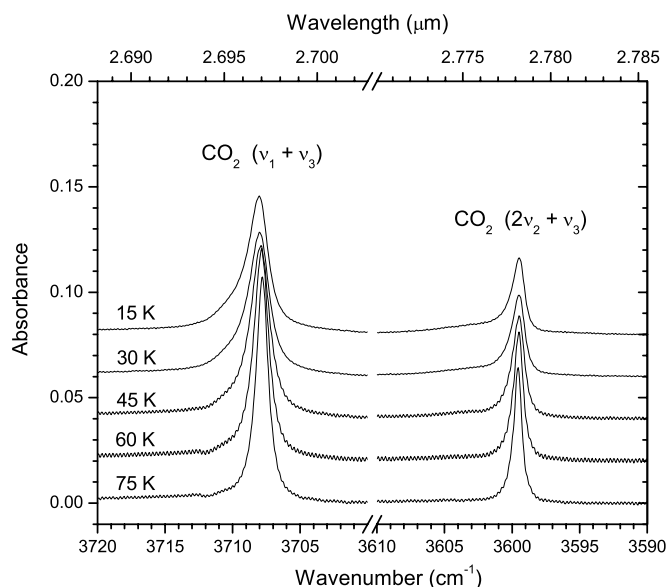


Figure 5.5 – High-resolution (0.1 cm^{-1}) solid-state IR spectra of pure CO_2 ice at 15–75 K showing the $(\nu_1 + \nu_3)$ and $(2\nu_2 + \nu_3)$ combination modes. The displayed spectra are baseline corrected.

CO_2 (ν_1) symmetric stretching fundamental at $\sim 1385\text{ cm}^{-1}$ ($7.22\text{ }\mu\text{m}$) is IR inactive (Falk & Seto 1986). The CO_2 ($\nu_1 + \nu_3$) combination band and $(2\nu_2 + \nu_3)$ combination/overtone bands appear at $\sim 3708\text{ cm}^{-1}$ ($2.70\text{ }\mu\text{m}$) and 3599 cm^{-1} ($2.78\text{ }\mu\text{m}$), respectively. The combination modes have narrow, relatively symmetric profiles. These bands are close to the broad H_2O stretching mode around 3300 cm^{-1} ($3.03\text{ }\mu\text{m}$) which typically dominates the observational ice spectra. However, unlike the strong ν_2 and ν_3 modes, the CO_2 combination and the $^{13}\text{CO}_2$ (ν_3) modes are weak and unaffected by grain shape effects. Thus, their band shape profiles depend only on the chemical composition of interstellar CO_2 ice (*e.g.*, Keane et al. 2001).

5.3.1 Corrections

In the laboratory, the CO_2 ice feature around 2350 cm^{-1} is easily contaminated with absorptions of gaseous CO_2 along the IR beam path. Variable concentrations relative to the background spectrum may cause under- or over-subtraction of interfering rotational lines. Same is true for the CO_2 bending mode around 660 cm^{-1} where an absorption line is seen around 668 cm^{-1} . The spectra are corrected using a gaseous CO_2 spectrum extracted from the background spectrum (Fig. 5.6). The bending mode region also suffers from spectral artifacts due to being located in the edge of the spectrometer spectral range. The (ν_2) bands presented here are therefore smoothed by superposition of several Gaussians. All spectra have been baseline corrected, and are available in reduced as well as in raw format in the Leiden ice database at http://www.strw.leidenuniv.nl/lab/databases/co2_hires/.

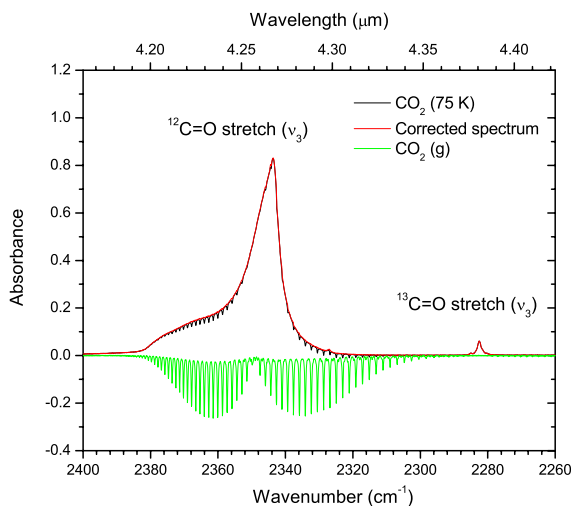


Figure 5.6 – Spectral corrections performed on the CO₂ (ν_3) mode. Rotational fine-structure of gaseous CO₂ (green trace), overlapping with the CO₂ (ν_3) ice band, is subtracted from the raw spectrum (black trace). The corrected spectrum is shown in red.

5.4 Discussion

Table 5.1 lists the band positions and bandwidths of pure CO₂ ice features for the five different temperatures in the 0.1 cm⁻¹ resolution spectra. The values are obtained by the integration procedure in the Origin 7.5 software package. Fig. 5.7 visualizes the derived values, including relative peak intensity and integrated area, as a function of temperature, together with other values available from the literature. The values are normalized to those in 0.1 cm⁻¹ spectra at 15 K. The influence of thermal annealing on the peak position depends on the influence of the trapping site on the specific vibrational mode. In general, all CO₂ band widths decrease at elevated temperatures. The narrowing is gradual and is observed already between 15 and 30 K. During the thermal annealing process, molecules rearrange themselves by finding energetically more favorable orientations. As the range of environments is reduced, the band profiles become more narrow. Simultaneously, the peak intensities increase. The integrated area of all features peak around 40 K, after which they decline until the ice desorbs between 80 and 90 K.

Comparison of the peak positions in the high-resolution spectra with those from lower resolution studies (Sandford & Allamandola 1990, Ehrenfreund et al. 1997, van Broekhuizen et al. 2006) generally shows agreement within the limitations due to resolution, assuming that at 1 cm⁻¹ resolution, the error in position is 0.5 cm⁻¹. At 15 K, the CO₂ (ν_2) bending mode peaks at 659.7 and 654.5 cm⁻¹. The low-wavenumber component shifts by 0.2 cm⁻¹ between 45 and 75 K. The observed shift is below the resolution of previous studies. The high-wavenumber component does not shift with temperature. The CO₂ (ν_3) stretching mode, peaking at 2344.4 cm⁻¹ in the 15 K spectrum, red-shifts by 0.7 cm⁻¹ for temperatures greater than 30 K. The ¹³CO₂ stretching mode undergoes a smaller (0.3 cm⁻¹) red-shift in a similar temperature range. The peak positions derived for the combination modes ($\nu_1 + \nu_3$) and ($2\nu_2 + \nu_3$) at 15 K are 3708.0 and 3599.5 cm⁻¹. The position of the combination

Table 5.1 – High-resolution (0.1 cm^{-1}) band positions ($\tilde{\nu}$) and linewidths (FWHM) in pure CO_2 ice.

T (K)	$\tilde{\nu}$ (cm^{-1})	<i>FWHM</i> (cm^{-1})	$\tilde{\nu}$ (cm^{-1})	<i>FWHM</i> (cm^{-1})
CO ₂ bend (ν_2)				
15	659.72	5.12	654.53	2.09
30	659.78	4.35	654.53	2.00
45	659.72	3.64	654.53	1.86
60	659.78	2.81	654.59	1.48
75	659.72	2.31	654.65	1.17
¹² CO ₂ stretch (ν_3)			¹³ CO ₂ stretch (ν_3)	
15	2344.41	13.39	2282.76	1.94
30	2344.41	12.88	2282.70	1.91
45	2344.35	11.94	2282.58	1.83
60	2343.81	10.57	2282.58	1.55
75	2343.69	9.23	2282.52	1.38
CO ₂ comb. ($\nu_1 + \nu_3$)			CO ₂ comb. ($2\nu_2 + \nu_3$)	
15	3708.02	1.92	3599.48	1.17
30	3708.02	1.91	3599.48	1.21
45	3707.90	1.73	3599.48	1.09
60	3707.84	1.32	3599.48	0.89
75	3707.78	1.10	3599.54	0.74

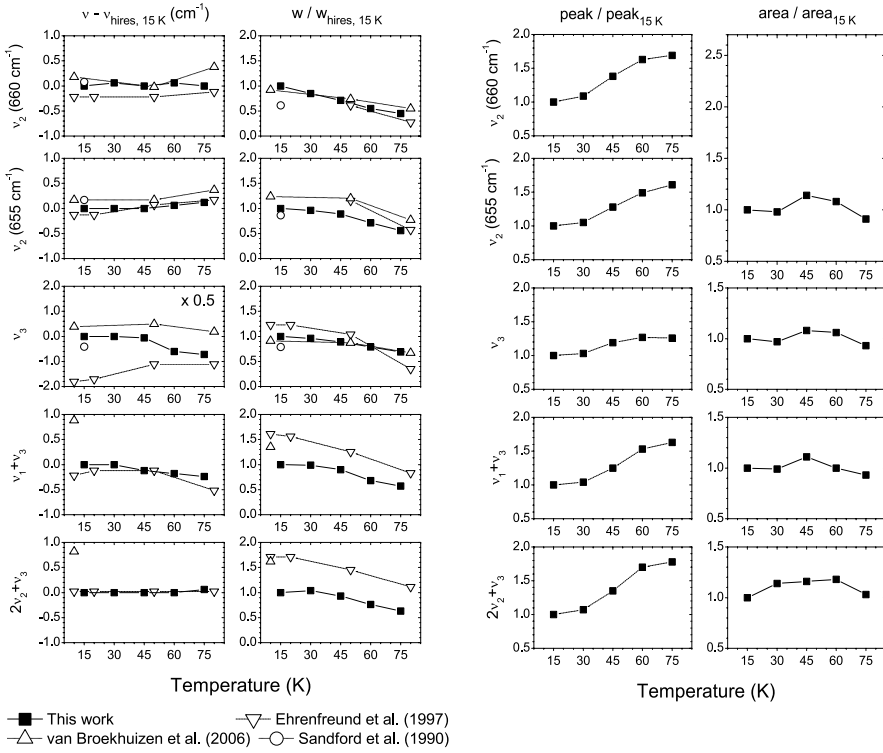


Figure 5.7 – Relative peak position (in cm⁻¹), width, peak intensity and integrated area of the CO₂ ice features as a function of temperature.

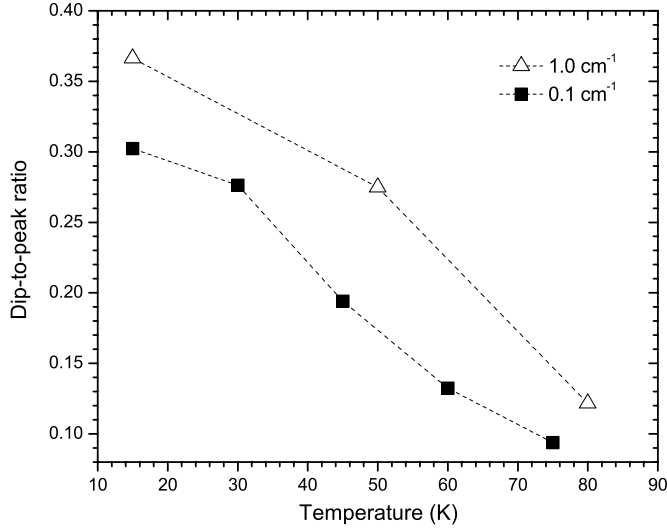


Figure 5.8 – Dip-to-peak ratio at different temperatures derived from the 0.1 cm^{-1} (filled squares) and 1.0 cm^{-1} (open triangles) resolution spectra of the CO_2 bending mode.

modes shifts $<0.5 \text{ cm}^{-1}$ between 15 and 75 K. The shift of the $(\nu_1 + \nu_3)$ band occurs after 30 K, towards lower wavenumbers. For the $(2\nu_2 + \nu_3)$ band a red-shift is observed after a temperature of 60 K is reached.

The main objective of this high-resolution study is to fully resolve the Davydov splitting in the CO_2 (ν_2) bending mode. Fig. 5.8 shows the dip-to-peak ratio, defined by Zasowski et al. (2009) as the local minimum to local maximum ratio of the blue peak, for 0.1 and 1.0 cm^{-1} resolution spectra as a function of temperature. For the high-resolution CO_2 ice feature, the dip-to-peak ratio decreases from 0.3 to <0.10 between 15 and 75 K. The ratio derived from the lower resolution spectra (Ehrenfreund et al. 1997) is $\sim 20 \%$ larger for all studied temperatures. A smaller dip-to-peak ratio indicates that the CO_2 bending mode and in particular the Davydov split is better resolved in the 0.1 cm^{-1} spectra.

The double peaked structure of the CO_2 bending mode is a diagnostic for the observed $15.2 \mu\text{m}$ CO_2 ice band. The interpretation of the CO_2 ice composition from observational spectra relies on laboratory spectra of CO_2 for different ice environments (Gerakines et al. 1999, Keane et al. 2001, Pontoppidan et al. 2008). The quality of the laboratory spectra therefore directly influences the derived ice composition from observations. Particularly for sources with larger contributions from pure CO_2 ice, a properly resolved Davydov splitting is a prerequisite for an accurate interpretation. Thus, the incorporation of 0.1 cm^{-1} resolution laboratory spectra (Table 5.1) into the fitting procedure will improve the interpretation of the astronomical observations.

In order to compare with astronomical observations, the thickness of the ice samples has to be known accurately. We derive the ice thickness from the infrared band strengths using eq. 5.1:

Table 5.2 – Thickness of the CO₂ ice samples as derived from different vibrational modes.

T (K)	$\int A d\tilde{\nu}$ [cm ⁻¹]	d [μm]	$\int A d\tilde{\nu}$ [cm ⁻¹]	d [μm]	$\int A d\tilde{\nu}$ [cm ⁻¹]	d [μm]	$\int A d\tilde{\nu}$ [cm ⁻¹]	d [μm]
	CO ₂ bend (ν_2)		¹² CO ₂ (ν_3)		CO ₂ ($\nu_1 + \nu_3$)		CO ₂ ($2\nu_2 + \nu_3$)	
15	1.798	0.208	13.460	0.226	0.256	0.233	0.089	0.253
30	1.756	0.204	13.087	0.220	0.253	0.230	0.102	0.290
45	2.055	0.238	14.502	0.243	0.283	0.258	0.103	0.293
60	1.945	0.226	14.280	0.240	0.255	0.232	0.105	0.299
75	1.639	0.190	12.578	0.211	0.237	0.216	0.092	0.260

$$N = \frac{\int \tau(\tilde{\nu}) d\tilde{\nu}}{A_i} = \frac{\ln 10 \int A(\tilde{\nu}) d\tilde{\nu}}{A_i}, \quad (5.1)$$

where N is the column density of the absorbing molecules (in cm⁻²), $\tau = \ln 10 A$ is the optical depth, $\int A(\tilde{\nu})$ is the integrated absorbance and A_i the intrinsic band strength of a given absorption band. Using the intrinsic band strengths from Gerakines et al. (1995) and Yamada & Person (1964), the derived thickness and integrated absorbance for the CO₂ ice bands are listed in Table 5.2. The thickness is calculated from the column density assuming a monolayer coverage of 1×10^{15} molecules cm⁻² and a monolayer thickness of 5.54 Å, the lattice constant for solid CO₂ (Keesom & Köhler 1934). These dimensional values are subject to variation in ice morphology, which changes with temperature and likely the ice growth method (Isokoski et al. 2013, A&A, in prep.). Moreover, the intrinsic band strengths reported for CO₂ ice at 14 K are assumed to be applicable for higher temperatures. The increase in thickness for higher temperatures is due to this approximation.

5.5 Optical Constants and Grain Shape-Corrections

The absorption profiles of strong interstellar ice bands are significantly affected by the shape and size of the absorbing particles. Grain shape effects originate from the polarization of interstellar dust by electromagnetic radiation, which produces an induced electric field on the grain surface. The strength of the induced field depends on both the complex dielectric constant of the particular particle and its shape (e.g., Bohren & Huffman 1983, Tielens et al. 1991). Thus, in order to allow for a realistic comparison to astronomical spectra, the absorption profiles of laboratory spectra must first be corrected for size and shape effects. However, such corrections require an accurate determination of the complex refractive index ($n + ik$) of the absorbing species. In this section, we provide a brief comparison between the pure CO₂ ice optical constants from Poteet et al. (2013, ApJ, Submitted) and those derived from the previous lower resolution study by Ehrenfreund et al. (1997). For this comparison, we examine the ν_2 bending mode only.

The real, n , and imaginary, k , parts of the complex refractive index are calculated, using a Kramers-Kronig analysis, from the high-resolution (0.1 cm⁻¹) and lower resolution (1 cm⁻¹) pure CO₂ absorption spectra, following the method previously described in Poteet et al. (2013, ApJ, submitted).

Similar to this study, a thickness of 520 monolayers (or $0.29 \mu\text{m}$) is estimated for the 10 K ice sample from Ehrenfreund et al. (1997), using the known absorption band strength of pure CO_2 ice (Eq. 5.1). A comparison of the optical constants for the high-resolution CO_2 bending mode with those derived from the lower resolution absorption spectrum is presented in Fig. 5.9. Differences between the optical constants at these resolving powers are apparent. In particular, the high-resolution refractive index exhibits additional substructure near 653 cm^{-1} that is not resolved in the lower resolution data from Ehrenfreund et al. (1997). For the imaginary part of the refractive index, differences in band width of the high-wavenumber component of the bending mode are found at the different resolving powers. Because the optical constants are consistently derived in the same manner and only a small variation in ice thickness is expected, the dissimilarities between the high- and lower-resolution optical constants are thought to be due to differences in the laboratory instrumental resolving power.

To directly compare the band shape profiles of laboratory-derived spectra to those of astronomical spectra, optical constants must be converted to an opacity. Assuming that an ensemble of interstellar grain shapes can be simulated using a continuous distribution of ellipsoids (CDE; all particle shapes are equally probable), the volume attenuation coefficient, $\langle C_{\text{abs}} \rangle / V$, is calculated in the Rayleigh limit ($15 \mu\text{m} \gg 2\pi a$, where a is the radius of the largest grains) for the ν_2 bending mode (Bohren & Huffman 1983). (For a more thorough discussion on grain shape effects, the reader is referred to Poteet et al. (2013, ApJ, Submitted).) A comparison between the 0.1 and 1 cm^{-1} resolution shape-corrected spectra is shown in Fig. 5.10. We find that the strength of the double-peaked profile is nearly invariable at the different resolving powers. However, similar to the imaginary part of the refractive index, we find that the band width of the high-wavenumber component of the 1 cm^{-1} resolution spectrum is narrower than that of the high-resolution spectrum. This variation is not expected to be due to the small difference in laboratory temperature, but may be a consequence of lower instrumental resolving power.

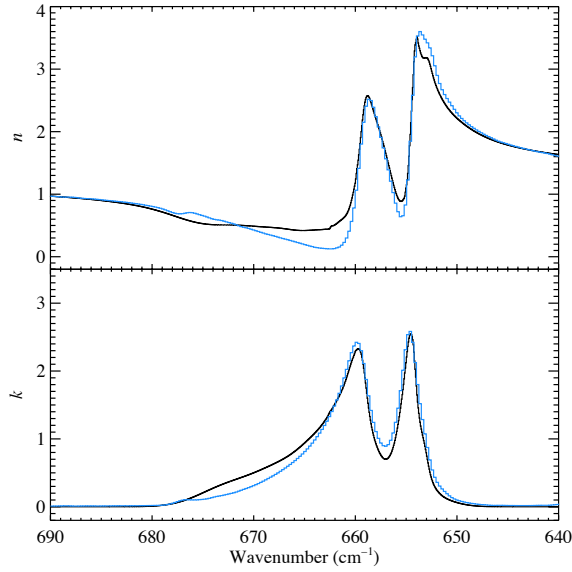


Figure 5.9 – High-resolution (black lines) and lower resolution (blue lines) optical constants for the ν_2 bending mode of pure CO₂ ice. The optical constants are derived using the 0.1 cm⁻¹ absorption spectrum ($T = 15$ K) and 1 cm⁻¹ absorption spectrum ($T = 10$ K) from [Ehrenfreund et al. \(1997\)](#).

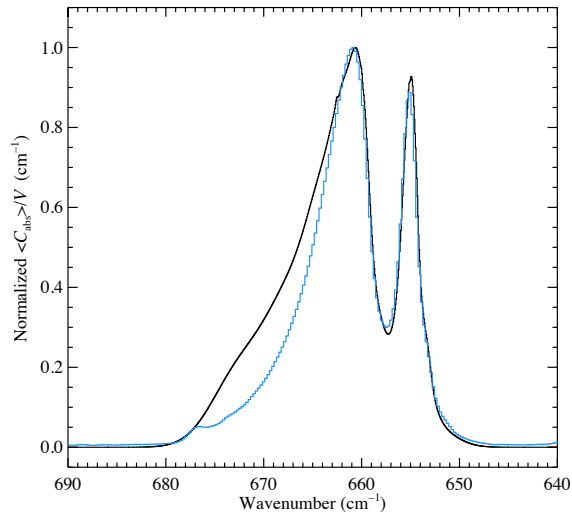


Figure 5.10 – The normalized volume attenuation coefficient ($\langle C_{\text{abs}} \rangle / V$) for the ν_2 bending mode of pure CO₂ ice. Grain shape-corrections are derived from the 0.1 cm⁻¹ optical constants ($T = 15$ K; black line) and 1 cm⁻¹ optical constants ($T = 10$ K; blue line) from [Ehrenfreund et al. \(1997\)](#), using a continuous distribution of ellipsoids (CDE) in the Rayleigh limit ([Bohren & Huffman 1983](#)).

5.6 Summary

In this work we provide highly resolved (0.1 cm^{-1}) IR spectra of pure CO_2 ice at a spectral range of $4000\text{--}400\text{ cm}^{-1}$, at temperatures 15, 30, 45, 60, 75 K. The spectral range covers the fundamental bending mode (ν_2), antisymmetric $^{12}\text{CO}_2$ and $^{13}\text{CO}_2$ stretching modes (ν_3) and the combination mode ($\nu_1 + \nu_3$) and combination/overtone mode ($2\nu_2 + \nu_3$). The improved spectral parameters are needed for a more accurate interpretation of astronomical ice data. Moreover, the high spectral resolution allows an accurate quantification of thermally induced changes in CO_2 band profiles that are below the resolution of previous work. This is particularly true for shifts in line position below 0.5 cm^{-1} . Also, the Davydov splitting in the ν_2 band is characterized more accurately and allows a better interpretation of astronomical spectra along lines of sight with thermally processed ices, where segregation and/or distillation causes CO_2 to be present in pure form as well. All data are available in the Leiden ice database at:

http://www.strw.leidenuniv.nl/lab/databases/co2_hires/.

Chapter VI

LASER DESORPTION TIME-OF-FLIGHT MASS SPECTROMETRY OF CRYOGENIC ICES

Laser desorption time-of-flight mass spectrometry of cryogenic ices

K. Isokoski, J.-B. Bossa, D. M. Paardekooper, and H. Linnartz

Reviews of Scientific Instruments, 2013, to be submitted.

Abstract

Our current understanding of complex solid state astrochemical processes in interstellar ices is limited by the available experimental techniques. The abundance of species decreases with increasing size and complexity, making sensitivity of the analysis methods crucial for characterizing processes leading to prebiotic molecules, while simultaneously maintaining the conditions relevant to the interstellar medium. In this paper we introduce a new sensitive technique for the controlled formation of complex molecules in interstellar ice analogs, with minimal chemical alteration as the primary objective. The experiment uses UV laser desorption combined with time-of-flight mass spectrometry, providing a tool for *in situ* and real-time analysis. The technique is demonstrated for astronomically relevant ice components: methanol (CH_3OH), methyl formate (HCOOCH_3) and ethane (C_2H_6). We show that UV photo-processing of solid C_2H_6 ice yields species with possibly up to 6 carbon atoms, most likely in cyclic unsaturated structures.

6.1 Introduction

Formation of complex organic interstellar molecules¹ is subject to intensive research due to its relevance to the origin of life. The presence of prebiotic species, such as aminoacids, in meteoritic samples (Kvenvolden et al. 1970, Cronin & Pizzarello 1997, Lawless et al. 1972, Ehrenfreund et al. 2001) suggests an exogenous formation mechanism (Botta & Bada 2002, Sephton 2002). As is the case for other solar system bodies, meteorites have their origin in icy dust grains, which act as important chemical catalysts in the sparse interstellar medium (ISM). In the cold (<100 K) protostellar phase the ice comprises a rich mixture of species accreted and formed on the grain surface (Tielens & Hagen 1982) which later become incorporated in meteorites and/or cometary material. Remote observations of interstellar ices are limited to major ice components with abundances $\gtrsim 1\%$ with respect to H_2O (e.g., CO , CO_2 , CH_3OH , CH_4 , NH_3) (Whittet et al. 1996, Gibb et al. 2004, Boogert et al. 2008, Pontoppidan et al. 2008, Bottinelli et al. 2010). However, after the thermal desorption of ice mantles (>100 K), several complex molecules are detected in the gas phase, particularly in hot molecular cores of protostars (Herbst & van Dishoeck 2009). Many of the observed complex molecules are likely to form in the solid state before ice mantle evaporation (Garrod & Herbst 2006, Garrod et al. 2008, Öberg et al. 2009b).

Experimental solid-state astrochemistry provides a way to study interstellar chemical reactions under controlled laboratory conditions and to identify the steps required for the formation of complex molecules. Formation of interstellar methanol (CH_3OH) has been shown to proceed through successive hydrogenation of CO ice (Hiraoka et al. 2002, Watanabe & Kouchi 2002, Fuchs et al. 2009). From CH_3OH , larger and more complex species, such as dimethylether (CH_3OCH_3) and glycolaldehyde (HOCH_2CHO), can form by UV photolysis and thermal radical-radical/radical-neutral recombinations (Öberg et al. 2009b). Despite their likely solid-state origin, these species have been detected in the ISM only in the gas phase (Snyder et al. 1974, Winnewisser & Gardner 1976, Hollis et al. 2000, Beltrán et al. 2009). In the laboratory, energetic processing of interstellar ice analogs comprising of species commonly observed in real interstellar ices results in rich mixtures of complex molecules including amino-acids (Hagen et al. 1979, Schutte et al. 1993b, Bernstein et al. 1995, Greenberg et al. 2000, Bernstein et al. 2002, Muñoz Caro et al. 2002, Muñoz Caro & Schutte 2003,

¹ Complex organic interstellar molecules = carbon-containing species with ≥ 6 atoms

[Elsila et al. 2007](#), [Nuevo et al. 2008, 2010](#)), yet to be observed in the ISM. The outcome of these initial experiments has however been questioned, as the analysis has not been done for samples *in situ*, under conditions relevant to the interstellar medium.

The analysis of non-volatile organic residue (including amino-acids) is typically done by Gas Chromatography-Mass Spectrometry (GC-MS) and Liquid Chromatography-Mass Spectrometry (LC-MS). GC and LC require thermal and chemical alteration of the sample, which is likely to change its composition. Temperature Programmed Desorption (TPD), commonly used for the analysis of more volatile ice components, also allows thermal reactions prior to the analysis. Although sensitive, these analysis techniques are thus inherently prone to uncertainty. Fourier Transform Infrared (FTIR) spectroscopy enables remote analysis of the sample composition without chemical alteration. Due to spectral overlap of different absorption features however, IR spectroscopy of ice analogs has a detection limit of $\sim 1\%$ making it unsuitable for detailed analysis of complex ice mixtures, where spectral overlap will cause ambiguity.

Laser desorption is a powerful alternative to bring non-volatile and/or thermally unstable molecules into the gas phase, and is widely used in mass-spectrometric sample characterization ([Levis 1994](#), [Posthumus et al. 1978](#), [Hahn et al. 1988](#), [Karas et al. 1987](#)). For interstellar ice analogues, the main advantage is that the method allows sampling at any temperature below sublimation. This technique has been recently demonstrated for polycyclic aromatic hydrocarbons in interstellar ice analogs ([Gudipati & Yang 2012](#)). Combined with Time-Of-Flight Mass Spectrometry (TOF-MS) ([Guilhaus 1995](#)), a complete mass spectrum can be recorded for each desorption pulse at a high repetition rate. Here we describe a new experiment, Mass-Analytical Tool for Reactions in Interstellar ICES (MATRI²CES), where pulsed laser desorption is applied to the analysis of astronomically relevant cryogenic (17-100 K) ice samples.

6.2 Instrumentation

Fig. 6.1 shows a schematic overview of the experimental setup. The setup is composed of (i) a main UHV chamber, (ii) an ionization chamber, and (iii) a TOF chamber (flight tube). The main chamber is where cryogenic samples are grown, processed and injected into the carrier gas by laser desorption. Carrier gas admitted from a pulsed valve transports the desorbates into the ionization chamber through two collimating skimmers. The desorbates are ionized by electron impact and accelerated into the TOF chamber for mass analysis.

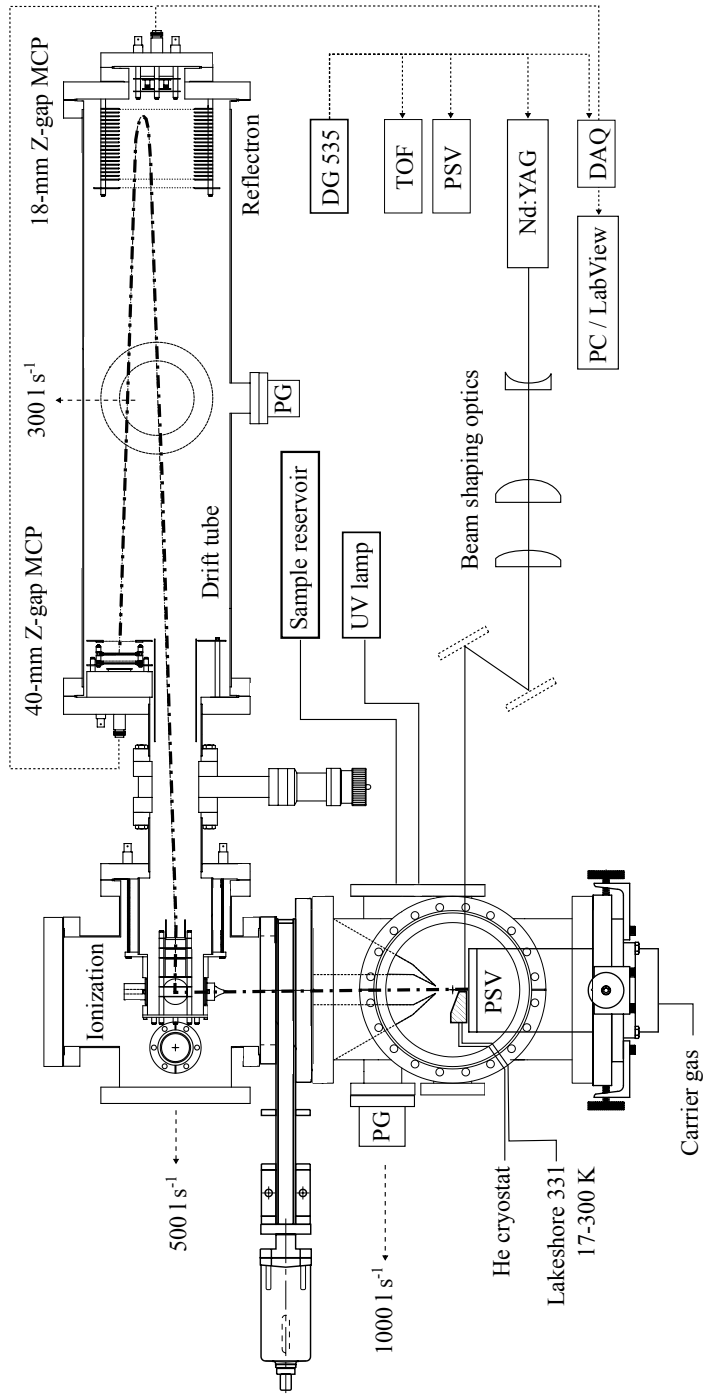


Figure 6.1 – Schematic diagram of MATRI²CES.

MATRI²CES is an Ultra-High Vacuum (UHV) experiment with a base pressure of $\sim 10^{-10}$ mbar. The main, ionization and TOF chambers are evacuated by turbomolecular pumps (Varian TV1001, TV551 and TV301 Navigator) at pumping speeds of ~ 1000 , 500 and 300 l s⁻¹, respectively. The turbomolecular pumps are backed by oil-free foreline dry scroll pumps (Varian TS300 for TV1001 and TS600 for both TV551 and TV301). Working pressures from main to TOF chamber are $\sim 10^{-6}$, 10^{-8} and 10^{-9} mbar. Details of the experiment and measuring procedure are given below.

6.2.1 Substrate

The sample substrate is located in the center of the main chamber. The substrate is a uniform gold-coated copper block with a 2×50 mm (or 15×50 mm) rectangular sampling area and a 20° knife edge to minimize disruption of the carrier flow (see Fig. 6.2). The substrate is connected to a closed-cycle helium cryostat (Advanced Research Systems, DE 202), which has a cooling capacity enabling temperatures as low as 17 K. Substrate temperature is controlled between 17 and 300 K by a temperature controller (LakeShore 331) with a resistive heater element and a chromel-gold/iron thermocouple mounted on the base of the substrate. To cover the 50-mm long sampling area, the cryostat is situated on top of a bellow with a motorized linear shift mechanism with an adjustable translation speed (UHV design, LSM64-50, McLennan, 23HT18C stepper motor with a SimStep single axis stepper system).

6.2.2 Sample deposition

Samples are grown onto the cold substrate by vapor deposition from an external gas reservoir. Gases are admitted into the vacuum chamber via a precision leak valve (Hositrad) with a metal capillary directed onto the substrate at a distance of ~ 2.5 cm. During deposition the substrate is translated vertically to obtain a uniform ice distribution across the sampling surface.

6.2.3 Processing

To trigger astronomically relevant chemical reactions, the deposited samples are exposed to vacuum UV irradiation from a microwave stimulated hydrogen flow discharge lamp, separated from the vacuum chamber by a MgF₂ window. The emission spectrum of the lamp peaks around Ly- α at 121.6 nm with coverage over 115-170 nm (7-10.5 eV) (Muñoz Caro & Schutte 2003). The photon flux of the lamp is estimated to be $\sim 5 \times 10^{13}$ s⁻¹ cm⁻² (Öberg et al. 2007). The emission of the lamp largely resembles the UV radiation field deep inside interstellar clouds (Kim et al. 1994, Muñoz Caro & Schutte 2003). In dense clouds, cosmic rays lead to the internal production of UV photons through secondary electron excitation of H₂ (Prasad & Tarafdar 1983, Gredel et al. 1989).

6.2.4 Laser desorption

Desorption of processed ice is induced by a 3-4-ns laser pulse from a 355-nm Nd:YAG laser (Polaris II, New Wave Research). The laser is operated at a repetition rate of 10 Hz and an adjustable pulse energy of 3-8 mJ. The beam diameter (2.5 mm) is reduced using a Galilean beam expander assembly

consisting of a plano-concave ($f = -2.5$ mm) and a plano-convex lens ($f = +25$ mm) resulting in a collimated 25-mm diameter beam. The expanded beam is subsequently focused onto the substrate by a cylindrical lens ($f = +750$ mm) producing a thin uniform intensity line focus across the entire substrate. The beam waist, w_F , is given by Eq. 6.1

$$w_F = \frac{\lambda f M^2}{\pi w_L} \quad (6.1)$$

where λ = laser wavelength, f = focal length of the focusing lens and w_L = radius of the collimated beam at the lens. M^2 is the laser beam quality factor (19.4). The resulting vertical thickness of the laser line, $2w_F$, is 0.09 mm. Two laser mirrors are used to align the laser focus onto the substrate. All components are anti reflection coated UV fused silica (SiO_2). The reflectivity of the optical components and the entry port to the vacuum chamber decreases the initial pulse energy by about 7 %.

6.2.5 Entrainment

A pulsed supersonic valve (PSV) (Jordan TOF Products, Inc.) is used to generate an intense short gas pulse, which carries the desorbed molecules from the ice surface to the ionization chamber. We use He as carrier gas to avoid condensation of carrier onto the cold substrate. The valve employs a magnetic beam repulsion principle in a current loop mechanism (Dimov 1968, Gentry & Giese 1978, Byer & Duncan 1981, Rorden & Lubman 1983). A 20- μs 4.2-kA current pulse passes through two parallel beam conductors in a hairpin configuration (Fig. 6.2). The consequent magnetic force lifts the top beam allowing gas to pass through the o-ring seal. The He gas (backing pressure ~ 7 bar) is thereby admitted to the 0.5-mm nozzle creating a ~ 60 μs expansion into the vacuum.

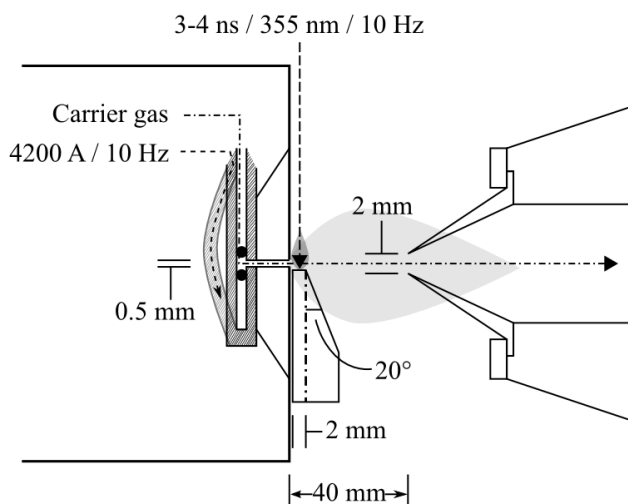


Figure 6.2 – Schematic drawing of the sampling area. PSV valve is depicted in the left, substrate immediately in front of it and front skimmer on the right.

The substrate is placed as close as possible to the valve body to minimize the disturbance to the gas expansion. A gap of ~ 1 mm is left to avoid thermal contact between the cooled substrate and the valve body. The substrate is mounted on an additional translator to adjust the distance to the gas expansion axis, which influences the entrainment of desorbates (Boogaarts 1996).

Sample molecules injected into the gas expansion are instantaneously cooled through multiple collisions with He atoms. The most efficient energy transfer occurs at the highest density region close to the nozzle, resulting in rotational temperatures as low as 5 K (Meijer et al. 1990).

The entrainment in supersonic gas allows fast transport (about 1800 m s^{-1}) of the desorbed molecules to the ionization region. Furthermore, in a supersonic beam, molecules travel at a narrow Maxwellian velocity distribution strongly peaking at the average velocity (Smalley et al. 1977). This prevents additional spatial spreading of molecules injected into the expansion. Fast collisional cooling of the desorbed molecules also minimizes chemical reactions during the transport. Before entering the ionization region, the resulting molecular expansion is collimated by two skimmers with orifices of 2 and 1 mm, situated at 4 and 31 cm from the nozzle orifice.

6.2.6 Time-of-flight mass analysis

The desorbates are analyzed mass spectrometrically in a custom-built Wiley-McLaren type orthogonal acceleration reflection time-of-flight mass spectrometer (ReTOF-MS, Jordan TOF Products, Inc.). The desorbates and He are ionized through electron impact (EI, see Sect. 6.2.7). Electrons are ejected from a hot wire filament and accelerated to 70 eV. At this energy the de Broglie wavelength matches the typical bond length in organic molecules giving a maximum ionization efficiency. The ions are generated between a repeller plate and an extraction grid, which for the duration of ionization ($10 \mu\text{s}$) are at equal potential (1500 V). After ionization, the grid voltage is lowered by 200 V, which extracts the generated cations to the next section. The cations are accelerated by an acceleration grid at ground potential. The accelerated ion beam crosses a focusing *Einsel lens* and deflection plates (60 V) before entering the field free drift (flight) tube.

Cations and radical cations with different m/z ratio separate in the drift tube (81 cm) according to the acquired velocities. The spectrometer can be operated in linear or reflection mode. In linear mode, the ions pass the grounded reflector assembly and are collected at a MCP (microchannel plate) detector (18 mm). In reflection mode, an assembly of retarder grid (+700 V) and reflector grid (+1200 V) mirrors the ions back into the field-free drift tube to be collected at a secondary MCP detector (40 mm). The detectors are high-sensitivity triple (Z-gap) MCP detectors with a $10^9 - 10^{11}$ fold gain and a sub-nanosecond rise time. The reflector increases the flight distance from ~ 115 to ~ 195 cm.

6.2.7 EI Ionization

EI ionization produces predominantly a singly charged radical cation (Eq. 6.2)



where M is the neutral analyte and $M^{\bullet+}$ is the radical cation. Molecular fragmentation (Eqs. 6.3 and 6.4) is common in EI sources which complicates the identification of the parent neutral, but can

also give information about its molecular structure.



where $M_1^{+\bullet}$ is the parent radical cation, $M_2^{+\bullet}$ is a radical cation fragment, M_2^+ is a cation fragment and M_n^\bullet is a neutral radical fragment.

6.3 Results

6.3.1 Calibration

The TOF mass spectrometer is calibrated using a noble gas mixture (He 88 %; Ar 4 %; Kr 4 %; Xe 4 %; Linde gas). Fig. 6.3 shows a TOF mass spectrum of the gas mixture as pulsed from the PSV. We employ a conventional TOF equation:

$$\text{TOF} = A + B \times \sqrt{m/z} \quad (6.5)$$

for 2-point calibration (Håkansson et al. 1998). To find parameters A and B we set $^4\text{He}^+$ at 4.00260 amu and $^{132}\text{Xe}^+$ at 131.90414 amu, while the other components and their isotopes are used to test the accuracy of the calibration. The resulting mass accuracy is better than 200 ppm for the used mass range.

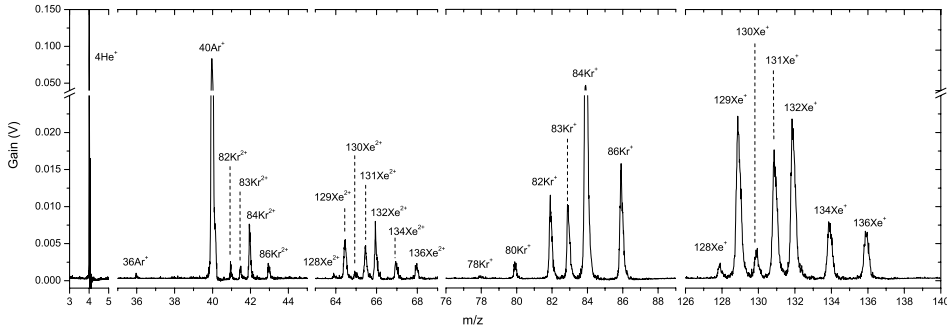


Figure 6.3 – TOF mass spectrum of the calibration gas mixture.

6.3.2 Carrier gas profile

In order to locate and characterize the profile of the He expansion, the MCP gain is monitored as a function of ion extraction time for $m/z = 4$ (He). Ion extraction before the arrival of He into the ionization zone leads to zero gain. Extraction during the transient He pulse leads to gain that

depends on the concentration of He atoms in the ionization region. Plotting the gain vs. extraction time thus gives the density profile of He in the gas expansion.

Fig. 6.4 shows the density profile of He in a pure gas expansion for different substrate positions. The different positions correspond to distance between the substrate surface and the expansion axis. The different results are a consequence of the actual configuration in which the substrate may entirely block or at least degrade the He flow. Almost no He is transmitted within a distance of ± 0.5 mm from the expansion axis. Between 0.5 and 3 mm the transmission gradually increases. The density profile gradually sharpens and shifts towards lower extraction time. At 2 mm the front of the He profile is indistinguishable from those at and beyond 3 mm. However, the rear of the profile is degraded. At substrate distances of 3 mm and beyond, the He profile does not change indicating that the substrate no longer disturbs the expansion. Table 6.1 shows the peak delay and FWHM of the He profile for different substrate positions.

For further experiments, we adopt a distance of 1 mm. Here the substrate is close to the expansion axis ensuring efficient entrainment of desorbates, while leaving the He expansion relatively structured. No significant difference in He profile is observed for substrates with different width.

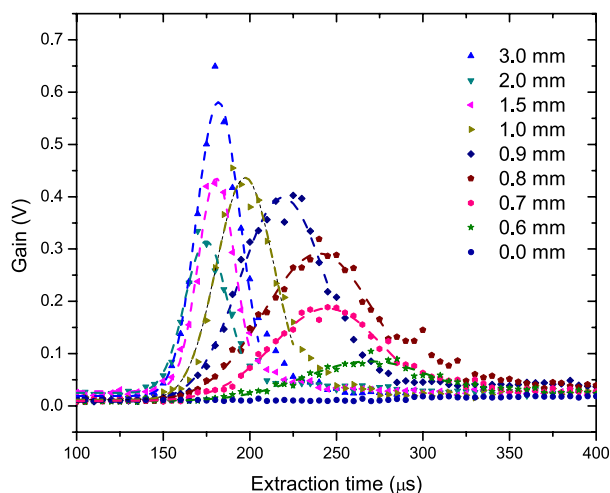


Figure 6.4 – He density profiles at different substrate positions, derived from the maximum intensity of m/z 4 as a function of extraction time. Position 0 mm corresponds to a configuration where the substrate surface coincides with the expansion axis. The dashed lines are Gaussian fits to the datasets, excluding tail structures characteristic to all positions.

6.3.3 Laser desorption of pure ices

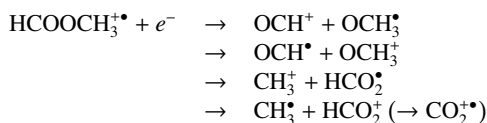
In order to test the laser desorption of cryogenic samples, ices composed of different astronomically relevant molecules are used; methyl formate (HCOOCH_3), ethane (C_2H_6) and methanol (CH_3OH). Ice samples are grown by directed vapor deposition on a 15 mm wide substrate at 17 K. Typical

Table 6.1 – Influence of the substrate on the density profile of the carrier gas pulse. Peak delay (relative to the undisturbed flow; in μs), FWHM (μs) and integrated area ($\text{V } \mu\text{s}$) for the He profiles are derived from Gaussian fits to the data sets shown in Fig. 6.4. The setting marked in bold is used for further experiments.

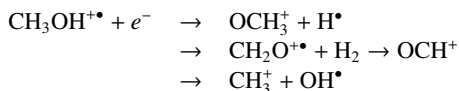
Distance (mm)	Delay (μs)	FWHM (μs)	Area ($\text{V } \mu\text{s}$)
0.6	88	75	7.1
0.7	63	63	13.9
0.8	58	64	22.5
0.9	38	48	22.2
1.0	16	33	17.7
1.5	-1	21	10.9
2.0	-7	25	9.0
3.0	0	25	17.8
4.0	-0	25	17.7
5.0	0	25	17.8

deposition time is ~ 15 min, during which ices of several thousands of monolayers thick ($\gg 1 \mu\text{m}$) are grown. Ices are laser desorbed at 17 K at a pulse energy of ~ 7 mJ and thereby injected into the He expansion. Ionization/extraction is carried out at an extraction time coincident with the peak intensity of the He profile. Fig. 6.5 shows the TOF mass spectra for laser-desorbed HCOOCH_3 , C_2H_6 and CH_3OH ice.

EI ionization of HCOOCH_3 proceeds through generation of the parent radical cation $\text{HCOOCH}_3^{+\bullet}$, followed by fragmentation:



C_2H_6 produces a parent radical cation $\text{C}_2\text{H}_6^{+\bullet}$ followed by fragmentation with most intense signal from $\text{C}_2\text{H}_4^{+\bullet}$. CH_3OH yields radical cation $\text{CH}_3\text{OH}^{+\bullet}$, which fragments through:



TOF mass spectra of laser-desorbed HCOOCH_3 , C_2H_6 and CH_3OH ice agree with the 70-eV electron ionization fragmentation pattern reported for these molecules in the NIST Chemistry Webbook (webbook.nist.gov/chemistry/). The similarity of the fragmentation pattern indicates that for the ices in question, the laser desorption process, as far as we are able to discriminate, does not chemically alter the sample. Indeed, the photon energy of the desorption laser (3.5 eV) is below the typical bond dissociation energy in organic molecules, and dissociation is therefore not expected

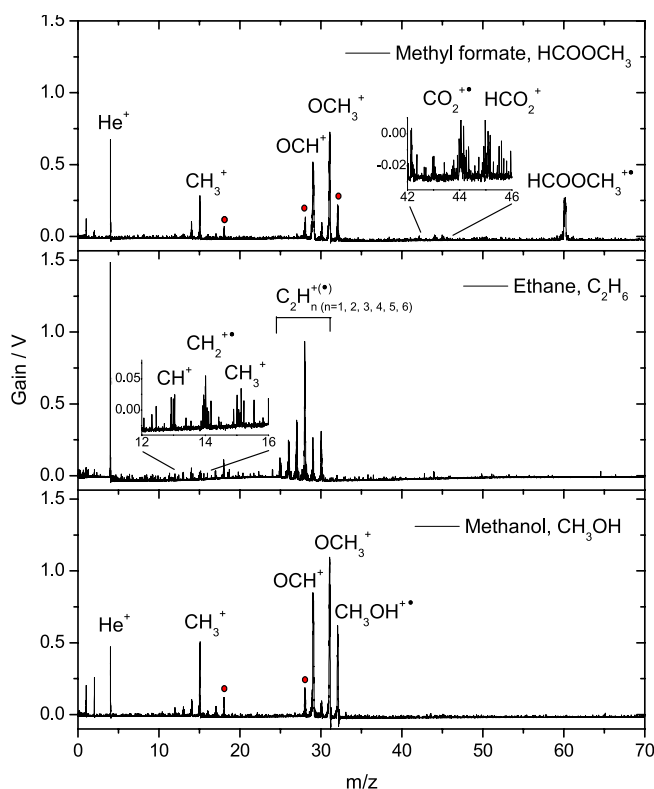


Figure 6.5 – Laser desorption (reflection) TOF mass spectra of pure HCOOCH_3 , C_2H_6 and CH_3OH ice at 17 K. The most prominent mass fragments are labeled. The masses marked with a red dot correspond to residual atmospheric gases H_2O , N_2 and O_2 .

to occur. However, a soft ionization technique (*e.g.*, single-photon ionization, SPI) will be beneficial in avoiding the fragmentation after ionization and thus in confirming the delicateness of the desorption process itself.

UV laser desorption is a suitable evaporation method for astronomical ices as demonstrated for pure HCOOCH_3 , C_2H_6 and CH_3OH ices. The UV desorption proceeds through coupling of the laser energy to the substrate, inducing fast local desorption of the cryogenic sample. For matrix-assisted laser desorption of biomolecules, a wavelength close to the absorption frequency of the matrix is used. For interstellar ice analogues rich in water, wavelengths resonant with H_2O (IR) may be more efficient for consistent desorption. Targeted desorption may also enable layer-by-layer desorption and hence depth profiling of samples. The composition of processed interstellar ice analogs is likely to be inhomogeneous due to the limited penetration depth of VUV photons and atom bombardment. The morphology of the ice analogues is also expected to influence the scanning depth of atoms.

6.3.4 Sensitivity

The main objective of the experiment is to provide a sensitive technique to unambiguously analyze highly dilute astronomical ice analogues. The sensitivity of the instrument is tested by laser desorption of a cryogenic sample with a known isotopologue composition. We use solid Argon, which is inert and does not undergo fragmentation. The ^{36}Ar isotope has a natural abundance of 0.337 %, which we estimate to be close to the current detection threshold. Fig. 6.6 shows the laser desorption TOF mass spectrum of Ar ice at 17 K. The ^{36}Ar isotope is detected at an abundance of 0.29 % relative to the main isotope. The S/N ratio of the ^{36}Ar is 3.8 (evaluated from the values containing 95 % of the data points) setting the detection limit to ~ 0.3 % for molecules produced in the ices. This is better than the currently available techniques to search for species newly formed in an ice, *e.g.*, FTIR spectroscopy (1 %).

Further improvement in sensitivity can be achieved by placing the sample substrate close to the ion source in the mass spectrometer (Gudipati & Yang 2012). This minimizes dilution and allows larger portion of the desorbed species to be collected at the mass spectrometer. Reducing the dilution is particularly important for thin astronomically relevant ice samples with thickness of few hundreds of monolayers.

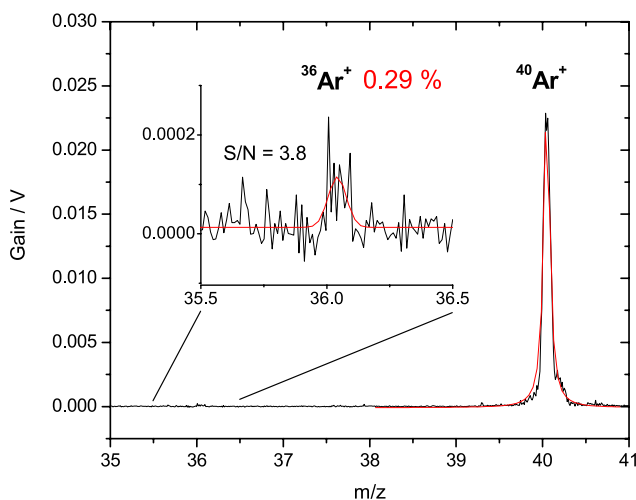


Figure 6.6 – Laser desorption TOF mass spectrum of solid argon at 17 K. The graph shows the m/z region with the Ar isotopologs ^{40}Ar and ^{36}Ar . The inset shows the expanded view of the ^{36}Ar peak.

6.3.5 VUV photoprocessed C_2H_6

Ethane (C_2H_6) is used as a test molecule for VUV (vacuum UV) photochemistry, due to its astronomical relevance and tendency for chemical complexation upon energetic processing. The relatively low thermal desorption temperature of 80 K makes C_2H_6 also a convenient test molecule. C_2H_2 produced through gas-phase reactions in dense cloud cores (Herbst 1995), undergoes further

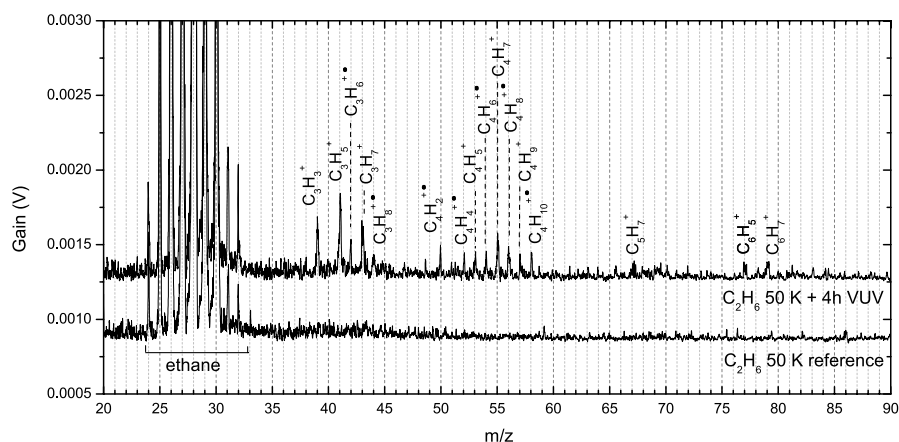


Figure 6.7 – Laser desorption TOF mass spectra of C_2H_6 at 50 K (lower trace) and after 4 h VUV photoprocessing at 50 K (upper trace). The mass signal from ethane (m/z 24–32) is saturated as a result of higher sensitivity used to see the photoproducts. The spectra are offset for clarity.

hydrogenation on grain surface yielding C_2H_6 (Charnley et al. 1995). In the laboratory C_2H_6 is readily produced through energetic processing (VUV, ion bombardment) of pure and mixed CH_4 ices (Stief et al. 1965, Gerakines et al. 1996, 2001, Kaiser & Roessler 1998, Moore & Hudson 1998, Bennett et al. 2006). Under further processing (ion/electron bombardment), C_2H_6 desaturates and polymerizes, providing a chemical route for the production ethylene (C_2H_4), acetylene (C_2H_2), methane (CH_4) as well as species with 4 carbon atoms; n-butane (C_4H_{10}) and butene (C_4H_8) (Scheer et al. 1962, Jackson et al. 1966, Strazzulla et al. 2002, Compagnini et al. 2009, Hudson et al. 2009, Kim et al. 2010).

C_2H_6 (99.99 %, Sigma Aldrich) is deposited onto a 25-mm wide substrate at 50 K. A laser desorption TOF mass spectrum of the unprocessed sample is taken for reference. A similar C_2H_6 film is deposited and subsequently exposed to VUV photons from the microwave discharge hydrogen lamp for 4 h corresponding to a dose of $\sim 7 \times 10^{17}$ photons cm^{-2} .

Fig. 6.7 shows the laser desorption TOF mass spectra of pure C_2H_6 ice before and after VUV irradiation. The heaviest mass detected for C_2H_6 corresponds to the molecular ion C_2H_6^+ at m/z 32. For VUV irradiated C_2H_6 , several peaks with $m/z > 32$ are observed. Assuming the production of only C and H-containing photoproducts (abundance of impurities is low as deduced from the mass peaks), the detected masses between m/z 36 and 44 can be attributed to molecules containing 3 carbon atoms, and those between m/z 48 and 58 to molecules containing 4 carbon atoms. Weak signal is detected at m/z 67, 77 and 79, which suggests the presence of species with 5 and 6 carbon atoms. The m/z 77 and 79 likely corresponds to C_6H_5^+ and C_6H_7^+ , respectively. The weakness and the small number of peaks, makes the detection however uncertain. These peaks may also correspond to fragments of a heavier molecular ion peak. Assuming the signal at m/z 77 and 79 corresponds to the most abundant fragments of a photoproduct with 6 carbon atoms, the fragmentation pattern points to cyclic structures; 1,3-hexadienyle and/or 1,4-hexadienyle (Fig. 6.8). Saturated aliphatic structures show maximum intensities at higher m/z values.

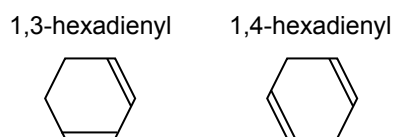


Figure 6.8 – 1,3-hexadienyl and 1,4-hexadienyl.

Chapter VII

CHEMISTRY OF MASSIVE YOUNG STELLAR OBJECTS WITH A DISK-LIKE STRUCTURE

Chemistry of massive young stellar objects with a disk-like structure

K. Isokoski, S. Bottinelli, and E. F. van Dishoeck

Astronomy & Astrophysics, 2013, accepted.

Abstract

Our goal is to make an inventory of complex molecules in three well-known high-mass protostars for which disks or toroids have been claimed and to study the similarities and differences with a sample of massive YSOs without evidence for such flattened disk-like structures. With a disk-like geometry, UV radiation can escape more readily and potentially affect the ice and gas chemistry on hot-core scales. A partial submillimeter line-survey, targeting CH_3OH , H_2CO , $\text{C}_2\text{H}_5\text{OH}$, HCOOCH_3 , CH_3OCH_3 , CH_3CN , HNCO , NH_2CHO , $\text{C}_2\text{H}_5\text{CN}$, CH_2CO , HCOOH , CH_3CHO and CH_3CCH , is performed toward three massive YSOs with disk-like structures, IRAS20126+4104, IRAS18089-1732 and G31.41+0.31. Rotation temperatures and column densities are determined by the rotation diagram method as well as by independent spectral modeling. The molecular abundances are compared with previous observations of massive YSOs without evidence for a disk structure, targeting the same molecules with the same settings and using the same analysis method. Consistent with previous studies, different complex organic species have different characteristic rotation temperatures and can be classified either as warm (>100 K) or cold (<100 K). The excitation temperatures and abundance ratios are similar from source to source and no significant difference can be established between the two source types. Acetone, CH_3COCH_3 , is detected for the first time in G31.41+0.31 and IRAS18089-1732. Temperatures and abundances derived from the two analysis methods generally agree well within factors of a few. The lack of chemical differentiation between massive YSOs with and without observed disks suggest either that the chemical complexity is already fully established in the ices in the cold pre-stellar phase or that the material experiences similar physical conditions and UV exposure through outflow cavities during the short embedded lifetime.

7.1 Introduction

Millimeter lines from complex organic molecules are widely associated with high-mass star forming regions and indeed form one of the signposts of the deeply embedded phase of star formation (e.g., [Blake et al. 1987](#), [Hatchell et al. 1998](#), [Gibb et al. 2000](#), [Fontani et al. 2007](#), [Requena-Torres et al. 2008](#), [Belloche et al. 2009](#), [Zernickel et al. 2012](#)). Many studies of the chemistry in such regions have been carried out, either through complete spectral surveys of individual sources or by targetting individual molecules in a larger number of sources (see [Herbst & van Dishoeck 2009](#), [Caselli & Ceccarelli 2012](#), for reviews). In spite of all this work, only few systematic studies of the abundances of commonly observed complex molecules have been performed across a sample of massive YSOs, to search for similarities or differences depending on physical structure and evolutionary state of the object. Intercomparison of published data sets is often complicated by the use of different telescopes with different beams, different frequency ranges and different analysis techniques.

Chemical abundances depend on the physical structure of the source such as temperature, density and their evolution with time, as well as the amount of UV radiation impinging on the gas and dust. In contrast with the case of solar-mass stars, the physical structures and mechanisms for forming massive ($M > 8 M_\odot$) stars are still poorly understood. Indeed, theoretically, the powerful UV radiation pressure from a high-mass protostellar object (HMPO) should prevent further accretion and so inhibit the formation of more massive stars ([Zinnecker & Yorke 2007](#)). However, a number of recent studies have claimed the presence of disk- or toroid-like ‘equatorial’ structures surrounding

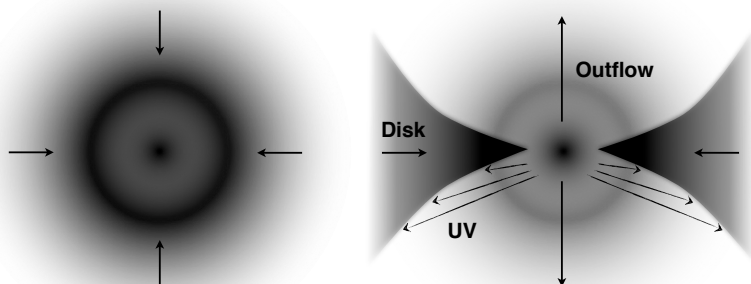


Figure 7.1 – Illustration of a protostar with a spherical structure (left) and a protostar with a flattened disk-like structure (right) with enhanced UV photons illuminating the walls of the outflow cavity.

a handful of high-mass protostars (Cesaroni et al. 2007). These data support theories in which high-mass star formation proceeds in a similar way as that of low-mass stars via a disk accretion phase in which high accretion rates and asymmetric structures overcome the problem of radiation pressure. The best evidence so far is that for a ~ 5000 AU disk in Keplerian rotation around IRAS20126+4104, claimed by Cesaroni et al. (1999) on the basis of the presence of a velocity gradient in the CH_3CN emission perpendicular to the direction of the outflow, as predicted by the disk-accretion paradigm. Surprisingly, even in the best case of IRAS20126+4104, the detailed chemistry of these (potential) disks has not yet been studied.

Most chemical models invoke grain surface chemistry to create different generations of complex organic molecules (Tielens & Charnley 1997). Hydrogenation of solid O, C, N and CO during the cold ($T_d < 20$ K) pre-stellar phase leads to ample production of CH_3OH and other hydrogenated species like H_2O , CH_4 and NH_3 (Tielens & Hagen 1982). Exposure to UV radiation results in photodissociation of these simple ices, with the fragments becoming mobile as the cloud core heats up during the protostellar phase. First generation complex molecules result from the subsequent recombination of the photofragments, and will eventually evaporate once the grain temperature rises above the ice sublimation temperature of ~ 100 K (Garrod & Herbst 2006, Garrod et al. 2008). Good examples are $\text{C}_2\text{H}_5\text{OH}$, HCOOCH_3 and CH_3OCH_3 resulting from mild UV processing of CH_3OH ice (Öberg et al. 2009b). Finally, a hot core gas phase chemistry between evaporated molecules can drive further complexity in second generation species (e.g., Millar et al. 1991, Charnley et al. 1992, 1995).

One of the most obvious consequences of an equatorial rather than spherical structure is that UV radiation can more easily escape the central source and illuminate the surface layers of the surrounding disk or toroid as well as the larger scale envelope (Bruderer et al. 2009, 2010) (Fig. 7.1). This can trigger enhanced formation of complex organic molecules in the ices relative to methanol. Another effect of UV radiation is that it drives increased photodissociation of gaseous N_2 and CO. The resulting atomic N and C would then be available for grain surface chemistry potentially leading to enhanced abundances of species like HNCO and NH_2CHO .

To investigate the effects of disk-like structures on the chemistry, we present here a single-disk

survey using the James Clerk Maxwell Telescope of three HMPOs for which large equatorial structures (size > 2000 AU) have been inferred, namely IRAS20126+4104, IRAS18089–1732, and G31.41+0.31. The results are compared with those of a recent survey of a sample of HMPOs by Bisschop et al. (2007) (hereafter BIS07), targeting many of the same molecules and settings. The use of the same telescope and analysis method allows a meaningful comparison between the two samples of sources. BIS07 found that the O-rich complex molecules are closely correlated with the grain surface product CH_3OH supporting the above general chemical scenario. N-rich organic molecules do not appear to be correlated with O-rich ones, but overall, the relative abundances of the various species are found to be remarkably constant within one chemical family. One of the main questions is whether this similarity in abundance ratios also holds for sources with disk-like structures. Although our observations do not spatially resolve these structures, they are sensitive enough and span a large enough energy range to determine abundances on scales of $\sim 1''$ and thereby set the scene for future high-angular resolution observations with interferometers like the Atacama Large Millimeter/submillimeter Array (ALMA). Moreover, current interferometers resolve out part of the emission, which is why single-dish observations are still meaningful.

This paper is organized as follows. In §2, the observed sources and frequency settings are introduced and the details of the observations are presented. §3 focuses on the data analysis methods. Specifically, two techniques are used to determine excitation temperatures and column densities: the rotation diagram method employed by BIS07 and spectral modeling tools in which the observed spectra are simulated directly. §4 presents the results from both analysis methods and discusses their advantages and disadvantages. Finally, §5 compares our results with those of BIS07 to draw conclusions on similarities and differences in chemical abundances between sources with and without large equatorial structures.

7.2 Observations

7.2.1 Observed sources

Table 7.1 gives the coordinates, luminosity L , distance d , galactocentric radius R_{GC} , velocity of the local standard of rest V_{LSR} and the typical line width for the observed sources. The selected sources are massive young stellar objects (YSOs), for which strong evidence exists for a circumstellar disk structure. All sources are expected to harbor a *hot core*: a compact, dense ($\geq 10^7 \text{ cm}^{-3}$) and warm ($\geq 100 \text{ K}$) region with complex chemistry triggered by the grain mantle evaporation (Kurtz et al. Kurtz et al. (2000)). CH_3CN emission from $\geq 100 \text{ K}$ gas is present in all sources. Moreover, CH_3OH 7_K-6_K transitions (338.5 GHz) with main beam temperatures of $\geq 1 \text{ K}$ have been observed for these sources. Sources also needed to be visible from the James Clerk Maxwell Telescope (JCMT) ¹.

¹ The James Clerk Maxwell Telescope is operated by the Joint Astronomy Centre, on behalf of the Particle Physics and Astronomy Research council of the United Kingdom, the Netherlands Organization for Scientific Research and the National Research Council of Canada. The project ID is m09bn10.

Table 7.1 – Coordinates, luminosity, distance, galactocentric radius, velocity of the local standard of rest, $^{12}\text{C}/^{13}\text{C}$ isotope ratio and the typical line width for the observed sources.

Sources	$\alpha(2000)$	$\delta(2000)$	L [$10^5 L_\odot$]	d [kpc]	R_{GC}^* [kpc]	V_{LSR} [km s^{-1}]	$^{12}\text{C}/^{13}\text{C}$	ΔV [km s^{-1}]
IRAS20126+4104	20:14:26.04	+41:13:32.5	0.13 ^a	1.64 ^b	8.3	-3.5	70	6 ^c
IRAS18089-1732	18:11:51.40	-17:31:28.5	0.32 ^d	2.34 ^e	6.2	33.8	54	5 ^c
G31.41+0.31	18:47:34.33	-01:12:46.5	2.6 ^f	7.9 ^g	4.5	97.0	41	6-10 ^h

(a) Cesaroni et al. (1997), (b) Moscadelli et al. (2011), (c) Leurini et al. (2007), (d) Sridharan et al. (2002), (e) Xu et al. (2011), (f) Cesaroni et al. (1994b), (g) Churchwell et al. (1990), (h) Fontani et al. (2007).

* The galactocentric radii were calculated using distances d in this table and a IAU recommended distance from the galactic center $R_0 = 8.5$ kpc. The $^{12}\text{C}/^{13}\text{C}$ isotope ratios are calculated from Eq. 7.11.

Table 7.2 – Observed frequency settings and molecular lines.

Molecule	Freq. [GHz]	E_{up} [K]	$\mu^2 S$ [D ²]	Transition	Additional molecules
CH ₃ CN	239.1195	144.77	811.86	13 _K – 12 _K	CH ₃ ¹³ CN, HCOOCH ₃ , CH ₃ OCH ₃
HNCO	219.7983	58.02	28.112	10 _{0,10,11} – 9 _{0,9,10}	H ₂ ¹³ CO, C ₂ H ₅ CN
	240.8809	112.53	30.431	11 _{1,11,12} – 10 _{1,10,11}	CH ₃ OCH ₃ , CH ₃ OH, HN ¹³ CO
HCOOCH ₃	222.3453	37.89	42.100	8 _{5,4} – 7 _{4,3}	CH ₃ OCH ₃ , NH ₂ CHO
	225.2568	125.50	33.070	18 _{6,12} – 17 _{6,12}	H ₂ CO, CH ₃ OCH ₃ , ¹³ CH ₃ OH
H ₂ CO	364.2752	158.42	52.165	5 _{3,3} – 4 _{3,2}	C ₂ H ₅ OH
CH ₃ CN	331.0716	151.11	513.924	18 _K – 17 _K	HCOOCH ₃ , HNCO, CH ₃ ¹³ CN
HNCO	352.8979	187.25	43.387	16 _{1,15,17} – 15 _{1,14,16}	C ₂ H ₅ CN, C ₂ H ₅ OH, HCOOCH ₃
NH ₂ CHO	345.1826	151.59	664.219	17 _{0,17} – 16 _{0,16}	HCOOCH ₃ , C ₂ H ₅ OH, ¹³ CH ₃ OH
HCOOCH ₃	354.6084	293.39	87.321	33 _{2,32} – 32 _{2,31}	NH ₂ CHO, C ₂ H ₅ CN

7.2.1.1 IRAS20126+4104

IRAS20126+4104 (hereafter IRAS20126) is a luminous ($\sim 10^4 L_{\odot}$) YSO located relatively nearby at a distance of 1.64 kpc (Moscadelli et al. 2011). It was first identified in the IRAS point source catalog by the IR colours typical of ultracompact HII regions and by H₂O maser emission characteristic of high-mass star formation (Comoretto et al. 1990). IRAS20126 features a ~ 0.25 -pc scale inner jet traced by H₂O maser spots in the SE-NW direction with decreasing velocity gradient (Tofani et al. 1995). Source and masers are embedded inside a dense, parsec-scale molecular clump (Estalella et al. 1993, Cesaroni et al. 1999). The inner jet feeds into a larger scale bipolar outflow with the two having reversed velocity lobes (Wilking et al. 1990, Cesaroni et al. 1999). The reversal is likely to be due to precession of the inner jet caused by a companion separated by a distance of $\sim 0.5''$ (850 AU) (Hofner et al. 1999, Shepherd et al. 2000, Cesaroni et al. 2005, Sridharan et al. 2005). A rotating, flattened, Keplerian disk structure has been detected perpendicular to the inner jet. Observations of CH₃CN transitions show a Keplerian circumstellar disk (radius ~ 1000 AU) with a velocity gradient perpendicular to the jet and a hot core with a diameter of ~ 0.0082 pc and a temperature of ~ 200 K at a geometric center of the outflow (Cesaroni et al. 1997, Zhang et al. 1998, Cesaroni et al. 1999). Direct near-infrared (NIR) observations show a disk structure as a dark line (Sridharan et al. 2005). The disk shows a temperature and density gradient and is going through infall of material with a rate of $\sim 2 \times 10^{-3} M_{\odot} \text{ yr}^{-1}$ as expected for a protostar of this mass and luminosity (Cesaroni et al. 2005). Recent modeling of the Spectral Energy Distribution (SED) of IRAS20126 shows indeed a better fit when a disk is included (Johnston et al. 2011).

7.2.1.2 IRAS18089-1732

IRAS18089-1732 (hereafter IRAS18089) is a luminous ($\sim 10^{4.5} L_{\odot}$, Sridharan et al. 2002) YSO located at a distance of 2.34 kpc (Xu et al. 2011). It was identified based on CS detections of bright IRAS point sources with colours similar to ultracompact HII regions and the absence of significant free-free emission (Sridharan et al. 2002), and with H₂O and CH₃OH maser emission (Beuther et al. 2002). The CO line profile shows a wing structure characteristic of an outflow, although no clear outflow structure could be resolved from the CO maps (Beuther et al. 2002). A collimated outflow in the Northern direction is however seen in SiO emission on scales of $5''$ (Beuther et al. 2004). IRAS18089 has a highly non-circular dust core of ~ 3000 AU diameter ($\sim 1''$), with optically thick CH₃CN at ~ 350 K (Beuther et al. 2005). HCOOCH₃ was found to be optically thin, with emission confined to the core, and showing a velocity gradient perpendicular to the outflow indicative of a rotating disk (Beuther et al. 2004). Also hot NH₃ shows a velocity gradient perpendicular to the outflow, although no Keplerian rotation was found, possibly due to infall and/or self gravitation (Beuther & Walsh 2008). Several hot-core molecules (HCOOCH₃, CH₃CN, CH₃OCH₃, HNCO, NH₂CHO, CH₃OH, C₂H₅OH) were mapped by Beuther et al. (2005) but no column densities or abundances were reported.

7.2.1.3 G31.41+0.31

G31.41+0.31 (hereafter G31) is a luminous ($2.6 \times 10^5 L_{\odot}$, Cesaroni et al. 1994b) YSO at a distance of 7.9 kpc (Churchwell et al. 1990). Preliminary evidence for a rotating disk with a perpendicular bipolar outflow was reported by Cesaroni et al. (1994a,b) and Olmi et al. (1996) showing a velocity gradient across the core in the NE-SW direction, similar to previously detected OH masers (Gaume

& Mutel 1987). High-angular resolution CH_3CN observations by Beltrán et al. (2005) could not detect Keplerian rotation typical for less luminous stars, nevertheless a toroidal structure undergoing gravitational collapse and fast accretion ($\sim 3 \times 10^{-2} \text{ M}_\odot \text{ yr}^{-1}$) onto the central object was found. The G31 hot molecular core (HMC) is part of a complex region in which multiple stellar sources are detected (Benjamin et al. 2003); indeed, it is separated from an ultracompact (UC) HII region by only $\sim 5''$ and overlaps with a diffuse halo of free-free emission, possibly associated with the UC HII region itself (Cesaroni et al. 1998). More recent interferometric observations confirm the velocity gradient in the NH_3 (4,4) inversion transition and in CH_3CN data (Cesaroni et al. 2010, 2011). Line profiles look like a rotating toroid with infall motion. Several complex hot-core molecules have been observed in G31, including glycolaldehyde CH_2OHCHO (Beltrán et al. 2009), but again no abundance ratios have been presented.

7.2.2 Observational details

The observations were performed at the JCMT on Mauna Kea, Hawaii, between August 2007 and September 2009. The observations of the 338 GHz region covering CH_3OH ($7_K \rightarrow 6_K$) transitions were taken from JCMT archive. The front ends consisted of the facility receivers A3 (230 GHz region) and HARP-B (340 GHz region). The back-end was the digital autocorrelation spectrometer (ACSIS), covering 400 and 250 MHz of instantaneous bandwidth for A3 and HARP-B, respectively, with a channel width of 50 kHz. The noise level was $T_{\text{rms}} \sim 20 \text{ mK}$ on a T_A^* scale when binned to 0.5 km s^{-1} . The integration time was $\sim 1 \text{ hr}$ and 1.8 hr for A3 and HARP-B, respectively. The spectra were scaled from the observed antenna temperature, T_A^* , to main-beam temperature, T_{MB} , using main beam efficiencies η_{MB} of 0.69 and 0.63 at 230 GHz and 345 GHz, respectively. We adopt a T_A^* calibration error of 20%.

The HPBW (half-power beam width, θ_B) for the 230 and 345 GHz band observations are $20\text{--}21''$ and $14''$, respectively. Emission from a volume with a source diameter $\theta_s \leq \theta_B$ undergoes beam dilution described by the beam-filling factor, η_{BF} :

$$\eta_{\text{BF}} = \frac{\theta_s^2}{\theta_s^2 + \theta_B^2}. \quad (7.1)$$

Table 7.2 gives the observed frequency settings and the targeted molecular lines. The settings were taken from BIS07 and were chosen to cover at least one strong line for the target molecules as well as lines of other interesting species. Strong lines of target molecules were chosen due to their high main-beam temperatures and minimum line-confusion in line surveys of Orion-KL by Sutton et al. (1985) and Schilke et al. (1997) at 230 GHz and 345 GHz, respectively. In order to determine rotation temperatures, we covered at least two transitions for a given species with $E_{\text{up}} < 100 \text{ K}$ and $E_{\text{up}} > 100 \text{ K}$ each. BIS07 used the single pixel receiver B3, the predecessor of HARP-B, together with DAS (Digital Autocorrelation Spectrometer) as the back-end, covering a larger instantaneous bandwidth of 500 MHz. Only the central spaxel of HARP-B array is analyzed here as no significant off source emission was detected in the complex molecules.

Data reduction and line fitting were done using the CLASS software package². Line assignments were done by comparison of observed frequencies corrected for source velocity with the JPL³,

² CLASS is part of the GILDAS software package developed by IRAM.

³ <http://spec.jpl.nasa.gov/ftp/pub/catalog/catform.html>

CDMS⁴ and NIST⁵ catalogs (Pickett et al. 1998, Müller et al. 2005). The line assignment/detection was based on Gaussian fitting with the following criteria: (i) the fitted line position had to be within ± 1 MHz of the catalog frequency, (ii) the FWHM had to be consistent with those given in Table 7.1 and (iii) a $S/N > 3$ is required on the peak intensity. Sect. A.1 in the Appendix describes in more detail the error analysis. In general, our errors on the integrated intensities are conservative and suggest a lower S/N than that on the peak intensity or obtained using more traditional error estimates.

7.3 Data analysis

7.3.1 Rotation diagrams

Rotation temperatures and column densities were obtained through the rotation diagram (RTD) method (Goldsmith & Langer 1999), when 3 or more lines are detected over a sufficiently large energy range. Integrated main-beam temperatures, $\int T_{\text{MB}} dV$, can be related to the column density in the upper energy level by:

$$\frac{N_{\text{up}}}{g_{\text{up}}} = \frac{3k \int T_{\text{MB}} dV}{8\pi^3 \nu \mu^2 S}, \quad (7.2)$$

where N_{up} is the column density in the upper level, g_{up} is the degeneracy of the upper level, k is Boltzmann's constant, ν is the transition frequency, μ is the dipole moment and S is the line strength. The total *beam-averaged* column density N_{T} in cm^{-2} can then be computed from:

$$\frac{N_{\text{up}}}{g_{\text{up}}} = \frac{N_{\text{T}}}{Q(T_{\text{rot}})} e^{-E_{\text{up}}/T_{\text{rot}}}, \quad (7.3)$$

where $Q(T_{\text{rot}})$ is the rotational partition function, and E_{up} is the upper level energy in K.

Blended transitions of a given species with similar E_{up} were assigned intensities according to their Einstein coefficients (A) and upper level degeneracies (g_{up}):

$$\int T_{\text{MB}} dV(i) = \int T_{\text{MB}} dV \times \frac{A^i g_{\text{up}}^i}{\sum_i A^i g_{\text{up}}^i}, \quad (7.4)$$

where the summation is over all the contributing transitions. Blended transitions with different E_{up} , or with contamination from transitions belonging to other species, were excluded from the RTD fit.

The beam averaged column density, N_{T} , is converted to the *source-averaged* column density N_{S} using the beam-filling factor η_{BF} :

$$N_{\text{S}} = \frac{N_{\text{T}}}{\eta_{\text{BF}}}. \quad (7.5)$$

The standard RTD method assumes that the lines are optically thin. Lines with strong optical depth, determined from the arguments in §4.1 as well as the models discussed in §3.2, were excluded from

⁴ <http://www.ph1.uni-koeln.de/vorhersagen>

⁵ <http://physics.nist.gov/PhysRefData/Micro/Html/contents.html>

the fit. For CH₃OH, also low- E_{up} lines arising from a cold extended component (see Sect. 7.4.4.1) were excluded.

Differential beam dilution is taken into account by multiplying the line intensities in the 230 GHz range by $\eta_{\text{BF}}(340 \text{ GHz})/\eta_{\text{BF}}(230 \text{ GHz})$. For warm and cold molecules, beam dilution is derived assuming source diameters $\theta_{T=100\text{K}}$ (see Eq. 7.10 below) and 14'', respectively (see Eq. 7.1). All emission is thus assumed to be contained within the smallest beam size.

The vibrational partition function was ignored assuming that all emission arises from the ground vibrational state so that the vibrational partition function can be set to unity. This approximation can cause an underestimation of the derived column densities for larger molecules, even at temperatures of 100–200 K. Indeed, [Widicus Weaver et al. \(2005\)](#) show that the error can be up to a factor of 2 for temperatures up to 300 K. Since this approximation affects all complex molecules (albeit at different levels), the overall error in abundance ratios will be less than a factor of 2 and well within the other uncertainties.

7.3.2 Spectral modeling

The alternative method for analyzing the emission is to model the observed spectra directly. For this purpose, we used the so-called ‘Weeds’ extension of the CLASS software package⁶, developed to facilitate the analysis of large millimeter and sub-millimeter spectral surveys ([Maret et al. 2011](#)). In this model, the excitation of a species is assumed to be in LTE (Local Thermodynamic Equilibrium) at a temperature T_{ex} . The brightness temperature, T_{B} , of a given species as a function of the rest frequency ν is then given by:

$$T_{\text{B}}(\nu) = \eta_{\text{BF}} \left[J_{\nu}(T_{\text{ex}}) - J_{\nu}(T_{\text{bg}}) \right] (1 - e^{-\tau(\nu)}), \quad (7.6)$$

where η_{BF} is the beam filling factor (see Eq. 7.1), J_{ν} is the radiation field such that:

$$J_{\nu}(T) = \frac{h\nu/k}{e^{h\nu/kT} - 1}$$

and T_{bg} is the temperature of the background emission. The HPBW θ_{B} is calculated within Weeds as $\theta_{\text{B}} = 1.22c/\nu D$, where c is the speed of light and D is the diameter of the telescope⁷. The opacity $\tau(\nu)$ is:

$$\tau(\nu) = \frac{c^2}{8\pi\nu^2} \frac{N_{\text{T}}}{Q(T_{\text{ex}})} \sum_i A^i g_{\text{up}}^i e^{-E_{\text{up}}^i/kT_{\text{ex}}} \left(e^{h\nu_0^i/kT_{\text{ex}}} - 1 \right) \phi^i \quad (7.7)$$

where the summation is over each line i of the considered species. ν_0^i is the rest frequency of the line and ϕ^i is the profile function of the line, given by:

$$\phi^i = \frac{1}{\Delta\nu \sqrt{2\pi}} e^{-(\nu-\nu_0^i)^2/2\Delta\nu^2}, \quad (7.8)$$

⁶ CLASS is part of the GILDAS software package developed by IRAM.

⁷ For JCMT with 15-m antenna diameter, the equation gives a θ_{B} of 21.9'' and 14.8'' for the 230 GHz band and 345 GHz bands, respectively.

Table 7.3 – Source radii with $T \geq 100$ K and source diameters.

Sources	$R_{T=100K}$ [AU]	$\theta_{S,T=100K}$ ["]
IRAS20126+4104	1753	2.2
IRAS18089-1732	2750	2.4
G31.41+0.31	7840	2.0

where $\Delta\nu$ is the line width in frequency units at $1/e$ height. $\Delta\nu$ can be expressed as a function of the line FWHM in velocity units ΔV by:

$$\Delta\nu = \frac{v_0^i}{c \sqrt{8 \ln 2}} \Delta V. \quad (7.9)$$

Note that the Weeds model computes the optical depths directly.

The input parameters in the model are the column density N_S in cm^{-2} , excitation temperature T_{ex} in K, the source diameter θ_S in arcseconds, offset velocity from the source LSR (Local Standard of Rest) in km s^{-1} and the line FWHM in km s^{-1} . All parameters excluding the source diameter are optimized manually to obtain the best agreement with the observed spectra. The source diameter for emission from cold species is allowed to vary over a larger area; generally $14''$ is used. The emission from hot-core molecules targeted in our work is assumed to originate from the central region with $T_{\text{dust}} \geq 100$ K. The source diameter for the warm emission is calculated using a relation derived from dust modeling of a large range of sources (BIS07):

$$R_{T=100 \text{ K}} \approx 2.3 \times 10^{14} \left(\sqrt{\frac{L}{L_{\odot}}} \right) \text{ cm}, \quad (7.10)$$

where L/L_{\odot} is the luminosity of the source relative to the solar luminosity. Table 7.3 gives the calculated $R_{T=100 \text{ K}}$ radii and diameters for the observed sources.

In the analysis for individual molecules, the initial values for T_{ex} were based on the T_{rot} from the RTD analysis in case of optically thin species. For optically thick species the value of T_{ex} from the ^{13}C -isotope was used. If T_{ex} for the isotopologue could not be obtained, the initial temperature was guessed. The T_{ex} value was then optimized visually based on the relative intensity of the emission lines. The simulated emission was not allowed to exceed the emission of optically thin lines in the spectrum in any of the observed spectral ranges. Coinciding and blended transitions, which together contribute to an optically thick line, are excluded in the analysis.

Due to the visual optimization and the possibility of overlapping lines (particularly in the line-rich source G31), the resulting T_{ex} values are only a rough estimate (± 50 -100 K) and do not differ significantly from those from the RTD method. The column density for each species was constrained by optically thin, unblended lines, where available.

For the specific case of CH_3OH , which requires two temperature components for a proper fit, the analysis was also done with the CASSIS analysis package⁸. CASSIS has the advantage that it can

⁸ CASSIS has been developed by IRAP-UPS/CNRS (<http://cassis.irap.omp.eu>).

properly model the emission from overlapping optically thick lines, as well as from nested regions of emission.

7.4 Results

7.4.1 General results and comparison between sources

The observed sources, IRAS20126, IRAS18089 and G31, differ from each other significantly in the observed chemical richness in the JCMT single-dish data. Fig. 7.2 presents two frequency ranges with lines from several observed species. For G31, strong lines of all complex organic species are detected, whereas for IRAS20126 many targeted lines are below the detection limit. Many complex molecules are also found in IRAS18089 but with weaker lines than for G31. Among the serendipitous discoveries acetone, CH_3COCH_3 , is possibly seen in G31 and IRAS18089 for the first time (see §7.7.4). Integrated line intensities for all detected lines and selected upper limits are given in Tables 7.8–7.20. The rotation diagrams for the detected species are shown in Figures 7.12–7.17 whereas the optimized parameters in the Weeds model for each molecule and source are available in Table 7.21.

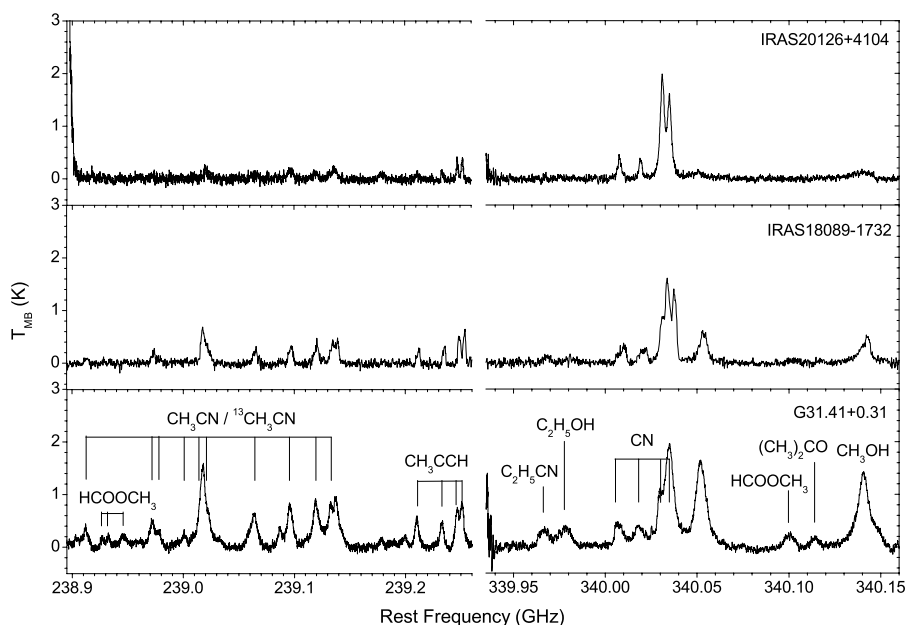


Figure 7.2 – Spectral ranges 238.83–239.26 GHz and 339.94–340.18 GHz (in velocity units) with lines from several targeted species for the three sources.

Table 7.4 – Isotopologue line intensity ratios in the observed sources. Lower limits are those for which the ^{13}C -isotopologue was not detected.

Species	IRAS20126+4104	IRAS18089-1732	G31.41+0.31
$\text{CH}_3\text{OH}/^{13}\text{CH}_3\text{OH}$	>6	>18	6
$\text{CH}_3\text{CN}/\text{CH}_3^{13}\text{CN}$	>65	4.7	4.5

7.4.2 Optical depth determinations

To assess the importance of optical depths effects, the ratio of lines of different isotopologues are compared. The expected $^{12}\text{C}/^{13}\text{C}$ isotope ratio depends on the galactocentric radius, R_{GC} , according to Eq. 7.11 (Wilson & Rood, 1994).

$$^{12}\text{C}/^{13}\text{C} = (7.5 \pm 1.9) R_{\text{GC}} [\text{kpc}] + (7.6 \pm 12.9) \quad (7.11)$$

The isotope ratios derived for our sources using Eq. 7.11 are given in Table 7.1. The galactocentric radii were calculated trigonometrically from the galactic coordinates using the IAU value for the distance to the Galactic center $R_0 = 8.5 \text{ kpc}$ (Kerr & Lynden-Bell 1986).

Table 7.4 lists the observed isotopologue intensity ratios for the most abundant species in our sources. The $\text{CH}_3\text{OH}/^{13}\text{CH}_3\text{OH}$ ratios are derived from a low-energy transition $2_{2,0,+0} - 3_{1,3,+0}$ with $E_{\text{up}} = 44.6 \text{ K}$. No high E_{up} transitions were reliably detected for $^{13}\text{CH}_3\text{OH}$ in our sources in our standard settings and the low E_{up} ratios are therefore taken to apply to cold methanol. For G31.41+0.31, one additional observation was carried out to cover a transition with $E_{\text{up}} > 100 \text{ K}$. A $\text{CH}_3\text{OH}/^{13}\text{CH}_3\text{OH}$ intensity ratio of 4.0 is derived for a transition with $E_{\text{up}} \approx 210 \text{ K}$ ($13_{1,12,-0} - 13_{0,13,+0}$). This indicates that also warm methanol is optically thick in this source.

The $\text{CH}_3\text{CN}/\text{CH}_3^{13}\text{CN}$ ratios are derived from the $13_3 - 12_3$ line intensities for G31 and IRAS18089 and indicate that CH_3CN is optically thick in these two sources, but not in IRAS20126. For H_2CO and HNCO , isotopologue lines are detected but for different transitions than the main isotopologues. Thus, a model is needed to infer the optical depths. Fits to each of the isotopologues independently at a fixed temperature of 150 K using the $R_{\text{T}=100 \text{ K}}$ source size gives column density ratios that are significantly smaller than the overall isotope ratios, suggesting that these species are also optically thick for G31 and IRAS18089. In practice, we have excluded the optically thick lines (as indicated by the Weeds model) from the RTD fits for all species.

7.4.3 Temperatures

Table 7.5 summarizes the derived temperatures from the RTD fit for the various species. As also found by BIS07, molecules can be classified into *cold* ($< 100 \text{ K}$) and *hot* ($> 100 \text{ K}$), and our categorization is similar to theirs. The Weeds analysis is consistent with this grouping. There is however variation in temperatures within the groups, with hot species having rotation temperatures from 70 to 300 K , and cold species from 40 to 100 K . Some variation is seen in rotation temperatures of individual species between different sources; the rotation temperatures are generally higher in G31 than in IRAS18089, while IRAS20126 has the lowest of the three.

Table 7.5 – Temperatures (K) derived from the RTD analysis and the Weeds or CASSIS (CH₃OH) model. The species are classified *warm* and *cold* according to BIS07. Square bracketed values are T_{rot} values for optically thick species and round bracketed values are T_{ex} values assumed based on temperatures in other sources.

	IRAS20126+4104		IRAS18089-1732		G31.41+0.31	
	RTD	model	RTD	model	RTD	model
H ₂ CO	123±21	150	204±82	(150)	157±44	(150)
CH ₃ OH (warm)	119±17	300	291±37	300	323±34	200
CH ₃ OH (cold)	–	14±1	–	15±2	–	14±2
C ₂ H ₅ OH	–	(100)	85±18	150	120±15	100
HNCO	–	(200)	92±25	200	111±32	200
NH ₂ CHO	–	300	72±28	100	94±50	300
CH ₃ CN	217±352	(200)	[346±106]	(200)	[311±68]	(300)
C ₂ H ₅ CN	–	(80)	84±33	80	105±23	80
HCOOCH ₃	–	(200)	118±20	200	173±11	300
CH ₃ OCH ₃	–	(100)	66±11	100	90±6	100
CH ₂ CO	–	(50)	71±11	50	–	50
CH ₃ CHO	–	(50)	–	(50)	42±10	50
HCOOH	–	(40)	–	(40)	21±5	40
CH ₃ CCH	40±22	35	51±17	40	75±21	80

– means not enough lines were detected for a rotation diagram.

Typical uncertainties in the Weeds excitation temperatures are ±50 K.

The T_{rot} value for CH₃OH is ~300 K for G31 and IRAS18089 and ~100 K for IRAS20126. For G31, several lines with $E_{\text{up}} > 400$ K are detected, which makes the RTD fit more robust. For IRAS18089 and IRAS20126 the accuracy of the RTD fits suffers from the small range of E_{up} in the detected transitions. In addition to optically thick lines, low- E_{up} lines have been excluded from the fit. These lines are underestimated by the RTD fit and probably originate from a colder extended region also seen in the ¹³C lines (Fig. 7.3). The T_{rot} from the RTD analysis therefore represents the warm CH₃OH only. See Sect. 7.4.4.1 for a more detailed discussion on the CH₃OH emission.

For CH₃CN, the T_{rot} values range from ~200 and ~350 K for the three sources. The CH₃¹³CN rotation diagram gives a value of T_{rot} of only 53 K, however. (Fig. 7.3). This illustrates the large uncertainties at high temperatures for optically thick species and the possibility of a cold component in addition to the hot one.

Contrary to the general trend, the T_{rot} value for H₂CO is somewhat higher (204 K) in IRAS18089 than in G31 (157 K). The discrepancy could be influenced by the small number of lines used for the analysis. All fitted lines are those belonging to the para-H₂CO, and the T_{rot} fits are thus not affected by fluxes from different spin states. A single transition of H₂¹³CO (3_{1,2} – 2_{1,1}) was covered, and no information on the excitation temperature can therefore be obtained from the minor isotopologue.

The T_{rot} values of the other complex species, HNCO, C₂H₅OH, C₂H₅CN, NH₂CHO and CH₃OCH₃ are around 100 K and are slightly higher in G31 than in IRAS18089. The T_{rot} of

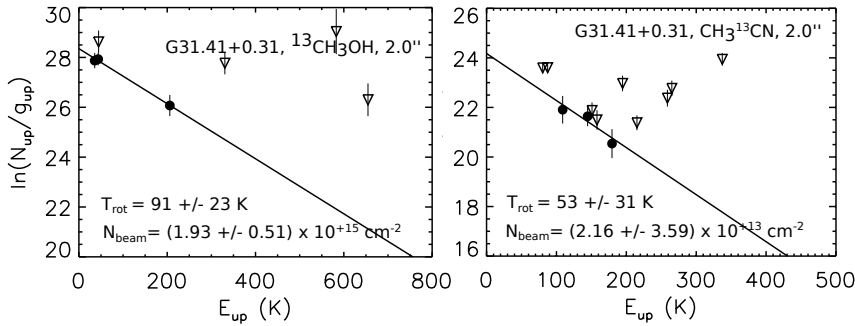


Figure 7.3 – Rotation diagrams for $^{13}\text{CH}_3\text{OH}$ (left panel) and $\text{CH}_3^{13}\text{CN}$ (right panel) in G31. Open triangles are blended lines and are excluded from the fit.

HCOOCH_3 stands out in both sources, in G31 being closer to 200 K. No lines belonging to these species were detected in IRAS20126.

The species classified as cold by BIS07, CH_2CO and CH_3CCH , indeed show cold rotation temperatures in all sources. Not enough lines of CH_3CHO or HCOOH , which are also classified as cold in BIS07, are observed in our sources for making rotation diagrams.

7.4.4 Column densities

Table 7.6 presents the column densities derived from the RTD analysis, Weeds or CASSIS model, and from the ^{13}C -isotopologues for the optically thick species. Following BIS07, the column densities for warm molecules are given as source-averaged values (see Eq. 7.5). The emission from cold molecules extends over a larger volume and the values are given as beam-averaged column densities. Typical uncertainty of the column densities derived from the RTD analysis is $\sim 40\%$. The column densities of warm and cold molecules are visualized in Fig. 7.4 and 7.5, respectively.

7.4.4.1 CH_3OH

An accurate determination of the CH_3OH column density is essential for comparing the abundance ratios of complex organic species. For hot-core molecules, it is particularly important to quantify the warm CH_3OH emission. The column densities of CH_3OH in BIS07 were determined by the RTD method excluding the optically thick lines. The same is done in our analysis. Our rotation diagrams however also show emission from low- E_{up} transitions, which are strongly underestimated by the RTD fit on the warm lines, providing further evidence for the presence of a colder component. We have therefore also excluded these transitions. The fit to the higher E_{up} , optically thin lines should give the warm CH_3OH column density obtained in a similar way as BIS07.

CH_3OH emission was also simulated using a two-component CASSIS model. A single-component model is not able to simultaneously reproduce the warm and cold lines without overestimating the lines from intermediate energy levels. Indeed, a better agreement is obtained using a two-component model, consisting of a warm compact component and a cold extended component. Table 7.22 shows

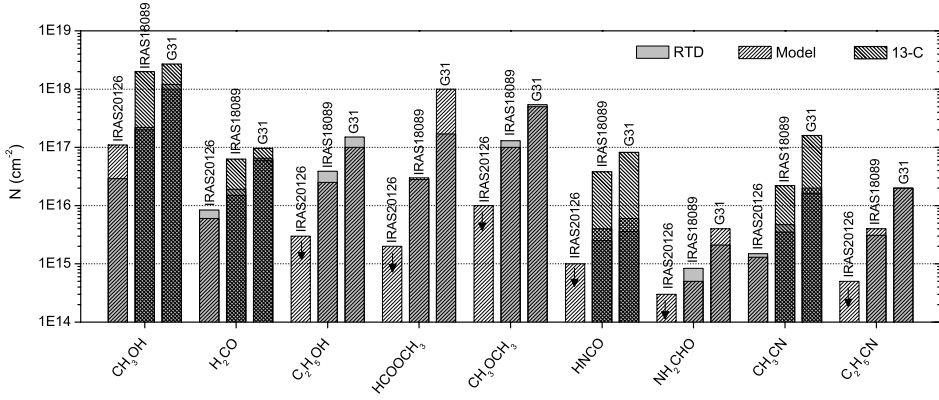


Figure 7.4 – Source-averaged column densities for the targeted warm species in $\theta_{T=100\text{ K}}$ volume. Column densities from the RTD analysis are marked in grey bars. The striped bars show column densities from the Weeds or CASSIS (CH₃OH) models and from ¹³C-isotopologue. Arrows indicate upper limits.

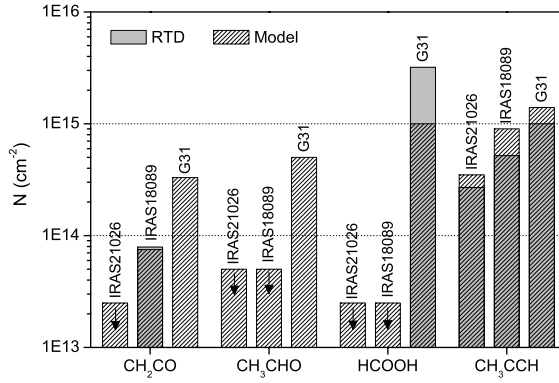


Figure 7.5 – Beam-averaged column densities for the targeted cold species. Column densities from the RTD analysis are marked in grey bars while the striped bars show column densities from the Weeds model. Arrows indicate upper limits.

the best model parameters obtained from the fitting. The warm components are fixed to $\theta_{T=100K}$ while the cold component is allowed to extend beyond the beam diameter. The warm CH_3OH column densities derived from the CASSIS fit are in agreement with the values derived from the RTD analysis. The best fits plotted onto the CH_3OH $7_K - 6_K$ transitions (338.5 GHz) are shown in Fig. 7.6.

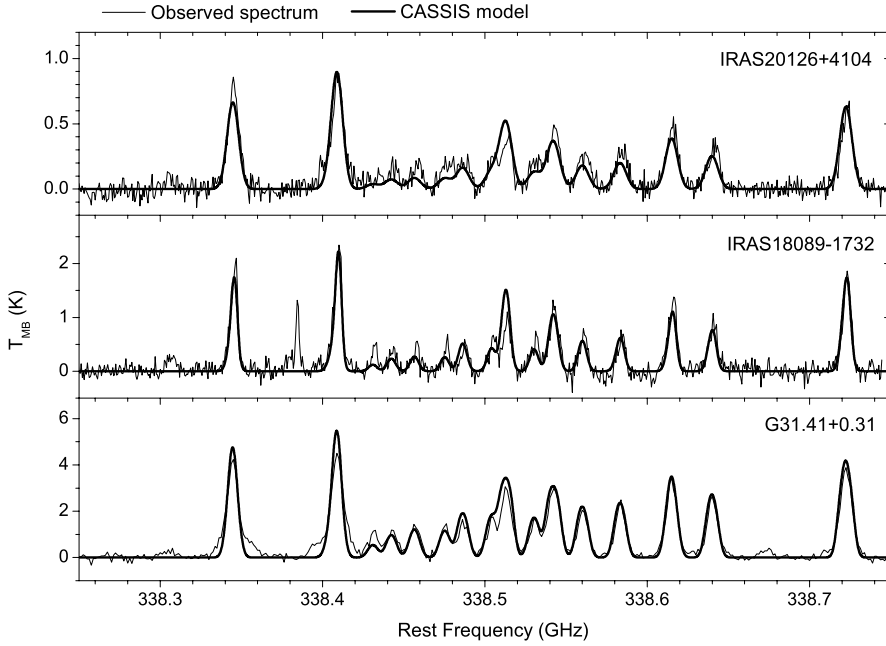


Figure 7.6 – CASSIS two-component model for CH_3OH emission in the observed sources.

Several $^{13}\text{CH}_3\text{OH}$ lines are detected in G31. However, only low- E_{up} lines are reliably detected since the high- E_{up} lines are very weak or blended. Assigning these lines to the cold component and assuming $T_{\text{rot}}=20$ K (Öberg et al. 2011b, Requena-Torres et al. 2008), the beam-averaged $^{13}\text{CH}_3\text{OH}$ column density is $2.1 \times 10^{15} \text{ cm}^{-2}$, corresponding to a CH_3OH column density of $1.7 \times 10^{17} \text{ cm}^{-2}$ for the $14''$ volume. This is more than an order of magnitude higher than found in the Weeds model for the cold component, supporting the optically thick interpretation of the cold component. Similarly, for the case of IRAS18089, the detected $^{13}\text{CH}_3\text{OH}$ lines may indicate a high optical depth.

As mentioned before, the $^{13}\text{CH}_3\text{OH}$ line with $E_{\text{up}} = 211$ K, covered in additional observations for G31, reveals optical thickness in the warm component as well. The CH_3OH column density derived from this line assuming temperature of 300 K is $2.7 \times 10^{18} \text{ cm}^{-2}$ and the CASSIS fit as well as the RTD analysis underestimate the warm column density by a factor of ~ 2.5 . In principle, the CASSIS analysis could be made consistent with the $^{13}\text{CH}_3\text{OH}$ value by letting the warm source size vary as well. However, since such information is not known for other molecules, as well as for consistency with BIS07, we have chosen to keep the warm source size fixed at the 100 K radius.

Table 7.6 – Column densities for the targeted species from the RTD analysis, Weeds or CASSIS (CH_3OH) models and those derived from ^{13}C -isotopologues. Column densities for the hot molecules are source-averaged, while those for cold molecules are beam-averaged. Column densities where optical depth has a significant effect are labeled as lower limits.

Species	IRAS20126+4104				IRAS18089-1732				G31.41+0.31			
	RTD	Model	70N(^{13}C)	RTD	Model	54N(^{13}C)	RTD	Model	RTD	Model	41N(^{13}C)	
H_2CO^a	8.4E+15	6.0E+15	<4.7E+16	1.9E+16	1.5E+16	6.3E+16	6.5E+16	6.0E+16	6.5E+16	6.0E+16	9.6E+16	
CH_3OH	2.9E+16	1.1E+17	<4.0E+17 ^b	2.2E+17	2.0E+17	2.0E+18 ^b	1.2E+18	1.0E+18	1.2E+18	1.0E+18	2.7E+18 ^c	
$\text{C}_2\text{H}_5\text{OH}$	–	<0.3E+16	–	3.9E+16	2.5E+16	–	1.5E+17	1.0E+17	1.5E+17	1.0E+17	–	
HNCO	–	1.0E+15	<7.0E+15	2.5E+15	0.4E+16	<3.8E+16	3.6E+15	0.6E+16	3.6E+15	0.6E+16	<8.2E+16	
NH_2CHO	–	0.3E+15	–	8.4E+14	0.5E+15	–	2.1E+15	0.4E+16	2.1E+15	0.4E+16	–	
CH_3CN	1.5E+15	1.3E+15	<1.4E+15	>4.7E+15	>3.5E+15	2.2E+16	>1.6E+16	>2.0E+16	>1.6E+16	>2.0E+16	1.6E+17	
$\text{C}_2\text{H}_5\text{CN}$	–	<0.5E+15	–	3.1E+15	0.4E+16	–	2.0E+16	2.0E+16	2.0E+16	2.0E+16	–	
HCOOCH_3	–	<0.2E+16	–	2.8E+16	3.0E+16	–	1.7E+17*	1.0E+18	1.7E+17*	1.0E+18	–	
CH_3OCH_3	–	<0.1E+17	–	1.3E+17	1.0E+17	–	5.4E+17	5.0E+17	5.4E+17	5.0E+17	–	
CH_2CO	–	<2.5E+13	–	7.9E+13	7.5E+13	–	–	3.3E+14	–	3.3E+14	–	
CH_3CHO	–	<0.5E+14	–	–	<0.5E+14	–	–	5.0E+14	–	5.0E+14	–	
HCOOH	–	<2.5E+13	–	–	<2.5E+13	–	3.2E+15	1.0E+15	3.2E+15	1.0E+15	–	
CH_3CCH	2.7E+14	3.5E+14	–	5.2E+14	0.9E+15	–	1.0E+15	1.4E+15	1.0E+15	1.4E+15	–	

* Rotation diagram fit on HCOOCH_3 on all lines, while Weeds model on the 230 GHz lines only.

^a Column density from ^{13}C -isotopologue from ortho- H_2^{13}CO , corrected using the statistical ortho to para ratio of 3:1.

^b Calculated from the line intensity of transition $2_{2,0,+0}-3_{1,3,+0}$ at 345.084 GHz with $E_{\text{up}}=44.6$ K, assuming a T_{rot} of 300 K.

^c Calculated from the line intensity of transition $13_{1,12,-0}-13_{0,13,+0}$ at 341.132 GHz with $E_{\text{up}}=206$ K, assuming a T_{rot} of 300 K.

In summary, it seems plausible that at least in our sources, methanol emission arises from two temperature components, a warm ($T_{\text{ex}} \approx 300$ K) compact component and a cold ($T_{\text{ex}} \approx 20$ K) slightly more extended component. At least for G31, the CH_3OH emission is optically thick in both components.

7.4.4.2 Other molecules

Overall, the column densities of the various species follow the same pattern in all sources, and hence seem to be well correlated relative to each other. CH_3OH is the most abundant complex molecule in all sources. The other species have in general half to one order of magnitude lower column densities.

The CH_3CN emission is optically thick for G31 and IRAS18089. Column densities from the RTD analysis are therefore underestimated. Due to a lack of sufficient optically thin lines, also the Weeds analysis underestimates the column densities. Values derived from the ^{13}C -isotopologues are thus more reliable, even though some fraction may arise from a colder component. Indeed, the column density for CH_3CN derived from the 13-isotopologue is an order of magnitude larger than that from the RTD of the main isotopologue alone. The same procedure was used by BIS07.

For H_2CO , the best estimates come from the RTD analysis on the optically thin para- H_2CO lines. The derived H_2CO column densities assuming T_{rot} from Table 7.5 and a statistical ortho-to-para ratio of 3 are given in Table 7.6. The column densities derived from the ^{13}C -isotopologue of ortho- H_2CO are still larger than from RTD analysis using optically thin lines, which indicates either larger ortho-to-para ratio in these sources (ratio of ~ 3 to 5 has been predicted for cold clouds by Kahane et al. 1984) or non LTE excitation. BIS07 derived the H_2CO column densities from the ^{13}C -isotopologue.

The column density derived for HCOOCH_3 from the RTD diagram is significantly smaller than that derived from the Weeds model. The HCOOCH_3 emission is stronger in the 230 GHz beam (20-21'') than in the 345 GHz beam (14'') probably indicating significant extended emission. The RTD analysis was performed on the entire dataset, while only lines in the 230 GHz band was used in the Weeds modeling.

7.5 Discussion

7.5.1 Comparison to massive YSOs without a disk structure

In order to see the effect of a flattened circumstellar structure on the chemistry around the YSO, we compare the temperatures and abundances of the complex organic molecules in sources studied in this work and those studied in BIS07. In addition to our sources (IRAS20126, IRAS18089 and G31), AFGL 2591 and NGC 7538 IRS1 from the BIS07 sample are now known to have disk structures as well (van der Tak et al. 2006, Wang et al. 2012, Pestalozzi et al. 2004, 2009, Knez et al. 2009). A disk-like structure may be present also for other sources but current evidence is not as strong as for the above sources. For the comparison with the BIS07 sample, we use the results primarily from the RTD method to exclude method based differences.

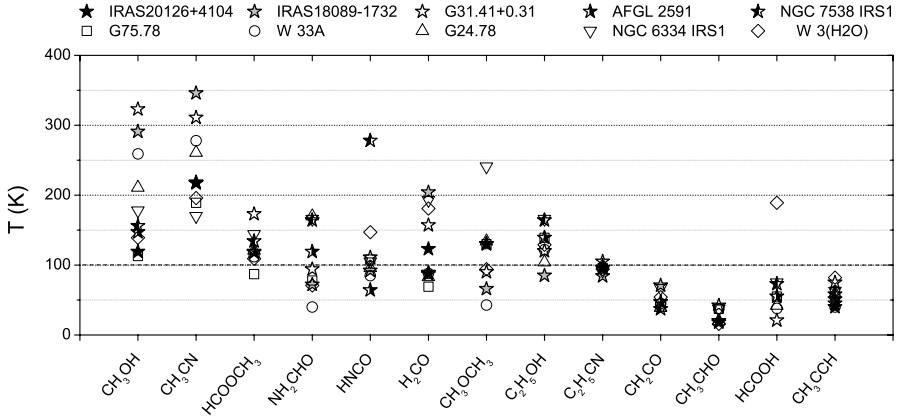


Figure 7.7 – Rotation temperatures for selected species in massive YSOs with (stars) and without observed disk structure.

7.5.1.1 Rotation temperatures

Figure 7.7 shows the rotation temperatures of the complex species for the observed sources together with those from BIS07. As in BIS07, we find that the complex molecules can be divided into warm and cold species based on their rotation temperatures. The rotation temperatures obtained for the molecules in our sources agree with the division; CH_3OH , H_2CO , $\text{C}_2\text{H}_5\text{OH}$, HCOOCH_3 , CH_3OCH_3 , HNCO , NH_2CHO , CH_3CN and $\text{C}_2\text{H}_5\text{CN}$ show rotation temperatures generally ≥ 100 K while CH_2CO , CH_3CHO , HCOOH and CH_3CCH have rotation temperatures < 100 K.

The rotation temperatures of the cold molecules show a very small scatter (± 25 K) from source to source, with or without a disk structure, ignoring the one outlier for HCOOH . Of the warm species, $\text{C}_2\text{H}_5\text{OH}$ has a consistent rotation temperature of 100–150 K from source to source. The RTD analysis for these species is reliable due to low optical depths and lack of anomalous excitation.

The other warm species show more scatter in the derived rotation temperatures. This is particularly the case for CH_3OH and CH_3CN , which have rotation temperatures ranging from 100 to 350 K. No systematic difference is seen between the two source types. Moreover, the HCOOCH_3 rotation temperatures for AFGL 2591 and NGC 7538 IRS1 are similar to the diskless sources, disproving any difference between the two source types. The scatter in the rotation temperatures could indicate that they exist in environments with different temperatures, but it may also be caused by optical depth effects (H_2CO , HNCO , CH_3OH and CH_3CN) and (anomalous) radiative excitation. The latter has been previously seen for, e.g., NH_2CHO and HCOOCH_3 (Nummelin et al. 2000) as well as HNCO (Churchwell et al. 1986). For species with significant radiative excitation, e.g., HCOOCH_3 , the scatter of the data points in the RTD plots is higher and results in additional uncertainty since the linear fits do not properly capture this scatter.

7.5.1.2 Column densities

Figures 7.8 and 7.9 show the column densities for the targeted species in our sources and those from BIS07 for warm and cold molecules, respectively. For the warm species the column densities within the sources vary by 1-2 orders of magnitude. There is also a significant variation between sources. G31 is chemically richest of the sources, with highest column densities of all the targeted species, compared to other sources. IRAS20126 is among the chemically poorest sources. The pattern of column densities is remarkably similar, however, and the disk sources do not stand out.

7.5.1.3 Abundance ratios

Table 7.7 gives the abundance ratios for the targeted species with respect to CH_3OH for oxygen-bearing species and HNCO for nitrogen-bearing species. Column densities from the RTD analysis are primarily used. In cases where column densities are not available from the RTD analysis (mainly for IRAS20126) the values are taken from the Weeds analysis.

The resulting abundance ratios are presented in Fig. 7.10. Values from the RTD method are shown in black bars and can thus be directly compared to BIS07, whereas those from the Weeds model and ^{13}C -isotopologue are in red and blue bars. In general, the abundance ratios in different sources have larger variations within the source types than between them. For example, H_2CO has both lowest and highest abundance ratio for two disk candidates, G31 and IRAS20126, respectively. The H_2CO results depend somewhat on the analysis method used.

$\text{C}_2\text{H}_5\text{OH}$, HCOOCH_3 and CH_3OCH_3 abundances peak for G31 and IRAS18089, and are generally lower for other sources. CH_3OCH_3 also peaks for some diskless sources. The N-bearing species NH_2CHO has a large variation in the abundance ratio with respect to HNCO . Among our sources, NH_2CHO peaks for G31, the source with largest abundance of O-bearing species, and the least clear disk structure.

Fig. 7.11 shows the abundance ratios of N-bearing species with respect to CH_3OH . Again, a lot of variation is seen within each source type, with no specific trend found for sources with a disk-like structure.

We stress that the absolute inferred column densities and abundance ratios are uncertain by a factor of a few up to an order of magnitude, as already indicated by the different analysis techniques. An independent assessment of the accuracy of the results can be made by comparison with the inferred column densities and abundances of Zernickel et al. (2012) for NGC 6334 I (=NGC 6334 IRS), who observed a completely different set of lines of the same molecules with *Herschel*-HIFI and the SMA in beams ranging from 2–40''. Comparison with the results of BIS07 shows good agreement within a factor of a few for the abundances of several species (CH_3OH , CH_3OCH_3 , CH_3OCHO , $\text{C}_2\text{H}_5\text{OH}$, $\text{C}_2\text{H}_5\text{CN}$) whereas others differ by an order of magnitude (H_2CO , CH_3CN). The species that show the largest discrepancy are those with highly optically thick lines and without a large set of isotopologue lines. Thus, a combination of differences in adopted source sizes and optical depth effects can account for the discrepancies. Because our approach is the same for all sources, the relative values from source to source should be more reliable.

Table 7.7 – Abundance ratios of complex species in the observed sources and those in other chemically rich environments. The abundances are column densities with respect to CH₃OH for oxygen-bearing species and with respect to HNCO for nitrogen-bearing species. The CH₃OH and HNCO column densities are taken from the RTD analysis when available.

Source	H ₂ CO	C ₂ H ₅ OH	NH ₂ CHO	HCOOCH ₃	CH ₃ OCH ₃
Massive protostellar objects with a disk structure					
IRAS20126+4104	0.29 ^p	<0.10	<0.30	<0.34	<0.34
IRAS18089-1732	0.09 ^p	0.18	0.34	0.13	0.60
G31.41+0.31	0.06 ^p	0.12	0.59	0.14	0.46
AFGL 2591 ¹	0.28 ^o	<0.02	<1.00	0.51	<0.16
NGC 7538 IRS1 ¹	0.21 ^o	0.05	0.25	0.12	<0.13
Massive protostellar objects with no detected disk structure					
G75.78 ¹	0.20 ^o	<0.02	0.05	0.06	0.21
W 33A ¹	0.27 ^o	0.02	0.32	0.13	0.14
G24.78 ¹	0.23 ^o	0.03	0.14	0.11	0.43
NGC 6334 IRS1 ¹	0.13 ^o	0.02	0.17	0.12	0.60
W 3(H ₂ O) ¹	0.18 ^o	0.01	0.27	0.05	0.15
Low-mass outflows					
B1-b core ²	1.2	<1.0	–	2.3	<0.8
SMM4-W ³	0.6	<0.4	–	3.5	1.1
L1157 outflow ^{4,5}	–	0.7	–	1.8	–
Low-mass protostars					
SMM1 ³	6.6	<3.4	–	10	5.3
SMM4 ³	2.2	<0.6	–	<1.0	0.8
NGC1333					
IRAS 4A env. ^{6,7,8}	–	–	–	56	<22
IRAS 4B env. ^{6,7,8}	–	–	–	26	<19
IRAS 16293 env. ^{8,9,10}	4	–	–	30	20
Low-mass hot corinos					
IRAS 16293 A ^{11,12}	<0.02	1.4	–	0.6	0.6
IRAS 16293 B ^{11,12}	0.6	–	–	0.8	1.6
NGC1333					
IRAS 2A ^{13,14}	–	–	–	–	2

^p para-H₂CO.

^o ortho-H₂CO.

References. (1) Bisschop et al. (2007); (2) Öberg et al. (2010); (3) Öberg et al. (2011b); (4) Bachiller & Perez Gutierrez (1997); (5) Arce et al. (2008); (6) Maret et al. (2005); (7) Bottinelli et al. (2007); (8) Herbst & van Dishoeck (2009); (9) van Dishoeck et al. (1995); (10) Cazaux et al. (2003); (11) Kuan et al. (2004); (12) Bisschop et al. (2008); (13) Huang et al. (2005); (14) Jørgensen et al. (2005).

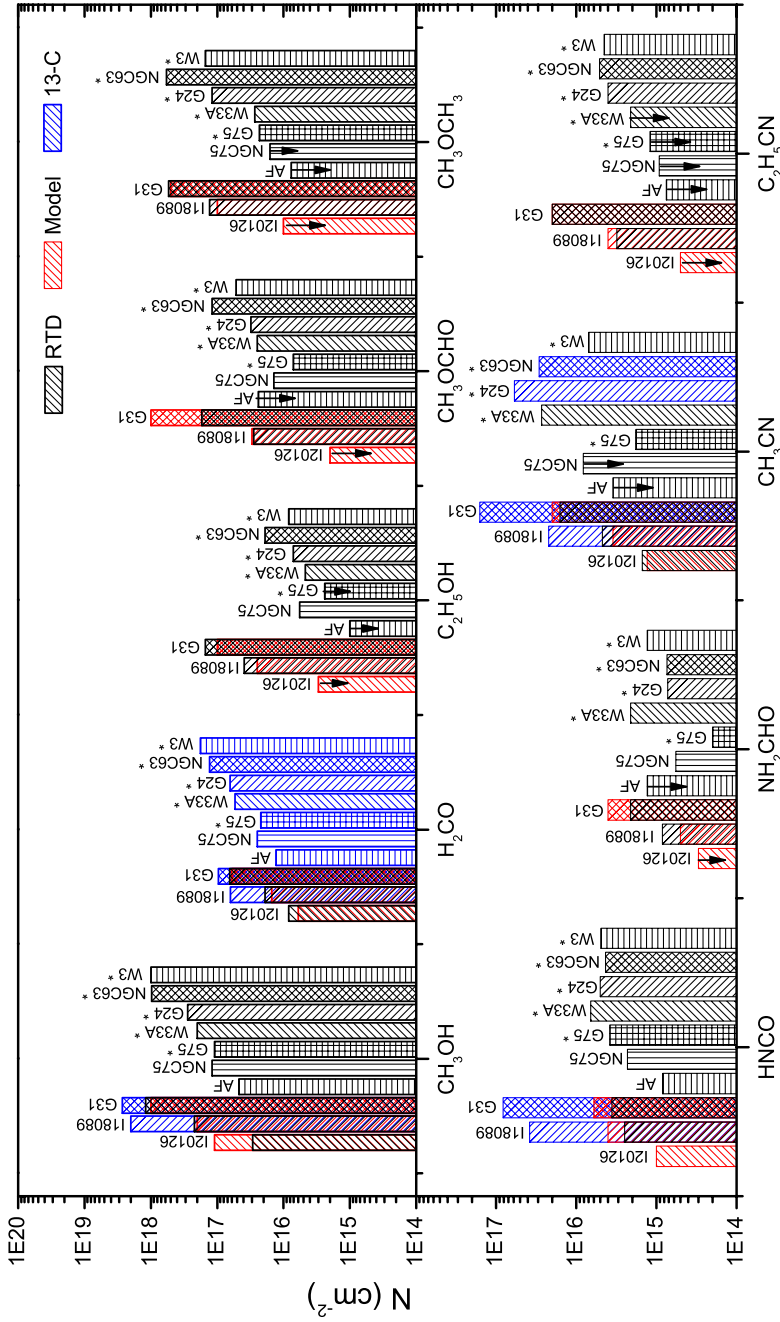


Figure 7.8 – Source-averaged column densities for warm molecules. Column densities from the RTD analysis are marked in black bars. Sources without disk structure are marked with an asterisk. The red and blue bars show column densities from the Weeds or CASSIS (CH_3OH) models and from ^{13}C -isotopologue, respectively. Upper limits are indicated with arrows.

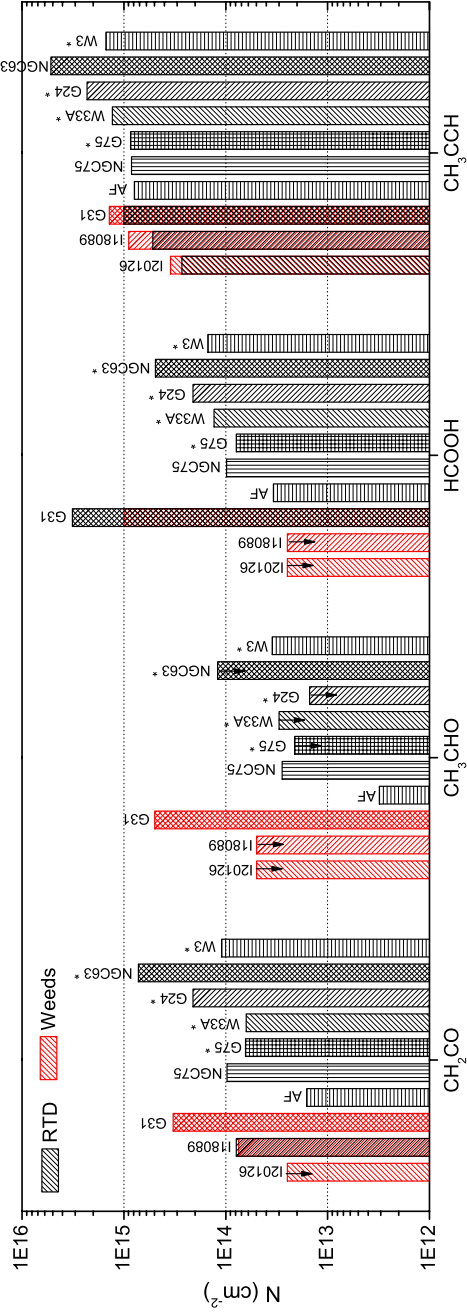


Figure 7.9 – Beam-averaged column densities for cold molecules in sources observed in this study and those from BIS07. Sources without disk structure are marked with an asterisk. Column densities from the RTD analysis are marked in black bars while the red bars show column densities from the Weeds model. Upper limits are indicated with arrows.

7.5.2 Chemical and physical implications

The main goal of this study is to investigate similarities and differences between sources with and without a disk-like structures. The presence of a flattened accretion disk should allow the UV radiation from the central object to escape more readily and then impinge on the gas and dust in the outer walls of a flared disk or outflow cavity (Bruderer et al. 2010). Increased UV radiation could manifest itself as enhancement in the complex organic species produced through UV photodissociation from CH_3OH in the solid state, such as CH_3OCH_3 , $\text{C}_2\text{H}_5\text{OH}$ and CH_3OCHO (Öberg et al. 2009b). In this scenario, CH_3OH is photodissociated into various radicals such as CH_3 , CH_3O and CH_2OH which can become mobile at higher ice temperatures (20–40 K) and form the observed complex organic molecules (Garrod & Herbst 2006). Higher temperatures favor diffusion of larger radicals resulting in the formation of larger complex organic molecules compared with small molecules like H_2CO . Another related parameter that plays a role is the CO content of ices, with H_2CO , CHO - and COOH -containing species enriched in cold, CO-rich CH_3OH ices in which CO has not evaporated. Indeed Öberg et al. (2011b) show that the increased abundance of HCOOCH_3 in low-mass YSOs compared with the high-mass sample of BIS07 may be due to this effect. Although only limited laboratory experiments exist on N-containing molecules, the abundance of N-bearing complex organic molecules could be enhanced due to photodissociation of N_2 or NH_3 .

Our results show that there is no consistent enhancement of complex organic species produced through CH_3OH photochemistry, nor of N-bearing species, that can be attributed to the presence of a flattened disk structure on the scales probed by our data. The variations within source types are larger than between the source types. One explanation for this lack of differentiation could be that all high-mass sources have a source structure through which UV radiation can impact the larger surroundings. In particular, just like low-mass sources, all high-mass YSOs are expected to have outflows and cavities through which UV radiation can escape and affect the chemistry, whether or not they have a large disk-like structure. This scenario can be tested with future high angular resolution data on $<1''$ scale with ALMA which should then reveal the emission from complex molecules coating the walls of the outflow cavities.

An alternative explanation is that enhanced temperature in the YSO environment is not needed for the production of complex organic molecules and that they are already formed in the pre-stellar stage through UV- and cosmic-ray processing of cold ices, using just the internal UV field produced by interaction of cosmic rays with H_2 (Prasad & Tarafdar 1983) rather than that of the star. This scenario has gained support over the last few years with the detection of HCOOCH_3 and CH_3OCH_3 in cold low-mass cores away from the YSO where the molecules are either released by shocks (Arce et al. 2008, Öberg et al. 2010) or by photodesorption (Bacmann et al. 2012) although the precise formation mechanisms are still unclear. Gas-phase processes may also contribute in some cases. Again, high spatial resolution and sensitivity such as ALMA will be key to testing this scenario.

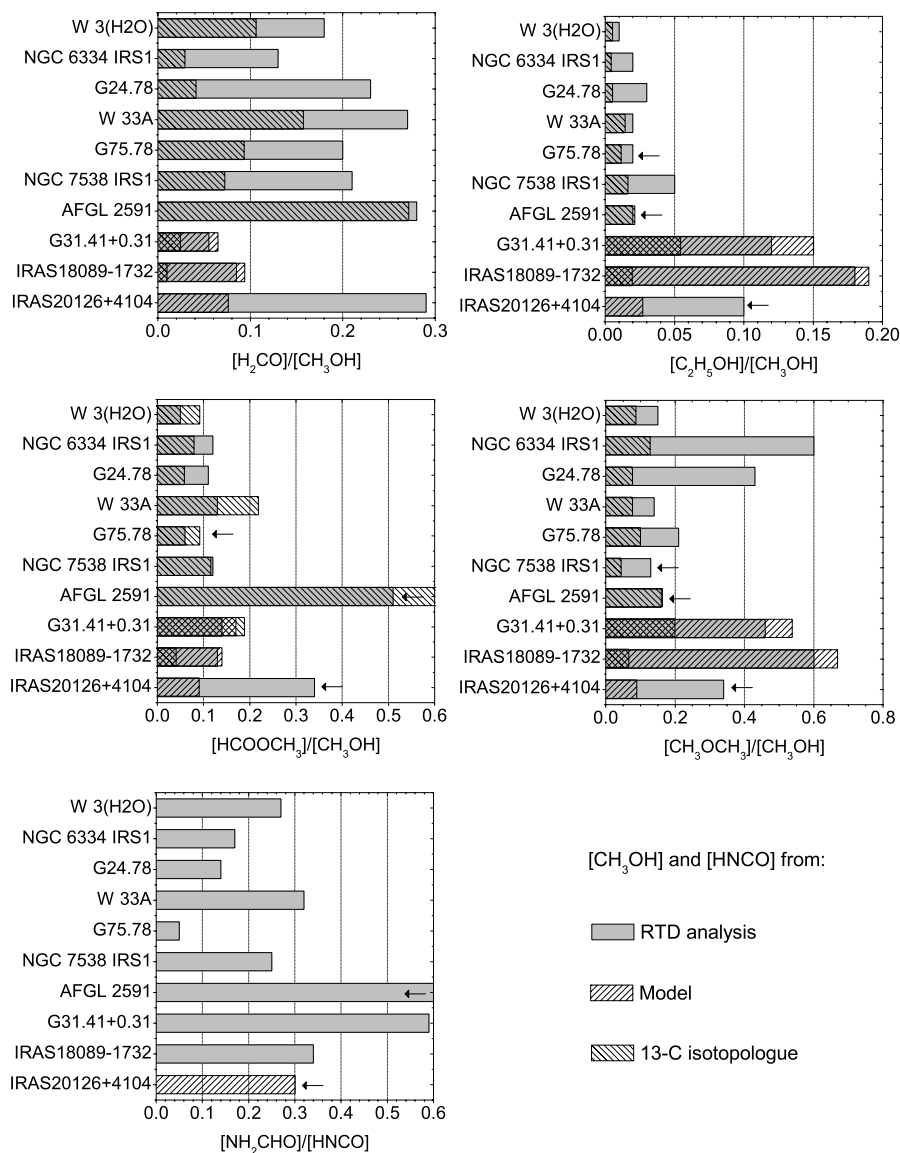


Figure 7.10 – Abundance ratios of complex species with respect to CH_3OH for oxygen-bearing species and HNCO for nitrogen-bearing species. The grey bars indicate abundance ratios calculated with the CH_3OH and HNCO column density derived from the RTD analysis similar to BIS07. The striped bars indicate abundance ratios where CH_3OH and HNCO column densities are derived from CASSIS or Weeds (HNCO) model. Upper limits are marked with arrows.

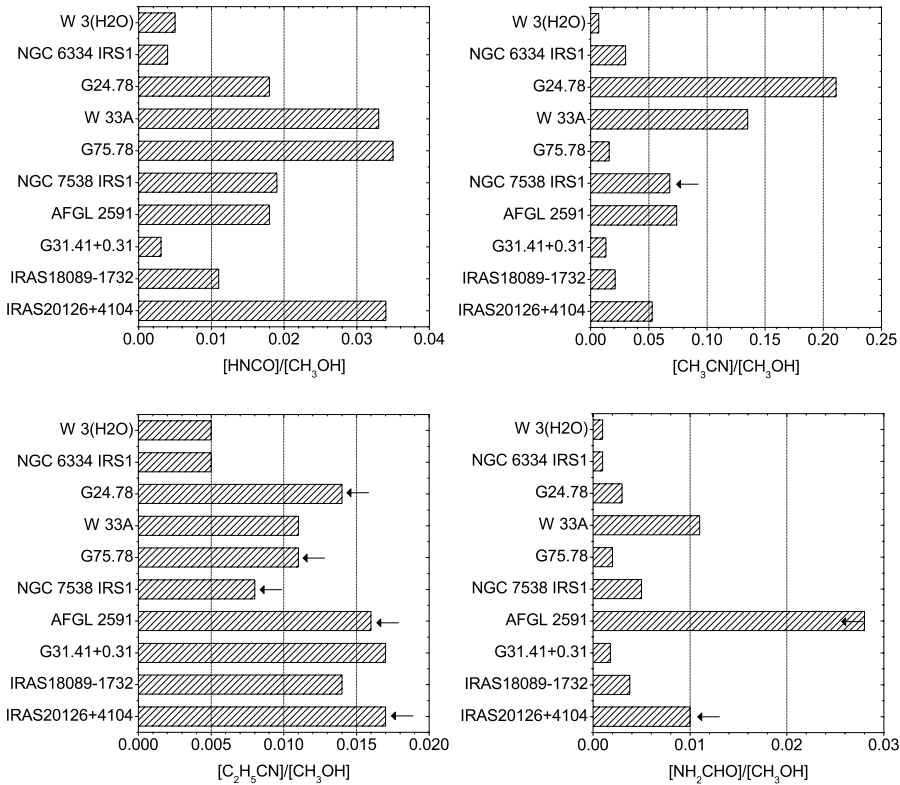


Figure 7.11 – Abundance ratios of N-bearing species HNCO, CH_3CN , $\text{C}_2\text{H}_5\text{CN}$ and NH_2CHO with respect to CH_3OH (from RTD analysis). Arrows indicate upper limits.

7.6 Summary and conclusions

We have carried out a partial submillimeter line-survey, targeting several complex organic species toward selected massive YSOs with strong evidence for a circumstellar accretion disks, IRAS 20126+4104, IRAS18089-1732 and G31.41+0.31. This is the first time that molecular abundances are reported for these well-known sources. The analysis is performed using both the rotation diagram method as well as spectral modeling. The inferred rotation temperatures and molecular abundances are compared to sources without reported disk structures analysed using the same techniques. The molecules can be divided into two different groups based on their rotation temperatures, independent of source type. In particular, the cold (<100 K) species have remarkably constant rotation temperatures from source to source. The warm (>100 K) species exhibit more scatter possibly due to optical depth effects, non-LTE conditions and radiative excitation. The column densities peak for the same sources, with G31.41+0.31 being chemically the most rich of the studied sources.

The relative abundances of species follow the same pattern, and no chemical differentiation could be established between the two source types within the (considerable) uncertainties. The lack of

chemical differentiation between massive YSOs with and without observed disk-like structure suggests similarity in the physical conditions and level of UV exposure for all sources, for example through outflow cavities. Alternatively, the complex molecules may already be formed in the cold pre-stellar stage under similar conditions. Ultimately and indirectly, these results imply that the mechanism of the formation of massive stars does not differ significantly from source to source. Future high angular and high sensitivity observations of optically thin lines will be key to distinguishing the different scenarios and derive accurate abundance ratios that can be directly compared with chemical models.

7.7 Appendix

7.7.1 Detected lines per species for all sources

The line assignment and detection is based on Gaussian fitting with the following criteria: (i) the fitted line position has to be within ± 1 MHz of the catalog frequency, (ii) the FWHM is consistent with the those given in table 7.1 and (iii) the peak intensity has at least a $S/N = 3$. The errors on the integrated intensities are computed as follows.

The integrated main beam temperatures, $\int T_{\text{MB}} dV$, were obtained by Gaussian fits to the lines (Eq. 7.12).

$$\int T_{\text{MB}} dV = c^{st} T_0 \Delta V \quad (7.12)$$

with

$$c^{st} = \frac{\sqrt{\pi/\ln 2}}{2}$$

where T_0 is the peak intensity and ΔV is the FWHM of the line. The error, $d \int T_{\text{MB}} dV$, is calculated from Eq. 7.13.

$$d \int T_{\text{MB}} dV = c^{st} [\Delta V d(T_0) + T_0 d(\Delta V)] \quad (7.13)$$

with

$$d(T_0) = \sqrt{\text{rms}^2 + (\text{cal} \times T_0)^2 + \sigma_{T_0}^2}$$

and

$$d(\Delta V) = \sigma_{\Delta V}$$

where rms is the root mean square amplitude of the noise in the spectral bin $\delta\nu$, cal is the calibration uncertainty of the telescope, and σ 's are the statistical errors on T_0 and ΔV from the Gaussian fits.

The errors on the integrated intensities derived from Eq. 7.13 include all statistical errors from the Gaussian fit.

$$d \int T_{\text{MB}} dV = c^{st} \Delta V \sqrt{\text{rms}^2 + (\text{cal} \times T_0)^2} \quad (7.14)$$

For undetected transitions the upper limits were determined as 3σ limits (Eq. 7.15) using:

$$\sigma = 1.2 \sqrt{\delta v \Delta V_{\text{rms}}}, \quad (7.15)$$

where 1.2 is the coefficient related to the calibration uncertainty of 20 %.

CLASS was used to determine the Gaussian fits and the uncertainties in the individual parameters. The formal errors on the integrated intensities derived from Eq. 7.14 in some cases yield a $S/N < 2.5$. This is caused by: (i) a conservative estimate of the statistical error on the FWHM parameter in the Gaussian fitter of CLASS; (ii) all statistical errors are included into our error calculation. Considering the higher S/N on the peak intensity, a more traditional error estimate without the statistical errors from the Gaussian fit (Eq. 7.14) would result in a $S/N > 3$ for the integrated intensity as well. All weak line fits were confirmed by visual inspection.

Table 7.8 – Observed line fluxes $\int T_{\text{MB}} dV$ (K km s⁻¹) for H₂CO and its isotopic species.

Frequency [GHz]	Transition	E_{up} [K]	A [s ⁻¹]	Sources	
H ₂ CO					
218.222 <i>P</i>	3 _{0,3} – 2 _{0,2}	21	2.8(-4)	2.82 (0.65)	–
218.476 <i>P</i>	3 _{2,2} – 2 _{2,1}	68	1.6(-4)	–	>7.14 (1.71)
363.946 <i>P</i>	5 _{2,4} – 4 _{2,3}	100	1.2(-3)	4.65 (1.08)	4.15 (1.03)
364.103 <i>P</i>	5 _{4,1/2} – 4 _{4,0/1}	241	5.0(-4)	1.90 (0.58)	9.92 (2.15)
364.275 <i>o</i>	5 _{3,3} – 4 _{3,2}	143/158	8.9(-4)	>5.08 (1.50)	4.25 (1.07)
364.289 <i>o</i>	5 _{3,2} – 4 _{3,1}	143/158	8.9(-4)	>5.78 (1.71)	>12.62 (3.34)
H ₂ ¹³ CO					
219.909 <i>o</i>	3 _{1,2} – 2 _{1,1}	33	2.6(-4)	<0.34	>20.46 (4.85)
The notation <i>a</i> (– <i>b</i>) stands for $a \times 10^{-b}$					
> means lower limit (optically thick line)					
– means frequency not observed					
<i>P</i> para-H ₂ CO					
<i>o</i> ortho-H ₂ CO					

Table 7.9 – Observed line fluxes $\int T_{\text{MB}} dV$ (K km s⁻¹) for CH₃OH and its isotopic species.

Frequency [GHz]	Transition	E_{up} [K]	A [s ⁻¹]	Sources	
CH ₃ OH					
218.440	4 _{2,0} – 3 _{1,0}	45	6.9(-5)	–	10.10 (2.22)::
219.984	2 _{5,0} – 2 _{4,0}	802	3.0(-5)	<1.33	<0.45 (0.24);
219.994	2 _{3,0} – 2 _{2,0}	776	2.6(-5)	<1.33	<1.74 (0.56);
240.739	2 _{6,1} – 2 _{5,0}	864	1.1(-4)	<0.20	<0.78 (0.47);
240.818	5 _{1,2} – 4 _{1,2}	834	8.5(-5)	<0.20	<3.58 (0.88);
240.861	5 _{4,2} – 4 _{4,2}	779	3.2(-5)	<0.20	<0.81 (0.37);

Continued on next page

Table 7.9 – continued from previous page

Frequency [GHz]	Transition	E_{up} [K]	A [s ⁻¹]	Sources	IRAS18089-1732	G31.41+0.31
240.870	$5_{0,2} - 4_{0,2}$	769	8.9(-5)	<0.20	<0.90 (0.71);	<3.26 (1.06);
240.916	$5_{3,-2/+2} - 4_{3,-2/+2}$	693	5.7(-5)	<0.20	<1.17 (0.46);	1.43 (0.45)
240.932	$5_{4,-2/+2} - 4_{4,-2/+2}$	649	3.2(-5)	<0.20	<0.57 (0.20)	~0.42 (0.21)
240.937	$5_{-2,2} - 4_{-2,2}$	680	7.4(-5)	<0.20	<1.03 (0.69);	~0.49 (0.24)
240.939	$5_{0,+2} - 4_{0,+2}$	543	1.2(-4)	<0.20	<1.03 (0.69);	2.54 (0.86)
240.948	$5_{3,2} - 4_{3,2}$	656	5.6(-5)	<0.20	~0.24 (0.12)*	~0.74 (0.30)*
240.952	$5_{2,2} - 4_{2,2}$	621	7.5(-5)	<0.20	~0.24 (0.12)*	~0.74 (0.30)*
240.959	$5_{-1,2} - 4_{-1,2}$	567	8.5(-5)	<0.20	1.18 (0.42);	1.74 (0.61);
240.961	$5_{1,+1} - 4_{1,+1}$	360	8.5(-5)	<0.20	1.18 (0.42);	1.74 (0.61);
241.043	$22_{-6,0} - 23_{-5,0}$	776	3.4(-5)	–	~0.35 (0.48)	<0.38 (0.54);
330.794	$8_{-3,0} - 9_{-2,0}$	146	8.0(-5)	~0.28 (0.57)	3.23 (1.12)	8.06 (2.43)
331.220	$16_{-1,0} - 15_{-2,0}$	321	7.8(-5)	<0.39 ^c	2.66 (0.79)	>3.19 (0.91) ^b
338.124	$7_{0,0} - 6_{0,0}$	78	2.5(-4)	–	–	30.57 (11.11)::
338.345	$7_{-1,0} - 6_{-1,0}$	70	2.5(-4)	7.29 (2.05)::	10.34 (2.58)::	38.03 (9.06)::
338.405	$7_{6,0} - 6_{6,0}$	244	6.7(-5)	<8.90 (2.54);	<12.95 (3.14);	<44.10 (10.87);
338.409	$7_{0,+0} - 6_{0,+0}$	65	2.5(-4)	8.90 (2.54)::	12.95 (3.14)::	44.10 (10.87)::
338.431	$7_{-6,0} - 6_{-6,0}$	254	6.7(-5)	~0.72 (0.14)	~2.23 (1.06)	8.49 (2.90)
338.442	$7_{6,-0/+0} - 6_{6,-0/+0}$	259	6.7(-5)	~1.20 (0.79);	~2.29 (1.27)	8.80 (3.44)
338.457	$7_{-5,0} - 6_{-5,0}$	189	1.2(-4)	1.80 (0.66);	~2.55 (1.44)	10.12 (3.74)
338.475	$7_{5,0} - 6_{5,0}$	201	1.2(-4)	~1.43 (0.94);	~1.89 (1.21)	9.22 (3.46)
338.486	$7_{5,-0/+0} - 6_{5,-0/+0}$	203	1.2(-4)	~2.86 (0.94);	>3.40 (3.00)	>13.31 (5.28)
338.504	$7_{-4,0} - 6_{-4,0}$	153	1.7(-4)	~1.78 (0.85)	~3.39 (1.88)	>12.14 (4.99)
338.5126	$7_{4/4,-0/+0} - 6_{4/4,-0/+0}$	145	1.7(-4)	>2.61 (0.94);	>5.87 (1.81);	>26.88 (9.59);
338.5129	$7_{2,-0} - 6_{2,-0}$	103	2.3(-4)	>2.61 (0.94);	>5.87 (1.81);	>26.88 (9.59);
338.530	$7_{4,0} - 6_{4,0}$	161	1.7(-4)	~1.34 (0.59)	~3.69 (2.22)	11.33 (4.40)
338.541	$7_{3,+0/-0} - 6_{3,+0/-0}$	115	2.1(-4)	>3.75 (1.24)	>8.71 (2.71)	>29.00 (8.01)
338.560	$7_{-3,0} - 6_{-3,0}$	128	2.1(-4)	~2.14 (0.95)	>4.50 (1.87)	14.94 (4.70)
338.583	$7_{3,0} - 6_{3,0}$	113	2.1(-4)	2.74 (1.17)	>4.02 (1.61)	18.35 (5.14)

Continued on next page

Table 7.9 – continued from previous page

Frequency [GHz]	Transition	E_{up} [K]	A [s ⁻¹]	Sources	IRAS20126+4104	IRAS18089-1732	G31.41+0.31
338.615	7 _{1,0} – 6 _{1,0}	86	2.5(-4)	4.48 (1.33)::	9.01 (2.57)::	28.49 (6.87)::	28.49 (6.87)::
338.640	7 _{2,+0} – 6 _{2,+0}	103	2.3(-4)	>2.99 (1.07)	>6.46 (2.36)	21.12 (5.79)	21.12 (5.79)
338.722	7 _{2,0} – 6 _{2,0}	87	2.3(-4)	2.60 (0.70)::	5.24 (1.36)::	17.99 (8.33)::	17.99 (8.33)::
338.723	7 _{-2,0} – 6 _{-2,0}	91	2.3(-4)	2.60 (0.70)::	5.24 (1.36)::	17.99 (8.33)::	17.99 (8.33)::
340.141	2 _{2,+0} – 3 _{1,+0}	45	4.1(-5)	1.56 (0.71)::	3.31 (1.04)::	12.35 (2.83)::	12.35 (2.83)::
342.730 ^a	13 _{1,12,-0} – 13 _{0,13,+0}	147	2.4(-5)	–	–	14.19 (3.54)	14.19 (3.54)
344.971	12 _{7,1} – 11 _{6,1}	762	1.3(-4)	<0.12	–	~2.27 (1.07)	~2.27 (1.07)
364.159	9 _{3,1} – 9 _{2,1}	522	6.5(-5)	~0.20 (0.41)	2.97 (1.10):	2.66 (0.77)	2.66 (0.77)
¹³ CH ₃ OH							
222.468	21 _{1,20,0} – 21 _{0,21,0}	544	3.6(-5)	<0.23	<0.32	<0.59	<0.59
225.404	16 _{2,14,0} – 15 _{3,12,0}	331	2.0(-5)	<0.19	<0.45 (0.35):	<3.49 (1.55):	<3.49 (1.55):
338.760	13 _{0,13,+0} – 12 _{1,12,+0}	206	2.2(-4)	<0.20	<0.39	~5.55 (2.36)	~5.55 (2.36)
341.132 ^a	13 _{1,12,-0} – 13 _{0,13,+0}	211	2.4(-5)	–	–	3.55 (2.22)	3.55 (2.22)
345.084	2 _{2,0,+0} – 3 _{1,3,+0}	45	2.9(-5)	<0.29	<0.24	<1.69 (0.77):	<1.69 (0.77):
345.133	4 _{0,4,0} – 3 _{-1,3,0}	36	8.2(-5)	<0.29	1.81 (0.70)	4.06 (1.25)	4.06 (1.25)
354.446	4 _{1,3,0} – 3 _{0,3,0}	44	1.3(-4)	<0.18	1.68 (0.65)	6.32 (1.59)	6.32 (1.59)
363.924	14 _{3,12,1} – 14 _{2,13,1}	655	4.7(-5)	<0.24	<2.06 (0.94):	<1.40 (0.92):	<1.40 (0.92):

The notation $a(-b)$ stands for $a \times 10^{-b}$ ^a from additional observations on G31 only^b line close to the edge of the frequency band^c used to constrain the RTD fit

> means lower limit (optically thick line)

< means upper limit

– means frequency not observed

: means blended frequency

:: cold ($E_{\text{up}} < 100$ K) CH₃OH line (treated as a blend with cold component)

* calculated flux (see Eq. 7.4)

Table 7.10 – Observed line fluxes $\int T_{\text{MB}} dV$ (K km s^{-1}) for $\text{C}_2\text{H}_5\text{OH}$ and its isotopic species.

Frequency [GHz]	Transition	E_{up} [K]	A [s^{-1}]	Sources	IRAS18089-1732	G31.41+0.31
$\text{C}_2\text{H}_5\text{OH}$						
218.461	$5_{3,2,2} - 4_{2,3,2}$	24	6.6(-5)	–	–	<2.60 (0.52); ~0.77 (0.65)
218.554	$21_{5,16,2} - 21_{4,17,2}$	226	6.2(-5)	–	–	<1.29 (0.26); ~0.26 (0.24)
222.217	$20_{5,15,2} - 20_{4,16,2}$	208	6.5(-5)	<0.22	~0.56 (0.59)	~0.66 (0.42)
222.419	$20_{4,17,1} - 19_{5,15,0}$	256	1.1(-5)	<0.22	<0.34 (0.30); ~0.40 (0.42)	~0.74 (0.42)
222.519	$26_{4,23,2} - 26_{3,24,2}$	316	6.7(-5)	<0.22	<0.27	<0.55 (0.43); ~1.16 (1.12)
225.105	$13_{10,3/4,0} - 12_{10,2/3,0}$	255	4.2(-5)	<0.19	<0.25	~1.86 (0.84)
225.108	$13_{11,2/3,0} - 12_{11,1/2,0}$	280	2.9(-5)	<0.19	<0.25	~1.98 (1.05)
225.110	$13_{6,8/7,1} - 12_{6,7/6,1}$	181	8.0(-5)	<0.19	<0.25	<2.76 (0.55); ~2.34 (0.93)
225.112	$13_{5,5/4,0} - 12_{5,4/3,0}$	231	5.3(-5)	<0.19	<0.25	~1.61 (0.77)*
225.116	$13_{12,1/2,0} - 12_{12,0/1,0}$	308	1.5(-5)	<0.25	<0.25	~1.61 (0.77)*
225.131	$13_{8,5/6,0} - 12_{8,4/5,0}$	211	6.4(-5)	<0.19	<0.25	0.74 (0.32)*
225.171	$13_{7,6/7,0} - 12_{7,5/6,0}$	192	7.3(-5)	<0.19	<0.25	0.74 (0.32)*
225.210	$19_{5,14,2} - 19_{4,15,2}$	191	6.7(-5)	<0.19	<0.25	~0.95 (0.48)
225.229	$17_{2,15,2} - 16_{3,14,2}$	137	2.5(-5)	<0.19	~0.37 (0.24)	<2.28 (0.46); ~4.79 (0.96); ~0.92 (0.18); –
225.249	$13_{6,8/7,0} - 12_{6,7/8,0}$	176	8.1(-5)	<0.19	~0.40 (0.30)	<3.38 (0.68); ~0.85 (0.52)
225.279	$13_{5,9,1} - 12_{5,8,1}$	168	8.7(-5)	<0.19	<0.25	
225.283	$13_{5,8,1} - 12_{5,7,1}$	168	8.7(-5)	<0.19	<0.25	
225.400	$13_{5,9,0} - 12_{5,8,0}$	163	8.7(-5)	<0.19	~0.13 (0.15)	
225.404	$13_{5,8,0} - 12_{5,7,0}$	163	8.7(-5)	<0.19	~0.13 (0.15)	
225.457	$13_{3,11,1} - 12_{3,10,1}$	148	9.7(-5)	<0.19	<0.25	
238.841	$21_{2,19,0} - 21_{1,21,1}$	258	4.8(-5)	–	<0.22	
239.020	$28_{4,25,2} - 27_{5,22,2}$	362	2.9(-5)	<0.21	<0.22	
239.186	$16_{6,16,1} - 15_{1,14,0}$	171	4.4(-5)	<0.21	<0.22	
240.654	$4_{2,2,1} - 3_{1,2,0}$	75	4.1(-5)	–	<0.22	
240.782	$15_{2,13,0} - 14_{1,13,1}$	163	2.9(-5)	<0.2	<0.23	
240.839	$14_{1,13,0} - 13_{0,13,1}$	147	5.1(-5)	<0.20	~0.20 (0.33)	

Continued on next page

Table 7.10 – continued from previous page

Frequency [GHz]	Transition	E_{up} [K]	A [s ⁻¹]	Sources IRAS20126+4104	IRAS18089-1732	G31.41+0.31
330.985	6 _{3,4,1} – 5 _{2,4,0}	90	1.2(-4)	<0.31	–	~1.46 (0.84)
331.027	13 _{5,8,1} – 13 _{4,10,0}	168	1.1(-4)	<0.29	<0.29	<1.84 (0.37);
331.079	43 _{7,37,2} – 43 _{6,38,2}	860	2.2(-4)	<0.29	~0.36 (0.39)	~0.15 (0.22)
331.095	27 _{7,20,2} – 27 _{6,21,2}	380	2.1(-4)	<0.29	<0.29	~0.33 (0.55)
338.088	25 _{1,24,1} – 24 _{2,22,0}	332	5.9(-5)	–	–	~3.64 (1.99)
338.099	18 _{7,11,2} – 18 _{6,12,2}	205	2.1(-4)	–	–	~2.05 (1.54)*
338.110	18 _{7,12,2} – 18 _{6,13,2}	205	2.1(-4)	–	–	~2.05 (1.54)*
338.163	10 _{2,8,1} – 9 _{1,8,0}	113	8.6(-5)	–	–	2.05 (0.98)
338.412	17 _{7,10,2} – 17 _{6,11,2}	190	2.1(-4)	<4.41 (1.31);	<13.78 (3.29);	<21.70 (5.13);
338.417	17 _{7,11,2} – 17 _{6,12,2}	190	2.1(-4)	<4.41 (1.31);	<0.71	<21.70 (5.13);
338.672	16 _{7,9,2} – 16 _{6,10,2}	176	2.0(-4)	<0.32	<0.83	1.63 (0.85)*
338.674	16 _{7,10,2} – 16 _{6,11,2}	176	2.0(-4)	<0.32	<0.83	1.63 (0.85)*
339.979	9 _{4,6,2} – 8 _{3,5,2}	58	2.2(-4)	<0.15	~0.55 (0.47)	3.23 (0.93)
345.174	7 _{7,0/1,0} – 6 _{6,0/1,1}	140	2.5(-4)	<0.26	~1.16 (0.70)	~2.28 (1.56)
345.229	21 _{1,21,0} – 20 _{1,20,0}	242	3.7(-4)	<0.29	~0.58 (0.37)	<5.52 (1.10);
345.295	21 _{1,21,1} – 20 _{1,20,1}	246	3.7(-4)	<0.29	~1.03 (1.00)	~2.91 (1.31)
345.312	22 _{3,19,1} – 21 _{4,17,0}	286	5.0(-5)	<0.29	<0.19	<0.39
345.333	21 _{0,21,0} – 20 _{0,20,0}	242	3.7(-4)	<0.29	<6.54 (1.31);	<17.35 (3.47);
345.408	21 _{0,21,1} – 20 _{0,20,1}	246	3.7(-4)	<0.29	~0.75 (0.47)	~2.47 (1.13)
352.858	21 _{1,20,2} – 20 _{2,19,2}	196	1.2(-4)	<0.18	~0.51 (0.43)	~1.56 (0.78)
353.034	12 _{3,9,2} – 11 _{2,10,2}	77	1.9(-4)	<0.16	~0.61 (0.59)	3.12 (1.00)
354.758	20 _{3,17,1} – 19 _{3,16,1}	249	4.0(-4)	<0.18	~0.59 (0.52)	3.96 (1.05)
363.968	21 _{7,15/14,1} – 20 _{7,14/13,1}	314	3.9(-4)	<0.22	~0.64 (0.44)	2.66 (1.02)
364.001	21 _{8,14/13,0} – 20 _{8,13/12,0}	327	3.7(-4)	<0.22	~0.70 (0.48)	2.28 (0.80)
364.233	21 _{7,15/14,0} – 20 _{7,14/13,0}	309	3.9(-4)	<0.24	~0.64 (0.56)	~1.94 (1.48)

Continued on next page

Table 7.10 – continued from previous page

Frequency [GHz]	Transition	E_{up} [K]	A [s ⁻¹]	Sources
				IRAS20126+4104 IRAS18089-1732 G31.41+0.31

The notation $a(-b)$ stands for $a \times 10^{-b}$

– means frequency not observed

< means upper limit

~ means uncertain detection, $S/N \lesssim 2$

: means blended line

* calculated flux (see Eq. 7.4)

Table 7.11 – Observed line fluxes $\int T_{\text{MB}} dV$ (K km s⁻¹) for HNC and its isotopic species.

Frequency [GHz]	Transition	E_{up} [K]	A [s ⁻¹]	Sources
				IRAS20126+4104 IRAS18089-1732 G31.41+0.31
HNC				
219.657	10 _{3,8} 7/9/11/10 – 9 _{3,7} 6/9/10/8	447	1.4(-4)	<1.33 <0.73 (0.70): <1.52 (0.63):
219.736	10 _{2,9} 8/9/11/10 – 9 _{2,8} 7/9/10/8	231	1.4(-4)	<0.28 <0.84 (0.75): ~0.64 (0.91)
219.798	10 _{0,10} 9/11/10 – 9 _{0,9} 9/10/8	58	1.5(-4)	<0.28 1.31 (0.50) 1.22 (0.55)
240.876	11 _{1,11} 10/12/11 – 10 _{1,10} 10/11/9	113	2.0(-4)	<0.20 <0.82 (0.54) <3.10 (0.93):
330.849	15 _{1,14} 14/16/15 – 14 _{1,13} 14/15/13	170	5.2(-4)	~0.32 (0.31) <1.53 (0.71): 2.01 (0.71)
352.898	16 _{1,15} 15/17/16 – 15 _{1,14} 15/16/14	187	6.3(-4)	<0.18 ~1.84 (1.00) <3.12 (1.02):
HN¹³CO				
219.664	10 _{3,8} 7/10 – 9 _{3,7} 6/10	47	1.4(-4)	<1.32 <0.21 <0.41
219.740	10 _{2,9} 11/9/10 – 9 _{2,8} 10/8/9	31	1.4(-4)	<0.28 <0.24 <0.26
219.744	10 _{2,8} 11/9/10 – 9 _{2,7} 10/8/9	31	1.4(-4)	<0.28 <0.24 <0.26
219.804	10 _{0,10} 10/9/8 – 9 _{0,9} 10/9/8	58	1.5(-4)	<0.28 <0.24 <0.63
240.881	11 _{1,11} 12/11/10 – 10 _{1,10} 11/10/9	113	2.0(-4)	<0.20 <0.23 <0.98
330.860	15 _{1,14} 16/14/15 – 14 _{1,13} 15/13/14	170	5.2(-4)	<0.31 <0.32 <0.31

Continued on next page

Table 7.11 – continued from previous page

Frequency [GHz]	Transition	E_{up} [K]	A [s ⁻¹]	Sources
				IRAS20126+4104 IRAS18089-1732 G31.41+0.31

The notation $a(-b)$ stands for $a \times 10^{-b}$

< means upper limit

~ means uncertain detection, $S/N \lesssim 2$

– means frequency not observed

: means blended line

Table 7.12 – Observed line fluxes $\int T_{\text{MB}} dV$ (K km s⁻¹) for NH₂CHO and its isotopic species.

Frequency [GHz]	Transition	E_{up} [K]	A [s ⁻¹]	Sources
				IRAS20126+4104 IRAS18089-1732 G31.41+0.31
NH ₂ CHO				
218.460	10 _{0,1,9} – 9 _{0,1,8}	61	7.5(-4)	– <2.45 (0.49);
339.716	16 _{6,8,8/9} – 15 _{15,8,7/8}	329	2.2(-3)	<0.17 <4.04 (0.81);
339.781	16 _{6,7,10/9} – 15 _{15,7,9/8}	284	2.3(-3)	~0.29 (0.29) <2.66 (1.20);
339.904	16 _{6,6,11/10} – 15 _{15,6,10/9}	246	2.5(-3)	~0.48 (0.30) ~1.41 (0.76)
340.135	16 _{6,5,12} – 15 _{15,5,11}	213	2.6(-3)	<1.40 (0.28); <1.11 (0.22);
340.139	16 _{6,5,11} – 15 _{15,5,10}	213	2.6(-3)	<1.40 (0.28); <1.11 (0.22);
345.183	17 _{7,0,17} – 16 _{16,0,16}	151	3.0(-3)	1.16 (0.53) 2.42 (0.94)
345.327	16 _{6,1,15} – 15 _{15,1,14}	145	3.0(-3)	<1.87 (0.37); <5.46 (1.09);

The notation $a(-b)$ stands for $a \times 10^{-b}$

< means upper limit

~ means uncertain detection, $S/N \lesssim 2$

– means frequency not observed

: means blended line

Table 7.13 – Observed line fluxes $\int T_{\text{MB}} dV$ (K km s^{-1}) for CH_3CN and its isotopic species.

Frequency [GHz]	Transition	E_{up} [K]	A [s^{-1}]	Sources	
CH_3CN					
238.844	$13_8 - 12_8$	537	5.0(-4)	–	<0.17
238.913	$13_7 - 12_7$	430	5.8(-4)		1.82 (0.62)
238.972	$13_6 - 12_6$	337	6.4(-4)	<0.21	3.22 (1.11)
239.023	$13_5 - 12_5$	259	6.9(-4)	~0.33 (0.38)	3.19 (0.88)
239.064	$13_4 - 12_4$	195	7.4(-4)	~0.93 (0.49)	<6.43 (1.29)*
239.096	$13_3 - 12_3$	145	7.7(-4)	~0.51 (0.38)	1.17 (0.45)
239.120	$13_2 - 12_2$	109	7.9(-4)	1.04 (0.40)	1.64 (0.55)
239.133	$13_1 - 12_1$	87	8.1(-4)	~0.63 (0.38)	1.80 (0.61)
239.138	$13_0 - 12_0$	80	8.1(-4)	0.73 (0.26)*	1.72 (0.52)*
330.843	$18_6 - 17_6$	408	1.9(-3)	0.73 (0.26)*	4.60 (1.15)
330.913	$18_5 - 17_5$	329	2.0(-3)	~0.31 (0.26)	7.44 (2.20)
330.970	$18_4 - 17_4$	265	2.1(-3)	–	5.91 (1.87)
331.014	$18_3 - 17_3$	215	2.1(-3)	–	6.70 (2.07)
331.046	$18_2 - 17_2$	180	2.2(-3)	–	8.26 (2.38)
331.065	$18_1 - 17_1$	158	2.2(-3)	–	10.24 (2.87)
331.072	$18_0 - 17_0$	151	2.2(-3)	–	6.25 (1.96)
				–	7.86 (2.30)
$\text{CH}_3^{13}\text{CN}$					
238.855	$13_6 - 12_6$	337	9.2(-4)	–	<0.22
238.905	$13_5 - 12_5$	259	1.0(-3)		<10.23 (2.58)*
238.946	$13_4 - 12_4$	195	1.1(-3)	<0.21	<1.00 (0.48)*
238.978	$13_3 - 12_3$	145	1.1(-3)	<0.21	2.21 (0.70)
239.001	$13_2 - 12_2$	109	1.2(-3)	<0.21	~0.35 (0.31)
239.015	$13_1 - 12_1$	87	1.2(-3)	<0.21	<0.22
239.020	$13_0 - 12_0$	80	1.2(-3)	<0.21	~0.62 (0.35)
330.806	$18_4 - 17_4$	265	3.0(-3)	<0.21	4.61 (0.97)*
330.851	$18_3 - 17_3$	215	3.1(-3)	<0.31	4.61 (0.97)*
					<8.08 (2.52)*
					<4.12 (1.23)*

Continued on next page

Table 7.13 – continued from previous page

Frequency [GHz]	Transition	E_{up} [K]	A [s ⁻¹]	Sources
330.882	18 ₂ – 17 ₂	179	3.1(-3)	IRAS20126+4104
330.901	18 ₁ – 17 ₁	158	3.2(-3)	IRAS18089-1732
330.908	18 ₀ – 17 ₀	151	3.2(-3)	IRAS20126+4104

The notation $a(-b)$ stands for $a \times 10^{-b}$

< means upper limit

~ means uncertain detection, $S/N \lesssim 2$

– means frequency not observed

: means blended line

* calculated flux (see Eq. 7.4)

Table 7.14 – Observed line fluxes $\int T_{\text{MB}} dV$ (K km s⁻¹) for C₂H₅CN and its isotopic species.

Frequency [GHz]	Transition	E_{up} [K]	A [s ⁻¹]	Sources
C ₂ H ₅ CN				
218.390	24 _{3,21} – 23 _{3,20}	140	8.7(-4)	IRAS20126+4104
219.903	12 _{3,10} – 11 _{2,9}	44	3.0(-5)	IRAS18089-1732
225.236	25 _{4,21} – 24 _{4,20}	158	9.4(-4)	IRAS20126+4104
225.307	12 _{3,9} – 11 _{2,10}	44	3.2(-5)	IRAS18089-1732
225.317	23 _{2,22} – 22 _{1,21}	122	4.8(-5)	IRAS20126+4104
240.699	16 _{9,7/8} – 17 _{8,10/9}	148	7.9(-6)	IRAS18089-1732
240.861	28 _{1,28} – 27 _{0,27}	169	1.0(-4)	IRAS20126+4104
338.143	37 _{3,34} – 36 _{3,33}	317	3.3(-3)	IRAS18089-1732
339.895	39 _{2,38} – 38 _{2,37}	334	3.3(-3)	IRAS20126+4104
339.968	38 _{2,36} – 37 _{2,35}	327	3.3(-3)	IRAS18089-1732
340.149	39 _{1,38} – 38 _{1,37}	334	3.3(-3)	IRAS20126+4104
352.992	21 _{2,19} – 20 _{1,20}	105	1.4(-5)	IRAS18089-1732

Continued on next page

Table 7.14 – continued from previous page

Frequency [GHz]	Transition	E_{up} [K]	A [s ⁻¹]	Sources
353.089	23 _{3,20} – 22 _{2,21}	129	5.8(-5)	IRAS20126+4104
354.477	40 _{3,38} – 39 _{3,37}	361	3.8(-3)	IRAS18089-1732
				G31.41+0.31
				~0.58 (0.29)
				<0.24
				<3.38 (0.68):
				1.33 (0.65)

The notation $a(-b)$ stands for $a \times 10^{-b}$

< means upper limit

~ means uncertain detection, $S/N \lesssim 2$

– means frequency not observed

: means blended line

Table 7.15 – Observed line fluxes $\int T_{\text{MB}} dV$ (K km s⁻¹) for HCOOCH₃ and its isotopic species.

Frequency [GHz]	Transition	E_{up} [K]	A [s ⁻¹]	Sources
HCOOCH ₃				IRAS20126+4104
218.281	17 _{3,14,2} – 16 _{3,13,2}	100	1.5(-4)	IRAS18089-1732
218.298	17 _{3,14,0} – 16 _{3,13,0}	100	1.5(-4)	G31.41+0.31
219.584	18 _{3,5/6,3} – 17 _{3,4/5,3}	401	7.7(-5)	1.38 (0.42)
219.592	28 _{9,19,2} – 28 _{8,20,2}	295	1.6(-5)	1.00 (0.430)
219.623	18 _{2,6/7,3} – 17 _{12,5/6,3}	384	8.9(-5)	~0.17 (0.15)
219.642	18 _{3,6,4} – 17 _{13,5,4}	401	7.7(-5)	~0.30 (0.22)
219.696	18 _{1,8/7,3} – 17 _{11,7/6,3}	369	1.0(-4)	~0.66 (0.32)
219.705	18 _{4,15,3} – 17 _{4,14,3}	300	1.5(-4)	~0.55 (0.43)
219.764	18 _{9,9,5} – 17 _{9,8,5}	342	1.2(-4)	0.69 (0.25)
219.822	18 _{0,9/8,3} – 17 _{10,8/7,3}	355	1.1(-4)	0.77 (0.27)
222.149	18 _{6,12,3} – 17 _{6,11,3}	312	1.5(-4)	0.61 (0.24)
222.177	18 _{6,12,5} – 17 _{6,11,5}	312	1.5(-4)	<0.21
222.421	18 _{8,10,2} – 17 _{8,9,2}	144	1.3(-4)	1.25 (0.25):
222.438	18 _{8,11,0} – 17 _{8,10,0}	144	1.3(-4)	<3.05 (0.83):
				<0.20
				~1.14 (0.67)
				1.62 (0.45)
				0.35 (0.16)*
				1.07 (0.39)*

Continued on next page

Table 7.15 – continued from previous page

Frequency [GHz]	Transition	E_{up} [K]	A [s ⁻¹]	Sources	IRAS20126+4104	IRAS18089-1732	G31.41+0.31
222.440	18 _{8,10,0} – 17 _{8,9,0}	144	1.3(-4)	<0.22	<0.22	0.35 (0.16)*	1.07 (0.39)*
222.442	18 _{8,11,1} – 17 _{8,10,1}	144	1.3(-4)	<0.22	<0.22	0.35 (0.16)*	1.07 (0.39)*
225.372	20 _{2,9,3} – 19 _{2,8,3}	307	1.7(-4)	<0.19	<0.19	<0.31	1.38 (0.56)
225.449	20 _{1,9,3} – 19 _{1,8,3}	307	1.7(-4)	<0.19	<0.19	<0.18	<1.30 (0.55);
238.927	20 _{3,18,1} – 19 _{2,17,2}	128	2.1(-5)	<0.21	<0.21	<0.22	~0.40 (0.23)
238.933	20 _{3,18,0} – 19 _{2,17,0}	128	2.1(-5)	<0.21	<0.21	<0.22	~0.47 (0.20)
238.947	19 _{3,16,3} – 18 _{3,15,5}	309	2.0(-4)	<0.21	<0.21	~0.29 (0.26)	~0.88 (0.38);
239.111	7 _{6,2,4} – 6 _{5,2,4}	227	2.7(-5)	<0.21	<0.21	<0.22	<0.15 (0.17)
241.059	30 _{3,27,0} – 30 _{3,28,0}	281	5.8(-6)	–	–	<0.23	~0.33 (0.31)
241.068	30 _{3,27,0} – 30 _{2,28,0}	281	1.1(-5)	–	–	<0.23	~0.76 (0.53)
330.941	30 _{2,1,29,4/5} – 29 _{2,1,28,4/5}	443	5.5(-4)	<0.31	<0.31	~0.73 (0.38)	~0.75 (0.83)
331.021	25 _{5,21,0} – 24 _{4,20,0}	210	3.5(-5)	<0.34	<0.34	<0.40	<8.29 (1.66);
331.036	25 _{5,21,1} – 24 _{4,20,2}	210	3.5(-5)	<0.32	<0.32	<0.34	<10.01 (3.05);
331.121	27 _{1,2,16,4} – 26 _{1,2,15,4}	505	4.5(-4)	<0.29	<0.29	–	<0.74 (0.69)
331.149	28 _{4,25,1} – 27 _{4,24,1}	248	5.3(-4)	<0.29	<0.29	0.69 (0.31)	2.60 (1.39)
331.160	28 _{4,25,0} – 27 _{4,24,0}	248	5.3(-4)	<0.29	<0.29	<0.99 (0.42);	<2.24 (1.15);
331.161	27 _{1,1,17/16,3} – 26 _{1,1,16/15,3}	490	4.6(-4)	<0.29	<0.29	<0.99 (0.42);	<2.24 (1.15);
338.338	27 _{8,19,2} – 26 _{8,18,2}	267	5.4(-4)	<0.26	<0.26	<0.39	6.26 (2.37)
338.356	27 _{8,19,0} – 26 _{8,18,0}	267	5.4(-4)	<0.23	<0.23	<0.44	5.09 (2.08)
338.393	28 _{5,24,3} – 27 _{5,23,3}	443	5.7(-4)	<0.23	<0.23	<0.43	<3.80 (2.05);
338.396	27 _{7,21,1} – 26 _{7,20,1}	258	5.5(-4)	<0.23	<0.23	<0.45	<3.80 (2.05);
338.414	27 _{7,21,0} – 26 _{7,20,0}	258	5.5(-4)	<8.06 (2.04);	<8.06 (2.04);	<0.45	<43.32 (9.59);
339.882	29 _{3,26,3} – 28 _{3,25,3}	450	5.8(-4)	<0.22	<0.22	<0.79 (0.16);	~0.73 (0.33)
340.044	29 _{4,26,4} – 28 _{4,25,4}	450	5.8(-4)	<0.15	<0.15	<0.12	<3.75 (0.75);
340.115	27 _{7,20,5} – 26 _{7,19,5}	444	5.5(-4)	<0.15	<0.15	~0.30 (0.31);	0.77 (0.32)
345.068	28 _{4,14,2} – 27 _{14,13,2}	370	4.7(-4)	<0.26	<0.26	0.28 (0.11)	<3.93 (1.62);
345.069	28 _{4,15/14,0} – 27 _{14,14/13,0}	370	4.7(-4)	<0.26	<0.26	0.56 (0.22)	<3.93 (1.62);
345.073	16 _{6,11,0} – 15 _{5,10,0}	104	3.9(-5)	<0.26	<0.26	<0.19	<5.62 (1.29);

Continued on next page

Table 7.15 – continued from previous page

Frequency [GHz]	Transition	E_{up} [K]	A [s ⁻¹]	Sources	
345.085	19 _{3,6,2} – 19 _{12,7,2}	224	3.5(-5)	–	G31.41+0.31
345.091	28 _{4,15,1} – 27 _{14,14,1}	370	4.7(-4)	<0.26	<1.73 (0.35);
345.148	28 _{6,23,3} – 27 _{6,22,3}	452	6.0(-4)	<0.26	<0.50 (0.32);
345.163	11 _{8,3,5} – 10 _{7,3,5}	269	7.1(-5)	<0.26	<0.55 (0.34)
345.230	18 _{3,5,2} – 18 _{12,6,2}	213	3.2(-5)	<0.25	<0.19
345.242	18 _{3,6,1} – 18 _{12,7,1}	213	3.2(-5)	<0.25	<0.59 (0.40)
345.248	28 _{10,19,4} – 27 _{10,18,4}	493	5.5(-4)	<0.26	<8.18 (3.04);
352.817	33 _{0/1/0/1,33,3} – 32 _{1/1/0/0,32,3}	479	1.1(-4)	<0.18	<8.18 (3.04);
352.841	33 _{1/0,33,4/5} – 32 _{1/0,32,4/5}	479	7.7(-4)	<0.18	<0.34
352.912	31 _{2,29,2} – 30 _{3,28,1}	286	8.5(-5)	<0.18	<2.68 (0.76);
352.918	31 _{3,29,1} – 30 _{3,28,1}	286	6.6(-4)	<0.18	1.72 (0.47)
352.922	31 _{2,29,2} – 30 _{2,28,2}	286	6.6(-4)	<0.18	0.30 (0.08)
352.926	31 _{3,29,0} – 30 _{3,28,0}	286	6.6(-4)	<0.18	2.32 (0.62)*
352.930	31 _{2,29,0} – 30 _{2,28,0}	286	6.6(-4)	<0.18	2.32 (0.62)*
354.427	29 _{16,13/14,3} – 28 _{16,12/13,3}	614	4.7(-4)	<0.18	2.32 (0.62)*
354.477	29 _{15,15,4} – 28 _{15,14,4}	593	5.0(-4)	<0.13	~1.04 (0.64)
354.574	12 _{8,5/4,3} – 11 _{7,4/5,3}	276	7.4(-5)	<0.23	<0.40 (0.58);
354.605	29 _{15,15/14,3} – 28 _{15,14/13,3}	593	5.0(-4)	<0.18	<1.44 (0.78);
354.608	33 _{1/0,33,1/2} – 32 _{1/0,32,1/2}	293	7.2(-4)	<0.18	1.96 (0.46)
354.608	33 _{0/1,33,2/1} – 32 _{1/0,32,1/2}	293	6.8(-4)	<0.18	3.14 (0.49)*
354.629	28 _{7,21,5} – 27 _{7,20,5}	461	6.4(-4)	<0.18	2.75 (0.47)*
354.742	12 _{8,5,1} – 11 _{7,5,1}	88	7.3(-5)	<0.18	~1.20 (0.68)
354.759	12 _{8,4,2} – 11 _{7,4,2}	88	7.3(-5)	<0.16	1.19 (0.44)
354.806	12 _{8,5/4,0} – 11 _{7,4/5,0}	88	7.3(-5)	<0.18	<3.23 (0.65);
354.839	29 _{14,15/16,3} – 28 _{14,14/15,3}	574	5.2(-4)	<0.15	3.90 (1.18)
364.297	33 _{1/2,32,2/1} – 32 _{1,31,2}	308	7.3(-4)	<0.24	<4.91 (1.40);
364.302	33 _{2/1,32,0} – 32 _{2/1,31,0}	308	7.3(-4)	0.80 (0.91)	<3.67 (1.16);

Continued on next page

Table 7.15 – continued from previous page

Frequency [GHz]	Transition	E_{up} [K]	A [s ⁻¹]	Sources	
				IRAS20126+4104	IRAS18089-1732
					G31.41+0.31

The notation $a(-b)$ stands for $a \times 10^{-b}$

< means upper limit

~ means uncertain detection, $S/N \lesssim 2$

– means frequency not observed

: means blended line

* calculated flux (see Eq. 7.4)

Table 7.16 – Observed line fluxes $\int T_{\text{MB}} dV$ (K km s⁻¹) for CH₃OCH₃ and its isotopic species.

Frequency [GHz]	Transition	E_{up} [K]	A [s ⁻¹]	Sources	
				IRAS20126+4104	IRAS18089-1732
					G31.41+0.31
CH ₃ OCH ₃					
218.490	2 _{3,2,1,2/3} – 2 _{3,2,2,2,2/3}	264	3.4(-5)	<0.18	–
218.492	2 _{3,2,1,1} – 2 _{3,2,2,2,1}	264	3.4(-5)	<0.18	–
218.495	2 _{3,2,1,0} – 2 _{3,2,2,2,0}	264	3.4(-5)	<0.18	–
222.239	4 _{3,2,2} – 3 _{2,1,2}	22	2.8(-5)	<0.22	0.82 (0.56)
222.248	4 _{3,2,3/1} – 3 _{2,1,3/1}	22	4.2(-5)	<0.22	~0.43 (0.20)
222.255	4 _{3,2,0} – 3 _{2,1,0}	22	4.9(-5)	<0.22	~0.62 (0.21)
222.259	4 _{3,1,1} – 3 _{2,1,1}	22	1.6(-5)	<0.22	~0.30 (0.21)*
222.260	4 _{3,1,2} – 3 _{2,1,2}	22	2.1(-5)	<0.22	~0.11 (0.21)*
222.326	2 _{5,3,23,0} – 2 _{4,4,20,0}	308	7.9(-6)	<0.22	<0.27
222.327	2 _{5,3,22,1} – 2 _{4,4,20,1}	308	7.9(-6)	<0.22	<0.27
222.329	2 _{5,3,22/23,2/3} – 2 _{4,4,20/20,2/3}	308	7.9(-6)	<0.22	<0.27
222.414	4 _{3,2,2} – 3 _{2,2,2}	22	2.1(-5)	<0.22	~0.20 (0.10)
222.423	4 _{3,2,1} – 3 _{2,2,1}	22	1.6(-5)	<0.22	~0.56 (0.30)
222.427	4 _{3,1,3} – 3 _{2,2,3}	22	4.9(-5)	<0.22	~0.23 (0.12)
222.434	4 _{3,1,1,0} – 3 _{2,2,1,0}	22	4.2(-5)	<0.22	1.68 (0.63)

Continued on next page

Table 7.16 – continued from previous page

Frequency [GHz]	Transition	E_{up} [K]	A [s^{-1}]	Sources	
222.435	$4_{3,1,2} - 3_{2,2,2}$	22	2.8(-5)	IRAS20126+4104	G31.41+0.31
225.202	$24_{4,2,1,2/3} - 24_{3,22,2/3}$	296	4.7(-5)	<0.22	<0.34 (0.10);
225.204	$24_{4,2,1,1} - 24_{3,22,1}$	296	4.7(-5)	<0.19	0.55 (0.18)*
225.205	$24_{4,2,1,0} - 24_{3,22,0}$	296	4.7(-5)	<0.19	0.87 (0.28)*
238.975	$29_{5,25,2/3/1/0} - 28_{6,22,2/3/1/0}$	432	1.6(-5)	<0.21	0.55 (0.18)*
239.020	$24_{5,19,5/3} - 24_{4,20,5/3}$	309	6.1(-5)	<0.21	<1.64 (0.64);
239.021	$24_{5,19,1} - 24_{4,20,1}$	309	6.1(-5)	<0.21	<0.68 (0.14);
239.021	$24_{5,19,0} - 24_{4,20,0}$	309	6.1(-5)	<0.21	<1.82 (0.36);
240.978	$5_{3,3,2} - 4_{2,2,2}$	26	4.5(-5)	<0.20	<0.68 (0.14);
240.983	$5_{3,3,3} - 4_{2,2,3}$	26	5.4(-5)	<0.20	2.16 (0.66)*
240.985	$5_{3,3,1} - 4_{2,2,1}$	26	5.1(-5)	<0.20	0.19 (0.06)*
240.990	$5_{3,3,0} - 4_{2,2,0}$	26	5.4(-5)	<0.20	1.49 (0.46)*
The notation $a(-b)$ stands for $a \times 10^{-b}$					
< means upper limit					
~ means uncertain detection, $S/N \lesssim 2$					
– means frequency not observed					
: means blended line					
* calculated flux (see Eq. 7.4)					

Table 7.17 – Observed line fluxes $\int T_{\text{MB}} dV$ (K km s^{-1}) for CH_2CO and its isotopic species.

Frequency [GHz]	Transition	E_{up} [K]	A [s^{-1}]	Sources	
CH_2CO					
222.120	$11_{4,8/7} - 10_{4,7/6}$	273	1.1(-4)	IRAS20126+4104	G31.41+0.31
222.198	$11_{0,11} - 10_{0,10}$	65	1.2(-4)	<0.22	<0.54 (0.10);
222.201	$11_{3,9/8} - 10_{3,8/7}$	181	1.1(-4)	<0.22	<0.81 (0.26);
Continued on next page					

Table 7.17 – continued from previous page

Frequency [GHz]	Transition	E_{up} [K]	A [s ⁻¹]	Sources	
222.229	11 _{2,10} – 10 _{2,9}	116	1.2(-4)	IRAS20126+4104	IRAS18089-1732 G31.41+0.31
222.315	11 _{2,9} – 10 _{2,8}	116	1.2(-4)	<0.22	<0.28 (0.06):
363.937!	18 _{2,16} – 17 _{2,15}	218	5.5(-4)	<0.22	~0.24 (0.22)
				<4.65 (1.08):	<0.22

The notation $a(-b)$ stands for $a \times 10^{-b}$

< means upper limit

~ means uncertain detection, $S/N \lesssim 2$

– means frequency not observed

: means blended line

! frequency from CDMS

Table 7.18 – Observed line fluxes $\int T_{\text{MB}} dV$ (K km s⁻¹) for CH₃CHO and its isotopic species.

Frequency [GHz]	Transition	E_{up} [K]	A [s ⁻¹]	Sources	
CH ₃ CHO					
330.822	5 _{3,3,1} – 4 _{2,3,1}	34	1.2(-4)	<0.31	~0.71 (0.80)
331.039	17 _{3,14,3} – 16 _{3,13,3}	367	1.2(-3)	<1.18 (0.88):	<0.42 (0.29):
354.458	18 _{2,16,3} – 17 _{2,15,3}	375	1.5(-3)	<0.18	<3.11 (1.11):
354.525	19 _{0,19,5} – 18 _{0,18,5}	377	1.5(-3)	<0.17	<0.19
354.813	18 _{2,16,2} – 17 _{2,15,2}	170	1.5(-3)	<0.18	<0.23
354.844	18 _{2,16,0} – 17 _{2,15,0}	170	1.5(-3)	<0.18:	<1.13 (0.55):

The notation $a(-b)$ stands for $a \times 10^{-b}$

< means upper limit

~ means uncertain detection, $S/N \lesssim 2$

– means frequency not observed

: means blended line

Table 7.19 – Observed line fluxes $\int T_{\text{MB}} dV$ (K km s^{-1}) for HCOOH and its isotopic species.

Frequency [GHz]	Transition	E_{up} [K]	A [s ⁻¹]	Sources		
HCOOH						
222.110	$7_{2,6} - 7_{1,7}$	43	1.9(-6)	<0.22	<0.27	<0.24
225.086	$10_{4,7} - 9_{4,6}$	110	1.0(-4)	<0.18	<0.18	<1.97 (1.70):
225.091	$10_{4,6} - 9_{4,5}$	110	1.0(-4)	<0.18	<0.18	<1.97 (1.70):
225.238	$10_{3,8} - 9_{3,7}$	88	1.1(-4)	<0.19	<0.39 (0.24):	<2.59 (0.78):
330.931	$4_{3,1} - 4_{2,2}$	39	5.1(-6)	<0.31	<0.32	~ 0.47 (0.63)
331.145	$3_{3,0} - 3_{2,1}$	35	3.6(-6)	<0.29	<0.29:	<2.77 (1.80):
338.109	$15_{1,15} - 14_{0,14}$	127	1.1(-5)	—	—	<5.11 (3.10):
338.202	$15_{3,13} - 14_{3,12}$	158	4.1(-4)	—	—	<13.55 (6.28):
345.031	$16_{0,16} - 15_{0,15}$	143	4.5(-4)	<0.26	~ 0.30 (0.30)	~ 1.18 (0.70)
345.253	$14_{3,12} - 14_{2,13}$	142	8.3(-6)	<0.29	<0.19:	<1.59 (1.01):
354.448	$17_{0,17} - 16_{1,16}$	161	1.3(-5)	<0.18	<1.70 (0.57):	<6.42 (1.60):

The notation $a(-b)$ stands for $a \times 10^{-b}$

< means upper limit

 \sim means uncertain detection, $S/N \lesssim 2$

– means frequency not observed

: means blended line

Table 7.20 – Observed line fluxes $\int T_{\text{MB}} dV$ (K km s^{-1}) for CH_3CCH and its isotopic species.

Frequency [GHz]	Transition	E_{up} [K]	A [s ⁻¹]	Sources	
CH ₃ CCH					
222.099	13 ₄ – 12 ₄	190	3.4(-5)	<0.22	<0.65 (0.35); <2.79 (0.56);
222.129	13 ₃ – 12 ₃	140	3.6(-5)	~0.29 (0.17)	1.14 (0.43) 3.15 (0.94)
222.150	13 ₂ – 12 ₂	104	3.7(-5)	~0.41 (0.19)	1.25 (0.46) <4.25 (0.85);

Continued on next page

Table 7.20 – continued from previous page

Frequency [GHz]	Transition	E_{up} [K]	A [s ⁻¹]	Sources		
				IRAS20126+4104	IRAS18089-1732	G31.41+0.31
222.163	13 ₁ – 12 ₁	82	3.8(-5)	0.74 (0.29)	2.20 (0.68)	3.14 (1.01)
222.167	13 ₀ – 12 ₀	75	3.8(-5)	0.93 (0.35)	2.13 (0.70)	3.27 (0.97)
239.088	14 ₆ – 13 ₆	346	3.9(-5)	<0.21	<0.22 (0.05):	<2.40 (0.48):
239.138	14 ₅ – 13 ₅	267	4.1(-5)	<0.21	<2.38 (0.48):	<6.39 (1.28):
239.179	14 ₄ – 13 ₄	202	4.3(-5)	0.71 (0.14)	<0.68 (0.14):	~0.39 (0.21)
239.211	14 ₃ – 13 ₃	151	4.5(-5)	~0.40 (0.24)	~0.75 (0.41)	2.47 (0.64)
239.234	14 ₂ – 13 ₂	115	4.6(-5)	0.36 (0.16)	~0.89 (0.89)	2.06 (0.63)
239.248	14 ₁ – 13 ₁	93	4.7(-5)	0.79 (0.23)	1.62 (0.52)	2.91 (0.74)
239.252	14 ₀ – 13 ₀	86	4.7(-5)	0.87 (0.24)	1.68 (0.43)	3.46 (1.07)

The notation $a(-b)$ stands for $a \times 10^{-b}$

< means upper limit

~ means uncertain detection, $S/N \lesssim 2$

– means frequency not observed

: means blended line

7.7.2 Rotation diagrams

RTD diagrams for H_2CO , CH_3OH , $\text{C}_2\text{H}_5\text{OH}$, HNCO , NH_2CHO , CH_3CN , $\text{C}_2\text{H}_5\text{CN}$, HCOOCH_3 , CH_3OCH_3 , CH_2CO and CH_3CCH . Lines from different frequency bands are corrected for differential beam dilution assuming a $R_{T=100\text{K}}$ source size for the warm species and $14''$ source size for the cold species, as indicated in the plots. Optically thin, unblended lines with $S/N \gtrsim 2$ are marked with filled circles. Lines with high S/N ratio ($\lesssim 2$) are marked with diamonds, those included in the fit with filled diamonds. Optically thick lines and blended lines are marked with open squares and triangles, respectively. Upper limits are marked with arrows. Upper limits used to constrain the fit are marked with filled stars. The error bars are calculated using Eq. 7.13. For H_2CO , all lines included into the fit belong to para- H_2CO . For CH_3OH , lines with $E_{\text{up}} < 100$ K are considered contaminated with the cold CH_3OH and are excluded from the fit as blends.

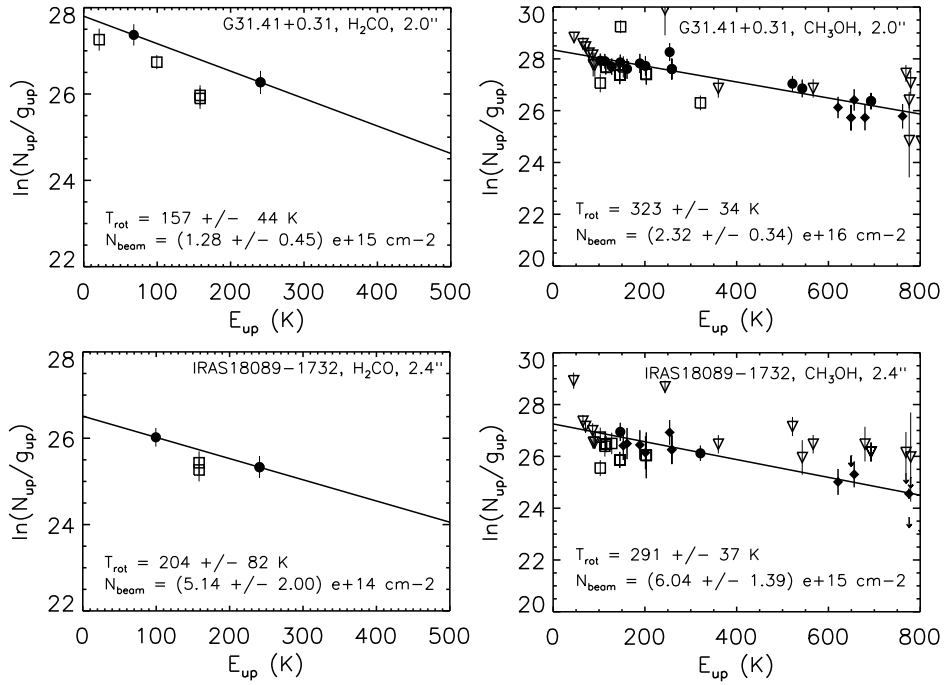


Figure 7.12 – Rotation diagram (RTD) plots for the observed species 1/6.

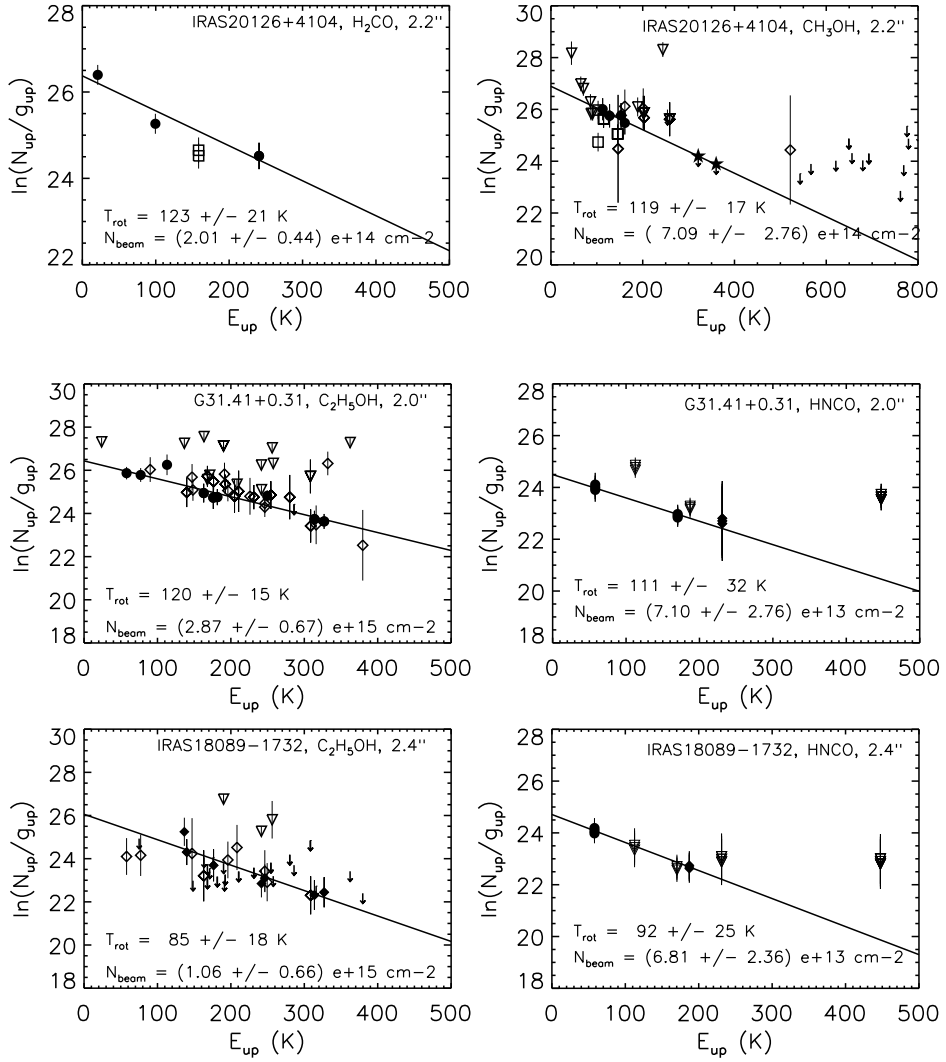


Figure 7.13 – Rotation diagram (RTD) plots for the observed species 2/6.

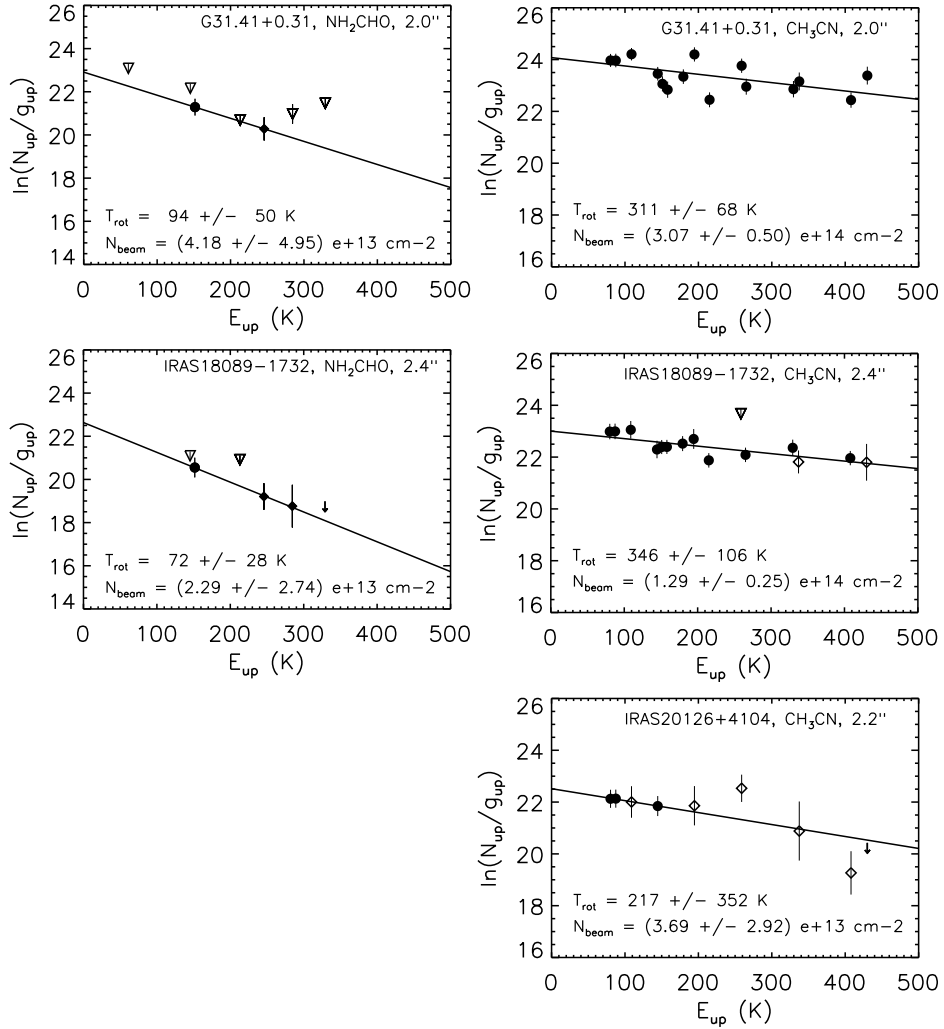


Figure 7.14 – Rotation diagram (RTD) plots for the observed species 3/6.

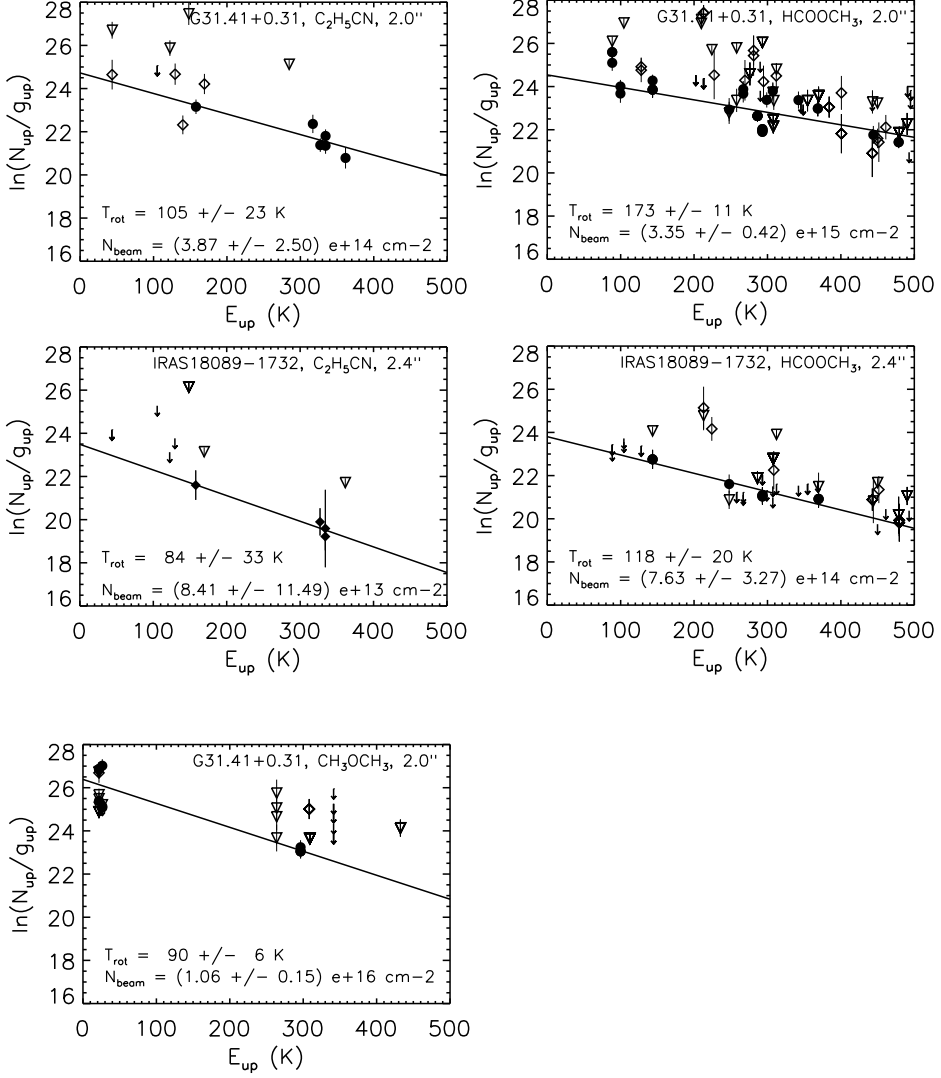


Figure 7.15 – Rotation diagram (RTD) plots for the observed species 4/6.

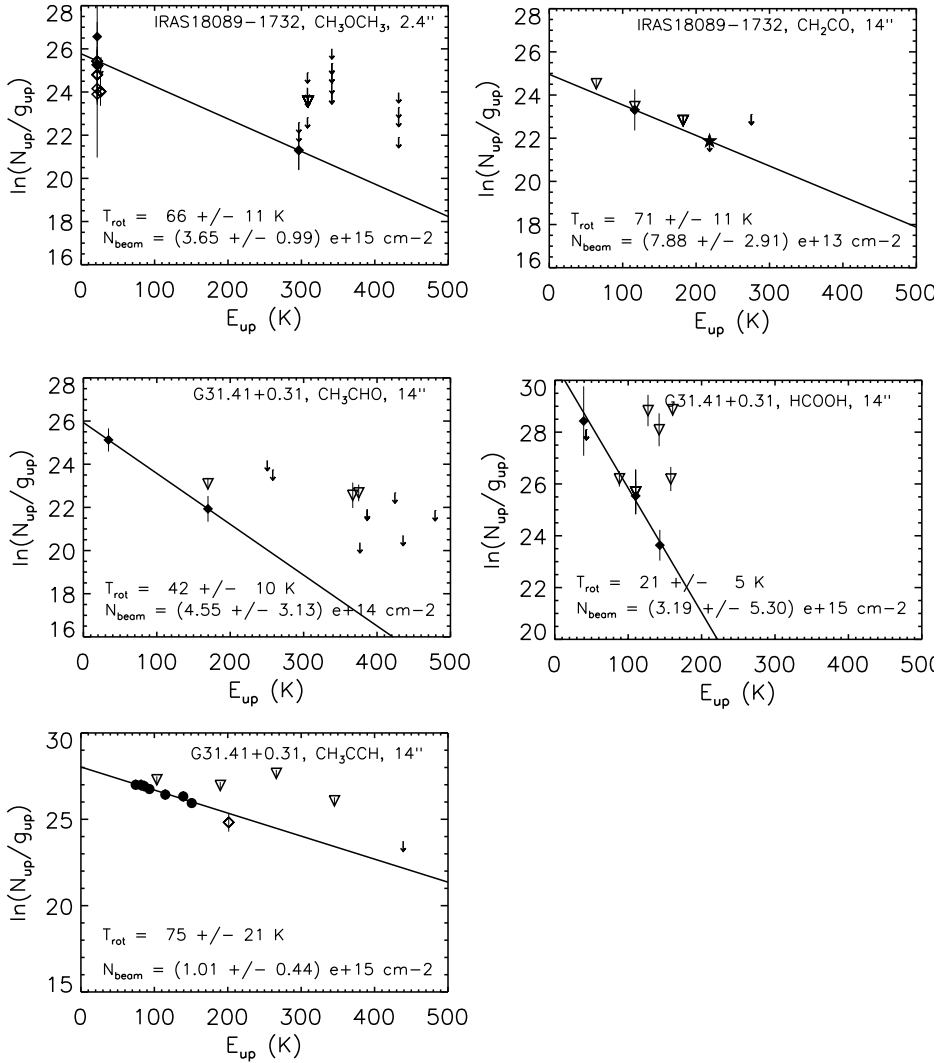


Figure 7.16 – Rotation diagram (RTD) plots for the observed species 5/6.

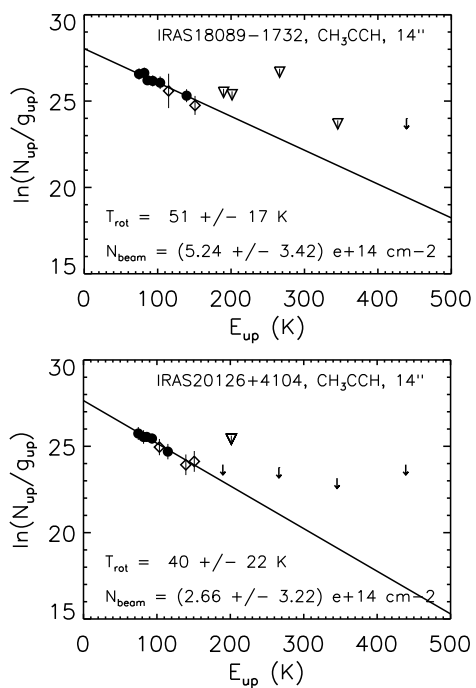


Figure 7.17 – Rotation diagram (RTD) plots for the observed species 6/6.

7.7.3 Weeds and CASSIS model parameters

Table 7.21 – Weeds model parameters.

Species	IRAS20126+4104					IRAS18089-1732					G31.41+0.31				
	N _S [cm ⁻²]	T _{ex} [K]	θ _S ["]	Δν [km/s]		N _S [cm ⁻²]	T _{ex} [K]	θ _S ["]	Δν [km/s]		N _S [cm ⁻²]	T _{ex} [K]	θ _S ["]	Δν [km/s]	
CH ₃ OH	1.50E+17	300	2.2	6		3.50E+17	300	2.4	5		2.00E+18	300	2.0	7	
CH ₃ OH	4.80E+16	20	3.0	5		2.60E+17	20	3.0	5		2.70E+17	20	5.0	7	
¹³ CH ₃ OH	—	—	—	—		—	—	—	—		—	—	—	—	
H ₂ CO	6.00E+15	150	2.2	6		1.50E+16	150	2.4	6		6.00E+16	150	2.0	6	
H ₂ ¹³ CO	<2.0E+15	150	2.2	6		3.50E+15	150	2.4	6		7.00E+15	150	2.0	6	
CH ₃ CN ^a	1.30E+15	200	2.2	6		3.50E+15	200	2.4	6		2.00E+16	300	2.0	7	
CH ₃ ¹³ CN	<2.0E+13	200	2.2	6		4.00E+14	200	2.4	6		2.00E+15	300	2.0	7	
HNCO	1.00E+15	200	2.2	6		4.00E+15	200	2.4	6		6.00E+16	200	2.0	7	
HN ¹³ CO	<1.0E+14	200	2.2	6		7.00E+14	200	2.4	6		2.00E+15	200	2.0	7	
C ₂ H ₅ OH	<3.0E+15	100	2.2	6		2.50E+16	150	2.4	6		2.00E+17	100	2.0	7	
C ₂ H ₅ CN	<5.0E+14	80	2.2	5		4.00E+15	80	2.4	5		2.00E+16	80	2.0	5	
CH ₃ OCH ₃	<1.0E+16	100	2.2	6		1.00E+17	100	2.4	6		1.00E+18	100	2.0	5	
HCOOCH ₃	<2.0E+15	200	2.2	6		3.00E+16	200	2.4	6		1.00E+18 ^b	300	2.0	7	
NH ₂ CHO	3.00E+14	300	2.2	6		5.00E+14	100	2.4	6		4.00E+15	300	2.0	7	
CH ₂ CO	<5.0E+13	50	14.0	6		1.50E+14	50	14.0	5		6.50E+14	50	14.0	6	
CH ₃ CHO	<1.0E+14	50	8.0	6		<1.0E+14	50	8.0	6		1.00E+15	50	8.0	6	
HCOOH	<5.0E+13	40	8.0	6		<5.0E+13	40	8.0	6		2.00E+15	40	8.0	6	
CH ₃ CCH	7.00E+14	35	14.0	2		1.80E+15	40	14.0	3.5		2.80E+15	60	14.0	4	
Additional species															
CH ₃ COCH ₃	<0.1E+17	300	2.2	5		5.00E+16	300	2.4	5		1.00E+17	100	2.0	7	
HCCCN	1.00E+13	100	14	7		3.00E+13	150	14	6		7.00E+13	150	14	7	
SO	3.00E+14	50	14	6		1.00E+15	50	14	6		7.00E+14	50	14	8	
³⁴ SO	2.00E+13	50	14.0	6		5.00E+13	50	14.0	6		1.00E+14	50	14.0	6	
SO ₂	3.00E+14	50	14.0	6		5.00E+14	50	14.0	6		1.00E+15	50	14.0	7	

Continued on next page

Table 7.21 – continued from previous page

Species	IRAS20126+4104					IRAS18089-1732					G31.41+0.31				
	N_S [cm ⁻²]	T_{ex} [K]	θ_S ["]	$\Delta\nu$ [km/s]		N_S [cm ⁻²]	T_{ex} [K]	θ_S ["]	$\Delta\nu$ [km/s]		N_S [cm ⁻²]	T_{ex} [K]	θ_S ["]	$\Delta\nu$ [km/s]	
³³ SO ₂	5.00E+13	50	14.0	5		5.00E+14	50	14.0	5		1.00E+15	50	14.0	6	
HCN	4.00E+13	50	14.0	20		2.00E+14	50	14.0	7		2.00E+14	50	14.0	12	
HCN	4.00E+13	50	14.0	5		-5.00E+13	50	14.0	4		-6.00E+13	50	14.0	6	
H ¹³ CN	1.00E+12	50	14.0	6		1.50E+13	50	14.0	6		2.00E+13	50	14.0	6	
CN, $v = 0, 1$	2.00E+14	50	14	2		4.00E+14	50	14	5		8.00E+14	50	14	6	
NH ₂ CN						1.00E+13	50	14	7		3.00E+13	50	14	7	
O ¹³ CS						5.00E+14	50	14.0	7		5.00E+14	50	14	5	
OC ³⁴ S											1.00E+15	50	14.0	7	
CP															
C ³⁴ S						5.00E+14	50	14.0	4		1.00E+15	50	14.0	6	
HCOCH ₂ OH						1.40E+14	50	14.0	5		2.00E+14	50	14.0	7	
S ₃						5.00E+15	300	2.0	6		2.00E+16	300	2.0	7	
CH ₃ NH ₂											1.50E+16	15	14	6	
¹³ CH ₃ OH											1.00E+17	150	2.0	7	

¹³CH₃OH is not available in the JPL database used for Weeds modeling.^a based on 21'' beam spectra.^b based on 21'' beam spectra, 1.5E+17 in the 14'' beam spectra.

Table 7.22 – CASSIS model parameters for CH₃OH in the observed sources.

Source	Component ^a	N_S [cm ⁻²]	T_{ex} [K]	FWHM [km s ⁻¹]	θ_S [$''$]	V_{LSR} [km s ⁻¹]	χ^2
IRAS20126+4104	comp.	(1.1±0.1)E+17	300 ^c	8.15±0.60	2.2 ^b	-4.05 ± 0.70	1.9
	ext.	(2.2 ^{+0.9} _{-0.7})E+15	14±1	7.00 ^{+0.60} _{-0.75}	≥14.0	-4.25 ^{+0.80} _{-0.25}	
IRAS18089-1732	comp.	(2.0 ^{+0.1} _{-0.2})E+17	300 ^c	5.45 ^{+0.40} _{-0.5}	2.4 ^b	33.4±0.2	4.4
	ext.	(2.4 ^{+1.4} _{-0.5})E+15	15±2	3.50 ^{+0.50} _{-0.55}	≥14.0	32.3 ^{+0.4} _{-0.2}	
G31.41+0.31	comp.	(1.0±0.2)E+18	200 ^c	6.35±0.35	2.0 ^b	97.2±0.2	7.4
	ext.	(1.2±0.6)E+16	14±2	3.95±0.40	≥14.0	97.2 ^{+0.2} _{-0.3}	

^a “comp.” for hot, compact component ; “ext.” for colder, more extended component.^b Fixed to $\theta_S, T=100\text{K}$.^c Fixed.

7.7.4 Additional detections

Several lines of other species were found in the observed frequency ranges, particularly in the line-rich G31.41+0.31. Table 7.23 lists additional detections with column densities obtained from the Weeds analysis with the best T_{ex} when this could be derived. Several transitions of acetone, CH_3COCH_3 , are detected. In G31, the best agreement is obtained at 100 K, whereas for IRAS18089, this is $T_{\text{ex}}=300$ K. No CH_3COCH_3 was detected in IRAS20126, and the tabulated value is an upper limit at 300 K. Figure 7.18 shows the strongest acetone lines in G31 together with the Weeds model.

Glycolaldehyde, HCOCH_2OH , has previously been detected in G31 (Beltrán et al. 2009), has several lines in the covered ranges. All lines are however blended with other transitions, and only upper limit could therefore be derived reliably. The tabulated column density is for a temperature of 300 K, constrained by non-detection of lines with low E_{up} .

Two transitions of HC_3N are detected at 218.325 GHz ($E_{\text{up}}131.0$ K) ($J = 24 \rightarrow 23$) and 354.697 GHz ($E_{\text{up}}340.5$ K) ($J = 39 \rightarrow 38$). The Weeds model on the two lines, well separated in E_{up} , gives a beam averaged column density of $7 \times 10^{13} \text{ cm}^{-2}$ and a temperature of 150 K for G31. The HC_3N emission cannot be matched with emission contained within a $2.0''$ volume as the low- E_{up} transition becomes optically thick. For IRAS20126, the tabulated column density is at 100 K, constrained by the two transitions. Only the high E_{up} transition was covered for IRAS18089 giving a column density of $3 \times 10^{13} \text{ cm}^{-2}$ at 150 K and $6 \times 10^{13} \text{ cm}^{-2}$ at 100 K.

Several CH_3NH_2 transitions are observed with a T_{ex} of 150 K. Blends with other species make the rotation temperature and column density inaccurate, however. Several unidentified lines coincide with $\text{NH}_2\text{CH}_2\text{CH}_2\text{OH}$, but only upper limits of $1.0 \times 10^{16} \text{ cm}^{-2}$ at 100–300 K could be derived reliably using Weeds.

Several weak lines of NH_2CN are detected, with a T_{ex} of 50 K derived from the Weeds model, but line blends make the rotation temperature and column density inaccurate. For CN, SO, ^{34}SO , O^{13}CS , OC^{34}S , SO_2 , $^{33}\text{SO}_2$, C^{34}S , and CP not enough lines were observed to derive T_{ex} values, and tabulated column densities are assuming a temperature of 50 K.

One line of HCN, $J=4-3$, was observed. HCN emission in G31 is composed of a broad (12 km s^{-1}) and a narrow (6 km s^{-1}) component (redshifted by 2.5 km s^{-1}) causing self-absorption. For IRAS18089, the broad component has a width of 7 km s^{-1} and narrow 4 km s^{-1} (redshifted by 1 km s^{-1}). For IRAS20126 the HCN emission has a very broad 20 km s^{-1} component blueshifted by 2 km s^{-1} and a narrow (5 km s^{-1}) component redshifted by 1 km s^{-1} . The tabulated column densities are those derived from the H^{13}CN column density.

Table 7.23 – Additional detections. Column densities given are source averaged for species with $T_{\text{ex}} > 100$ K and beam averaged for species with $T_{\text{ex}} < 100$ K (except for HCCCN, the emission of which is warm and arises from extended volume). The tabulated values are those obtained from Weeds analysis with the best T_{ex} .

Species	IRAS20126+4104	IRAS18089-1732	G31.41+0.31
Source-averaged column densities			
CH ₃ COCH ₃	<0.1E+17	0.5E+17	1.0E+17
HCOCH ₂ OH	–	<0.5E+16	<0.2E+17
CH ₃ NH ₂	–	–	2.4E+14
NH ₂ CH ₂ CH ₂ OH	–	–	<1.0E+16
Beam-averaged column densities			
NH ₂ CN	–	<0.1E+14	7.0E+14
OC-13-S	–	–	5.0E+14
OC-34-S	–	0.5E+15	1.0E+15
HCCCN	1.0E+13	3.0E+13	7.0E+13
S ₃	–	–	1.5E+16
CN, $v = 0, 1$	0.2E+15	0.4E+15	0.8E+15
SO ₂	0.3E+15	0.5E+15	0.1E+16
SO	0.3E+15	1.0E+15	7.0E+14
CS-34	–	1.4E+14	2.4E+14
CP	–	–	1.0E+15
S-33-O ₂	<0.5E+14	0.5E+15	1.0E+15
S-34-O	0.2E+14	0.5E+14	1.0E+14
HCN	8E+13	2.0E+14	2.0E+14
HC-13-N	0.1E+13	1.5E+13	2.0E+13

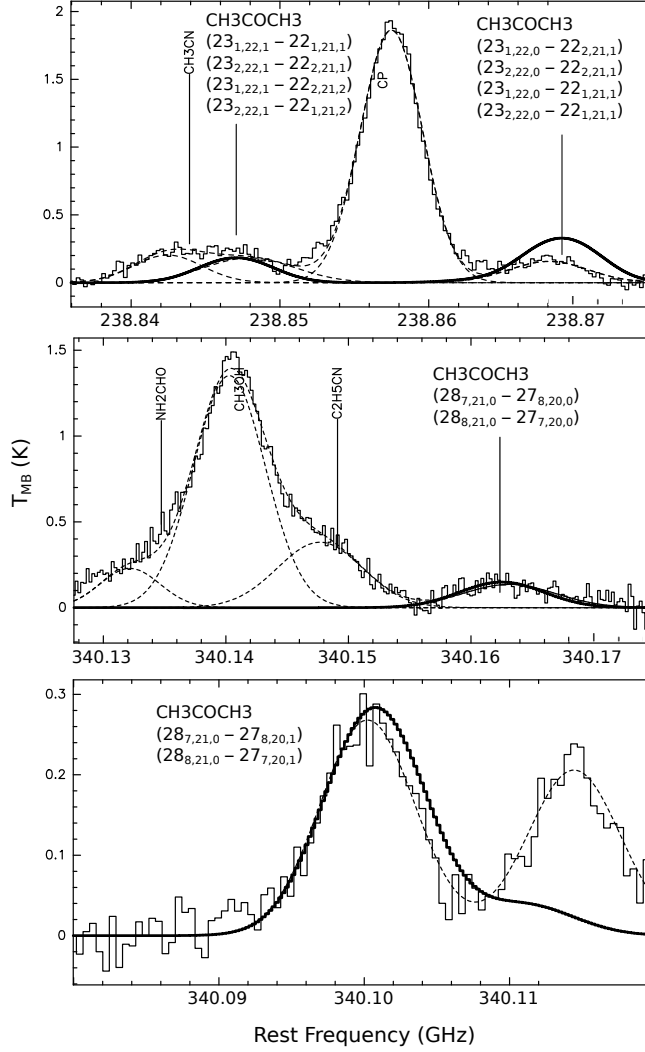


Figure 7.18 – Beam-averaged spectra of CH_3COCH_3 ($23_{1/2,22,1}-22_{1/2,21,1}$), ($23_{1/2,22,0}-22_{1/2,21,1}$), ($28_{7/8,21,0}-27_{8/7,20,0}$) and ($28_{7/8,21,1}-27_{8/7,20,1}$) towards G31.41+0.31 hot core. Dashed lines indicate Gaussian fits to the lines and red solid line show the Weeds model on the CH_3COCH_3 lines at 100 K.

Literature

- Al-Halabi, A., Fraser, H. J., Kroes, G. J., & van Dishoeck, E. F. 2004, *A&A*, 422, 777
- Allamandola, L. J., Sandford, S. A., & Valero, G. J. 1988, *Icarus*, 76, 225
- Arce, H. G., Santiago-García, J., Jørgensen, J. K., Tafalla, M., & Bachiller, R. 2008, *ApJ*, 681, L21
- Ayotte, P., Smith, R. S., Stevenson, K. P., et al. 2001, *J. Geophys. Res.*, 106, 33387
- Bachiller, R. & Perez Gutierrez, M. 1997, *ApJ*, 487, L93
- Bacmann, A., Taquet, V., Faure, A., Kahane, C., & Ceccarelli, C. 2012, *A&A*, 541, L12
- Bar-Nun, A., Dror, J., Kochavi, E., & Laufer, D. 1987, *Phys. Rev. B*, 35, 2427
- Bar-Nun, A. & Owen, T. 1998, in *Astrophysics and Space Science Library*, Vol. 227, *Solar System Ices*, ed. B. Schmitt, C. de Bergh, & M. Festou, 353
- Barabási, A.-L. & Stanley, H. E. 1995, *Fractal concepts in surface growth* (Cambridge university press)
- Baragiola, R. A. 2003, *Planet. Space Sci.*, 51, 953
- Baratta, G. A. & Palumbo, M. E. 1998, *Journal of the Optical Society of America A*, 15, 3076
- Baratta, G. A., Palumbo, M. E., & Strazzulla, G. 2000, *A&A*, 357, 1045
- Belloche, A., Garrod, R. T., Müller, H. S. P., et al. 2009, *A&A*, 499, 215
- Beltrán, M. T., Cesaroni, R., Neri, R., et al. 2005, *A&A*, 435, 901
- Beltrán, M. T., Codella, C., Viti, S., Neri, R., & Cesaroni, R. 2009, *ApJ*, 690, L93
- Benjamin, R. A., Churchwell, E., Babler, B. L., et al. 2003, *PASP*, 115, 953
- Bennett, C. J., Jamieson, C., Mebel, A. M., & Kaiser, R. I. 2004, *Physical Chemistry Chemical Physics (Incorporating Faraday Transactions)*, 6, 735
- Bennett, C. J., Jamieson, C. S., Osamura, Y., & Kaiser, R. I. 2006, *ApJ*, 653, 792
- Bennett, C. J. & Kaiser, R. I. 2007, *ApJ*, 661, 899
- Bergin, E. A., Langer, W. D., & Goldsmith, P. F. 1995, *ApJ*, 441, 222
- Bergin, E. A., Melnick, G. J., Gerakines, P. A., Neufeld, D. A., & Whittet, D. C. B. 2005, *ApJ*, 627, L33
- Bergin, E. A., Neufeld, D. A., & Melnick, G. J. 1998, *ApJ*, 499, 777
- Bergin, E. A. & Tafalla, M. 2007, *ARA&A*, 45, 339
- Berland, B. S., Brown, D. E., Tolbert, M. A., & George, S. M. 1995, *Geophys. Res. Lett.*, 22, 3493
- Bernstein, M. P., Dworkin, J. P., Sandford, S. A., Cooper, G. W., & Allamandola, L. J. 2002, *Nature*, 416, 401
- Bernstein, M. P., Sandford, S. A., & Allamandola, L. J. 2000, *ApJ*, 542, 894
- Bernstein, M. P., Sandford, S. A., Allamandola, L. J., Chang, S., & Scharberg, M. A. 1995, *ApJ*, 454, 327
- Beuther, H., Hunter, T. R., Zhang, Q., et al. 2004, *ApJ*, 616, L23
- Beuther, H., Schilke, P., Sridharan, T. K., et al. 2002, *A&A*, 383, 892
- Beuther, H. & Walsh, A. J. 2008, *ApJ*, 673, L55
- Beuther, H., Zhang, Q., Sridharan, T. K., & Chen, Y. 2005, *ApJ*, 628, 800
- Bisschop, S. E. 2007, PhD thesis, Leiden Observatory, Leiden University, P.O. Box 9513, 2300 RA

Leiden, The Netherlands

- Bisschop, S. E., Jørgensen, J. K., Bourke, T. L., Bottinelli, S., & van Dishoeck, E. F. 2008, *A&A*, 488, 959
- Bisschop, S. E., Jørgensen, J. K., van Dishoeck, E. F., & de Wachter, E. B. M. 2007, *A&A*, 465, 913
- Bjerkeli, P., Liseau, R., Olberg, M., et al. 2009, *A&A*, 507, 1455
- Blake, G. A., Sutton, E. C., Masson, C. R., & Phillips, T. G. 1987, *ApJ*, 315, 621
- Bohren, C. F. & Huffman, D. R. 1983, *Absorption and scattering of light by small particles*
- Boogaarts, M. 1996, PhD thesis, Katholieke Universiteit Nijmegen
- Boogert, A. C. A., Ehrenfreund, P., Gerakines, P. A., et al. 2000, *A&A*, 353, 349
- Boogert, A. C. A., Hogerheijde, M. R., & Blake, G. A. 2002, *ApJ*, 568, 761
- Boogert, A. C. A., Pontoppidan, K. M., Knez, C., et al. 2008, *ApJ*, 678, 985
- Boogert, A. C. A., Pontoppidan, K. M., Lahuis, F., et al. 2004, *ApJS*, 154, 359
- Boonman, A. M. S., van Dishoeck, E. F., Lahuis, F., & Doty, S. D. 2003, *A&A*, 399, 1063
- Born, M. & Wolf, E. 1975, *Principles of optics. Electromagnetic theory of propagation, interference and diffraction of light*
- Bossa, J.-B., Isokoski, K., de Valois, M. S., & Linnartz, H. 2012, *A&A*, 545, A82
- Bossa, J.-B., Paardekooper, D. M., Isokoski, K., & Linnartz, H. in prep., *A&A*
- Botta, O. & Bada, J. L. 2002, *Surveys in Geophysics*, 23, 411, 10.1023/A:1020139302770
- Bottinelli, S., Boogert, A. C. A., Bouwman, J., et al. 2010, *ApJ*, 718, 1100
- Bottinelli, S., Ceccarelli, C., Williams, J. P., & Lefloch, B. 2007, *A&A*, 463, 601
- Bouwman, J., Ludwig, W., Awad, Z., et al. 2007, *A&A*, 476, 995
- Bruderer, S., Benz, A. O., Doty, S. D., van Dishoeck, E. F., & Bourke, T. L. 2009, *ApJ*, 700, 872
- Bruderer, S., Benz, A. O., Stäuber, P., & Doty, S. D. 2010, *ApJ*, 720, 1432
- Buch, V. 1992, *J. Chem. Phys.*, 96, 3814
- Buch, V. & Devlin, J. P. 1991, *J. Chem. Phys.*, 94, 4091
- Byer, R. L. & Duncan, M. D. 1981, *J. Chem. Phys.*, 74, 2174
- Caselli, P. & Ceccarelli, C. 2012, *A&A Rev.*, 20, 56
- Cazaux, S., Cobut, V., Marseille, M., Spaans, M., & Caselli, P. 2010, *A&A*, 522, A74
- Cazaux, S., Tielens, A. G. G. M., Ceccarelli, C., et al. 2003, *ApJ*, 593, L51
- Cesaroni, R., Beltrán, M. T., Zhang, Q., Beuther, H., & Fallscheer, C. 2011, *A&A*, 533, A73
- Cesaroni, R., Churchwell, E., Hofner, P., Walmsley, C. M., & Kurtz, S. 1994a, *A&A*, 288, 903
- Cesaroni, R., Felli, M., Jenness, T., et al. 1999, *A&A*, 345, 949
- Cesaroni, R., Felli, M., Testi, L., Walmsley, C. M., & Olmi, L. 1997, *A&A*, 325, 725
- Cesaroni, R., Galli, D., Lodato, G., Walmsley, C. M., & Zhang, Q. 2007, *Protostars and Planets V*, 197
- Cesaroni, R., Hofner, P., Araya, E., & Kurtz, S. 2010, *A&A*, 509, A50
- Cesaroni, R., Hofner, P., Walmsley, C. M., & Churchwell, E. 1998, *A&A*, 331, 709
- Cesaroni, R., Neri, R., Olmi, L., et al. 2005, *A&A*, 434, 1039
- Cesaroni, R., Olmi, L., Walmsley, C. M., Churchwell, E., & Hofner, P. 1994b, *ApJ*, 435, L137
- Charnley, S. B. 1997, *ApJ*, 481, 396
- Charnley, S. B., Kress, M. E., Tielens, A. G. G. M., & Millar, T. J. 1995, *ApJ*, 448, 232
- Charnley, S. B., Rodgers, S. D., & Ehrenfreund, P. 2001, *A&A*, 378, 1024
- Charnley, S. B., Tielens, A. G. G. M., & Millar, T. J. 1992, *ApJ*, 399, L71

- Chiar, J. E., Adamson, A. J., Kerr, T. H., & Whittet, D. C. B. 1994, *ApJ*, 426, 240
- Churchwell, E., Walmsley, C. M., & Cesaroni, R. 1990, *A&AS*, 83, 119
- Churchwell, E., Wood, D., Myers, P. C., & Myers, R. V. 1986, *ApJ*, 305, 405
- Collings, M. P., Dever, J. W., Fraser, H. J., McCoustra, M. R. S., & Williams, D. A. 2003, *ApJ*, 583, 1058
- Comoretto, G., Palagi, F., Cesaroni, R., et al. 1990, *A&AS*, 84, 179
- Compagnini, G., D'Urso, L., Puglisi, O., Baratta, G. A., & Strazzulla, G. 2009, *CARBON*, 47, 1605
- Cook, A. M., Whittet, D. C. B., Shenoy, S. S., et al. 2011, *ApJ*, 730, 124
- Cronin, J. R. & Pizzarello, S. 1997, *Science*, 275, 951
- Cuppen, H. M. & Herbst, E. 2007, *ApJ*, 668, 294
- Cuppen, H. M., Ioppolo, S., Romanzin, C., & Linnartz, H. 2010, *Physical Chemistry Chemical Physics (Incorporating Faraday Transactions)*, 12, 12077
- Cuppen, H. M., Penteado, E. M., Isokoski, K., van der Marel, N., & Linnartz, H. 2011, *MNRAS*, 417, 2809
- Cuppen, H. M., van Dishoeck, E. F., Herbst, E., & Tielens, A. G. G. M. 2009, *A&A*, 508, 275
- Dartois, E., Schutte, W., Geballe, T. R., et al. 1999, *A&A*, 342, L32
- Davydov, A. 1962, *Nucl. Phys. A*, 37, 106
- Demyk, K., Dartois, E., D'Hendecourt, L., et al. 1998, *A&A*, 339, 553
- d'Hendecourt, L. B., Allamandola, L. J., & Greenberg, J. M. 1985, *A&A*, 152, 130
- d'Hendecourt, L. B. & Jourdain de Muizon, M. 1989, *A&A*, 223, L5
- Dickens, J. E., Langer, W. D., & Velusamy, T. 2001, *ApJ*, 558, 693
- Dimov, G. I. 1968, *Pribory i Tekhnika Experimenta*
- Dohnálek, Z., Kimmel, G. A., Ayotte, P., Smith, R. S., & Kay, B. D. 2003, *J. Chem. Phys.*, 118, 364
- Dulieu, F., Amiaud, L., Congiu, E., et al. 2010, *A&A*, 512, A30
- Ehrenfreund, P., Boogert, A. C. A., Gerakines, P. A., et al. 1996, *A&A*, 315, L341
- Ehrenfreund, P., Boogert, A. C. A., Gerakines, P. A., Tielens, A. G. G. M., & van Dishoeck, E. F. 1997, *A&A*, 328, 649
- Ehrenfreund, P., Dartois, E., Demyk, K., & D'Hendecourt, L. 1998, *A&A*, 339, L17
- Ehrenfreund, P., Glavin, D. P., Botta, O., Cooper, G., & Bada, J. L. 2001, *Proceedings of the National Academy of Science*, 98, 2138
- Ehrenfreund, P., Kerkhof, O., Schutte, W. A., et al. 1999, *A&A*, 350, 240
- Elkind, P. & Fraser, H. 2012, private communication
- Elsila, J. E., Dworkin, J. P., Bernstein, M. P., Martin, M. P., & Sandford, S. A. 2007, *ApJ*, 660, 911
- Ennis, C., Bennett, C. J., Jones, B. M., & Kaiser, R. I. 2011, *ApJ*, 733, 79
- Estalella, R., Mauersberger, R., Torrelles, J. M., et al. 1993, *ApJ*, 419, 698
- Falk, M. 1987, *J. Chem. Phys.*, 86, 560
- Falk, M. & Seto, P. F. 1986, *Canadian J. Spectrosc.*
- Fayolle, E. C., Öberg, K. I., Cuppen, H. M., Visser, R., & Linnartz, H. 2011, *A&A*, 529, A74
- Fontani, F., Pascucci, I., Caselli, P., et al. 2007, *A&A*, 470, 639
- Fraser, H. J., Collings, M. P., Dever, J. W., & McCoustra, M. R. S. 2004, *MNRAS*, 353, 59
- Fuchs, G. W., Cuppen, H. M., Ioppolo, S., et al. 2009, *A&A*, 505, 629
- Gálvez, O., Maté, B., Herrero, V. J., & Escribano, R. 2010, *ApJ*, 724, 539

- Garrod, R. T. & Herbst, E. 2006, *A&A*, 457, 927
- Garrod, R. T., Weaver, S. L. W., & Herbst, E. 2008, *ApJ*, 682, 283
- Gaume, R. A. & Mutel, R. L. 1987, *ApJS*, 65, 193
- Gentry, W. R. & Giese, C. F. 1978, *Review of Scientific Instruments*, 49, 595
- Geppert, W. D., Hamberg, M., Thomas, R. D., et al. 2006, *Faraday Discussions*, 133, 177
- Gerakines, P. A., Moore, M. H., & Hudson, R. L. 2001, *J. Geophys. Res.*, 106, 33381
- Gerakines, P. A., Schutte, W. A., & Ehrenfreund, P. 1996, *A&A*, 312, 289
- Gerakines, P. A., Schutte, W. A., Greenberg, J. M., & van Dishoeck, E. F. 1995, *A&A*, 296, 810
- Gerakines, P. A., Whittet, D. C. B., Ehrenfreund, P., et al. 1999, *ApJ*, 522, 357
- Gibb, E., Nummelin, A., Irvine, W. M., Whittet, D. C. B., & Bergman, P. 2000, *ApJ*, 545, 309
- Gibb, E. L., Whittet, D. C. B., Boogert, A. C. A., & Tielens, A. G. G. M. 2004, *ApJS*, 151, 35
- Givan, A., Loewenschuss, A., & Nielsen, C. J. 1996, *Vib. Spectrosc.*, vol. 12, p. 1-14 (1996)., 12, 1
- Goldsmith, P. F. & Langer, W. D. 1999, *ApJ*, 517, 209
- Goumans, T., Catlow, C. R. A., Brown, W. A., Kästner, J., & Sherwood, P. 2009, *Phys. Chem. Chem. Phys.*, 11, 5431
- Gredel, R., Lepp, S., Dalgarno, A., & Herbst, E. 1989, *ApJ*, 347, 289
- Greenberg, J. M., Gillette, J. S., Muñoz Caro, G. M., et al. 2000, *ApJ*, 531, L71
- Grim, R. J. A. & Greenberg, J. M. 1987, *ApJ*, 321, L91
- Gudipati, M. S. & Yang, R. 2012, *ApJ*, 756, L24
- Guilhaus, M. 1995, *Journal of Mass Spectrometry*, 30, 1519
- Hagen, W. 1981, *Chemical Physics*, 56, 367
- Hagen, W., Allamandola, L. J., & Greenberg, J. M. 1979, *Ap&SS*, 65, 215
- Hagen, W., Tielens, A. G. G. M., & Greenberg, J. M. 1983, *A&AS*, 51, 389
- Hahn, J. H., Zenobi, R., Bada, J. L., & Zare, R. N. 1988, *Science*, 239, 1523
- Håkansson, K., Zubarev, R., & Håkansson, P. 1998, *Rapid Commun. in Mass Spectrom.*, 12, 705
- Hallbrucker, A., Mayer, E., & Johari, G. P. 1989, *Journal of Physical Chemistry*
- Hasegawa, T. I., Herbst, E., & Leung, C. M. 1992, *ApJS*, 82, 167
- Hatchell, J., Thompson, M. A., Millar, T. J., & MacDonald, G. H. 1998, *A&AS*, 133, 29
- Herbst, E. 1995, *Annual Review of Physical Chemistry*, 46, 27
- Herbst, E., Green, S., Thaddeus, P., & Klemperer, W. 1977, *ApJ*, 215, 503
- Herbst, E. & van Dishoeck, E. F. 2009, *ARA&A*, 47, 427
- Hessinger, J., White, Jr., B. E., & Pohl, R. O. 1996, *Planet. Space Sci.*, 44, 937
- Hiraoka, K., Sato, T., Sato, S., et al. 2002, *ApJ*, 577, 265
- Hodyss, R., Johnson, P. V., Orzechowska, G. E., Goguen, J. D., & Kanik, I. 2008, *Icarus*, 194, 836
- Hofner, P., Cesaroni, R., Rodríguez, L. F., & Martí, J. 1999, *A&A*, 345, L43
- Hollis, J. M., Lovas, F. J., & Jewell, P. R. 2000, *ApJ*, 540, L107
- Horimoto, N., Kato, H. S., & Kawai, M. 2002, *J. Chem. Phys.*, 116, 4375
- Horn, A., Møllendal, H., Sekiguchi, O., et al. 2004, *ApJ*, 611, 605
- Howett, C. J. A., Carlson, R. W., Irwin, P. G. J., & Calcutt, S. B. 2007, *Journal of the Optical Society of America B Optical Physics*, 24, 126
- Huang, H.-C., Kuan, Y.-J., Charnley, S. B., et al. 2005, *Advances in Space Research*, 36, 146
- Hudgins, D. M., Sandford, S. A., Allamandola, L. J., & Tielens, A. G. G. M. 1993, *ApJS*, 86, 713
- Hudson, R. L. & Moore, M. H. 1999, *Icarus*, 140, 451
- Hudson, R. L., Moore, M. H., & Raines, L. L. 2009, *Icarus*, 203, 677

- Ioppolo, S., Cuppen, H. M., Romanzin, C., van Dishoeck, E. F., & Linnartz, H. 2008, *ApJ*, 686, 1474
- Ioppolo, S., Cuppen, H. M., Romanzin, C., van Dishoeck, E. F., & Linnartz, H. 2010, *Physical Chemistry Chemical Physics (Incorporating Faraday Transactions)*, 12, 12065
- Ioppolo, S., Palumbo, M. E., Baratta, G. A., & Mennella, V. 2009, *A&A*, 493, 1017
- Ioppolo, S., van Boheemen, Y., Cuppen, H. M., van Dishoeck, E. F., & Linnartz, H. 2011, *MNRAS*, 413, 2281
- Isokoski, K., Poteet, C., & Linnartz, H. in prep., *A&A*
- Jackson, W. M., Faris, J., & Buccos, N. J. 1966, *J. Chem. Phys.*, 45, 4145
- Jamieson, C. S., Mebel, A. M., & Kaiser, R. I. 2006, *ApJS*, 163, 184
- Jenniskens, P. & Blake, D. F. 1994, *Science*, 265, 753
- Jenniskens, P., Blake, D. F., Wilson, M. A., & Pohorille, A. 1995, *ApJ*, 455, 389
- Jing, D., He, J., Brucato, J., et al. 2011, *ApJ*, 741, L9
- Johnston, K. G., Keto, E., Robitaille, T. P., & Wood, K. 2011, *MNRAS*, 415, 2953
- Jørgensen, J. K., Bourke, T. L., Myers, P. C., et al. 2005, *ApJ*, 632, 973
- Kahane, C., Lucas, R., Frerking, M. A., Langer, W. D., & Encrenaz, P. 1984, *A&A*, 137, 211
- Kaiser, R. I. & Roessler, K. 1998, *ApJ*, 503, 959
- Karas, M., Bachmann, D., Bahr, U., & Hillenkamp, F. 1987, *International Journal of Mass Spectrometry and Ion Processes*, 78, 53
- Keane, J. V., Boogert, A. C. A., Tielens, A. G. G. M., Ehrenfreund, P., & Schutte, W. A. 2001, *A&A*, 375, L43
- Keesom, W. H. & Köhler, J. W. L. 1934, *Physica*, 1, 655
- Kerr, F. J. & Lynden-Bell, D. 1986, *MNRAS*, 221, 1023
- Kerr, T. H., Adamson, A. J., & Whittet, D. C. B. 1993, *MNRAS*, 262, 1047
- Kim, H. J., Evans, II, N. J., Dunham, M. M., Lee, J.-E., & Pontoppidan, K. M. 2012, *ApJ*, 758, 38
- Kim, S.-H., Martin, P. G., & Hendry, P. D. 1994, *ApJ*, 422, 164
- Kim, Y. S., Bennett, C. J., Chen, L.-H., O'Brien, K., & Kaiser, R. I. 2010, *ApJ*, 711, 744
- Kimmel, G. A., Dohnálek, Z., Stevenson, K. P., Smith, R. S., & Kay, B. D. 2001a, *J. Chem. Phys.*, 114, 5295
- Kimmel, G. A., Stevenson, K. P., Dohnálek, Z., Smith, R. S., & Kay, B. D. 2001b, *J. Chem. Phys.*, 114, 5284
- Knez, C., Boogert, A. C. A., Pontoppidan, K. M., et al. 2005, *ApJ*, 635, L145
- Knez, C., Lacy, J. H., Evans, II, N. J., van Dishoeck, E. F., & Richter, M. J. 2009, *ApJ*, 696, 471
- Kouchi, A. & Yamamoto, T. 1995, *Progress in Crystal Growth and Characterization of Materials*
- Kuan, Y.-J., Huang, H.-C., Charnley, S. B., et al. 2004, *ApJ*, 616, L27
- Kurtz, S., Cesaroni, R., Churchwell, E., Hofner, P., & Walmsley, C. M. 2000, *Protostars and Planets IV*, 299
- Kvenvolden, K., Lawless, J., Pering, K., et al. 1970, *Nature*, 228, 923
- Lawless, J. G., Kvenvolden, K. A., Peterson, E., & Ponnampertuma, C. 1972, *Nature*, 236, 66
- Laurini, S., Schilke, P., Wyrowski, F., & Menten, K. M. 2007, *A&A*, 466, 215
- Levis, R. J. 1994, *Annual Review of Physical Chemistry*, 45, 483
- Loerting, T., Salzmann, C., Kohl, I., Mayer, E., & Hallbrucker, A. 2001, *Physical Chemistry Chemical Physics (Incorporating Faraday Transactions)*, 3, 5355
- Manca, C. 2000, *Chemical Physics Letters*, 330, 21

- Manicò, G., Ragunì, G., Pirronello, V., Roser, J. E., & Vidali, G. 2001, *ApJ*, 548, L253
- Maret, S., Ceccarelli, C., Tielens, A. G. G. M., et al. 2005, *A&A*, 442, 527
- Maret, S., Hily-Blant, P., Pety, J., Bardeau, S., & Reynier, E. 2011, *A&A*, 526, A47
- Markwick, A. J., Millar, T. J., & Charnley, S. B. 2000, *ApJ*, 535, 256
- Martin, C. 2002, *Surface Science*, 502, 280
- Matar, E., Congiu, E., Dulieu, F., Momeni, A., & Lemaire, J. L. 2008, *A&A*, 492, L17
- Mayer, E. & Pletzer, R. 1986, *Nature*, 319, 298
- McKee, C. F. & Ostriker, E. C. 2007, *ARA&A*, 45, 565
- Meijer, G., de Vries, M. S., Hunziker, H. E., & Wendt, H. R. 1990, *Applied Physics B: Lasers and Optics*, 51, 395
- Melnick, G. J. & Bergin, E. A. 2005, *Advances in Space Research*, 36, 1027
- Mennella, V., Palumbo, M. E., & Baratta, G. A. 2004, *ApJ*, 615, 1073
- Millar, T. J., Herbst, E., & Charnley, S. B. 1991, *ApJ*, 369, 147
- Mishima, O. 1996, *Nature*, 384, 546
- Mishima, O., Calvert, L. D., & Whalley, E. 1984, *Nature*, 310, 393
- Miyauchi, N., Hidaka, H., Chigai, T., et al. 2008, *Chemical Physics Letters*, 456, 27
- Mokrane, H., Chaabouni, H., Accolla, M., et al. 2009, *ApJ*, 705, L195
- Moore, M. H. & Hudson, R. L. 1998, *Icarus*, 135, 518
- Moscadelli, L., Cesaroni, R., Rioja, M. J., Dodson, R., & Reid, M. J. 2011, *A&A*, 526, A66
- Mottier, P. & Valette, S. 1981, *Appl. Opt.*, 20, 1630
- Muñoz Caro, G. M., Meierhenrich, U. J., Schutte, W. A., et al. 2002, *Nature*, 416, 403
- Muñoz Caro, G. M. & Schutte, W. A. 2003, *A&A*, 412, 121
- Müller, H. S. P., Schlöder, F., Stutzki, J., & Winnewisser, G. 2005, *Journal of Molecular Structure*, 742, 215
- Narten, A. H., Venkatesh, C. G., & Rice, S. A. 1976, *J. Chem. Phys.*, 64, 1106
- Novozamsky, J. H., Schutte, W. A., & Keane, J. V. 2001, *A&A*, 379, 588
- Nuevo, M., Auger, G., Blanot, D., & D'Hendecourt, L. 2008, *Origins of Life and Evolution of the Biosphere*, 38, 37
- Nuevo, M., Bredehöft, J. H., Meierhenrich, U. J., d'Hendecourt, L., & Thiemann, W. H.-P. 2010, *Astrobiology*, 10, 245
- Nummelin, A., Bergman, P., Hjalmarsen, Å., et al. 2000, *ApJS*, 128, 213
- Nummelin, A., Whittet, D. C. B., Gibb, E. L., Gerakines, P. A., & Chiar, J. E. 2001, *ApJ*, 558, 185
- Oba, Y., Miyauchi, N., Hidaka, H., et al. 2009, *ApJ*, 701, 464
- Öberg, K. I., Boogert, A. C. A., Pontoppidan, K. M., et al. 2011a, *ApJ*, 740, 109
- Öberg, K. I., Bottinelli, S., Jørgensen, J. K., & van Dishoeck, E. F. 2010, *ApJ*, 716, 825
- Öberg, K. I., Fayolle, E. C., Cuppen, H. M., van Dishoeck, E. F., & Linnartz, H. 2009a, *A&A*, 505, 183
- Öberg, K. I., Fuchs, G. W., Awad, Z., et al. 2007, *ApJ*, 662, L23
- Öberg, K. I., Garrod, R. T., van Dishoeck, E. F., & Linnartz, H. 2009b, *A&A*, 504, 891
- Öberg, K. I., van Broekhuizen, F., Fraser, H. J., et al. 2005, *ApJ*, 621, L33
- Öberg, K. I., van der Marel, N., Kristensen, L. E., & van Dishoeck, E. F. 2011b, *ApJ*, 740, 14
- Olmi, L., Cesaroni, R., & Walmsley, C. M. 1996, *A&A*, 307, 599
- Palumbo, M. E. 2005, *Journal of Physics Conference Series*, 6, 211
- Palumbo, M. E. 2006, *A&A*, 453, 903

- Palumbo, M. E., Baratta, G. A., Leto, G., & Strazzulla, G. 2010, *Journal of Molecular Structure*, 972, 64
- Palumbo, M. E., Pendleton, Y. J., & Strazzulla, G. 2000, *ApJ*, 542, 890
- Palumbo, M. E. & Strazzulla, G. 1993, *A&A*, 269, 568
- Papoular, R. 2005, *MNRAS*, 362, 489
- Pendleton, Y. J., Tielens, A. G. G. M., Tokunaga, A. T., & Bernstein, M. P. 1999, *ApJ*, 513, 294
- Pestalozzi, M. R., Elitzur, M., & Conway, J. E. 2009, *A&A*, 501, 999
- Pestalozzi, M. R., Elitzur, M., Conway, J. E., & Booth, R. S. 2004, *ApJ*, 603, L113
- Pickett, H. M., Poynter, R. L., Cohen, E. A., et al. 1998, *J. Quant. Spec. Radiat. Transf.*, 60, 883
- Pontoppidan, K. M. 2006, *A&A*, 453, L47
- Pontoppidan, K. M., Boogert, A. C. A., Fraser, H. J., et al. 2008, *ApJ*, 678, 1005
- Pontoppidan, K. M., Dartois, E., van Dishoeck, E. F., Thi, W.-F., & d'Hendecourt, L. 2003a, *A&A*, 404, L17
- Pontoppidan, K. M., Fraser, H. J., Dartois, E., et al. 2003b, *A&A*, 408, 981
- Pontoppidan, K. M., van Dishoeck, E. F., & Dartois, E. 2004, *A&A*, 426, 925
- Posthumus, M. A., Kistemaker, P. G., Meuzelaar, H. L. C., & Ten Noever de Brauw, M. C. 1978, *Analytical Chemistry*, 50, 985
- Poteet, C. A., Megeath, S. T., Watson, D. M., et al. 2011, *ApJ*, 733, L32
- Prasad, S. S. & Tarafdar, S. P. 1983, *ApJ*, 267, 603
- Raut, U., Famá, M., Loeffler, M. J., & Baragiola, R. A. 2008, *ApJ*, 687, 1070
- Raut, U., Famá, M., Teolis, B. D., & Baragiola, R. A. 2007a, *J. Chem. Phys.*, 127, 204713
- Raut, U., Teolis, B. D., Loeffler, M. J., et al. 2007b, *J. Chem. Phys.*, 126, 244511
- Requena-Torres, M. A., Martín-Pintado, J., Martín, S., & Morris, M. R. 2008, *ApJ*, 672, 352
- Romanescu, C., Marschall, J., Kim, D., Khatiwada, A., & Kalogerakis, K. S. 2010, *Icarus*, 205, 695
- Romanzin, C., Ioppolo, S., Cuppen, H. M., van Dishoeck, E. F., & Linnartz, H. 2011, *J. Chem. Phys.*, 134, 084504
- Rorden, R. J. & Lubman, D. M. 1983, *Review of Scientific Instruments*, 54, 641
- Roser, J. E., Vidali, G., Manicò, G., & Pirronello, V. 2001, *ApJ*, 555, L61
- Rowland, B. & Devlin, J. P. 1991, *J. Chem. Phys.*, 94, 812
- Rowland, B., Fisher, M., & Devlin, J. P. 1991, *J. Chem. Phys.*, 95, 1378
- Sandford, S. A. & Allamandola, L. J. 1990, *ApJ*, 355, 357
- Sandford, S. A., Allamandola, L. J., Tielens, A. G. G. M., & Valero, G. J. 1988, *ApJ*, 329, 498
- Satorre, M. Á., Domingo, M., Millán, C., et al. 2008, *Planet. Space Sci.*, 56, 1748
- Scheer, M. D., McNesby, J., & Klein, R. 1962, *J. Chem. Phys.*, 36, 3504
- Schilke, P., Groesbeck, T. D., Blake, G. A., & Phillips, T. G. 1997, *ApJS*, 108, 301
- Schmitt, B., Greenberg, J. M., & Grim, R. J. A. 1989, *ApJ*, 340, L33
- Schutte, W. A. 1988, PhD thesis, PhD thesis, University of Leiden, Leiden, (1988)
- Schutte, W. A., Allamandola, L. J., & Sandford, S. A. 1993a, *Icarus*, 104, 118
- Schutte, W. A., Allamandola, L. J., & Sandford, S. A. 1993b, *Science*, 259, 1143
- Schutte, W. A., Boogert, A. C. A., Tielens, A. G. G. M., et al. 1999, *A&A*, 343, 966
- Schutte, W. A. & Greenberg, J. M. 1997, *A&A*, 317, L43
- Sciortino, F., Geiger, A., & Stanley, H. E. 1992, *J. Chem. Phys.*, 96, 3857
- Sephton, M. A. 2002, *Nat. Prod. Rep.*, 19, 292

- Shepherd, D. S., Yu, K. C., Bally, J., & Testi, L. 2000, *ApJ*, 535, 833
- Shu, F. H., Adams, F. C., & Lizano, S. 1987, *ARA&A*, 25, 23
- Skinner, C. J., Tielens, A. G. G. M., Barlow, M. J., & Justtanont, K. 1992, *ApJ*, 399, L79
- Smalley, R. E., Wharton, L., Levy, D. H., & Chandler, D. W. 1977, *Journal of Molecular Spectroscopy*, 66, 375
- Snyder, L. E. 2006, *Proceedings of the National Academy of Science*, 103, 12243
- Snyder, L. E., Buhl, D., Schwartz, P. R., et al. 1974, *ApJ*, 191, L79
- Sridharan, T. K., Beuther, H., Schilke, P., Menten, K. M., & Wyrowski, F. 2002, *ApJ*, 566, 931
- Sridharan, T. K., Williams, S. J., & Fuller, G. A. 2005, *ApJ*, 631, L73
- Stevenson, K. P., Kimmel, G. A., Dohnalek, Z., Smith, R. S., & Kay, B. D. 1999, *Science*, 283, 1505
- Stief, L. J., Decarlo, V. J., & Hillman, J. J. 1965, *J. Chem. Phys.*, 43, 2490
- Strazzulla, G., Baratta, G. A., Domingo, M., & Satorre, M. A. 2002, *Nuclear Instruments and Methods in Physics Research B*, 191, 714
- Sutton, E. C., Blake, G. A., Masson, C. R., & Phillips, T. G. 1985, *ApJS*, 58, 341
- Teixeira, T. C., Emerson, J. P., & Palumbo, M. E. 1998, *A&A*, 330, 711
- Thi, W.-F., van Dishoeck, E. F., Dartois, E., et al. 2006, *A&A*, 449, 251
- Tielens, A. G. G. M. & Allamandola, L. J. 1987, in *NATO ASIC Proc. 210: Physical Processes in Interstellar Clouds*, ed. G. E. Morfill & M. Scholer, 333–376
- Tielens, A. G. G. M. & Charnley, S. B. 1997, *Origins of Life and Evolution of the Biosphere*, 27, 23
- Tielens, A. G. G. M. & Hagen, W. 1982, *A&A*, 114, 245
- Tielens, A. G. G. M., Tokunaga, A. T., Geballe, T. R., & Baas, F. 1991, *ApJ*, 381, 181
- Tofani, G., Felli, M., Taylor, G. B., & Hunter, T. R. 1995, *A&AS*, 112, 299
- Tso, T. & Lee, E. 1985, *J. Phys. Chem.*
- van Broekhuizen, F. A., Groot, I. M. N., Fraser, H. J., van Dishoeck, E. F., & Schlemmer, S. 2006, *A&A*, 451, 723
- van der Tak, F. F. S., Walmsley, C. M., Herpin, F., & Ceccarelli, C. 2006, *A&A*, 447, 1011
- van Dishoeck, E. F. 2004, *ARA&A*, 42, 119
- van Dishoeck, E. F., Blake, G. A., Jansen, D. J., & Groesbeck, T. D. 1995, *ApJ*, 447, 760
- van Dishoeck, E. F. & Helmich, F. P. 1996, *A&A*, 315, L177
- van Dishoeck, E. F., Helmich, F. P., de Graauw, T., et al. 1996, *A&A*, 315, L349
- Wakelam, V., Smith, I. W. M., Herbst, E., et al. 2010, *Space Sci. Rev.*, 156, 13
- Wang, K.-S., van der Tak, F. F. S., & Hogerheijde, M. R. 2012, *A&A*, 543, A22
- Warren, S. G. 1984, *Appl. Opt.*, 23, 1206
- Watanabe, N. & Kouchi, A. 2002, *ApJ*, 567, 651
- Watanabe, N., Nagaoka, A., Hidaka, H., et al. 2006, *Planet. Space Sci.*, 54, 1107
- Watanabe, N., Nagaoka, A., Shiraki, T., & Kouchi, A. 2004, *ApJ*, 616, 638
- Westley, M. S., Baratta, G. A., & Baragiola, R. A. 1998, *J. Chem. Phys.*, 108, 3321
- White, D. W., Gerakines, P. A., Cook, A. M., & Whittet, D. C. B. 2009, *ApJS*, 180, 182
- Whittet, D. C. B., Cook, A. M., Chiar, J. E., et al. 2009, *ApJ*, 695, 94
- Whittet, D. C. B., Gerakines, P. A., Tielens, A. G. G. M., et al. 1998, *ApJ*, 498, L159
- Whittet, D. C. B., Schutte, W. A., Tielens, A. G. G. M., et al. 1996, *A&A*, 315, L357
- Whittet, D. C. B., Shenoy, S. S., Bergin, E. A., et al. 2007, *ApJ*, 655, 332

- Widicus Weaver, S. L., Butler, R. A. H., Drouin, B. J., et al. 2005, *ApJS*, 158, 188
- Wilking, B. A., Blackwell, J. H., & Mundy, L. G. 1990, *AJ*, 100, 758
- Willacy, K., Klahr, H. H., Millar, T. J., & Henning, T. 1998, *A&A*, 338, 995
- Williams, D. A., Hartquist, T. W., & Whittet, D. C. B. 1992, *MNRAS*, 258, 599
- Winnewisser, G. & Gardner, F. F. 1976, *A&A*, 48, 159
- Wooden, D. H., Harker, D. E., & Brearley, A. J. 2005, in *Astronomical Society of the Pacific Conference Series*, Vol. 341, *Chondrites and the Protoplanetary Disk*, ed. A. N. Krot, E. R. D. Scott, & B. Reipurth, 774
- Woon, D. E. 2008, *The astrochymist*
- Xu, Y., Moscadelli, L., Reid, M. J., et al. 2011, *ApJ*, 733, 25
- Yamada, H. & Person, W. B. 1964, *J. Chem. Phys.*, 41, 2478
- Zasowski, G., Kemper, F., Watson, D. M., et al. 2009, *ApJ*, 694, 459
- Zernickel, A., Schilke, P., Schmiedeke, A., et al. 2012, *A&A*, 546, A87
- Zhang, Q., Hunter, T. R., & Sridharan, T. K. 1998, *ApJ*, 505, L151
- Zinnecker, H. & Yorke, H. W. 2007, *ARA&A*, 45, 481
- Ziurys, L. M. & McGonagle, D. 1993, *ApJS*, 89, 155

Nederlandse samenvatting:

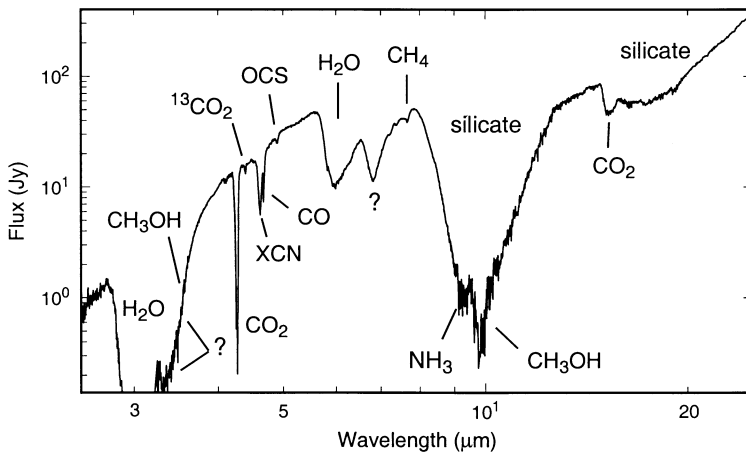
Fysica en chemie van het interstellaire ijs

Introductie

Interstellair ijs speelt een belangrijke rol in een aantal astrochemische processen. Gasfase reacties die afhankelijk zijn van botsingen tussen drie deeltjes zijn zeer zeldzaam in het ijle interstellaire medium. Maar aan het oppervlak van koude stofdeeltjes kunnen moleculen blijven plakken - er ontstaan laagjes ijs - en op en in dit molecuul reservoir kunnen vooral vrije atomen en radicalen reacties aangaan. De samenstelling en structuur van het ijs heeft een belangrijke invloed op deze processen. Daarnaast weerspiegelen de eigenschappen van interstellair ijs de geschiedenis hoe het is gevormd en is geëvolueerd is. Het proefschrift dat hier voor u ligt bespreekt de natuurkundige en chemische processen in interstellaire ijs, die zijn onderzocht met behulp van zowel astronomische waarnemingen als experimentele laboratorium technieken.

Het interstellaire medium (ISM) – per definitie al het materiaal dat zich bevindt tussen de sterren in een sterrenstelsel – is inhomogeen verdeeld over gas (99%) en stof (1%). In sommige gebieden van het ISM - grote moleculaire gaswolken - is de aanwezige massa zo hoog dat materiaal onder zijn eigen zwaartekracht ineens kan storten, hetgeen uiteindelijk leidt tot de geboorte van een nieuwe ster. De buitenkant van dit soort wolken, absorbeert het energierijk interstellair Ultraviolet (UV) licht dat het interstellaire stralingsveld domineert. Daardoor neemt binnenin de wolken de temperatuur sterk af. Onder 25 K vriezen vrijwel alle moleculen vast op stofdeeltjes en hierbij ontstaat interstellair ijs op een tijdschaal van ~400,000 jaar. De moleculaire samenstelling van dit nieuw gevormde interstellaire ijs wordt gedomineerd door water (H_2O), maar bevat ook significante hoeveelheden H_2CO , CO_2 , H_2O_2 , NH_3 , CH_4 , CO en CH_3OH (figuur 1). Afgeschermd van het UV licht, kunnen deze atomen en moleculen reacties met elkaar aan gaan.

In tegenstelling tot interstellair UV licht, kan kosmische straling diep doordringen in moleculaire wolken. Naast directe interactie met het ijs kan deze straling ook H_2 exciteren. Als gevolg hiervan zal H_2 straling uitzenden, rond 121 nm. Dit UV licht heeft een lagere stralingsdichtheid dan de energierijke UV straling buiten de wolk, maar is nog steeds sterk genoeg om fotochemische reacties in het interstellair ijs te veroorzaken. Zowel UV als kosmische straling kan bindingen in ijs moleculen breken, waardoor zeer reactieve radicalen ontstaan. De radicalen kunnen recombineren tot de oorspronkelijke moleculen of, wanneer ze voldoende energie hebben, zich verplaatsen door het ijs en reageren met andere deeltjes, waardoor nieuwe moleculen ontstaan. Radicalen kunnen ook vast

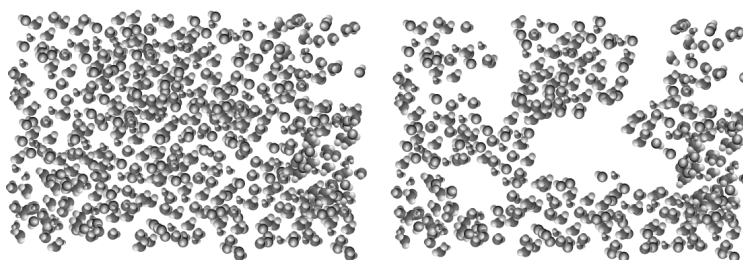


Figuur 1 – Infrarood spectrum van de W33A protoster (uit [Gibb et al. \(2000\)](#)).

komen te zitten in het ijs, en zijn dan verankerd totdat er een verandering ontstaat in de ijscondities. De geboorte van een nieuwe ster en de continue inval van materiaal zorgt ervoor dat de temperatuur van het interstellair ijs in de buurt van de ster toeneemt. Eén van de consequenties hiervan is dat atomen, moleculen en radicalen, mobiel worden en met elkaar kunnen reageren, waardoor grotere moleculen ontstaan. De reactie efficiëntie van dit proces wordt mede beïnvloed door structurele veranderingen in het interstellaire ijs. De hoeveelheid oppervlak die een ijs heeft, bijvoorbeeld, dient voor sommige reacties als katalysator, en de mate van porositeit van een ijs bepaalt dus de efficiëntie van deze reacties. Niet alleen de structuur van het ijs is van belang, ook de samenstelling. Die laatste verandert weer met de temperatuur. Op hogere temperaturen zullen vluchtige componenten verdampen, waardoor er een segregatie ontstaat van gemengde ijs componenten. Uiteindelijk zal al het ijs dichtbij de ster verdampen

Verschillende complexe moleculen, zoals C_2H_2OH , $HCOOCH_3$ en CH_3OCH_3 zijn met telescopen gedetecteerd in de gasfase. De waargenomen dichtheden kunnen niet worden verklaard met gasfase reacties van eenvoudige moleculen. Men denkt dat een groot gedeelte van de gevonden complexe moleculen ontstaan moet zijn in het ijs op stofdeeltjes en dat deze pas later, toen de temperatuur verder opliep, verdampen. Alles wijst erop, dat in interstellair ijs een complex netwerk van vaste stof reacties plaats vindt, maar veel van deze processen zijn nog niet goed begrepen.

Dit proefschrift draagt bij aan het begrip van de fysische en chemische eigenschappen van interstellair ijs. Eén van de doelen is om te begrijpen wat de structuur en samenstelling van ijs in de ruimte is, en hoe deze worden beïnvloed door het verwarmingsproces vlak voor de geboorte van een ster (hoofdstuk 2 en 3). We proberen de samenstelling van interstellaire ijs te begrijpen door spectra uit het laboratorium te vergelijken met spectra verkregen met telescopen (hoofdstuk 4 en 5). Dit proefschrift beschrijft verder een nieuwe experimentele opstelling waarmee de vorming van complexe moleculen in ijs onder interstellaire condities wordt nagebootst (hoofdstuk 6) en laat zien hoe dergelijke stoffen gebruikt kunnen worden als observationele indicatoren voor grote schaal processen in het ISM.



Figuur 2 – Compact (links) en poreus (rechts) amorf water ijs.

Morfologie van het interstellair ijs

De structuur van ijs beïnvloedt de chemie in het interstellair medium. Figuur 2 illustreert het verschil tussen compact en poreus water ijs. Poreus H_2O -ijs heeft een zeer groot oppervlak (in de grootte orde van $\sim 100 \text{ m}^2/\text{g}$), en dit werkt als katalysator voor interstellair oppervlakte reacties. Wanneer de porositeit (en dus de hoeveelheid oppervlak) afneemt, zal de efficiëntie van deze oppervlakte reacties afnemen. Gelijktijdig kan een dergelijke verandering ook de chemische reactiviteit van vastzittende moleculen en radicalen versnellen.

Het doel van hoofdstuk 2 en 3 is om de structurele veranderingen, als gevolg van een opwarm proces (zoals rond een jonge ster) voor poreus H_2O en CO_2 ijs te karakteriseren. In het interstellair medium wordt ijs mogelijk zeer poreus gevormd. Verwarming door de ster zorgt er voor dat de porositeit geleidelijk aan af neemt. In het laboratorium, wordt dit waargenomen als het dunner worden van het ijs en het verzwakken van spectrale vingerafdrukken die typisch zijn voor een poreus ijs. In het geval van H_2O ijs, neemt de dikte met 12% af tussen 22 en 120 K en zorgt een fase overgang voor een versnelling van dit proces bij 38 K. Het is opmerkelijk dat niet alle porositeit verloren gaat in het opwarm proces. Het ijs heeft een geheugen van zijn oorspronkelijke structuur, tot op het moment dat ijs moleculen verdampen. De aanwezigheid van porositeit bij hogere temperaturen draagt bij aan de katalytische eigenschappen van het ijs. Daarnaast kunnen vluchtige moleculen vast komen te zitten in poriën, en verdampen pas wanneer ook de ijs matrix zelf verdampt. Men is er tot nu toe vanuit gegaan, dat interstellair H_2O ijs compact en amorf is, zogenaamd c-ASW, voornamelijk op grond van de missende spectrale vingerafdrukken die typisch zijn voor H_2O moleculen die deels vrij kunnen trillen aan oppervlaktes. In dit proefschrift wordt aangetoond, dat thermische processen deze vingerafdrukken doen verdwijnen, terwijl een gedeelte van de porositeit gewoon blijft voortbestaan. Het is waarschijnlijk dat in de ruimte meer poreus amorf ijs (zogenaamd p-ASW) voorhanden is, dan tot nu toe werd aangenomen.

Spectroscopie van interstellair ijs

Hoofdstuk 4 en 5 richten zich op de interpretatie van de spectroscopische kenmerken van interstellair ijs. Na H_2O is vooral CO prominent aanwezig als component van interstellair ijs. CO ijs is waargenomen in pure vorm, gemengd met CO_2 en in een waterstof-binding-rijke omgeving. In de

afgelopen jaren werd vooral water genoemd als mengcomponent om zo'n omgeving te verklaren. Echter laboratorium metingen aan CO en H₂O ijs waren niet in staat om de astronomische waarnemingen te reproduceren. In hoofdstuk 4 is daarom de spectroscopische vingerafdruk van CO onderzocht voor wisselwerkingen met verschillende, waterstof bevattende moleculen, en de resulterende spectra zijn met waarnemingen vergeleken. Het werk in hoofdstuk 4 laat zien, dat het mogelijk is de astronomische waarnemingen te verklaren met een ijs mengsel van CO en CH₃OH (methanol), maar zonder water. Inderdaad tonen laboratorium experimenten aan, dat methanol uit CO gevormd kan worden door toevoeging van waterstof atomen en de gevonden spectra zijn volledig consistent met de chemische modellen.

In hoofdstuk 5 worden de spectrale eigenschappen van puur CO₂ ijs besproken. De spectrale eigenschappen van CO₂ ijs zijn uitermate gevoelig voor de omgeving waarin het CO₂ zich bevindt, en kunnen net als bij CO ijs, gebruikt worden om de samenstelling van interstellair ijs af te leiden. Een aantal banden van CO₂ ijs zijn zeer smal, en mede daarom tot op heden niet goed gekarakteriseerd in laboratorium metingen. Daardoor is de interpretatie van interstellair CO₂ ijs, met name richting bronnen met een grote hoeveelheid puur CO₂ ijs niet volledig betrouwbaar. In dit hoofdstuk worden de ontbrekende hoge resolutie data in het infrarood voor puur CO₂ ijs gepresenteerd voor temperaturen tussen 15 en 75 K.

Complexe moleculen in het laboratorium

Het waarnemen van complexe moleculen in de ruimte verklaart niet hoe deze zijn ontstaan. Hiervoor zijn laboratorium metingen vereist. In hoofdstuk 6 wordt een nieuwe opstelling beschreven, MATRI2CES, waarmee het mogelijk is om reacties in interstellair ijs te simuleren onder volledig gecontroleerde laboratorium omstandigheden. Een zeer hoge gevoeligheid is nodig, om ook zeer geringe hoeveelheden nieuw gevormde moleculen waar te kunnen nemen. MATRI2CES - Mass Analytical Tool for Reactions in Interstellar ICES) combineert 'time-of-flight' massa spectrometrie met laser verdamping van ijs waarin met behulp van ultraviolet licht reacties zijn gestart. De nieuwe opstelling biedt inzicht in de wijze waarop in de ruimte complexe moleculen - ook moleculen die van belang zijn als bouwstenen van het leven - ontstaan.

Complexe moleculen in stervormings gebieden

In hoofdstuk 7 worden complexe moleculen gebruikt als indicatoren voor de vorming van massieve sterren, een proces dat nog steeds niet goed begrepen wordt. De vorming van lichte sterren, met een massa vergelijkbaar met die van onze zon, leidt ertoe dat het invallende materiaal zich meer en meer in een vlak bevindt. Hierdoor kunnen UV fotonen van het centrale object (de protoster) ontsnappen en zo het ijs aan de buitenkant van het omhulsel bestralen. Onze hypothese is dat deze extra UV straling leidt tot een hogere hoeveelheid complexe organische moleculen in de gasfase. In dit hoofdstuk worden de relatieve hoeveelheden van complexe moleculen vergeleken tussen twee bron-types, een met een vlakke schijf structuur en een zonder een schijf structuur. De conclusie is dat er geen substantieel verschil bestaat in de hoeveelheid complexe moleculen in beide bron-types. Een mogelijke verklaring is dat alle massieve sterren gevormd worden in een vergelijkbare geometrie. Een andere mogelijkheid is dat het extra UV licht van de ster geen rol van betekenis

speelt in de productie van complexe moleculen en dat hun ontstaan vooral wordt bepaald door de koude fase van de moleculaire wolk.

Publications

Refereed papers

1. *Morphology of porous amorphous solid water and CO₂ containing ices*
K. Isokoski, J.-B. Bossa and H. Linnartz
Astronomy & Astrophysics, to be submitted (Chapter 3)
2. *Laser-desorption time-of-flight analysis of interstellar ices*
K. Isokoski, J.-B. Bossa, D. M. Paardekooper and H. Linnartz
Reviews of Scientific Instruments, to be submitted (Chapter 6)
3. *Highly resolved infrared spectra of pure CO₂ ice (15-75 K)*
K. Isokoski, C. A. Poteet and H. Linnartz
Astronomy & Astrophysics, to be submitted (Chapter 5)
4. *Anomalous CO₂ ice toward HOPS-68: a tracer of protostellar feedback*
C. A. Poteet, K. M. Pontoppidan, S. T. Megeath, D. M. Watson, **K. Isokoski**, J. E. Bjorkman,
P. D. Sheehan and H. Linnartz
The Astrophysical Journal, in press (Chapter 5)
5. *Chemistry of massive young stellar objects with a disk-like structure*
K. Isokoski, S. Bottinelli, E. F. van Dishoeck
Astronomy & Astrophysics, accepted (Chapter 7)
6. *Thermal collapse of porous interstellar ice*
J.-B. Bossa, **K. Isokoski**, M. S. de Valois and H. Linnartz
Astronomy & Astrophysics, 2012, 545, A82 (Chapter 2)
7. *CO mixed in CH₃OH: the answer to the non-detection of the 2152 cm⁻¹ band*
H. M. Cuppen, E. M. Penteado, **K. Isokoski**, N. van der Marel and H. Linnartz
Monthly Notices of the Royal Astronomical Society, 2011, 417, 2809-2816 (Chapter 4)
8. *HXeOBr in a xenon matrix*
L. Khriachtchev, S. Tapio, A. V. Domanskaya, M. Räsänen, **K. Isokoski** and J. Lundell
Journal of Chemical Physics, 2011, 134 (12)
9. *A Small Neutral Molecule with Two Noble-Gas Atoms: HXeOXeH*
L. Khriachtchev, **K. Isokoski**, A. Cohen, M. Räsänen and R. B. Gerber
Journal of American Chemical Society, 2008, 130 (19), 6114–6118
10. *Vibration rotation Fourier transform infrared spectrum of the C–D and C–C stretching fundamental, ν_1 and ν_2 , band systems of deuterated monobromoacetylene*
O. Vaittinen, R. Z. Martinez, P. Suero, **K. Isokoski** and L. Halonen
Journal of Molecular Spectroscopy, 2006, 236, 16-20

Conference proceedings

1. *Solid State Pathways towards Molecular Complexity in Space*
H. Linnartz, J.-B. Bossa, J. Bouwman, H. M. Cuppen, S. H. Cuylle, E. F. van Dishoeck,
E. C. Fayolle, G. Fedoseev, G. W. Fuchs, S. Ioppolo, **K. Isokoski**, T. Lamberts, K. I. Öberg,
C. Romanzin, E. Tenenbaum, J. Zhen
IAU Symposium 280: The Molecular Universe, 2011, 390–404

Curriculum vitae

I was born on 31st of May, 1982, in the town of Nivala, Finland. Soon after, my family moved to the neighboring town of Ylivieska, where I grew up.

After finishing senior high-school at Ylivieskan Lukio in the year 2001, I moved to Helsinki to pursue my studies in Chemistry at the University of Helsinki. Having a special interest in Physical Chemistry, I did my Master's research project in the Solid State Spectroscopy and Photochemistry Research Group, under the supervision of Prof. Markku Räsänen and Dr. Leonid Khriachtchev. Our research on the photochemistry of water in a xenon matrix resulted in the discovery of a new noble-gas compound, HXeOXeH. The Finnish Chemical Society awarded me the young researcher's prize for the best thesis in chemistry.

In 2009 I moved to Leiden, the Netherlands, where I started my PhD studies at the Raymond and Beverly Sackler laboratory for astrophysics, under the supervision of Prof. Harold Linnartz and Prof. Ewine van Dishoeck. The principal project was the construction of a new experimental instrument for the study of reactions leading to complex molecules in interstellar ices. The project was funded by the Netherlands research school for astronomy (NOVA). Other research projects during my PhD have focussed on the characterization of the morphology and composition of interstellar ices using a range of experimental techniques. I also had a chance to become familiar with observational astronomy during my stay at the James Clerk Maxwell Telescope (JCMT) at Mauna Kea, Hawaii. During my PhD I have supervised students and I have had the opportunity to present my work at several international conferences, including "The molecular universe" IAU Symposium 280 in Toledo (Spain), "European conference on surface science" in Groningen (Netherlands), "The chemical cosmos" COST annual meeting in Catania (Italy), and "New astronomical challenges for surface science" AstroSurf meeting in Edinburgh (UK). After my PhD, I am moving to Sydney, Australia.

Acknowledgements

This thesis would not have been possible without the support of many people in Leiden. I would like to express my gratitude to Martijn from the fine mechanical workshop (FMD) for being integral in the construction and repair of experimental instruments in the laboratory. I would like to thank René, Raymond, Peter and Arno from the electronic workshop (ELD) for always being committed to help, regardless of the feasibility of the problem. I want to thank Siva from the Expeditie for numerous awkward and hazardous deliveries to the lab. I am grateful to the computer group, Erik, David, Aart, Tycho and Niels, for their help in solving miscommunications and conflicts between the digital world and me. Equally important is the role of the secretariat Liesbeth, Anita and Jeanne. I also want to thank Yvonne Kluijt from the HR department for making bureaucracy a positive experience. I want to thank Jan, Evelijn and Pieter Taam (FSSC) for their help with the financial aspects of my research.

Doing astronomy with a chemistry background is not always easy. I am grateful to Remo for support during the observations at the JCMT, and to Sandrine Bottinelli for advice and patience during the data analysis and writing. I also thank Irene, Joe, Kalle, Kuo-Song and Umut for sharing their astronomer tricks with me. I am happy to have been part of the the Sackler laboratory group, and would like to thank the current and former members for creating a friendly working environment: Anton, Dongfeng, Claire, Edith, Emily, Gleb, Herma, Jean-Baptiste, Junfeng, Karin, Nadine, Steven and Thanja. I am particularly grateful to Sergio, Jordy and Rafael, who made me feel welcome on the 5th floor from early on, and Daniel for his help with the Nederlandse samenvatting. I also want to thank my office mates, Francisco, Simon, Silvia and Kirstin, for maintaining an excellent silence-to-chat ratio.

I might not have had the drive to complete this thesis without the *sisu* of my friend, colleague, and all-weather running partner, Carina. I would like to express my gratitude to my parents, my brother, Anna, Leena, Laura, and my other friends who I always look forward to seeing back in Finland. Last but not least, I thank my husband Joseph, who has given me irreplaceable support, advice and clarity during my PhD.

